Atom-light interactions in a photonic crystal waveguide

Thesis by
Jonathan David Hood

In Partial Fulfillment of the Requirements for the
degree of
Doctor of Philosophy

CALIFORNIA INSTITUTE OF TECHNOLOGY
Pasadena, California

2017
Defended September 21, 2016

ACKNOWLEDGEMENTS

In some sense, my time with Jeff's group started for me as an undergraduate at the University of Maryland, College park, since my undergraduate research advisor, Luis Orozco, was one of Jeff's first graduate students. Thanks to Luis's support, respect, and patience during those two years, I began to learn how to approach research.

I started in Jeff's group in August of 2010, having been thoroughly warned about the intensity and demand of the quantum optics group at Caltech. Joining a lab with a history of so many important contributions is a bit intimidating. The conference room is surrounded by the photographs of well-known physicists who originated from the group. What I didn't expect was how much I would learn from, and have my scientific methods and attitude shaped by, the other students who were also attracted to the group. In my first two years, I worked in the optomechanics group with Dalziel Wilson —- my initial source of wisdom about how to survive in the group — and Kang-Kuen Ni and Richard Norte, whose exciting research on levitating a silicon nitride micro-disk created the foundation for the fabrication of my later research.

In my second year, Jeff started to steer the group, me included, towards the goal of coupling atoms near nanophotonics devices. As a group, we had to transition from vacuum chambers and high finesse mirrors to the tiny world of nanophotonics, but we were extremely fortunate to be collaborating with one of the leaders of the community, Oskar Painter. Oskar and members of his group, Sean Meenehan, Richard Norte, and Justin Cohen, imparted vasts amount of knowledge and experience to our group. I spent much of the first few years characterizing and fabricating devices with Su-Peng Yu, whose incredibly creative approach to research led to a lot of advances and inspired my own work, and whose friendship made it a great time.

In the Lab 11, Aki Goban, Chen-Lung, and I tore down the old CQED experiment and designed a new experiment for trapping atoms near photonic crystal waveguides. Chen-Lung and Aki's expertise, ambition, and positive attitudes guided the experiment in the right direction. Aki and I spent a lot of time together in Lab 11, and I was constantly learning from his extensive knowledge and appreciation of the field of atomic physics. I was inspired by his ability to stay optimistic and "focus on the science." In my last year in the lab, I worked with Mingwu-Lu — who always emphasized the importance of learning things carefully, and Xingsheng – who took over the experiment ten times faster than I thought possible, and with whom I trust the experiment will have a bright future.

We were joined in our research efforts by the lab down the hall, Lab 2. Andrew McClung always challenged me and taught me new ways to do things, Juan Muniz inspired me with his determination and skill, Mike Martin shared his vast experiences from JILA and joined me in characterizing the devices, and Lucas Peng figured out how to do stuff on the computer no one else could. I am also thankful for the many game nights, Taco Tuesdays, Quantum optics band sessions, and sport nights.

We were fortunate to have a close collaboration with Darrick Chang and his group, which served as the inspiration for much of our work with band-gaps, as well as the optomechanics experiment. In my last year, we were joined by a member of his group, Ana Asenjo-Garcia, whose energetic and passionate approach to research helped us develop a new formalism to describe what we had been seeing in the lab. I was also thankful for Ana's advice and support as I was navigating the chaotic storm which is the last year of graduate school.

The journey into the world of atoms coupled to photonic crystals was of course led by my advisor Jeff Kimble, who saw the possibilities it would eventually open up. Of all of Jeff's sayings, the most memorable for me was "If you know what you are doing, don't do it." My initial reaction to this was honestly confusion, since this is perhaps not what you want to hear from the leader of your group. But I have learned from Jeff that feeling of “not knowing” is necessary to push the field into new areas. Jeff's incorrigible passion and high scientific standards have made my six years at Caltech an incredible experience.

But six years has felt like a long time to spend on the opposite coast of Kaitlyn's and my families, and we are thankful that we have always been able to rely on them for infinite support and love, and regularly reminding us how great life outside school and the lab can be.

And finally, Kaitlyn. We started dating at the end of our time at Maryland, and moved to Los Angeles to start graduate school together. Being able to share all of the experiences - the initial complete confusion, the eventual feeling that we might know what we are doing, the regular need to completely forget about everything in the lab - has been the best part of graduate school. Our relationship has grown so much in the last six years, and it is by far the thing I am most proud for my time in LA.

ABSTRACT

New opportunities for optical physics emerge from the integration of cold atoms with nanophotonic devices. Due to their small optical loss and tight field confinement, these nanoscale dielectric devices are capable of mediating strong atom-light interactions and open new avenues for quantum transport and quantum many-body phenomena. In particular, coupling atoms to the band edge of a photonic crystal waveguide (PCW) provides a unique platform for generating tunable range coherent atom-atom interactions which are mediated by the guided mode photons. Due to the evanescent nature of the field in the band gap, dissipation into the structure is suppressed exponentially. We have experimentally observed the transition into the bandgap for the first time by shifting the band edge frequency of the PCW relative to the D1 line of atomic cesium with an average of 3 atoms trapped along the PCW . In addition, we have developed a formalism that provides a clear mapping between the transmission spectra and the local Green's function, which allows us to identify signatures of dispersive and dissipative interactions between the atoms .

PUBLISHED CONTENT AND CONTRIBUTIONS

[1] J. D. Hood, A. Goban, A. Asenjo-Garcia, M. Lu, Y. Yu, D. E. Chang, and H. J. Kimble, "Atom-atom interactions around the band edge of a photonic crystal waveguide", Proceedings of the National Academy of Sciences **113**, 10507–10512 (2016) `10.1073/pnas.1603788113`, `http://www.pnas.org/content/113/38/10507.full.pdf`,
J.D.H. helped fabricate the structure, take data, perform data analysis, and prepare the manuscript.

[2] A. Asenjo-Garcia, J. D. Hood, D. E. Chang, and H. J. Kimble, "Atom-light interactions in quasi-one-dimensional nanostructures: A Green's-function perspective", Physical Review A - Atomic, Molecular, and Optical Physics **95**, 1–16 (2017) `10.1103/PhysRevA.95.033818`, `https://journals.aps.org/pra/abstract/10.1103/PhysRevA.95.033818`,
J.D.H. helped with theory and prepare the manuscript.

[3] S. P. Yu, J. D. Hood, J. A. Muniz, M. J. Martin, R. Norte, C. L. Hung, S. M. Meenehan, J. D. Cohen, O. Painter, and H. J. Kimble, "Nanowire photonic crystal waveguides for single-atom trapping and strong light-matter interactions", Applied Physics Letters **104** (2014) `10.1063/1.4868975`, `http://aip.scitation.org/doi/abs/10.1063/1.4868975`,
J.D.H. helped fabricate the structure, take data, and perform data analysis.

[4] A. Goban, C.-L. Hung, J. D. Hood, Y. Yu, J. A. Muniz, O. Painter, and H. J. Kimble, "Superradiance for Atoms Trapped along a Photonic Crystal Waveguide", Physical Review Letters **115**, 063601 (2015) `10.1103/PhysRevLett.115.063601`, `http://link.aps.org/doi/10.1103/PhysRevLett.115.063601`,
J.D.H. helped take data, perform data analysis, and prepare the manuscript.

[5] A. Goban, C.-L. Hung, Y. Yu, J. D. Hood, J. A. Muniz, J. H. Lee, M. J. Martin, A. C. McClung, K. S. Choi, D. E. Chang, O. Painter, and H. J. Kimble, "Atom-light interactions in photonic crystals", Nature communications **5**, 3808 (2014) `10.1038/ncomms4808`, `https://www.nature.com/articles/ncomms4808`,
J.D.H. helped take data and perform data analysis.

[6] K.-K. Ni, R. Norte, D. J. Wilson, J. D. Hood, D. E. Chang, O. Painter, and H. J. Kimble, "Enhancement of mechanical Q factors by optical trapping", Physical Review Letters **108**, 1–14 (2012) `10.1103/PhysRevLett.108.214302`, `https://journals.aps.org/prl/abstract/10.1103/PhysRevLett.108.214302`,
J.D.H. helped take data and perform data analysis.

TABLE OF CONTENTS

LIST OF ILLUSTRATIONS

Number *Page*

Chapter 1

INTRODUCTION

1.1 The fundamentals of strong atom-light interactions

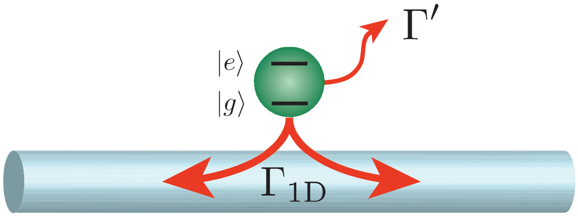

Figure 1.1: Atoms coupled to a quasi-1D system. The decay rate into the quasi-1D system is Γ_{1D}, and the decay into free-space modes and other modes of the 1D system is Γ'.

The building blocks for many quantum information protocols rely on the strong interaction between atoms and light. As a way characterize the strength of the interaction, Fig. 1.1 introduces a few basic concepts for atoms coupled to a quasi-1D optical system, by which we mean a system where the propagation is confined along one axis. The 1D structure can represent a variety of different systems, i.e. a free-space paraxial mode, nanofiber, cavity, or photonic crystal waveguide. In the past decade, atoms and other quantum emitters have been interfaced with the electromagnetic fields of a plethora of quasi-1D nanostructured reservoirs, ranging from high-quality optical [1–6] and microwave [7, 8] cavities to dielectric [9–15], metallic [16–19], and superconducting [20, 21] waveguides.

Γ_{1D} is the decay rate into a particular 1D mode, and Γ' is the decay rate into all other free-space modes and 1D modes. A more physical interpretation of these rates is that the the reflection coefficient for a single photon in the particular 1D mode is given by the ratio

$$R = \left(\frac{\Gamma_{1D}}{\Gamma' + \Gamma_{1D}}\right)^2. \tag{1.1}$$

The condition $\Gamma_{1D}/\Gamma' \gtrsim 1$ can be the standard by which we call the interaction strong, and results in a reflection coefficient $R \gtrsim 0.25$. As we will derive in

Chapter 2, the decay rate into a 1D mode is approximately given by

$$\Gamma_{1D}/\Gamma_0 \approx \frac{1}{2}\left(\frac{\sigma_0}{A}\right)\left(\frac{c}{v_g}\right), \tag{1.2}$$

where Γ_0 is the free-space decay. The first factor is the ratio of the atom's optical cross-section σ_0 to the optical mode's effective area A. The second factor is the slow light enhancement due to a reduced group velocity of light in the optical mode.

Nature has unfortunately conspired to make achieving strong atom-light interactions exceedingly difficult. The on-resonant optical cross-section of a two-state atom is $\sigma_0 \approx \lambda^2/2$ (see Sec. 2.3). As shown in Fig. 1.2(a), the smallest area that light can be focused down to in free-space, which is set by the diffraction limit, is also $A \approx \lambda^2$, resulting in inherently weak free-space interactions between atoms and photons. Another way to understand this weak interaction is that dipole radiation pattern of an atom poorly overlaps with modes of free-space light propagation, such as tightly focused Gaussian beams.

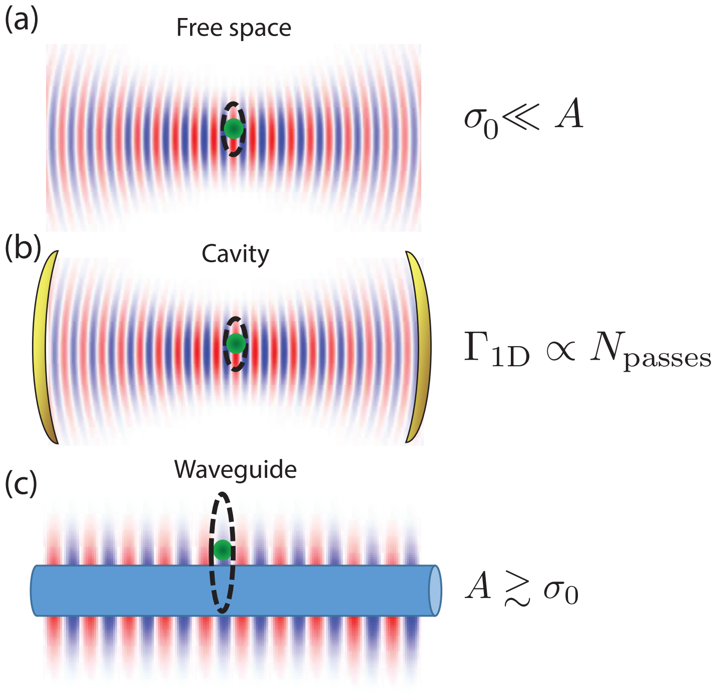

Figure 1.2: Coupling an atom (green), whose optical cross-section is represented by the dashed black line, to **(a)** free-space, **(b)** cavity, and a **(c)** dielectric waveguide.

Historically, there have been two primary methods for overcoming this limitation. The first method is to enhance the interaction by placing the atoms between two good mirrors, as shown in Fig. 1.2(b). Light reflects back and forth, and Γ_{1D} in Eq. (1.2) is enhanced by the roughly the number of times the photon passes the atom. This enhancement is used in the field CQED, pioneered by Jeff Kimble [22] in the optical domain and Herbert Walther and Serge Haroche [23] in the microwave domain, to achieve strong coupling. In the field of CQED, the ratio Γ_{1D}/Γ' is instead expressed as the cooperativity $C = g_c^2/\kappa_c\Gamma'$, where g_c is the half-vacuum Rabi frequency, and κ_c the cavity decay rate. While strong-atom light interactions are regularly achieved in CQED, the systems have proven difficult to scale. The left picture in Fig. 1.3 is the cavity from one of Jeff's old experiments, and the corresponding lab is on the right (which is in fact the lab we sadly dissembled to start our project).

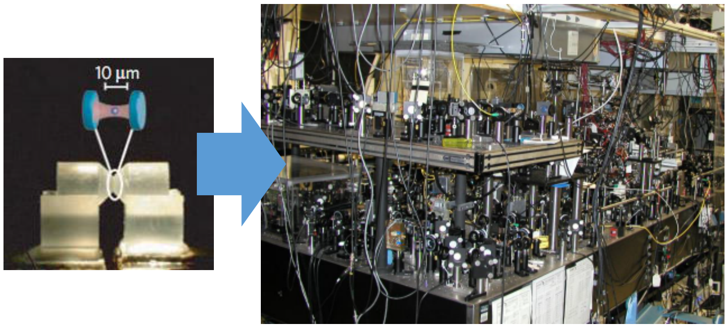

Figure 1.3: The cavity and lab from one of Jeff Kimble's CQED experiments [24].

A second method for increasing the interaction strength is to minimize the mode area in Eq. (1.2) by more tightly confining the light into a waveguide, as shown in Fig. 1.2(c). This has been used in the nanophotonics community to achieve strong interactions between dielectrics and solid state emitters. While there have been many experiments with atoms coupled to dielectric systems [3, 25], most of them have relied on the high optical Q or large number of atoms rather than the reduce mode area to achieve strong interactions. In the early 2000's, Hakuta's group performed experiments coupling the fluorescence of a cloud of atoms to a nanofiber going through the cloud [26, 27]. In the pioneering work by Rauschenbeutal's group [12], and now in many other groups [13–15], atoms are optically trapped around a sub-wavelength diameter nanofiber by the optical guided modes of the fiber. This system is convenient for its straightforward loading and cooling scheme, but is still restricted to small mode area since the atoms are trapped in the evanescent tail of the optical mode, resulting in $\Gamma_{1D}/\Gamma' \approx 0.03$ or $R \ll 1$.

The field of nanophotonics has provided a new opportunity for atom-light interactions. With fabrication precision now at the nanometer level, systems can be made with sufficient optical quality to achieve strong interactions. The solid state community has led the effort to couple quantum emitters to nanophotonic structures which both achieve a small mode area and high optical Q. Quantum dots [28], diamond color centers [29], and rare earth ions [30] have been coupled to photonic crystal cavities, waveguides, pillars, and microdisks. But with the convenient embedding of the quantum emitter into the dielectric comes the problems of inhomogeneous broadening, non-radiative decay, and varying resonance frequencies. Atoms have the reverse problem. They have ideal optical properties but are challenging to cool and trap near the dielectric structure.

The broad goal of our experiment has been to integrate atoms into a nanophotonic circuit. While this exciting new platform can lead to strong atom-light interactions in nanophotonic cavities [31] and waveguides [32], it is interesting to ask whether it is possible to create new types of optical systems with novel atom-photon, photon-photon, and atom-atom interactions.

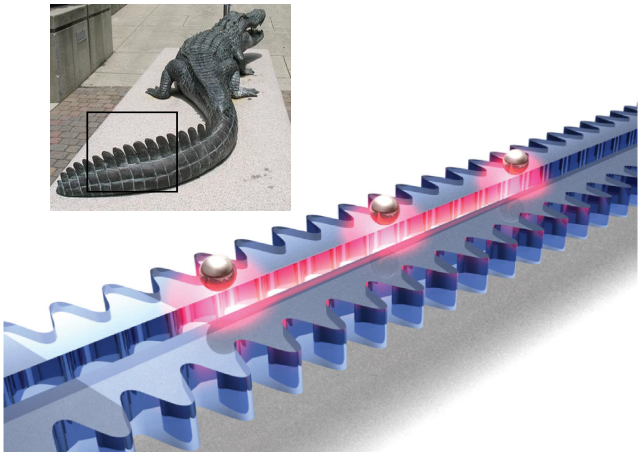

Figure 1.4: The Alligator photonic crystal waveguide.

This goal has led us to the Alligator photonic crystal waveguide (PCW), shown in Fig. 1.4. First, we will explain how the unique design of the device leads to strong-atom light interactions. As shown in Fig. 1.5(a), the waveguide has been cut in half, which is so that the atom can be positioned at the center of the device where the optical mode is the strongest. The atom is no longer in the tail of the mode's evanescent field, as is the case in the nanofiber. The optical mode area (defined in Eq. 2.87) for various atom positions is shown in Fig. 1.5(b) for the transverse-electric (TE) mode near the dielectric mode band-edge. At the center of the device, the mode area is $A \approx 0.3\,\lambda^2$.

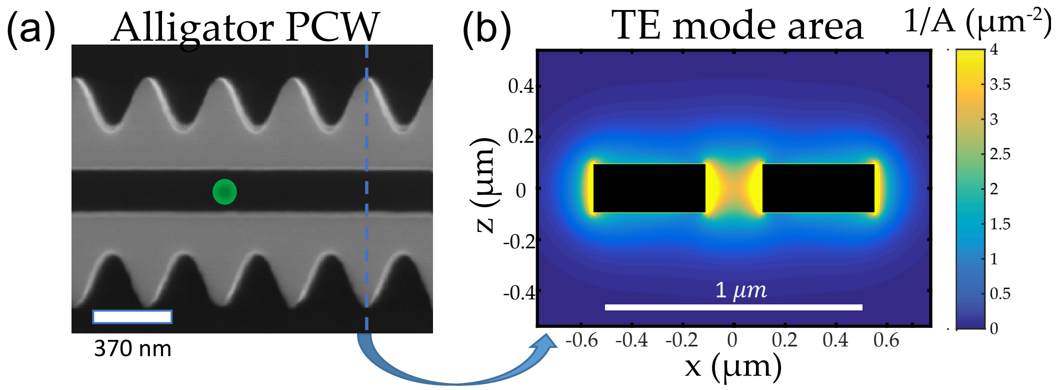

Figure 1.5: **(a)** SEM of an Alligator PCW. **(b)** Cross-section of the intensity of the TE mode near the lower band-edge. The units are in inverse mode area to show the mode area for the various atom positions. For the upper band-edge, the effective mode area is approximately two times smaller.

The second important feature of the structure is that the side walls are modulated to form the "teeth" of the waveguide. As shown in Fig. 1.6(a), a uniform waveguide has a approximately linear dispersion relation. Introducing just one tooth would result in scattering of the guided mode into free-space. But when the modulation is periodic, deconstructive interference of all the scatterers results in loss-less propagation through the waveguide. The periodic dielectric structure is called a photonic crystal waveguide (PCW) and has a much richer dispersion relation, as shown in Fig. 1.6(b). For certain bands of frequencies, the reflections from all the teeth constructively interfere in the backward propagating direction so that all the light is reflected, and the field decays evanescently. These frequencies constitute the bandgap. The group velocity of light $v_g = \frac{\mathrm{d}\omega}{\mathrm{d}k}$ is the slope of the dispersion relation. Near the band-edges, the group velocity is reduced and approaches zero at the band-edge. The slow light results in increased interaction time with the atom, which results in an increased interaction strength. This slow light enhancement can be seen from the second factor of $\Gamma_{1\mathrm{D}}$ in Eq. (1.2).

A simulated dispersion relation for the Alligator PCW is shown in Fig. 1.7(a). The photonic structure admits multiple modes, and we have plotted the dispersion relation for the transverse-electric (TE), which is mostly polarized in the plane of the waveguide, and the transverse-magnetic (TM), which is mostly polarized out of the plane of the waveguide. Modes in the shaded area are above the light line and are not guided [33]. The dimensions of the Alligator PCW are chosen to align the TE band-edges near the Cs $D1$ and $D2$ lines. Figure 1.7(b) shows the group velocity for the TE mode near the lower band-edge. In our experiment, we operate with a group index of $n_g \sim 10$, which requires aligning the band-edge to within 100 GHz of a Cs atomic resonant frequency.

The Cs D1 and D2 are aligned to the lower and upper band-edges so that the optical modes, shown in Fig. 1.8, have the same periodicity, which is set by the lattice constant a. The lower frequency band-edge is called the "dielectric mode" since

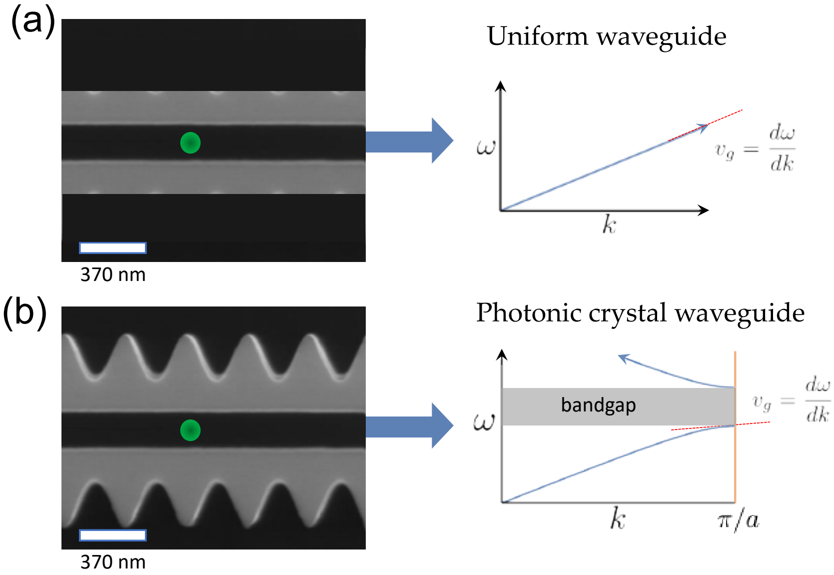

Figure 1.6: **(a)** A uniform waveguide has an approximately linear dispersion relation, while a **(b)** photonic crystal waveguide (PCW) has a band-gap and reduced group velocity near the band-edges. Note that the straightness of the uniform waveguide dispersion relation is exaggerated. A uniform waveguide also has dispersion due to the changing of the mode field as a function of frequency, which can be seen away from the bandgap in Fig. 1.7 .

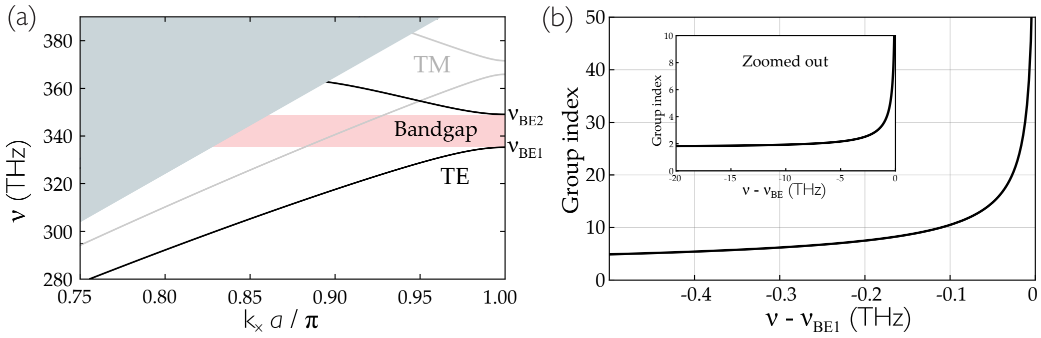

Figure 1.7: **(a)** Dispersion relations for the TE (black) and TM (gray) modes of an Alligator PCW [34]. The gray shaded area represents the light line. **(b)** Group index near the dielectric band. The inset is for a larger range, and shows that the group index converging to ~ 2 far away from the band-edge

the field is concentrated in the dielectric material. The upper frequency band-edge is called the "air mode" since the field is concentrated in the air. As worked on in Ref. [35], these two optical potentials can be combined with the Casimir-Polder potential to form an optical trap for the atoms.

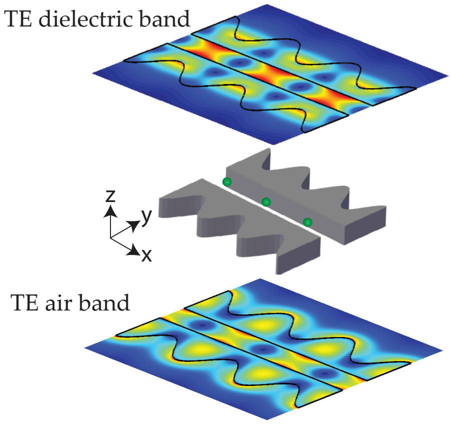

Figure 1.8: TE dielectric (top) and air (bottom) modes near the band-edge for an Alligator PCW.

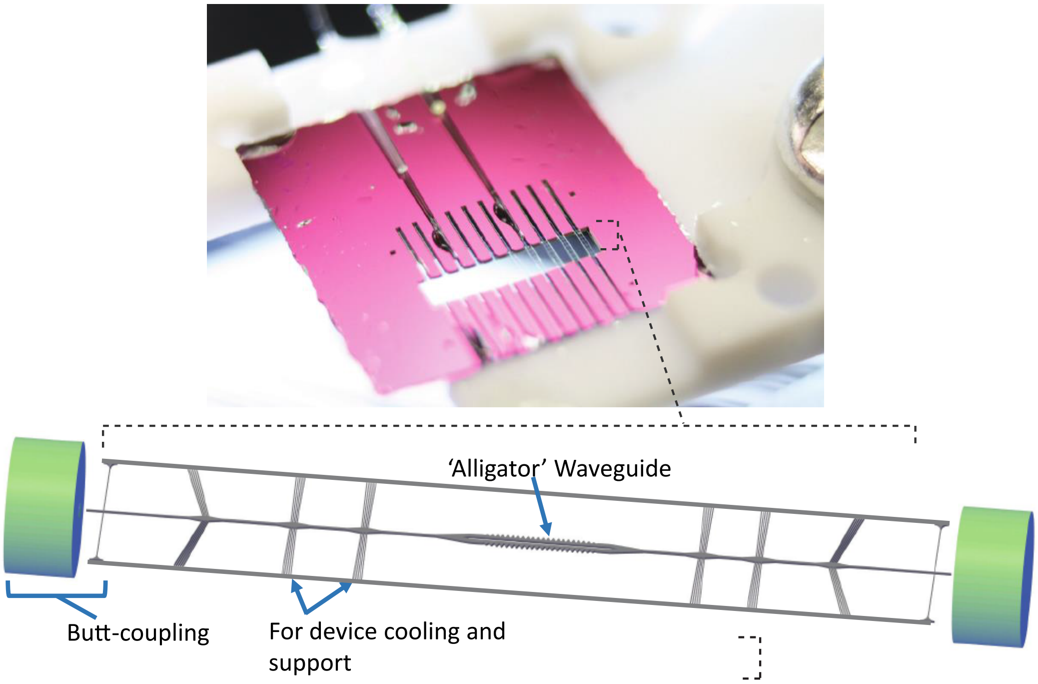

Figure 1.9: Photograph of the Alligator PCW chip and schematic of the device.

A photograph of an Alligator PCW chip is shown in Fig. 1.9. The details of the fabrication are described in Ref. [36]. The 1 × 1 cm chip consists of 200 nm thick silicon nitride on top of 200 μm thick silicon. As shown in the schematic beneath the photograph, the devices are suspended across the 2×6 mm window. Optical fibers (green) are positioned in V-grooves on both sides to couple light into and out of the device. The mode overlap between the waveguide and the ~ 6 μm diameter fiber mode is maximized by decreasing the waveguide width to $\sim$ 130 nm. This "butt-coupling" technique was developed in the Painter group, and typically gives a single pass transmission of $\sim$70%. One main limitation in the efficiency is actually the scattering caused by the 80 nm thick tether that holds the waveguide. The remaining structures in the schematic, such as the support rails on both sides and the tethers supporting the waveguide, are there to provide cooling and mechanical stability. The initial devices could only handle a few μW, but the thermal coupling to the 10 μm wide rails increased the limit to around 1 mW.

The Alligator PCW has been the result of a huge effort in both Oskar's and our group. One technical challenge has been suspending the few hundred nanometer wide structures across a 2 mm window. The devices are already very fragile, and the window allows the flow of liquids during the wet etching and cleaning. Another challenge has been to align the band-edge of the device to within a few hundred GHz of the Cs atomic resonance. This level of precision requires sub-nanometer precision. Initially, we had to scan the parameters of many devices to find one which was aligned, but we later learned tricks like atomic layer deposition (ALD) and a slow CF4 etch to fine-tune the dimensions after release. A collection of SEM scans of the entire length of a suspended Alligator PCW is shown in Fig. 1.10.

The purpose of the large window is to allow optical access for the trapping and cooling beams. Inspired by the nanofiber loading scheme, we trap atoms around the device in a magneto-optical trap (MOT). To maximize the number of atoms, we first load the atoms into a large MOT outside the window. The atoms are transferred to the "mini-MOT" in the MOT by abruptly changing the quadrapole center of the MOT, as shown in Fig. 1.11.

In the our first results with the Alligator PCW in Ref. [32] and Ref. [37], the atomic resonance frequency was outside the band-gap, and the results were similar to those of a cavity or waveguide. Outside the bandgap the propagation still goes as e^{ikx}, where k is the Bloch-wave vector. In particular, in Ref. [37] we trapped Cesium (Cs) atoms above the waveguide in a standing wave formed by a reflected field. The Cs atomic transition was only 100 GHz from the band-edge, resulting in a group velocity of $\sim c/10$. By measuring superradiant decay of the atoms, we inferred

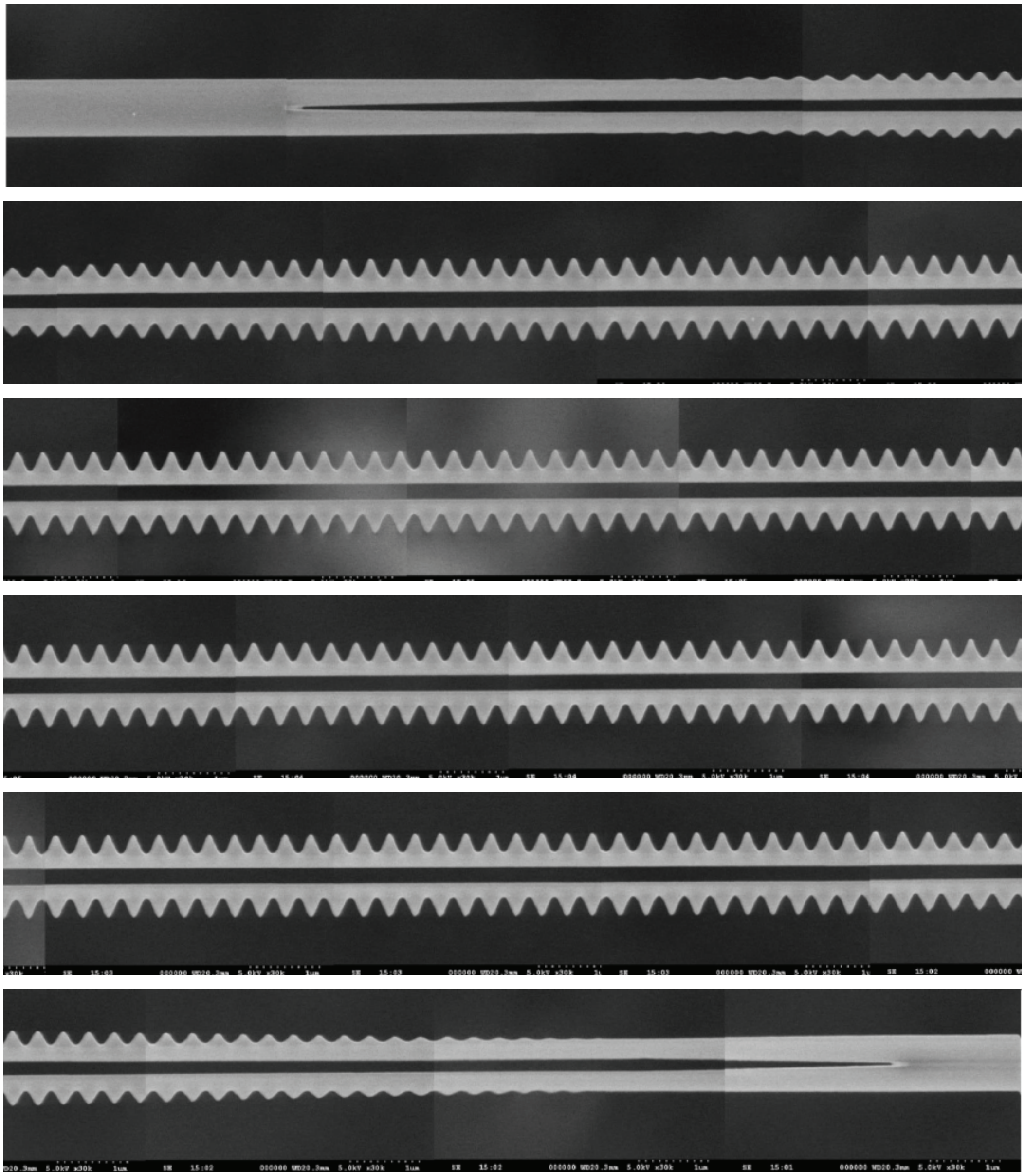

Figure 1.10: A collection of SEM's of the full length of a suspended Alligator PCW. The Alligator has 150 uniform cells, and 30 tapering cells on each side. I fabricated this particular structure.

$\Gamma_{1D}/\Gamma' \sim 1$ and around $N \sim 3$ atoms.

But what happens when the atom is coupled with its transition frequency inside the bandgap of the photonic crystal waveguide? The fields for frequencies in the bandgap decay exponentially, closely analogous to the attenuation of light in conducting material. So what happens when you put the atomic transition frequency in the bandgap?

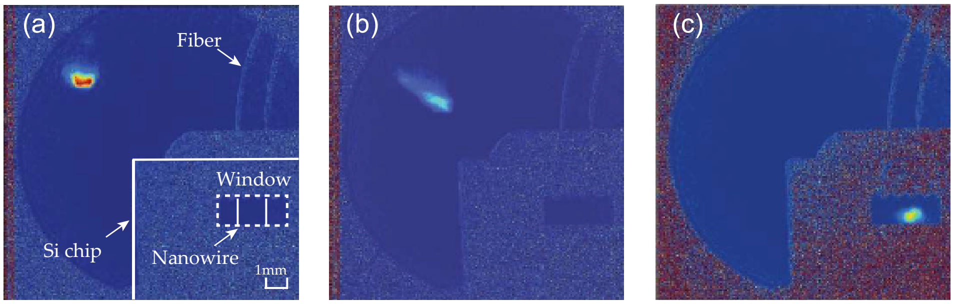

Figure 1.11: Absorption imaging of atoms trapped near a PCW chip. The atoms are transferred from a larger MOT outside the window of the chip to a "mini-MOT" in the window of the chip. The atomic cloud in (a) is called the "science MOT". The atomic cloud in (c) is called the "mini-MOT".

Imagine that an excited atom is coupled to the photonic crystal waveguide, but that the resonance frequency lies within the bandgap. As shown in Fig. 1.12, the atom can still emit a photon into the structure, but the photon decays exponentially. One way to interpret this is that the atom induces a cavity mode, and when the atom moves, the cavity follows it. This is of course in stark contrast to a cavity mode, where the cavity mode is defined by the position of the mirrors. Since the photon cannot leave the 1D system, the decay rate into the guided mode Γ_{1D} is zero, and we are left with only conservative interactions between the atoms. As we will derive in Chapter 3, this situation results in a Hamiltonian $H = \sum_{i,j=1}^{N} J_{ij}\hat{\sigma}_i^{\dagger}\hat{\sigma}_i$, where $\hat{\sigma}$ and $\hat{\sigma}^{\dagger}$ are the raising and lowering operators for the atomic ground and excited states. The coherent coupling J_{ij} between two atoms is proportional to he overlap of their photonic modes and scales with $e^{-\kappa|x_i-x_j|}$, where κ^{-1} is the field decay length. As a result, photonic crystal waveguides have been proposed as promising candidates to study long- and tunable-range coherent interactions between quantum emitters [38–41].

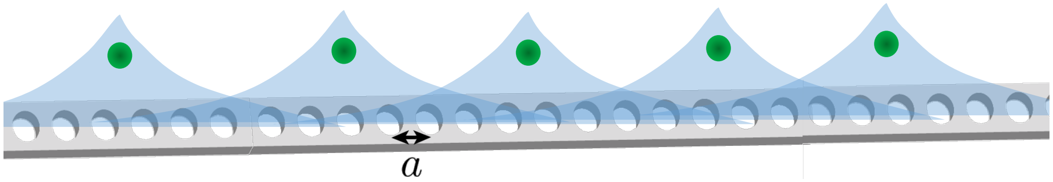

Figure 1.12: Atoms coupled to the bandgap of a photonic crystal waveguide. The atoms and photon cloud form atom-photon bound states.

In Ref. [42], we report the first observation of cooperative atom-atom interactions around the band-edge of a photonic crystal waveguide. Our experiment opens the door to fascinating new scenarios, such as exploring many-body physics with large spin exchange energies and low dissipation [43].

While there are successful formalisms for quantum light-matter interactions in cavities (the Jaynes-Cummings Hamiltonian) and waveguides (the scattering matrix formalism), the finite photonic crystal waveguide does not fit either of those categories. To explore these new types of quasi-1D optical systems, we therefore require a generalized model. The quantization scheme based on Green's function formalism (reviewed in Chapter 3) provides an elegant description of light-matter interactions where the details of the optical system, whether a cavity, waveguide, or photonic crystal waveguide, is captured in the electromagnetism Green's function. In Ref. [44], we used this formalism to create a generalized description of the transmission spectra for atoms coupled to arbitrary quasi-1D systems. We show a direct mapping between the transmission spectra and the Green's function at the position of the atoms.

1.2 Summary of Thesis

- Chapter 2 reviews the classical interactions of atoms and light in the context of the electromagnetic Green's function.
- Chapter 3 introduces the formalism for the quantization of the electromagnetic field in the presence of dielectric media. At its heart is the electromagnetic Green's function. The equations of motions for multiple atoms coupled is derived in the low-saturation regime to show the similarity to the classical results of Chapter 2, and then an effective master equation describing the atom-atom interactions is derived using the Markov approximation.
- Chapter 4 explores the spectral features of atoms coupled to quasi-1D systems using the low-saturation formalism developed in Chapter 3. The special cases of cavities, waveguides, and photonic crystal waveguides are considered.
- Chapter 5 describes experimental results for atoms trapped near an Alligator PCW, and the transmission spectra are fitting using the models from Chapter 4 to measure the coherent and dissipation coupling rates at the positions of the atoms.
- Chapter 6 provides further details for the experiment in Chapter 5.

Chapter 2

STRONG ATOM-LIGHT INTERACTIONS: THE MOSTLY CLASSICAL STORY

2.1 Introduction

At the heart of quantum optics is the goal of strong atom-light interactions. In free-space, the strength is limited by the diffraction limit for how tightly light can be focused. The interaction probability is typically around a few percent or less. There have been three main strategies for increasing the interaction strength.

One is to place the atom in a cavity between two highly reflective mirrors, thereby increasing the interaction strength by the number of times the light passes the atom. Another strategy is to focus the light even more tightly by confining the light to a dielectric (nanophotonic) or metallic (plasmonic) waveguide. When the light's transverse area, the mode area, is small as compared to the atom's optical cross-section, the interaction probability is increased.

A strategy that is less commonly used is to slow the light down by confining it to a highly dispersive waveguide, for example a photonic crystal. The interaction probability is proportional to the amount of time it takes for light to pass the atom.

Due to the highly nonlinear nature of the atom, the complete description requires a quantum mechanical formalism for both the atom and the light. However, the classical case is much easier to derive and learn from, and shares many of the same results as the quantum case. This chapter treats the classical case, and Chapter 3 will describe the more complete quantum case.

In this chapter, we derive a formalism to the describe the interaction strength between atoms and waveguide, where the atoms will be approximated as classical dipole oscillators (an excellent approximation to the quantum case in the low saturation limit). The electromagnetic Green's function, which is the propagator of the electromagnetic field, will have a prominent role in both the classical and quantum formalism. Section 2.2 derives the Green's function for a waveguide from Maxwell's equations. Section 2.3 addresses the interaction of a single atom with the field, and section 2.4 addresses the case of multiple atom which can interact with each through their fields. The interactions will be described in terms of the Green's function, and section 2.5 derives expressions for the Green's function of a dielectric waveguide.

2.2 Electromagnetic wave equation and Green's function

In this section, we will derive the wave equation for the electric field. The macroscopic Maxwell's equations in linear isotropic dielectrics are [45, 46]

$$\nabla \cdot \mathbf{D}(\mathbf{r},t) = \rho_f(\mathbf{r},t) \tag{2.1}$$

$$\nabla \cdot \mathbf{B}(\mathbf{r},t) = 0 \tag{2.2}$$

$$\nabla \times \mathbf{E}(\mathbf{r},t) = -\frac{\partial}{\partial t}\mathbf{B}(\mathbf{r},t) \tag{2.3}$$

$$\nabla \times \mathbf{H}(\mathbf{r},t) = \frac{\partial}{\partial t}\mathbf{D}(\mathbf{r},t) + \mathbf{J}_f(\mathbf{r},t). \tag{2.4}$$

Here, ρ_f is the free charge density and $\mathbf{J}_f$ is the free current density. To convert to frequency space, we assume that all variables are oscillating with $e^{-i\omega t}$, i.e. $\mathbf{E}(\mathbf{r},t) = \mathrm{Re}\big[\mathbf{E}(\mathbf{r},\omega)e^{-i\omega t}\big]$. Maxwell's equations in frequency space are

$$\nabla \cdot \mathbf{D}(\mathbf{r},\omega) = \rho_f(\mathbf{r},\omega) \tag{2.5}$$

$$\nabla \cdot \mathbf{B}(\mathbf{r},\omega) = 0 \tag{2.6}$$

$$\nabla \times \mathbf{E}(\mathbf{r},\omega) = \mathrm{i}\omega\mathbf{B}(\mathbf{r},\omega) \tag{2.7}$$

$$\nabla \times \mathbf{H}(\mathbf{r},\omega) = -\mathrm{i}\omega\mathbf{D}(\mathbf{r},\omega) + \mathbf{J}_f(\mathbf{r},\omega). \tag{2.8}$$

The displacement field $\mathbf{D}(\mathbf{r},\omega)$ and magnetizing field $\mathbf{H}(\mathbf{r},\omega)$ are related to the electric field and magnetic field by the dielectric constant and magnetic susceptibility respectively,

$$\mathbf{D}(\mathbf{r},\omega) = \epsilon_0\epsilon(\mathbf{r},\omega)\mathbf{E}(\mathbf{r},\omega), \qquad \mathbf{B}(\mathbf{r},\omega) = \mu_0\mu(\mathbf{r},\omega)\,\mathbf{H}(\mathbf{r},\omega). \tag{2.9}$$

Properties of the dielectric constant are discussed in Sec. 3.3. For dielectric optical structures, we will assume that there is no free charge, $\rho_f(\mathbf{r},\omega) = 0$, and that the material is not magnetic, $\mu(\mathbf{r},\omega) = 1$. The wave equation for the electric field in the presence of a dielectric material is obtained by substituting Eq. (2.9) into Maxwell's equations, taking the curl of both sides of Eq. (2.7), and then replacing the resulting $\nabla \times \mathbf{B}$ term with Eq. (2.8). The resulting wave equation is

$$\nabla \times \nabla \times \mathbf{E}(\mathbf{r},\omega) - \frac{\omega^2}{c^2}\epsilon(\mathbf{r},\omega)\mathbf{E}(\mathbf{r},\omega) = i\mu_0\omega\mathbf{J}_f(\mathbf{r},\omega). \tag{2.10}$$

The source term on the right side is the free current density $\mathbf{J}_f(\mathbf{r},\omega)$. An oscillating polarization density also results in a current given by $\mathbf{J}_f(\mathbf{r},t) = \frac{\mathrm{d}}{\mathrm{d}t}\mathbf{P}(\mathbf{r},t)$, or in frequency space $\mathbf{J}_f(\mathbf{r},\omega) = -\mathrm{i}\omega\,\mathbf{P}(\mathbf{r},\omega)$. In the classical approximation, the atoms will be treated as oscillating dipole moments, and the source will be more conveniently expressed in terms of an oscillating polarization density,

$$\nabla \times \nabla \times \mathbf{E}(\mathbf{r}, \omega) - \frac{\omega^2}{c^2}\epsilon(\mathbf{r}, \omega)\mathbf{E}(\mathbf{r}, \omega) = \mu_0\omega^2\, \mathbf{P}(\mathbf{r}, \omega). \tag{2.11}$$

An oscillating point dipole source $\mathbf{p}_0$ at position $\mathbf{r}_0$ results in a polarization density $\mathbf{P}(\mathbf{r}, \omega) = \mathbf{p}_0\, \delta(\mathbf{r} - \mathbf{r}_0)$. The resulting electric field from the point dipole source is closely related to the Green's function, which is defined as the solution of the wave equation with a delta function source at position $\mathbf{r}'$,

$$\nabla \times \nabla \times \mathbf{G}(\mathbf{r}, \mathbf{r}'; \omega) - \frac{\omega^2}{c^2}\epsilon(\mathbf{r}, \omega)\mathbf{G}(\mathbf{r}, \mathbf{r}'; \omega) = \overset{\leftrightarrow}{\mathbf{I}}\, \delta(\mathbf{r} - \mathbf{r}'). \tag{2.12}$$

The Green's function is useful for calculating the electric field from an arbitrary polarization source. The resulting electric field is obtained by integrating the Green's function over the polarization density, as shown by Dyson's equation[1]

$$\mathbf{E}(\mathbf{r}, \omega) = \mathbf{E}_0(\mathbf{r}, \omega) + \mu_0\omega^2 \int \mathrm{d}^3\mathbf{r}'\, \mathbf{G}(\mathbf{r}, \mathbf{r}', \omega)\, \mathbf{P}(\mathbf{r}', \omega). \tag{2.13}$$

Here $\mathbf{E}_0(\mathbf{r}, \omega)$ is the homogeneous solution — the solution with no sources.

For an oscillating point dipole moment at position r_0 with polarization density $\mathbf{P}(\mathbf{r}, \omega) = \mathbf{p}_0\, \delta(\mathbf{r} - \mathbf{r}_0)$, Dyson's equation reduces to

$$\mathbf{E}(\mathbf{r}, \omega) = \mathbf{E}_0(\mathbf{r}, \omega) + \mu_0\omega^2\mathbf{G}(\mathbf{r}, \mathbf{r}_0, \omega) \cdot \mathbf{p}_0. \tag{2.14}$$

Ignoring the homogeneous solution, the electric field at position $\mathbf{r}$ due to an oscillating dipole moment at position $\mathbf{r}_0$ is proportional to the Green's function between those points. In fact, the Green's function is often calculated by performing a numerical simulation of the electric field from a point dipole source.

Here, I give a few useful Green's function identities. One important identity for the Green's function which we will often use is the reciprocity identity [46]

$$\mathbf{G}^T(\mathbf{r}, \mathbf{r}'; \omega) = \mathbf{G}(\mathbf{r}', \mathbf{r}; \omega), \tag{2.15}$$

---

[1] The proof of Dyson's equation is as follows. We define the operator $\mathcal{L}_E = \nabla \times \nabla \times -\frac{\omega^2}{c^2}\epsilon(\mathbf{r}, \omega)$, and write the wave equation as $\mathcal{L}_E\mathbf{E}(\mathbf{r}, \omega) = \mu_0\omega^2\mathbf{P}(\mathbf{r}, \omega)$. The Green's function differential equation is $\mathcal{L}_E\mathbf{G}(\mathbf{r}, \mathbf{r}'; \omega) = \overset{\leftrightarrow}{\mathbf{I}}\delta(\mathbf{r} - \mathbf{r}')$. We multiply both sides of this by $\mu\omega^2\mathbf{P}(\mathbf{r}')$ and integrate over all $\mathbf{r}'$-space to get $\int \mathrm{d}^3\mathbf{r}'\mathcal{L}_E\mathbf{G}(\mathbf{r}, \mathbf{r}')\mu_0\omega^2\mathbf{P}(\mathbf{r}', \omega) = \mu_0\omega^2\mathbf{P}(\mathbf{r}) = \mathcal{L}_E\mathbf{E}(\mathbf{r}, \omega)$, where in the last expression we have substituted the wave equation. When the operator and integral commute, we can take the operator $\mathcal{L}_E$ outside the integral. The result is $\mathcal{L}_E \int \mathrm{d}^3\mathbf{r}'\mathbf{G}(\mathbf{r}, \mathbf{r}')\mu_0\omega^2\mathbf{P}(\mathbf{r}', \omega) = \mathcal{L}_E\mathbf{E}(\mathbf{r}, \omega)$. Then we remove the operator $\mathcal{L}_E$ from both sides to get Dyson's equation.

which is related to the fact that if a source and a detector are swapped, the detected field is the same. Another important identity comes from the requirement that in the time domain, $\mathbf{G}(\mathbf{r}, \mathbf{r}', \tau)$ is real,

$$\mathbf{G}^*(\mathbf{r}, \mathbf{r}', \omega) = \mathbf{G}(\mathbf{r}, \mathbf{r}', -\omega). \tag{2.16}$$

Further, causality requires that $\mathbf{G}(\mathbf{r}, \mathbf{r}', \tau) = 0$ for $\tau < 0$, which leads to $\mathbf{G}^*(\mathbf{r}, \mathbf{r}', \omega)$ being analytic in the upper half of the complex plane. These properties are discussed more in Chapter 3.

The free-space Green's function

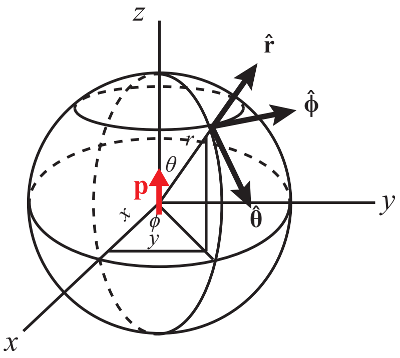

Figure 2.1: Coordinate system for the oscillating dipole. The dipole **p** is orientated along the $\hat{\mathbf{z}}$-axis.

For most systems, we will have to rely on numerical solutions for the Green's functions. However, the free-space Green's function, which we have already seen is proportional to the electric field due to an oscillating dipole moment, has a simple analytic solution [45]. For a dipole oriented in the $\hat{\mathbf{z}}$-direction as shown in Fig. 2.1, the emitted electric field is

$$E_\theta = \mu_0 \omega^2 |\mathbf{p}| \sin\theta \frac{\omega}{4\pi c} \left[e^{ikr} \left(\overbrace{\frac{1}{k^3 r^3}}^{\text{NF}} - \overbrace{\frac{i}{k^2 r^2}}^{\text{IF}} - \overbrace{\frac{1}{kr}}^{\text{FF}} \right) \right] \tag{2.17}$$

$$E_r = \mu_0 \omega^2 |\mathbf{p}| \cos\theta \frac{\omega}{4\pi c} \left[e^{ikr} \left(\frac{2}{k^3 r^3} - \frac{2i}{k^2 r^2} \right) \right]. \tag{2.18}$$

The wave-vector k is $k = \omega/c$. These expressions are separated into terms representing the near-field $(1/kr)$, intermediate-field $(1/k^2r^2)$, and far-field $(1/k^3r^3)$. Figure 2.2 shows the electric field orientation and magnitude for both the far-field and near-field. The far-field only contains transverse fields (E_θ), which are symmetric around the $\hat{\mathbf{z}}$-axis and form the typical donut-shape associated with radiation from a dipole or a linear antenna.

The near-field, shown in Fig. 2.2(b), contains both transverse fields (E_θ) and the longitudinal fields (E_r). In the limit of $kr \to 0$, the electric field simplifies to the DC dipole solution, $E_\theta = \frac{|p|}{4\pi\epsilon_0}\frac{\sin(\theta)}{r^3}$ and $E_r = \frac{|p|}{4\pi\epsilon_0}\frac{2\cos(\theta)}{r^3}$, or as is more commonly written

$$\mathbf{E}_{\mathrm{NF}} = \frac{1}{4\pi\epsilon_0}\frac{1}{r^3}\left[3(\mathbf{p}\cdot\hat{\mathbf{r}}) - \mathbf{p}\right]. \tag{2.19}$$

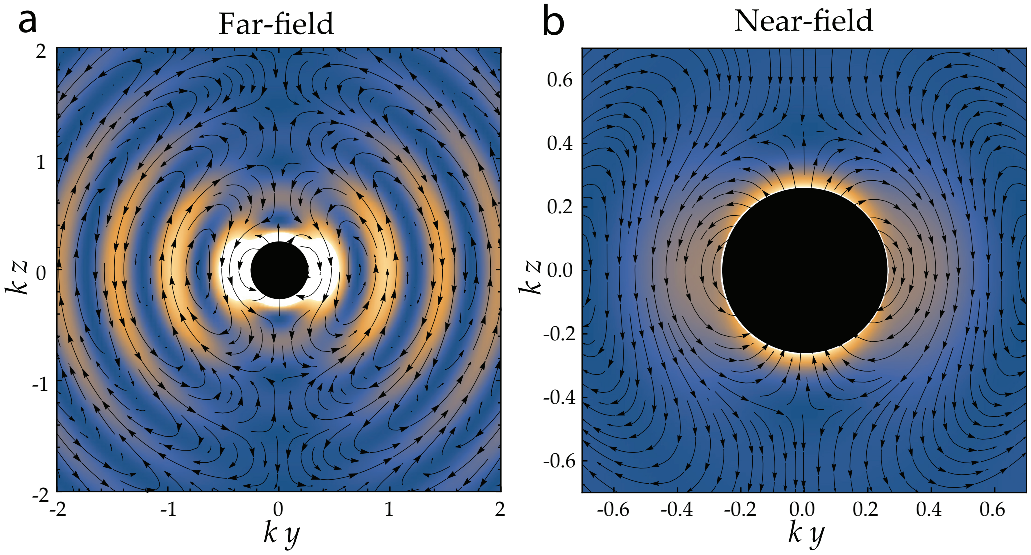

Figure 2.2: Far-field **(a)** and near-field **(b)** of the electric field $\mathbf{E}(\mathbf{r}, \omega)$ radiated from a linear oscillating dipole. The vectors represent the direction of the electric field, while the color represents the magnitude (blue is low magnitude, yellow is large magnitude). The black circle is included to compare the scales of the two plots.

2.3 The power radiated by an oscillating dipole

An oscillating dipole radiates energy into the environment, and the amount of power radiated is in turn influenced by the environment. Systems can be designed to either enhance or suppress the dipole radiation and thereby decrease or increase the decay rate. In this section, we will see how the decay rate of the dipole energy is related to the Green's function.

The time averaged power radiated out of a system P_{rad} can calculated by performing a surface integral of the normal component of the Poynting vector over a surface surrounding the oscillating dipole. It can also be calculated by integrating the line-current $\mathbf{j}(\mathbf{r})$ with the in-phase electric field, which performs work on the line-current,

$$P_{\mathrm{rad}} = -\frac{1}{2}\int \mathrm{d}^3\mathbf{r}\,\mathrm{Re}[\mathbf{j}(\mathbf{r})\cdot\mathbf{E}(\mathbf{r},\omega)]. \tag{2.20}$$

An oscillating dipole moment at position $\mathbf{r}_0$ results in the line-current $\mathbf{j}(\mathbf{r}) = -i\omega\mathbf{p}\delta(\mathbf{r}-\mathbf{r}_0)$, and therefore the power radiated is

$$P_{\mathrm{rad}} = \frac{\omega}{2}\,\mathrm{Im}\left[\mathbf{p}^* \cdot \mathbf{E}(\mathbf{r}_0,\omega)\right]. \tag{2.21}$$

Using Dyson's equation, we replace the electric field at the dipole $\mathbf{E}(\mathbf{r}_0)$ with the self-Green's function, $\mathbf{E}(\mathbf{r}_0,\omega) = \mu_0\omega^2\mathbf{G}(\mathbf{r}_0,\mathbf{r}_0,\omega)\cdot\mathbf{p}$, which then gives

$$P_{\mathrm{rad}} = \frac{\omega^3|\mathbf{p}|^2}{2\epsilon_0 c^2}\,\hat{\mathbf{n}}_p \cdot \mathrm{Im}\left[\mathbf{G}(\mathbf{r}_0,\mathbf{r}_0,\omega)\right]\cdot\hat{\mathbf{n}}_p. \tag{2.22}$$

Here, $\hat{\mathbf{n}}_p$ is the unit vector of the dipole, $\mathbf{p} = |\mathbf{p}|\hat{\mathbf{n}}_p$. Note that we have assumed that $\hat{\mathbf{n}}_p$ is real, e.g. for a linear dipole moment. In order to convert the power radiated into a decay rate, we must also know the initial total energy $W(t{=}0)$ of the dipole. The averaged energy of a dipole is the sum of the averages of the kinetic and potential energy, $W = \langle m\dot{x}^2/2 + kx^2/2\rangle = \langle \frac{m}{2q^2}(\omega_0^2 p^2(t) + \dot{p}^2(t))\rangle = \frac{m\omega_0^2}{2q^2}|p_0|^2$, where q is the charge of the oscillator and m is the mass. Assuming that the energy decays exponentially as $W(t) = W(0)e^{-\Gamma t}$, the power radiated is related to the total energy and decay rate by $P_{\mathrm{rad}}(0) = \frac{\mathrm{d}}{\mathrm{d}t}W(t)|_{t=0} = -\Gamma W(t=0)$. Solving for the decay rate and substituting the energy W and power P_{rad} gives

$$\Gamma = 2\mu_0\omega^2\frac{q^2}{2m\omega}\,\hat{\mathbf{n}}_p \cdot \mathrm{Im}\left[\mathbf{G}(\mathbf{r}_0,\mathbf{r}_0,\omega)\right]\cdot\hat{\mathbf{n}}_p. \tag{2.23}$$

The decay rate of an oscillating dipole is proportional to the imaginary part of the self-Green's function $\mathbf{G}(\mathbf{r}_0,\mathbf{r}_0,\omega)$ at the position of the dipole. The decay rate of a dipole can be enhanced or inhibited by the environment.

We will often want to take the ratio of the decay rate in a system to the decay rate in free-space, a ratio which is known as the Purcell factor [47]. To find the free-space Green's function at the source ($\mathbf{r} = 0$), we perform a Taylor series of the electric field in Eq. (2.17) and (2.18) over small kr. Keeping both the first order real and imaginary terms, the result is

$$\lim_{kr\to 0}\mathbf{E}(\mathbf{r},\omega) = \mu_0\omega^2|\mathbf{p}|\frac{\omega}{4\pi c}\left[\frac{2}{(kr)^3} - i\frac{2}{3}\right]\hat{\mathbf{z}}. \tag{2.24}$$

The electric field is parallel to the dipole orientation. The real part is the same as the DC dipole case and diverges at $\mathbf{r} = 0$. The divergence is a result of the dipole being infinitesimally small and would go away if we considered instead an oscillating polarization density for a sphere of any radius. In contrast, the imaginary part of the electric field, which is out-of-phase with the oscillating dipole, is finite. Using Dyson's equations, the imaginary part of the self-Green's function is

$$\mathrm{Im}[\mathbf{G}_0(\mathbf{r}_0, \mathbf{r}_0, \omega)] = \frac{\omega}{6\pi c}\overleftrightarrow{\mathbf{I}}. \tag{2.25}$$

Inserting this result into the decay rate gives the classical expression for the free-space decay rate,

$$\Gamma_0 = \mu_0 \omega^2 \frac{q^2}{2m\omega}\frac{\omega}{3c}, \tag{2.26}$$

which depends on the particle's charge q and mass m. The Purcell factor - the ratio between the decay rate and the free-space decay rate- is then

$$\mathrm{PF} = \Gamma/\Gamma_0 = \frac{6c}{\omega}\, \hat{\mathbf{n}}_p \cdot \mathrm{Im}\left[\mathbf{G}(\mathbf{r}_0, \mathbf{r}_0, \omega)\right] \cdot \hat{\mathbf{n}}_p. \tag{2.27}$$

The Purcell factor is independent of the charge and mass, and is also valid for the Purcell factor of a two level system in the quantum derivation (see Sec. 3).

In the quantum theory for an atom, the free-space decay rate of a non-degenerate excited state $|e\rangle$ to a ground state $|g\rangle$ is instead

$$\Gamma_0 = \frac{\mu_0 \omega_0^2}{\hbar}\left(\frac{\omega_0 |\langle g|\hat{p}|e\rangle|^2}{3\pi c}\right), \tag{2.28}$$

which can be calculated using the Wigner-Weisskopf approximation [48]. The quantum result can be obtained from our classical result by replacing the dipole energy with $\hbar\omega_0$, and by replacing the dipole moment with half of the dipole moment matrix element, $\mathbf{p} \longrightarrow \langle g|\hat{\mathbf{p}}|e\rangle/2$. The factor of $1/2$ is due to the fact that the Fourier transform of the classical dipole moment spans positive and negative frequencies.

Optical cross-section.

Another way to characterize the power radiated by a dipole is in terms of the optical cross section σ, which can be interpreted as the source area for an incoming plane wave that is scattered. It is calculated by dividing the power radiated over the incoming intensity I_{in}, $\sigma = P_{\mathrm{rad}}/I_{\mathrm{in}}$. Remarkably, the on-resonant optical cross-section for an oscillating dipole is independent of the charge and mass, and is given by

$$\sigma_0 = \frac{3\lambda^2}{2\pi}. \tag{2.29}$$

This result only requires that the decay of the dipole oscillator is due only to radiated power, or equivalently to the radiative back-action caused by resulting field. In the quantum formalism, this result will also be true for the on-resonant optical cross-section of a two level system.

The proof of the optical cross-section is the following. The intensity for an incoming plane wave of amplitude $\mathbf{E}_0$ is given by $I_{\text{in}} = \frac{c\epsilon_0}{2}|\mathbf{E}_0|^2$. The power radiated (see Eq. (2.21)) is $P_{\text{rad}} = \frac{\omega}{2}\text{Im}[\mathbf{p}^* \cdot \mathbf{E}(\mathbf{r}_0, \omega)]$, which after substituting polarizability equation $\mathbf{p} = \alpha(\omega)\mathbf{E}(\mathbf{r}_0, \omega)$, gives

$$P_{\text{rad}} = \frac{\omega}{2}|\mathbf{E}(\mathbf{r}_0, \omega)|^2 \text{Im}[\alpha(\omega)].$$

The optical cross-section is defined as the ratio of the radiated power to the incoming intensity, $\sigma = P_{\text{rad}}/I_{\text{in}}$. Under the Born approximation, $\mathbf{E}(\mathbf{r}, \omega) \approx \mathbf{E}_0$, in which case $\sigma(\omega) = \frac{\omega_0}{2}\text{Im}[\alpha(\omega)]$. From Eq. (2.32), the on-resonant polarizability for a dipole is $\alpha(\omega_0) = \mathrm{i}q^2/m\omega_0\Gamma_0$, and then the on-resonant optical cross-section is $\sigma_0 = q^2/m\epsilon_0 c\Gamma_0$. After substituting the decay rate from Eq. (2.26) into this equation, the charge and mass terms cancel, and we get $\sigma_0 = \frac{3\lambda^2}{2\pi}$.

2.4 Radiatively coupled dipoles

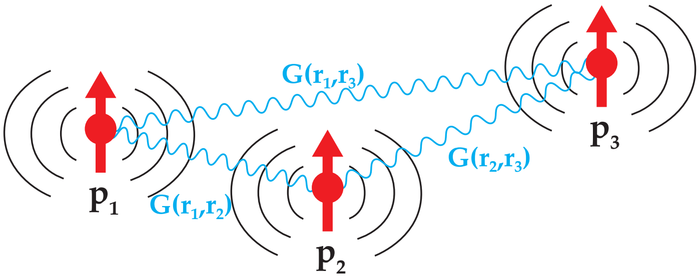

Figure 2.3: Radiatively coupled dipoles.

In the previous section, we saw how the behavior of a dipole oscillator is influenced by the environment. Next, we consider a system with N oscillating dipoles, as shown in Fig. 2.3. The dipoles again interact with the environment, but they also interact with each other through their electric fields. The equation of motion for a single dipole $\mathbf{p}_i$ with damping Γ' and resonance frequency ω_0 is given by[1]

$$\frac{d^2\mathbf{p}_i}{dt^2} + \Gamma'\frac{d\mathbf{p}_i}{dt} + \omega_0^2\mathbf{p}_i = \frac{q^2}{m}\mathbf{E}(\mathbf{r}_i, t). \tag{2.30}$$

Here, $\mathbf{E}(\mathbf{r}_i, t)$ is the total electric field at the dipole. The field can have contributions from the dipole itself, other dipoles, or from an external source. To simplify the problem, we will assume that the electric field $\mathbf{E}(\mathbf{r}, t)$ is due to radiation in a specific mode of interest, for example a guided mode of a nanofiber or a mode of a cavity.[2] The damping rate Γ' is the decay rate independent of the single mode. Similarly, ω_0 is the resonance frequency of the dipole oscillator independent of the single mode.

We would like to solve the system of equations for the dipoles. First, we switch to the frequency domain by assuming that $\mathbf{p}_i(t)$ and $\mathbf{E}(\mathbf{r}_i, t)$ oscillate with frequency ω (i.e. $\mathbf{p}_i(t) = \mathbf{p}_i e^{-\mathrm{i}\omega t}$),

$$(\omega_0^2 - \omega^2 - \mathrm{i}\omega\Gamma')\mathbf{p}_i = \frac{q^2}{m}\mathbf{E}(\mathbf{r}_i, \omega). \tag{2.31}$$

This equation is just the polarizability equation $\mathbf{p}_i = \boldsymbol{\alpha} \cdot \mathbf{E}(\mathbf{r}_i, \omega)$, where the polarizability is

$$\alpha(\omega) = \frac{q^2/m}{(-\omega^2 + \omega_0^2 - \mathrm{i}\omega\Gamma')} \approx \frac{q^2/2\omega m}{(\Delta - \mathrm{i}\Gamma'/2)}. \tag{2.32}$$

Here the detuning is $\Delta = \omega - \omega_0$. In the last part of the equation, we have assumed that the detuning is small so that $\omega^2 - \omega_0^2 = (\omega + \omega_0)(\omega - \omega_0) \approx 2\omega(\omega - \omega_0)$. This approximation is analogous to the rotating wave approximation in the quantum mechanical formalism.

The electric field $\mathbf{E}(\mathbf{r}, \omega)$ in the system contains contributions from the driving source field $\mathbf{E}_0(\mathbf{r}, \omega)$ as well as from the N radiating dipoles. From Eq. (2.14), the total electric field is [45, 49]

$$\mathbf{E}(\mathbf{r}, \omega) = \mathbf{E}_0(\mathbf{r}, \omega) + \mu_0\omega^2 \sum_{j=1}^{N} \mathbf{G}(\mathbf{r}, \mathbf{r}_j, \omega) \cdot \mathbf{p}_j. \tag{2.33}$$

Substituting this expression into the polarizability equation $\mathbf{p}_i = \boldsymbol{\alpha}\mathbf{E}(\mathbf{r}_i, \omega)$ results in the following system of equations:

$$\frac{1}{\boldsymbol{\alpha}}\mathbf{p}_i - \mu_0\omega^2 \sum_{j=1}^{N} \mathbf{G}(\mathbf{r}_i, \mathbf{r}_j, \omega) \cdot \mathbf{p}_j = \mathbf{E}_0(\mathbf{r}_i, \omega). \tag{2.34}$$

---

[1] This equation is more obvious when it is written in terms of position $\mathbf{r} = \mathbf{d}/e$ and forces as $m\frac{d^2\mathbf{r}_i}{dt^2} + \Gamma' m\frac{d\mathbf{r}_i}{dt} + m\omega_0^2\mathbf{r}_i = q\mathbf{E}(\mathbf{r}_i, t)$.

[2] If we make $\mathbf{E}(\mathbf{r}, \omega)$ the total electric field here, then we would not need to include Γ' on the left hand side since the damping will naturally come from the atom's interactions with the modes of the system. The problem arises from the divergence of the real part of the self-Green's function, which is a result of us assuming an infinitely small dipole. We would therefore get a divergent frequency shift. To avoid this problem, we instead assume that $\mathbf{E}(\mathbf{r}, \omega)$ is due a finite set of modes, for which we do not have this divergence problem.

To simplify this expression, we assume that all the dipoles are orientated in the same direction and dot product both sides of Eq. (2.34) by the dipole unit vector $\hat{\mathbf{n}}_p$,

$$\frac{1}{\alpha} p_i - \mu_0 \omega^2 \sum_{j=1}^{N} \hat{\mathbf{n}}_p \cdot \mathbf{G}(\mathbf{r}_i, \mathbf{r}_j, \omega) \cdot \hat{\mathbf{n}}_p \; p_j = E_0(\mathbf{r}_i, \omega), \tag{2.35}$$

where I have used $\mathbf{p}_i = p_i \hat{\mathbf{n}}_p$ and $\hat{\mathbf{n}}_p \cdot \mathbf{E}_0(\mathbf{r}_i) = E_0(\mathbf{r}_i)$. Next, we substitute the polarizability from Eq. (2.32) into the first term and multiply by $-q^2/2m\omega$ to get

$$(\Delta + \mathrm{i}\Gamma'/2) p_i + \mu_0 \omega^2 \frac{q^2}{2m\omega} \sum_{j=1}^{N} \hat{\mathbf{n}}_p \cdot \mathbf{G}(\mathbf{r}_i, \mathbf{r}_i, \omega) \cdot \hat{\mathbf{n}}_p \; p_j = -E_0(\mathbf{r}_i, \omega) \frac{q^2}{2m\omega}. \tag{2.36}$$

Next we define the complex coupling rate,

$$g_{ij} = \mu_0 \omega^2 \frac{q^2}{2m\omega} \hat{\mathbf{n}}_p \cdot \mathbf{G}(\mathbf{r}_i, \mathbf{r}_j, \omega) \cdot \hat{\mathbf{n}}_p \equiv J_{ij} + \mathrm{i}\Gamma_{ij}/2. \tag{2.37}$$

and we define real and imaginary parts of this complex coupling rate as the spin-exchange rate J_{ij} (called Lamb shift when $i = j$) and dissipation rate Γ_{ij},[2]

$$J_{ij} = \mu_0 \omega^2 \frac{q^2}{2m\omega} \hat{\mathbf{n}}_p \cdot \mathrm{Re}[\mathbf{G}(\mathbf{r}_i, \mathbf{r}_j, \omega)] \cdot \hat{\mathbf{n}}_p \tag{2.38}$$

$$\Gamma_{ij} = 2\mu_0 \omega^2 \frac{q^2}{2m\omega} \hat{\mathbf{n}}_p \cdot \mathrm{Im}[\mathbf{G}(\mathbf{r}_i, \mathbf{r}_j, \omega)] \cdot \hat{\mathbf{n}}_p. \tag{2.39}$$

In terms of these rates, the system of equations for the N oscillating dipoles and external source $E_0(\mathbf{r}, \omega)$ are

$$\boxed{(\Delta + \mathrm{i}\Gamma'/2)\, p_i + \sum_{j=1}^{N} (J_{ij} + \mathrm{i}\Gamma_{ij}/2)\, p_j = -E_0(\mathbf{r}_i, \omega) \frac{q^2}{2m\omega}.} \tag{2.40}$$

A single dipole

To interpret the system of equations in Eq. (2.40), we first look at the case of a single dipole p_1, for which the equation is

$$\left[\Delta + J_{11} + \mathrm{i}(\Gamma' + \Gamma_{11})/2\right] \, p_1 = -E_0(\mathbf{r}_1, \omega) \frac{q^2}{2m\omega}. \tag{2.41}$$

---

[2] Using the same procedure that we used to convert the classical free-space decay rate into the quantum decay rate of a two-level system, we can convert these rates to their corresponding quantum analogue. We substitute the averaged dipole energy with $\hbar\omega$ and the dipole moment with half the dipole matrix element ($\mathbf{d} = \langle g|\hat{\mathbf{r}}|e\rangle$) to obtain the coefficients in the quantum case:

$$J_{ij} = \frac{\mu_0 \omega^2}{\hbar} \mathrm{Re}[\mathbf{d}^* \cdot \mathbf{G}(\mathbf{r_i}, \mathbf{r_j}, \omega) \cdot \mathbf{d}],$$

$$\Gamma_{ij} = 2\frac{\mu_0 \omega^2}{\hbar} \mathrm{Im}[\mathbf{d}^* \cdot \mathbf{G}(\mathbf{r_i}, \mathbf{r_j}, \omega) \cdot \mathbf{d}.$$

This equation can be interpreted as a polarizability equation, where the dipole has a modified polarizability due to its interaction with the new mode. The total decay rate is increased to $\Gamma' + \Gamma_{11}$, and the resonance frequency is shifted to $\omega_0 - J_{11}$. The increased decay rate is in agreement with the previous section which found that Γ_{11} is proportional to work done on the dipole by its own field (radiative back-action). The frequency shift J_{11} is proportional to the component of the electric field that is in phase with the oscillating, and thus does not do work on the dipole. However, it does modify its effective resonance frequency.

Two radiatively coupled dipoles

Next we look at the system of equations in Eq. (2.40) for two dipoles which interact through their electric fields. The system of equations in matrix notation is

$$\begin{pmatrix} \Delta + \mathrm{i}\Gamma'/2 + g_{11} & g_{12} \\ g_{21} & \Delta + \mathrm{i}\Gamma'/2 + g_{22} \end{pmatrix} \begin{pmatrix} p_1 \\ p_2 \end{pmatrix} = -\frac{q^2}{2m\omega} \begin{pmatrix} E_0(\mathbf{r}_1, \omega) \\ E_0(\mathbf{r}_2, \omega) \end{pmatrix}. \tag{2.42}$$

Due the reciprocity condition for the Green's function in Eq. (2.15), the complex coupling rate $g_{ij} = J_{ij} + \mathrm{i}\Gamma_{ij}$ has the symmetry $g_{21} = g_{12}$, and correspondingly $J_{21} = J_{12}$ and $\Gamma_{21} = \Gamma_{12}$. Therefore, the matrix on the left, which we will call $\mathbf{M}$ is symmetric. We express the matrix and vectors in tensor notation so that the system of equations is $\mathbf{M}\,\mathbf{p} = -\frac{q^2}{2m\omega}\mathbf{E}_0$. We can solve this system of equations by finding the two eigenvectors $\mathbf{p}_\pm$ and eigenvalues $\lambda_\pm$ of the eigenvalue equation $\mathbf{M}\,\mathbf{p}_\pm = \lambda_\pm \mathbf{p}_\pm$. To simplify the results, we assume that the self-interactions for the two dipoles are the same, $g_{22} = g_{11}$, which will often be the case for systems we will look at. The two eigenvectors and eigenvalues are

$$\mathbf{p}_\pm = \begin{pmatrix} 1 \\ \pm 1 \end{pmatrix}, \quad \lambda_\pm = \Delta + \mathrm{i}\Gamma'/2 + g_{11} \pm g_{12}. \tag{2.43}$$

These two eigenmodes correspond to when the dipoles are oscillating in-phase and out-of-phase with each other, as shown in Fig. 2.4. One mode decays with rate $\Gamma^+_{\mathrm{tot}} = \Gamma' + \Gamma_{11} + \Gamma_{12}$ and the other with decay rate $\Gamma^-_{\mathrm{tot}} = \Gamma' + \Gamma_{11} - \Gamma_{12}$. We will assume that $\Gamma_{12} > 0$, in which case $\mathbf{p}_+$ is called the "bright" eigenmode (since it has enhanced decay), and $\mathbf{p}_-$ is called the "dark" eigenmode (since it has suppressed decay).

In the time domain, the eigenmodes $\mathbf{p}_\pm(t) = \mathrm{Re}[\mathbf{p}_\pm e^{i\lambda_\pm t} e^{-i\omega_0 t}]$ are

$$\mathbf{p}_\pm(t) = p_0 \begin{pmatrix} 1 \\ \pm 1 \end{pmatrix} e^{-(\Gamma' + \Gamma_{11} \pm \Gamma_{12})t} \cos[(\omega_0 + J_{11} \pm J_{12})t]. \tag{2.44}$$

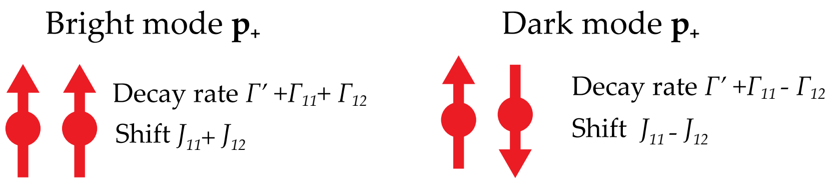

Figure 2.4: Bright and dark eigenmodes, and their decay rates and frequency shifts. We have assumed that $\Gamma_{12} > 0$, but if $\Gamma_{12} < 0$, then the names are reversed.

To understand how the atoms interact with each other, we look at the solution for when only one dipole is initially excited, $p_1(0) = p_0$ and $p_2(0) = 0$. The solution is

$$p_{1,2}(t) = e^{-(\Gamma'+\Gamma_{11}-\Gamma_{12})t}\mathrm{Re}\left[\frac{1}{2}\, e^{\mathrm{i}(\omega_0+J_{11})t}\left(\pm e^{-\mathrm{i}J_{12}t} + e^{\mathrm{i}J_{12}t}\, e^{-2\Gamma_{12}t}\right)\right]. \tag{2.45}$$

The behavior of the expression in the parenthesis is determined by the decay term $e^{-2\Gamma_{12}t}$. For short times $t \ll \frac{1}{2\Gamma_{12}}$, the expression in the parenthesis results in energy oscillation between the two atoms (called spin-exchange in the quantum language) at a rate J_{12},

$$p_1(t < \frac{1}{2\Gamma_{12}}) \approx \overbrace{e^{-(\Gamma'+\Gamma_{11}-\Gamma_{12})t/2}}^{\text{decay}}\ \overbrace{\cos[(\omega_0 + J_{11})t]}^{\text{fast-oscillation}}\ \overbrace{\cos[J_{12}t]}^{\text{spin-exchange}} \tag{2.46}$$

$$p_2(t < \frac{1}{2\Gamma_{12}}) \approx -e^{-(\Gamma'+\Gamma_{11}-\Gamma_{12})t/2}\ \sin[(\omega_0 + J_{11})t]\ \sin[J_{12}t]. \tag{2.47}$$

But for longer times $t \gg \frac{1}{2\Gamma_{12}}$, the second term in the parentheses vanishes, and we are left with the dark eigenmode

$$p_{1,2}(t) = \pm\frac{1}{2}\,\overbrace{e^{-(\Gamma'+\Gamma_{11}-\Gamma_{12})t}}^{\text{decay}}\ \overbrace{\cos[(\omega + J_{11} - J_{12})t]}^{\text{fast oscillation}}\,. \tag{2.48}$$

This example clarifies the roles of the rates in the problem, and they are summarized in the following table:

Spin-exchange rate	J_{12}
Decoherence of spin-exchange	$2\,\Gamma_{12}$
Decay rate	$\Gamma' + \Gamma_{11} - \Gamma_{12}$
Fast dipole oscillation freq	$\omega_0 + J_{11}\ (t \ll \frac{1}{2\Gamma_{12}})$ or $\omega_0 + J_{11} - J_{12}\ (t \gg \frac{1}{2\Gamma_{12}})$

We plot the solutions for a few specific physical systems to observe the characteristic behavior of the two dipoles. To simplify the plots, the decay rate due to all the other modes Γ' is negligible. The additional of Γ' just results in an additional exponential decay to the overall profile.

The simplest physical system is a uniform waveguide, for example in a nanofiber or in a single free-space mode. As will be shown in Sec. 2.5, the Green's function for a 1D uniform waveguide is proportional to $G(x_i, x_j, \omega) \propto \mathrm{i}\, e^{\mathrm{i}k|x_i - x_j|}$, which means that

$$\Gamma_{ij} \propto \cos(k|x_i - x_j|), \quad J_{ij} \propto \sin(k|x_i - x_j|). \tag{2.49}$$

Here, k is the effective wave-vector of the guided mode. The nature of the interactions depends on the separation distance between the dipoles, but the self-interaction is always purely dissipative, since $J_{11} = J_{22} = 0$.

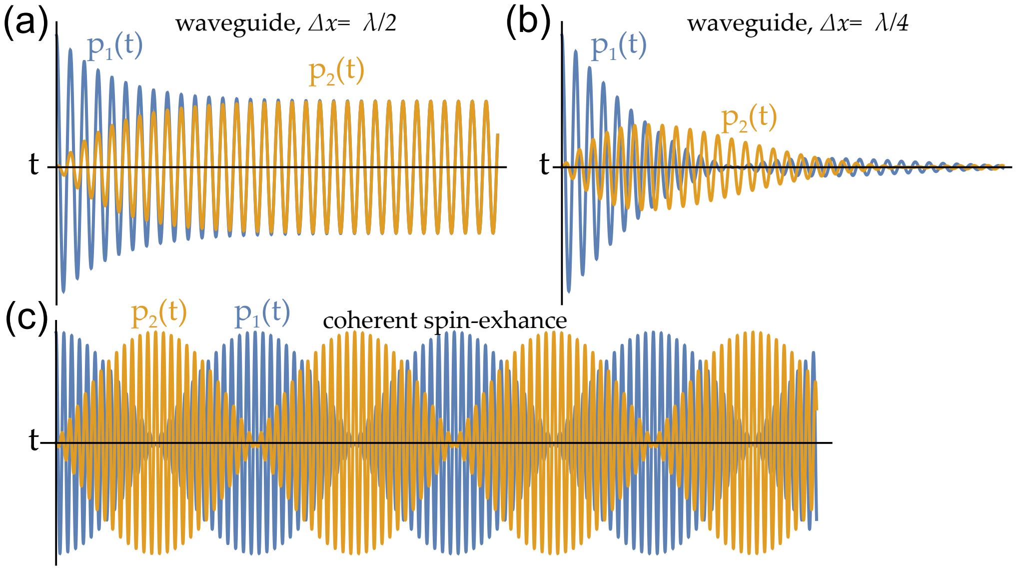

Figure 2.5: Solutions for two radiatively coupled dipoles with dipole $p_1(t=0) = p_0$ initially excited and dipole $p_2(t=0) = 0$ unexcited. **(a)** Dipoles coupled to waveguide and separated by $\lambda/2$. The interaction are all dissipative. **(b)** Dipoles coupled to a waveguide and separated by $\lambda/4$. The self-interactions are dissipative, but the interactions between the atoms are coherent. **(c)** Dipoles coupled to a system with predominantly coherent interactions, e.g. a far-off-resonant cavity or a photonic crystal bandgap.

Fig. 2.5(a) shows the simulation for when the dipoles are coupled to a waveguide and separated by a distance $m\lambda/2$, for integer m. For this case, $k|x_1 - x_2| = m\pi$, and the interaction is also purely dissipative with $J_{12} = 0$. This implies that there will be no spin-exchange. In the long time limit, only the dark mode remains.

Fig. 2.5(b) shows a simulation for when the dipoles are coupled to a waveguide and separated by a distance $\lambda/4 + m\lambda/2$, for integer m. For this case, $k|x_1 - x_2| = \pi/2 + m\pi$. The self-interaction is still purely dissipative, but now the interaction term is purely coherent, with $\Gamma_{12} = 0$. Therefore, spin-exchange will occur indefinitely, but the overall profile decays with a rate $\Gamma' + \Gamma_{11}$.

Another common physical system is a cavity. When the bare dipoles are on-resonance with the cavity, the self-interaction and interaction are both purely dissipative ($J_{11} = J_{12} = 0$), as will be shown later in Sec. 2.5. The simulation is the same as the case of the waveguide with the atoms spaced by $m\lambda/2$. However, in the cavity case, the rates Γ_{11} and Γ_{12} are enhanced by the Finesse of the cavity (the number of times light bounces back and forth).

One last interesting case is when all the interactions are coherent ($\Gamma_{11} = \Gamma_{12} = 0$), as shown in Fig. 2.5(c). The energy oscillates between the dipoles indefinitely and overall energy does not decay. For a cavity, the ratio of the coherent rates to the dissipative rates is proportional to the detuning of the dipoles from the cavity resonance, so that in the far-off-resonance case the interactions are predominantly coherent. The photonic crystal band-gap is also a powerful system for observing coherent interactions, and the ratio of the coherent rates to the dissipative rates increases exponentially with detuning from the band-edge.

2.5 Solutions to the electromagnetic Green's function

In the previous sections, we have seen how an atom's interaction with the environment and other atoms can be described in terms of the electromagnetic Green's function. To study how atoms behave in various systems, we will need to calculate the Green's function. The free-space Green's function has a simple analytic solution, which was introduced in Sec. 2.2. Analytic solutions also exist for cylindrical waveguides [50–52] and rectangular waveguides [52, 53], but for more complex waveguides, we must resort to numerical solutions.

The relationship between the Green's function and the electric field radiated by a point dipole provides an efficient way to calculate the Green's function. The electric field $\mathbf{E}(\mathbf{r}, \omega)$ due to an oscillating dipole at $\mathbf{r}_0$ is proportional to $\mathbf{G}(\mathbf{r}, \mathbf{r}_0, \omega)$. Numerical techniques, such as finite-difference time-domain (FDTD) [54, 55], efficiently solve this problem. But a simulation of a dipole in a system much larger than the size of the wavelength can take many hours, and the full Green's function requires many of these simulations.

Another way to solve for the Green's function is to expand the Green's function in terms of the electric field eigenmodes, which can be solved by finite-element methods [34, 56]. The technique works well for systems such as uniform or periodic waveguide, or a high Q cavity. For more open systems where the modes extend outside the simulation volume, such as a finite periodic system or a bad cavity, we will still have to rely on numerical simulation or approximate solutions.

In this section, we will derive an expression for the Green's function in terms of the eigenmodes of the system. And then we will derive a simplified expression for the Green's function of a periodic or uniform waveguide. Finally, we will use this result to learn how to engineer a waveguide with strong atom-light interactions.

Eigenmodes and the Green's function

The wave equation in operator form and written as an eigenvalue equation is [57]

$$\mathcal{L}_E \mathbf{E}(\mathbf{r}) = \frac{\omega^2}{c^2}\mathbf{E}(\mathbf{r}), \quad \text{where} \quad \mathcal{L}_E = \frac{1}{\epsilon(\mathbf{r})}\nabla\times\nabla\times \ . \tag{2.50}$$

Note that we have taken away the frequency dependence of $\epsilon(\mathbf{r}, \omega)$, since now the frequency ω acts as an eigenvalue for the eigenvalue equation. The eigenmodes depend on the dielectric function as well as the boundary conditions of the system. Typical boundary conditions are periodic -where the field at one surface is the same as field at another surface times a phase- and closed- where electric field is zero at the boundary. Closed boundary conditions are used for cavities and result in a discrete set of modes. Periodic boundary conditions are used for photonic crystals, which have a periodic dielectric constant, and result in a continuous set of eigenvalues. Note that the periodic boundary condition also applies to a uniform waveguide, which is the limiting case of the lattice constant going to zero.

For dielectrics that are periodic in one dimension, the dielectric function satisfies $\epsilon(\mathbf{r}+\mathbf{a}) = \epsilon(\mathbf{r})$, where $\mathbf{a}$ is the lattice vector that defines the symmetry. Bloch's theorem states that the eigenmodes of a periodic operator can expressed as the product of a Bloch function $\mathbf{u}_{\mathbf{k}n}(\mathbf{r})$, which has the same periodicity as the dielectric constant, times a plane wave with a Bloch wave-vector $\mathbf{k}$, [33, 58, 59]

$$\mathbf{E}_{\mathbf{k}n}(\mathbf{r}) = \mathbf{u}_{\mathbf{k}n}(\mathbf{r})e^{i\mathbf{k}\cdot\mathbf{r}} \quad \text{with} \quad \mathbf{u}_{\mathbf{k}n}(\mathbf{r}+\mathbf{a}) = \mathbf{u}_{\mathbf{k}n}(\mathbf{r}). \tag{2.51}$$

For a 1D photonic crystal, the Bloch wave-vector $\mathbf{k}$ is parallel to $\mathbf{a}$, and takes on values $-\pi/a \leq |\mathbf{k}| \leq \pi/a$, a region which is sometimes called the Brillouin zone. Fig. 2.6 shows an example of a dispersion relation for a periodic system. Besides the Bloch wave-vector, the modes are also labeled by the band number $n = (1, 2, 3, \ldots)$. The dashed line shows a non-periodic waveguide that is also mapped into the Brillouin, although practically there is no advantage for doing so.

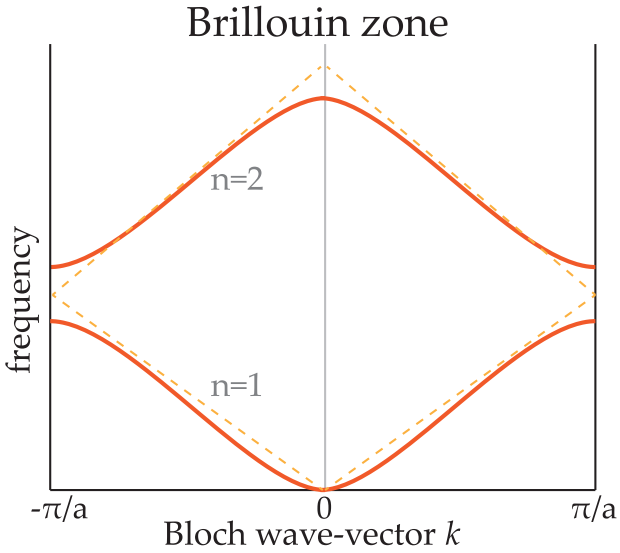

Figure 2.6: Dispersion relation for a 1D photonic crystal with lattice constant a. The dispersion relation is frequency versus the Bloch wave-vector k, where $-\pi/a < k < \pi/a$. The dashed line is the dispersion relation for a uniform 1D waveguide, which can also be folded over into the Brillouin zone.

A useful identity that follows from time reversal symmetry relates the forward and backward propagating modes,

$$\mathbf{E}_{-\mathbf{k}n}(\mathbf{r}) = \mathbf{E}^*_{\mathbf{k}n}(\mathbf{r}). \tag{2.52}$$

Using Bloch's theorem, we label the eigenmodes of the wave equation in Eq. (2.50) by the Bloch vector $\mathbf{k}$ and band number n. The eigenvalue equation is then

$$\mathcal{L}_E \mathbf{E}_{kn}(\mathbf{r}) = \frac{\omega_{kn}^2}{c^2} \mathbf{E}_{kn}(\mathbf{r}). \tag{2.53}$$

In the next section, we show that modes with different Bloch wave vectors or band numbers satisfy the orthogonality condition

$$\int_V d\mathbf{r}\, \epsilon(\mathbf{r}) \mathbf{E}^*_{k'n'}(\mathbf{r}) \cdot \mathbf{E}_{kn}(\mathbf{r}) = \delta_{k',k}\delta_{n',n}. \tag{2.54}$$

Note that due to our choice of normalization, the eigenmodes $\mathbf{E}_{kn}$ have units $1/\sqrt{V}$, where V is volume.

Since the eigenmodes are orthogonal and complete, the Green's function can be expanded in terms of the eigenmodes as (the proof is shown in the next section)

$$\boxed{\mathbf{G}(\mathbf{r},\mathbf{r}',\omega) = \frac{c^2}{\omega^2}\sum_{kn}\left(\frac{\omega_{kn}^2}{\omega_{kn}^2-\omega^2}\right)\mathbf{E}_{kn}(\mathbf{r})\otimes\mathbf{E}^*_{kn}(\mathbf{r}').} \tag{2.55}$$

This important result relates the Green's function to the eigenmodes. It also implies that the Green's function can be decomposed into subsets of eigenmodes. For example, we will often isolate the waveguide modes and write the total Green's function as $\mathbf{G} = \mathbf{G}_{\mathrm{wg}} + \mathbf{G}'$, where $\mathbf{G}_{\mathrm{wg}}$ is summed over the waveguides modes, and $\mathbf{G}'$ is summed over all other modes.

Derivation of the Green's function expansion

Here we derive the orthogonality and completeness condition for the eigenmodes, and then the expansion of the Green's function in terms of the eigenmodes. The derivations here is based on Sakoda's textbook in Ref. [57], but is also discussed in Ref. [60], [61], and the theses of two of Steve Hughes' students [62, 63], although note that they use a different normalization for the Green's function.

First we derive the orthogonality and completeness condition for the electric field eigenmodes. The operator in the wave equation of Eq. (2.53) is not Hermitian since $\int dV\ \mathbf{E}^*_{kn}(\mathcal{L}_E\mathbf{E}_{k'n'}) \neq \int dV\ (\mathcal{L}_E\mathbf{E}^*_{kn})\mathbf{E}_{k'n'}$. Thus the eigenmodes are not necessarily orthogonal. Instead we write the wave equation in terms of a Hermitian operator as [58]

$$\mathcal{L}_Q\mathbf{Q}_{kn}(\mathbf{r}) = \frac{\omega^2}{c^2}\mathbf{Q}_{kn}(\mathbf{r}), \tag{2.56}$$

where the Hermitian operator $\mathcal{L}_Q$ and eigenvectors $\mathbf{Q}_{kn}(\mathbf{r})$ are defined as

$$\mathcal{L}_Q = \frac{1}{\sqrt{\epsilon(\mathbf{r})}}\nabla\times\nabla\times\frac{1}{\sqrt{\epsilon(\mathbf{r})}} \quad \text{and} \quad \mathbf{Q}_{kn}(\mathbf{r}) = \sqrt{\epsilon(\mathbf{r})}\mathbf{E}_{kn}(\mathbf{r}). \tag{2.57}$$

These modes are quasi-transverse, since $\nabla\cdot\mathbf{D}_{kn}(\mathbf{r}) = \nabla\cdot[\epsilon(\mathbf{r})\mathbf{E}_{kn}(\mathbf{r})] = 0$, and we will sometimes label them as $\mathbf{Q}^{(T)}(\mathbf{r})$, although they will be implied when there is no label. There is also a set of non-physical zero eigenvalue solutions

$$\mathcal{L}_Q\mathbf{Q}^{(L)}_{kn}(\mathbf{r},\omega) = 0, \tag{2.58}$$

which are called the longitudinal modes ($\nabla\cdot\mathbf{D}_{kn}\neq 0$). Although these modes have no physical meaning, the modes must be included to form a complete set.

Since the operator $\mathcal{L}_Q$ is Hermitian, the eigenmodes $\mathbf{Q}_{kn}(\mathbf{r},\omega)$ are orthogonal,

$$\langle \mathbf{Q}^{(\alpha')*}_{k'n'}(\mathbf{r})|\mathbf{Q}^{(\alpha)*}_{kn}(\mathbf{r})\rangle = \int_V \mathrm{d}^3\mathbf{r}\; \mathbf{Q}^{(\alpha')*}_{k'n'}(\mathbf{r})\cdot\mathbf{Q}^{(\alpha)}_{kn}(\mathbf{r}) = \delta_{k'k}\delta_{n'n}\delta_{\alpha'\alpha}, \tag{2.59}$$

and form a complete set,[3]

$$\sum_{kn\alpha}\mathbf{Q}^{(\alpha)}_{kn}(\mathbf{r})\otimes\mathbf{Q}^{(\alpha)*}_{kn}(\mathbf{r}') = \overleftrightarrow{\mathbf{I}}\,\delta(\mathbf{r}-\mathbf{r}'). \tag{2.60}$$

In terms of the electric field, the orthogonality condition is

$$\int_V \mathrm{d}\mathbf{r}\,\epsilon(\mathbf{r})\mathbf{E}^{(\alpha')*}_{k'n'}\cdot\mathbf{E}^{(\alpha)}_{kn} = \delta_{k',k}\delta_{n',n}\delta_{\alpha',\alpha} \tag{2.61}$$

and completeness condition is

$$\sum_{kn}\mathbf{E}_{kn}(\mathbf{r})\otimes\mathbf{E}^{*}_{kn}(\mathbf{r}') + \sum_{kn}\mathbf{E}^{(L)}_{kn}(\mathbf{r})\otimes\mathbf{E}^{(L)*}_{kn}(\mathbf{r}') = \overleftrightarrow{\mathbf{I}}\frac{\delta(\mathbf{r}-\mathbf{r}')}{\epsilon(\mathbf{r})}, \tag{2.62}$$

where I have separated the longitudinal and transverse modes and omitted the transverse label, $\mathbf{E}(\mathbf{r}) \equiv \mathbf{E}^{(T)}(\mathbf{r})$.

Next, we use the completeness condition to derive the expansion of the Green's function in terms of the eigenmodes. The Green's function wave equation from Eq. (2.12) can be written in terms of the operator $\mathcal{L}_E$ (see Eq. (2.50)) as

$$\left(\mathcal{L}_E - \frac{\omega^2}{c^2}\right)\mathbf{G}(\mathbf{r},\mathbf{r}',\omega) = \frac{\delta(\mathbf{r}-\mathbf{r}')}{\epsilon(\mathbf{r})}\overleftrightarrow{\mathbf{I}}. \tag{2.63}$$

We substitute the delta function with the completeness relation to get

$$\left(\mathcal{L}_E - \frac{\omega^2}{c^2}\right)\mathbf{G}(\mathbf{r},\mathbf{r}',\omega) = \sum_{kn}\left(\mathbf{E}_{kn}(\mathbf{r})\otimes\mathbf{E}^{*}_{kn}(\mathbf{r}') + \mathbf{E}^{(L)}_{kn}(\mathbf{r})\otimes\mathbf{E}^{(L)*}_{kn}(\mathbf{r}')\right). \tag{2.64}$$

We multiply both sides by $\left(\mathcal{L}_E - \frac{\omega^2}{c^2}\right)^{-1}$, and use $\mathcal{L}_E\mathbf{E}_{kn} = (\omega^2_{kn}/c^2)\mathbf{E}_{\mathbf{k}n}$ and $\mathcal{L}_E\mathbf{E}^{(L)}_{\mathbf{k}n} = 0$ to get

$$\mathbf{G}(\mathbf{r},\mathbf{r}',\omega) = \frac{c^2}{\omega^2}\sum_{kn}\left[\left(\frac{\omega^2}{\omega^2_{kn}-\omega^2}\right)\mathbf{E}_{kn}(\mathbf{r})\otimes\mathbf{E}^{*}_{kn}(\mathbf{r}) - \mathbf{E}^{(L)}_{kn}(\mathbf{r})\otimes\mathbf{E}^{(L)*}_{kn}(\mathbf{r})\right]. \tag{2.65}$$

---

[3] Here $\otimes$ denote the tensor product $(\mathbf{A}\otimes\mathbf{B})_{ij} = A_iB_j$. As a way to understand this relation, consider the expansion of a vector $\mathbf{v}$ into 3D vectorial space. Since $\mathbf{v} = \sum_n \hat{\mathbf{e}}_n(\hat{\mathbf{e}}_n\cdot\mathbf{v})$, we could define tensor $\mathbf{T}_n = \hat{\mathbf{e}}_n\otimes\hat{\mathbf{e}}_n$ such that $\sum_n \mathbf{T}_n = 1$, and then the vector expansion can be written in terms of the tensor as $\mathbf{v} = \sum_n \mathbf{T}\cdot\mathbf{v}$.

Next, we use the completeness condition again to replace the longitudinal modes with the transverse modes and a delta function. Combining the two terms with transverse modes, we get

$$\mathbf{G}(\mathbf{r},\mathbf{r}',\omega) = \sum_{kn} \frac{c^2}{\omega^2}\left(\frac{\omega_{kn}^2}{\omega_{kn}^2-\omega^2}\right)\mathbf{E}_{kn}(\mathbf{r})\otimes\mathbf{E}_{kn}^*(\mathbf{r}) - \frac{c^2}{\omega^2}\frac{\delta(\mathbf{r}-\mathbf{r}')}{\epsilon(\mathbf{r})}\overleftrightarrow{\mathbf{I}}. \tag{2.66}$$

The delta function only contributes to the real part of the self-Green's function. For most applications, we can ignore the delta function and use

$$\mathbf{G}(\mathbf{r},\mathbf{r}',\omega) = \frac{c^2}{\omega^2}\sum_{kn}\left(\frac{\omega_{kn}^2}{\omega_{kn}^2-\omega^2}\right)\mathbf{E}_{kn}(\mathbf{r})\otimes\mathbf{E}_{kn}^*(\mathbf{r}'). \tag{2.67}$$

The cavity Green's function

For a cavity boundary condition, the sum over the wave-vector in the Green's function expansion of Eq. (2.55) is discrete, and we no longer have multiple bands. If we are closely detuned to one particular mode, then we can approximate the cavity Green's function by a single mode at frequency ω_0, [28, 61, 63]

$$\mathbf{G}_{\text{cavity}}(\mathbf{r},\mathbf{r}',\omega) \approx \left(\frac{c^2}{\omega_0^2-\omega^2-\mathrm{i}\omega_0\kappa_c/2}\right)\mathbf{E}_k(\mathbf{r})\otimes\mathbf{E}_k^*(\mathbf{r}'). \tag{2.68}$$

A non-ideal cavity has loss due to coupling to the environment, whether it is through leakage out the mirrors, an imaginary index within the cavity, or scattering of light out of the cavity mode. We have approximated this loss in Eq. (2.68) by giving the frequency a small imaginary component, $\omega_0 \to \omega_0 - \mathrm{i}\kappa_c/2$, and only keeping the first order term. κ_c is the cavity decay rate, and is also the full-width half-maximum. It is related to the cavity Q by $Q = \omega/\kappa_c$. Due to our choice of normalization, the eigenmodes $\mathbf{E}_{kn}$ have units $\sqrt{1/V}$, where V is volume. We renormalize the eigenmodes to make them unitless by defining the mode function

$$\mathbf{f}_k(\mathbf{r}) = \mathbf{E}_k(\mathbf{r})\sqrt{V_k}, \tag{2.69}$$

where the mode volume V_k is defined as

$$V_k = \frac{\int_{\text{cavity}} \mathrm{d}^3\mathbf{r}\,\epsilon(\mathbf{r})|\mathbf{E}_k(\mathbf{r})|^2}{\max\left[\,\epsilon(\mathbf{r})|\mathbf{E}_k(\mathbf{r})|^2\,\right]} \tag{2.70}$$

such that the maximum of the mode function is unity,

$$\max\left[\,\epsilon(\mathbf{r})|\mathbf{f}_k(\mathbf{r})|\,\right] = 1. \tag{2.71}$$

In terms of the unitless mode function, the cavity Green's function is

$$\begin{aligned}\mathbf{G}_{\text{cavity}}(\mathbf{r},\mathbf{r}',\omega) &= \left(\frac{c^2}{\omega_0^2-\omega^2-\mathrm{i}\omega_0\kappa_c/2}\right)\frac{1}{V_k}\,\mathbf{f}(\mathbf{r})\otimes\mathbf{f}^*(\mathbf{r}') \\ &\approx \frac{c^2}{2\omega_0 V_k}\left(\frac{1}{\Delta-\mathrm{i}\kappa_c/4}\right)\,\mathbf{f}(\mathbf{r})\otimes\mathbf{f}^*(\mathbf{r}'),\end{aligned} \tag{2.72}$$

where in the last we approximated $\omega_0^2 - \omega^2 \approx 2\omega_0(\omega-\omega_0)$ and defined cavity detuning $\Delta = \omega - \omega_0$. The on-resonant Green's function is

$$G_{\text{cavity}}(\mathbf{r},\mathbf{r}',\omega_0) = \mathrm{i}\frac{1}{6\pi}\left(\frac{\sigma_0 Q}{V_k}\right)\,\mathbf{f}(\mathbf{r})\otimes\mathbf{f}^*(\mathbf{r}'), \tag{2.73}$$

where I have used the optical cross-section from Eq. (2.29). Since the mode is a standing wave, the mode function typically is similar to $\mathbf{f}(\mathbf{r}) \approx \cos(kx)$, where k is the intra-cavity wave-vector. And if we separate the mode volume into $V_k = LA_k$, where L is an effective mode length and A_k is an effective mode area, the on-resonant cavity Green's function is $G_{\text{cavity}}(\mathbf{r},\mathbf{r}',\omega_0) \approx \mathrm{i}\frac{1}{6\pi}\left(\frac{\sigma_0}{A_k}\frac{Q}{L}\right)\cos(kx)\cos(kx')$.

The waveguide Green's function

As shown in previous section, the Green's function can be expanded in terms of the electric field eigenmodes of a system. In this section, we consider the Green's function specifically for the guided modes of a periodic or uniform waveguide.

The Green's function for the 1D wave equation is (see App. D or Refs. [52, 64])

$$G_{\text{1D}}(x,x') = \mathrm{i}\frac{c}{2\omega}e^{ik|x-x'|}, \tag{2.74}$$

where the traveling wave propagates with wave-vector $k = \omega/c$. The real and imaginary parts of the Green's function, which are associated with the spin-exchange rate and dissipation rate, are $\text{Im}[G_{\text{1D}}(x_i,x_j)] \propto \cos(k|x_i - x_j|)$ and $\text{Re}[G_{\text{1D}}(x_i,x_j)] \propto -\sin(k|x_i-x_j|)$. We might expect that a quasi-1D system could be modeled well by an effective 1D model with an effective wave-vector, and therefore we might expect to see a similar behavior for the Green's function. However, we should also expect that the quasi-1D Green's function has a mode function that characterizes the transverse size of the mode.

We start with the eigenmode expansion for the Green's function in Eq. (2.55). For the periodic boundary condition of a quasi-1D system with a lattice constant a, the sum is actually an integral of the wave-vector over the Brillouin zone, $\sum_k \to \frac{a}{2\pi}\int \mathrm{d}k$, with $\omega_{kn} \to \omega_n(k)$. The guided mode Green's function is

$$\mathbf{G}_{\text{wg}}(\mathbf{r},\mathbf{r}',\omega) = \frac{c^2}{\omega^2}\frac{a}{2\pi}\sum_n\int_{-\pi/a}^{\pi/a}\mathrm{d}k\left(\frac{\omega_n^2(k)}{\omega_n^2(k)-\omega^2}\right)\mathbf{E}_{kn}(\mathbf{r})\otimes\mathbf{E}^*_{kn}(\mathbf{r}'). \tag{2.75}$$

We write $\mathbf{E}_{kn}(\mathbf{r})$ in terms of the Bloch function, $\mathbf{E}_{kn}(\mathbf{r}) = \mathbf{u}_{kn}(\mathbf{r})e^{\mathrm{i}kx}$, where I have assumed that the the waveguide is along the x-axis. We also assume that the Green's function is monopolized by one band n and omit the band number sum and label. We also decompose the fraction into two terms. The Green's function expression is then

$$\mathbf{G}_{\mathrm{wg}}(\mathbf{r},\mathbf{r}',\omega) = \frac{a}{4\pi}\int_{-\pi/a}^{\pi/a} \mathrm{d}k \left(\frac{\omega(k)}{\omega(k)+\omega+\mathrm{i}\delta} + \frac{\omega(k)}{\omega(k)-\omega-\mathrm{i}\delta}\right)\mathbf{u}_k(\mathbf{r})\otimes\mathbf{u}_k^*(\mathbf{r}')e^{\mathrm{i}k(x-x')}. \tag{2.76}$$

An infinitesimal term δ has been added to the denominator to make the Green's function obey causality. The only pole is in the second term in the parentheses, and we use Cauchy's residue theorem to simplify this integral. First we consider the case of $x > x'$. The integral is taken around the upper-half of the complex plane. Since $x - x' > 0$, the integral along $-\pi/a + \mathrm{i}\infty$ to $\pi/a + \mathrm{i}\infty$ vanishes. The integrals along $-\pi/a$ to $-\pi/a + \mathrm{i}\infty$ and π/a to $\pi/a + \mathrm{i}\infty$ cancel each other, and we are left with

$$\mathbf{G}_{\mathrm{wg}}(x > x',\omega) = \frac{a}{4\pi}\,2\pi\mathrm{i}\,\mathrm{Res}|_{k_0}\left[\frac{\omega(k)}{\omega(k)-\omega}\right]\mathbf{u}_{k_0}(\mathbf{r})\otimes\mathbf{u}_{k_0}^*(\mathbf{r}')e^{\mathrm{i}k_0(x-x')}, \tag{2.77}$$

where k_0 is the pole. Using the residue theorem $\mathrm{Res}[P(k)/Q(k)] = P(k_0)/Q'(k_0)$, where $Q'(k_0)$ is the derivative with respect to k evaluated at the pole k_0, the waveguide Green's function is

$$\mathbf{G}_{\mathrm{wg}}(x > x',\omega) = \mathrm{i}\frac{ac}{2\omega}\frac{c}{v_g}\mathbf{u}_{k_0}(\mathbf{r})\otimes\mathbf{u}_{k_0}^*(\mathbf{r}')e^{\mathrm{i}k_0(x-x')}, \tag{2.78}$$

where the group velocity is $v_g = \frac{\partial\omega}{\partial k}$ evaluated at the pole.

For $x < x'$, we instead integrate around the lower-half of the complex plane. Combining the two results, we get [61, 62, 65]

$$\mathbf{G}_{\mathrm{wg}}(\mathbf{r},\mathbf{r}',\omega) = \mathrm{i}\frac{ac}{2\omega}\left(\frac{c}{v_g}\right)\Big[\mathbf{u}_k(\mathbf{r})\otimes\mathbf{u}_k^*(\mathbf{r}')e^{ik(x-x')}\Theta(x-x') \tag{2.79}$$

$$+\mathbf{u}_k^*(\mathbf{r})\otimes\mathbf{u}_k(\mathbf{r}')e^{-ik(x-x')}\Theta(x'-x)\Big]. \tag{2.80}$$

Here $\Theta(x)$ is the step function. Note that I omitted the subscript in k_0.

The Bloch function is normalized as (see Eq. (2.54))

$$\int_V \mathrm{d}\mathbf{r}\,\epsilon(\mathbf{r})\,\mathbf{u}_{kn}^*(\mathbf{r})\cdot\mathbf{u}_{kn}(\mathbf{r}) = 1, \tag{2.81}$$

where the integral is over the volume of the unit cell, which has a lattice constant a. The Bloch function has units $1/\sqrt{V}$, and therefore has information about the dimensions of the system. Just as we did for the cavity mode function, we renormalize the Bloch function to make it is unitless,

$$\mathbf{f}_{kn}(\mathbf{r}) = \mathbf{u}_{kn}(\mathbf{r})\sqrt{V_k}, \tag{2.82}$$

where now the mode volume V_k is defined in terms of the integral over a unit cell as

$$V_k = \frac{\int_{\text{cell}} \mathrm{d}^3\mathbf{r}\; \epsilon(\mathbf{r})|\mathbf{E}_k(\mathbf{r})|^2}{\max\left[\, \epsilon(\mathbf{r})|\mathbf{E}_k(\mathbf{r})|^2 \,\right]} \tag{2.83}$$

such that the maximum of the Bloch function is unity,[4]

$$\max\left[\, \epsilon(\mathbf{r})|\mathbf{f}_k(\mathbf{r})| \,\right] = 1. \tag{2.84}$$

The guided photonic crystal Green's function in terms of the dimensionless Bloch function is

$$\mathbf{G}_{\text{wg}}(\mathbf{r}, \mathbf{r}', \omega) = \mathrm{i}\frac{c}{2\omega}\left(\frac{c}{v_g}\right)\left(\frac{a}{V_k}\right)\Big[\mathbf{f}_k(\mathbf{r}) \otimes \mathbf{f}_k^*(\mathbf{r}')e^{ik(x-x')}\Theta(x - x') \tag{2.85}$$

$$+\mathbf{f}_k^*(\mathbf{r}) \otimes \mathbf{f}_k(\mathbf{r}')e^{-ik(x-x')}\Theta(x' - x)\Big]. \tag{2.86}$$

This result can easily be extended to the case of a uniform waveguide. We take the limit of $a \longrightarrow 0$ and assume that the mode function does not vary along the axis of the waveguide. Then we can separate the mode volume into $V_k = A_k a$, where the mode area A_k is defined in terms of an integral over the transverse area,

$$A_k = \frac{\int_{\text{area}} \mathrm{d}^2\mathbf{r}\; \epsilon(\mathbf{r})|\mathbf{E}_k(\mathbf{r})|^2}{\max\left[\, \epsilon(\mathbf{r})|\mathbf{E}_k(\mathbf{r})|^2 \,\right]}. \tag{2.87}$$

We can compare the quasi-1D Green's function to the 1D Green's function from Eq. (2.74). If we assume that the mode function $\mathbf{f}(\mathbf{r})$ is linearly polarized and unity at both atoms (e.g. $\mathbf{f}(\mathbf{r}) = \hat{\mathbf{x}}$), then the Green's function for the uniform waveguide is

$$G_{\text{xx}}^{\text{wg}}(\mathbf{r}, \mathbf{r}', \omega) = \mathrm{i}\frac{c}{2\omega}\left(\frac{c}{v_g}\right)\left(\frac{1}{A_k}\right)e^{\mathrm{i}k|x-x'|}. \tag{2.88}$$

Just as we expected, the 1D Green's function is multiplied by a factor related to the transverse mode area $1/A_k$, but it is also multiplied by the group index c/v_g.

---

[4] Note that the maximum can refer to the maximum value in the volume, but it can also refer to the maximum in air, or perhaps along a specific axis.

Note that when the mode function is elliptically polarized, as is often the case in waveguides away from the symmetry axes, this simplification does not work, and the full version in Eq. (2.85) must be used.

A single atom's decay rate and Lamb shift is related to the imaginary and real parts of the self-Green's function. The self-Green's function for a waveguide is

$$\mathbf{G}_{\mathrm{wg}}(\mathbf{r},\mathbf{r},\omega)=\mathrm{i}\frac{c}{2\omega}\left(\frac{c}{v_g}\right)\left(\frac{a}{V_k}\right)\left[\mathbf{f}_k(\mathbf{r})\otimes\mathbf{f}_k^*(\mathbf{r})\right]. \tag{2.89}$$

Interestingly, the self-interaction due to a quasi-1D waveguide is purely dissipative. The Purcell factor from Eq. (2.27) is

$$\boxed{\frac{\Gamma_{\mathrm{wg}}}{\Gamma_0}=\frac{1}{2}\frac{c}{v_g}\left(\frac{\sigma_0}{A_k}\right)|\hat{\mathbf{n}}_p^*\cdot\mathbf{f}_k(\mathbf{r})|^2,} \tag{2.90}$$

where $\hat{\mathbf{n}}_p$ is a unit vector in the direction of the dipole. In the quantum formalism for the decay of a two-level system, the Purcell factor is also given by this expression.

Equation (2.90) shows there are two ways to increase the atom-waveguide interaction strength. The first strategy is confine the light more tightly, for example in dielectric waveguide, so that the mode area is small as compared to the atom's optical cross-section. The second strategy is to decrease the group velocity of the light in the waveguide. When the group velocity is slower, the interaction time between the atom and the light increases, strengthening the interaction. In the next section, we will show how a photonic crystal waveguide addresses both of these strategies.

Chapter 3

QUANTUM ATOM-LIGHT INTERACTIONS WITH GREEN'S FUNCTIONS

3.1 Introduction

Chapter 2 explored the interactions of atoms and the electromagnetic field, where the atoms were approximated as classical dipole oscillators. We found that the Green's function, the propagator of the electromagnetic field, can be used to characterize the strength and nature (dissipative vs. dispersive) of the interactions of the atoms with the field and with each other. Real atoms, however, differ from classical dipoles in that the electrons occupy discrete energy levels, and a dipole oscillator is only a good approximation in the low saturation regime, where the atomic excited state population can be neglected. Due to the highly nonlinear nature of the atom's energy levels, the atom can often be approximated by only two energy states, i.e. Hyperfine levels for Alkali atoms. A single photon can excite the atom, resulting in saturation. Therefore, a fully quantum mechanical description of both the atoms and light is required to describe the system.

In free-space, the quantization of the electromagnetic field is most conventionally achieved by first constructing a conserved classical Lagrangian or Hamiltonian [66, 67]. This strategy does not work in the presence of dielectric media. The Kramers-Kronig relations for dielectrics show that there is a fundamental connection between the imaginary dielectric constant, which results in energy loss, and the real dielectric constant, which is used in nanophotonics to confine the light. And therefore energy dissipation is an indispensable property of dielectrics. The free-space quantization scheme does not work because the Hamiltonian is not conserved.

A strategy for quantizing the field in the presence of dielectric media is to incorporate the dissipation by including a reservoir of harmonic oscillators into which the field and material system can loose energy [68, 69]. The total Hamiltonian is then conserved, and so are the commutation relations.

This strategy is a familiar one in quantum mechanics. For example, dissipation can be added to a harmonic oscillator, or equivalently a cavity mode, with creation and annihilation operators $\hat{a}^\dagger$ and $\hat{a}$ by including in the Hamiltonian a reservoir of harmonic oscillators $\hat{b}_k$ and a coupling with strength g between them,

$$H = \hbar\omega\hat{a}^\dagger\hat{a} + \sum_k \hbar\omega_k\hat{b}_k^\dagger\hat{b}_k + \sum_k g_k\hat{a}^\dagger\hat{b}_k + \text{h.c.}. \tag{3.1}$$

By solving for the Heisenberg equations for the bath variables $\hat{b}_k$, substituting them into the Heisenberg equations for the harmonic oscillator a, and assuming that the time scale of the bath is much shorter than the time scale of the system, we get [48]

$$\dot{\hat{a}}(t) = (\mathrm{i}\omega - \kappa/2)\hat{a}(t) + \hat{F}_\mathrm{N}(t). \tag{3.2}$$

The decay rate of the harmonic oscillator is κ, but there is also a Langevin noise term $\hat{F}_\mathrm{N}(t)$, which is a function of the bath variables $\hat{b}_k$. The noise term has a typical spectral properties of a random noise, $\langle \hat{F}_\mathrm{N}^\dagger(t)\hat{F}_\mathrm{N}^\dagger(t')\rangle \propto \kappa\delta(t - t')$. As a result of the Langevin term, the commutation relation $[\hat{a}^\dagger, \hat{a}] = 1$ is conserved, whereas without it, the commutation relation would decay as $[\hat{a}^\dagger, \hat{a}] = e^{-\kappa t}$. This noise term can also be interpreted as a requirement of the fluctuation-dissipation theorem, which mandates that loss in a system is associated with a fluctuating "force".

Similarly, for the electromagnetic field in the presence of dielectric media, we will incorporate a bath of harmonic oscillator coupled to the polarization, and thereby obtain a Langevin noise term associated with energy loss that can be expressed in terms of a polarization noise P_N.

This quantization scheme will be described in this chapter. The formalism will also have a practical purpose besides incorporating loss, and that will be the prominent role of the Green's function. The Langevin polarization noise can be related to the field by the Green's function (see Dyson's equation in Eq. (2.13)). In the more conventional free-space quantization, or in its extension to real dielectrics, the fields are decomposed into the eigenmodes of the system. While this approach is well suited for simple geometries of approximately closed systems, such as cavities [48, 70] or uniform systems such as nanofibers [51, 71–74], it is not practical for more complicated open systems, such as finite photonic crystals.

In this chapter, we will first briefly review the free-space quantization scheme in Sec. 3.2. Then we will describe the Green's function quantization scheme for dielectrics in Sec. 3.3. In section 3.4, we will derive the quantum equations of motion for a dielectric system with atoms, and in section 3.4 and 3.4, these equations will be simplified in the time domain using the Markov approximation, and in the frequency domain by assuming the low saturation limit. While this chapter will be heavy with formalism, the next chapters will apply this formalism to study atoms coupled to quasi-1D photonic nanostructures.

3.2 Brief review of QED in free-space

The quantization of the electromagnetic field in vacuum [46, 66] is often achieved by first constructing a classical Langrangian or Hamiltonian for the field in terms of the vector potential $\mathbf{A}(\mathbf{r},t)$ and conjugate momentum $\mathbf{\Pi}(\mathbf{r},t) = \epsilon_0\dot{\mathbf{A}}(\mathbf{r},t)$. The conjugate variables are related to the electric field and magnetic field by $\mathbf{\Pi}(\mathbf{r},t) = -\epsilon_0\mathbf{E}(\mathbf{r},t)$ and $\mathbf{B}(\mathbf{r},t) = \nabla\times\mathbf{A}(\mathbf{r},t)$. The vector potential in vacuum is the solution of the wave equation

$$\nabla^2\mathbf{A}(\mathbf{r},t) + c^2\,\ddot{\mathbf{A}}(\mathbf{r},t) = 0. \tag{3.3}$$

The classical Hamiltonian is given by

$$H = \frac{1}{2}\int \mathrm{d}^3\mathbf{r}\left[\frac{1}{\epsilon_0}\mathbf{\Pi}(\mathbf{r},t)^2 + \frac{1}{\mu_0}(\nabla\times\mathbf{A}(\mathbf{r},t))^2\right], \tag{3.4}$$

which we can verify by replacing the conjugate variables with the electric and magnetic field and obtaining the expected total energy $H = \frac{1}{2}\int \mathrm{d}^3\mathbf{r}\left[\epsilon_0\mathbf{E}(\mathbf{r},t)^2 + \frac{1}{\mu_0}\mathbf{B}(\mathbf{r},t)^2\right]$. In this formalism, the conjugate variables satisfy the canonical commutation relations in terms of the Poisson brackets, $\{\mathbf{A}(\mathbf{r},t),\mathbf{\Pi}(\mathbf{r}',t)\} = \delta^{\perp}(\mathbf{r}-\mathbf{r}')$. And the time evolution of the field variables, i.e. $\mathbf{A}(\mathbf{r},t)$, is expressed in terms of the Poisson brackets by $\dot{\mathbf{A}} = \{\mathbf{A}, H\}$, which as expected reproduces Maxwell's equations.

The quantization of the field is simply obtained by upgrading the variables to non-commuting quantum operators, i.e. $\mathbf{A}(\mathbf{r},t) \longrightarrow \hat{\mathbf{A}}(\mathbf{r},t)$, and then setting the operator commutation relations to be the same as classical ones,

$$[\hat{\mathbf{A}}(\mathbf{r},t),\hat{\mathbf{\Pi}}(\mathbf{r}',t)] = \delta^{\perp}(\mathbf{r}-\mathbf{r}'). \tag{3.5}$$

The time evolution of the quantum operators, i.e. $\mathbf{A}(\mathbf{r},t)$, is determined by the commutation relations through the Heisenberg equation of motion

$$\dot{\hat{\mathbf{E}}}(\mathbf{r},t) = \frac{1}{\mathrm{i}\hbar}[\hat{\mathbf{E}}(\mathbf{r},t),\hat{H}]. \tag{3.6}$$

Thus by setting the quantum commutation relations equal to the classical commutation relations, we guarantee that the operators evolve similarly to their classical counterparts. But since the quantum operators do not commute, there are fundamental limits to the precision to which the operators can be measured, as quantified by Heisenberg's uncertainty relations.

While the Hamiltonian and commutation relations are sufficient, in practice the formalism is further simplified by introducing the eigenmodes $\mathbf{u}_k(\mathbf{r})$ of the wave-equation in Eq. (3.3) with the given boundary conditions of the system (i.e. the perfect conducting boundary conditions of a cavity). The vector potential, or equivalently the electric field, is expanded in terms of the eigenmodes as

$$\hat{\mathbf{E}}(\mathbf{r},t) = \mathrm{i}\omega\hat{\mathbf{A}}(\mathbf{r},t) = -\sum_k \sqrt{\frac{\hbar\omega_k}{2\epsilon_0}}\left[\mathbf{u}_k(\mathbf{r})\,\hat{a}_k(t) + \mathbf{u}_k^*(\mathbf{r})\,\hat{a}_k^\dagger(t)\right]. \tag{3.7}$$

Using the orthogonality condition of the eigenmodes $\int \mathrm{d}^3\mathbf{r}\,\mathbf{u}_j^*(\mathbf{r})\cdot\mathbf{u}_k(\mathbf{r}) = \delta_{jk}$ and the fundamental commutation relation from Eq. (3.5), we find that the annihilation and creation operators $\hat{a}$ and $\hat{a}^\dagger$ satisfy the simpler commutation relations $[\hat{a}_j^\dagger, \hat{a}_k] = \delta_{jk}$. Substituting the expansion in Eq. (3.7) into the Hamiltonian and performing the integration gives

$$\hat{H} = \sum_k \hbar\omega_k \left(\hat{a}_k^\dagger\hat{a}_k + \frac{1}{2}\right). \tag{3.8}$$

These expressions show the close analogy between a single electromagnetic mode and a harmonic oscillator.

3.3 QED with dielectrics

The quantization of the electromagnetic field in presence of dielectric media is not as straightforward as the free-space case. A dielectric material consists of a vast number of charge distributions, and a complete description would require an intractable set of coupled equations. To simplify the problem, we assume that the equilibrium charge distribution is only weakly affected by the field, and we describe the material by a uniform polarization density $\mathbf{P}(\mathbf{r},t)$. We further assume that the polarization of the material responds linearly and isotropically to the electric field, and therefore can be expressed in terms of a Langevin equation as

$$\mathbf{P}(\mathbf{r},t) = \epsilon_0 \int_{-\infty}^{\infty} \mathrm{d}\tau\,\chi(\mathbf{r},\tau)\mathbf{E}(\mathbf{r},t-\tau) + \mathbf{P}_\mathrm{N}(\mathbf{r},t). \tag{3.9}$$

The first term is the linear response to the electric field, and the response function is the electric susceptibility $\chi(\mathbf{r},\tau)$, which in order to satisfy causality has the constraint $\chi(\mathbf{r},\tau) = 0$ for $\tau < 0$. The second part is a polarization noise term $\mathbf{P}_\mathrm{N}(\mathbf{r},t)$, and is required by the fluctuation-dissipation theorem, which states that any loss in a system is accompanied by a fluctuating force in the system caused by the reservoir into which the energy is lost.

In Fourier space, the linear response equation is

$$\mathbf{P}(\mathbf{r},\omega) = \epsilon_0\chi(\mathbf{r},\omega)\mathbf{E}(\mathbf{r},\omega) + \mathbf{P}_{\mathrm{N}}(\mathbf{r},\omega), \tag{3.10}$$

where the realness of $\chi(\mathbf{r},\tau)$ requires that $\chi(\mathbf{r},-\omega) = \chi^*(\mathbf{r},\omega)$, and the causality conditions requires that $\chi(\mathbf{r},\omega)$ is analytic in the upper-half of the complex plane. From these two constraints, we can derive the Kramers-Kronig relations for dielectrics, which relate the imaginary and the real components of the permittivity $\epsilon(\mathbf{r},\omega) = 1 + \chi(\mathbf{r},\omega)$ and is given by [75, 76]

$$\mathrm{Re}\,\epsilon(\mathbf{r},\omega) \equiv \epsilon_R(\mathbf{r},\omega) = 1 + \frac{2}{\pi}\,\mathcal{P}\int_0^\infty \mathrm{d}\omega'\frac{\omega'\,\epsilon_I(\mathbf{r},\omega')}{\omega'^2-\omega^2} \tag{3.11}$$

$$\mathrm{Im}\,\epsilon(\mathbf{r},\omega) \equiv \epsilon_I(\mathbf{r},\omega) = -\frac{2\omega}{\pi}\,\mathcal{P}\int_0^\infty \mathrm{d}\omega'\frac{\epsilon_R(\mathbf{r},\omega')-1}{\omega'^2-\omega^2}. \tag{3.12}$$

The Kramers-Kronig relations show the intrinsic connection between the real dielectric constant, which is used in nanophotonis to optically confine light into waveguides, and the imaginary dielectric constant, which results in energy absorption. In fact, if we require $\epsilon_I(\mathbf{r},\omega) = 0$ for all frequencies, then the relations require that $\epsilon(\mathbf{r},\omega) = 1$ for all frequencies.

Therefore, absorption is a fundamental property of dielectrics and is required to satisfy causality. But a natural consequence of loss in a system is that the reservoir into which the energy is flowing can also act on the system, resulting in a noise force. This principle is outlined in the classical fluctuation-dissipation theorem [77] in statistical mechanics. For the case of dielectrics and the electromagnetic field, the classical theory states that the fluctuation of the polarization is proportional to the imaginary response function and the temperature of the reservoir,

$$\langle\Delta\mathbf{P}_{\mathrm{N}}(\mathbf{r},\omega)\;\Delta\mathbf{P}^*_{\mathrm{N}}(\mathbf{r}',\omega')\rangle = \frac{k_BT}{\pi\omega}\epsilon_0\,\mathrm{Im}\chi(\mathbf{r},\omega)\,\boldsymbol{\delta}(\mathbf{r}-\mathbf{r}')\delta(\omega-\omega'). \tag{3.13}$$

Here we use $\Delta x = (x - \langle x\rangle)$. The fundamental role of dissipation in the system presents a challenge for the quantization procedure. The Hamiltonian is not conserved, and consequently the commutation relations decay with time. For example, in the case of a uniform dielectric with a complex dielectric constant, the wave equation is

$$\nabla\times\nabla\times\hat{\mathbf{E}}(\mathbf{r},\omega) - \frac{\omega^2}{c^2}\left(\epsilon_R(\mathbf{r},\omega) + \mathrm{i}\epsilon_I(\mathbf{r},\omega)\right)\hat{\mathbf{E}}(\mathbf{r},\omega) = 0, \tag{3.14}$$

and Ref. [78] shows that the commutation relations $[\mathbf{E}(\mathbf{r},\omega),\mathbf{A}(\mathbf{r},\omega)]$ are not conserved.

One strategy for incorporating the loss is to a construct a Hamiltonian that includes the field, a set of harmonic oscillators that represent the material polarization, and a reservoir of harmonic oscillators which are weakly coupled to the polarization oscillators and into which the system can dissipate energy. Since the total Hamiltonian is then conserved, the dynamics are unitary and thus the commutation relations are conserved. Huttner and Barnett [68] (for summary see Ref. [69]) used this strategy for a homogeneous dielectric and diagonalized the entire Hamiltonian to solve for a set of polariton-like operators $\hat{\mathbf{f}}^\dagger(\mathbf{r},\omega)$ and $\hat{\mathbf{f}}(\mathbf{r},\omega)$ that create and annihilate excitations of the combined field, polarization, reservoir system. The total Hamiltonian is given by

$$\hat{H}_\mathrm{F} = \int \mathrm{d}^3\mathbf{r} \int_0^\infty \mathrm{d}\omega \; \hat{\mathbf{f}}^\dagger(\mathbf{r},\omega)\,\hat{\mathbf{f}}(\mathbf{r},\omega), \tag{3.15}$$

and the operators satisfy the commutation relations

$$[\hat{f}_k(\mathbf{r},\omega), \hat{f}^\dagger_{k'}(\mathbf{r}',\omega')] = \delta_{kk'}\delta(\omega-\omega')\delta(\mathbf{r}-\mathbf{r}') \tag{3.16}$$

$$[\hat{f}_k(\mathbf{r},\omega), \hat{f}_{k'}(\mathbf{r}',\omega')] = 0. \tag{3.17}$$

Huttner and Barnett showed how these elementary excitation operators are related to the other field variables. For example, the electric field satisfies

$$\nabla\times\nabla\times\hat{\mathbf{E}}(\mathbf{r},\omega) - \epsilon(\mathbf{r},\omega)\frac{\omega^2}{c^2}\hat{\mathbf{E}}(\mathbf{r},\omega) = \mu_0\,\hat{\mathbf{j}}(\mathbf{r},\omega), \tag{3.18}$$

where the current noise is $\hat{\mathbf{j}} = \mathrm{i}\omega\hat{\mathbf{P}}_\mathrm{N}$, and $\hat{\mathbf{P}}_\mathrm{N}$ is a Langevin force term that represents the polarization noise given by $\hat{\mathbf{P}}_N(\mathbf{r},\omega) = \mathrm{i}\sqrt{\frac{\hbar\epsilon_0}{\pi}\mathrm{Im}\epsilon(\mathbf{r},\omega)}\,\hat{\mathbf{f}}(\mathbf{r},\omega)$. Just as we saw in the introduction example of a harmonic oscillator coupled to a bath, the presence of the Langevin term preserves the commutation relations, and is required by the quantum fluctuation-dissipation theorem.

This strategy was generalized to non-homogeneous dielectric systems by Grunner and Welsch [78, 79]. Following the reverse process of Huttner and Barnett, they first introduce a Langevin force term to Maxwell's equations and define its properties to conserve the commutation relations, which in turn also makes the formalism satisfy the fluctuation-dissipation theorem. This quantization procedure is described here.

First, we require the quantum operators obey Maxwell's equations for non-magnetic dielectrics,

$$\nabla \cdot \hat{\mathbf{D}}(\mathbf{r}, \omega) = 0 \tag{3.19}$$

$$\nabla \cdot \hat{\mathbf{B}}(\mathbf{r}, \omega) = 0 \tag{3.20}$$

$$\nabla \times \hat{\mathbf{E}}(\mathbf{r}, \omega) - \mathrm{i}\omega\hat{\mathbf{B}}(\mathbf{r}, \omega) = 0 \tag{3.21}$$

$$\nabla \times \hat{\mathbf{B}}(\mathbf{r}, \omega) + \mathrm{i}\omega\mu_0\hat{\mathbf{D}}(\mathbf{r}, \omega) = 0. \tag{3.22}$$

We add a Langevin force term by introducing a polarization noise operator $\mathbf{P}_\mathrm{N}$ into the displacement operator

$$\hat{\mathbf{D}}(\mathbf{r}, \omega) = \epsilon_0\hat{\mathbf{E}}(\mathbf{r}, \omega) + \hat{\mathbf{P}}(\mathbf{r}, \omega) + \hat{\mathbf{P}}_\mathrm{N}(\mathbf{r}, \omega) = \epsilon_0\epsilon(\mathbf{r}, \omega)\hat{\mathbf{E}}(\mathbf{r}, \omega) + \hat{\mathbf{P}}_\mathrm{N}(\mathbf{r}, \omega). \tag{3.23}$$

Substituting $\hat{\mathbf{D}}$ into Eq. (3.19) and (3.22) gives

$$\epsilon_0\nabla \cdot \left[\epsilon(\mathbf{r}, \omega)\hat{\mathbf{E}}(\mathbf{r}, \omega)\right] = \rho_N(\mathbf{r}, \omega) \tag{3.24}$$

$$\nabla \times \hat{\mathbf{B}}(\mathbf{r}, \omega) + \mathrm{i}\frac{\omega}{c}\epsilon(\mathbf{r}, \omega)\hat{\mathbf{E}}(\mathbf{r}, \omega) = \mu_0\,\mathbf{j}_N(\mathbf{r}, \omega). \tag{3.25}$$

The noise current is related to the polarization noise by $\hat{\mathbf{j}}_N(\mathbf{r}, \omega) = -\mathrm{i}\omega\hat{\mathbf{P}}_N(\mathbf{r}, \omega)$, and to the noise charge by $\nabla \cdot \hat{\mathbf{j}}_N(\mathbf{r}, \omega) = \mathrm{i}\omega\rho_N(\mathbf{r}, \omega)$.

The polarization noise operator $\hat{\mathbf{P}}_\mathrm{N}(\mathbf{r}, \omega)$ describes the fluctuations caused by coupling to the loss reservoir. We next define its properties in order to satisfy the fluctuation-dissipation theorem. Note that we could have also defined it as to conserve the commutation relations $[\hat{\mathbf{A}}(\mathbf{r}, t), \hat{\mathbf{\Pi}}(\mathbf{r}', t)] = \delta^{\perp}(\mathbf{r} - \mathbf{r}')$, which gives the same result. We express the noise operator as

$$\hat{\mathbf{P}}_\mathrm{N}(\mathbf{r}, \omega) = \mathrm{i}\sqrt{\frac{\hbar\epsilon_0}{\pi}\mathrm{Im}\,\epsilon(\mathbf{r}, \omega)}\;\hat{\mathbf{f}}(\mathbf{r}, \omega) \tag{3.26}$$

and define the commutation relations which are typical for a noise term

$$[\hat{f}_k(\mathbf{r}, \omega), \hat{f}^{\dagger}_{k'}(\mathbf{r}', \omega')] = \delta_{kk'}\delta(\omega - \omega')\delta(\mathbf{r} - \mathbf{r}') \tag{3.27}$$

$$[\hat{f}_k(\mathbf{r}, \omega), \hat{f}_{k'}(\mathbf{r}', \omega')] = 0. \tag{3.28}$$

The constant in Eq. (3.26) is chosen so that the quantum fluctuation-dissipation theorem is satisfied when the system is in the ground state[1]

$$\langle 0|\mathcal{S}\left[\Delta\hat{\mathbf{P}}_\mathrm{N}(\mathbf{r}, \omega)\,\Delta\hat{\mathbf{P}}^{\dagger}_\mathrm{N}(\mathbf{r}', \omega')\right]|0\rangle = \frac{\hbar}{2\pi}\epsilon_0\mathrm{Im}\,\chi(\mathbf{r}, \omega)\delta(\mathbf{r} - \mathbf{r}')\delta(\omega - \omega'), \tag{3.29}$$

where $|0\rangle$ represents the ground state of the system, and $\mathcal{S}\left[a^{\dagger}b\right] = \frac{1}{2}(ab + ba)$. The average thermal energy k_BT appearing in the classical fluctuation-dissipation theorem is replaced by the quantum ground-state energy $\hbar\omega/2$ of a bosonic system.

Next we find an expression for the field operators in terms of the bosonic operators. In Chapter 2, we found that the electric field is related to an oscillating polarization by the Green's function. Inserting Eq. (3.26) into Dyson's equation from Eq. (2.13) gives

$$\begin{aligned}\hat{\mathbf{E}}(\mathbf{r},\omega) &= \mathrm{i}\mu_0\,\omega^2\sqrt{\frac{\hbar\epsilon_0}{\pi}}\int d\mathbf{r}'\,\sqrt{\mathrm{Im}\{\epsilon(\mathbf{r}',\omega)\}}\,\mathbf{G}(\mathbf{r},\mathbf{r}'\omega)\cdot\hat{\mathbf{f}}(\mathbf{r}',\omega) + \text{h.c.} \\ &\equiv \hat{\mathbf{E}}^{+}(\mathbf{r},\omega) + \hat{\mathbf{E}}^{-}(\mathbf{r},\omega),\end{aligned} \tag{3.30}$$

where the total electric field is

$$\hat{\mathbf{E}}(\mathbf{r},t) = \int_0^\infty \mathrm{d}\omega\,\left(\hat{\mathbf{E}}^{+}(\mathbf{r},\omega) + \text{h.c.}\right). \tag{3.31}$$

As shown in Hunter and Barnett's work, the bosonic operators can be interpreted as an excitation of the combined field, polarization, and reservoir system. The Hamiltonian is given by

$$\hat{H}_\mathrm{F} = \int \mathrm{d}^3\mathbf{r}\int_0^\infty \mathrm{d}\omega\;\hat{\mathbf{f}}^\dagger(\mathbf{r},\omega)\,\hat{\mathbf{f}}(\mathbf{r},\omega), \tag{3.32}$$

which can be obtained by inserting the expressions for the electric and magnetic field into $\hat{H}_F = \frac{1}{2}\int \mathrm{d}^3\mathbf{r}\epsilon_0\hat{\mathbf{E}}^2 + \frac{1}{\mu_0}\hat{\mathbf{B}}^2$, and using the Green's function identity[2]

$$\frac{\omega^2}{c^2}\int \mathrm{d}^3\mathbf{s}\;\epsilon_I(\mathbf{s},\omega)\mathbf{G}_{ik}(\mathbf{r},\mathbf{s},\omega)\mathbf{G}^*_{jk}(\mathbf{r}',\mathbf{s},\omega) = \mathrm{Im}\,\mathbf{G}_{ij}(\mathbf{r},\mathbf{r}',\omega). \tag{3.33}$$

---

[1] The proof of this is given here. Inserting the polarization noise in Eq. (3.26) gives

$$\langle 0|\mathcal{S}[\Delta\hat{\mathbf{P}}_\mathrm{N}(\mathbf{r},\omega)\,\Delta\hat{\mathbf{P}}^\dagger_\mathrm{N}(\mathbf{r}',\omega')]|0\rangle = \frac{\hbar\epsilon_0}{2\pi}\sqrt{\epsilon_I(\mathbf{r}',\omega')\epsilon_I(\mathbf{r},\omega)}\langle 0|\hat{\mathbf{f}}(\mathbf{r},\omega)\hat{\mathbf{f}}^\dagger(\mathbf{r}',\omega') + \hat{\mathbf{f}}^\dagger(\mathbf{r}',\omega')\hat{\mathbf{f}}(\mathbf{r},\omega)|0\rangle.$$

Next we use $\hat{\mathbf{f}}(\mathbf{r},\omega)|0\rangle = 0$ and $\langle 0|\hat{\mathbf{f}}^\dagger(\mathbf{r},\omega) = 0$ to get rid of second term. Then we use $\hat{\mathbf{f}}(\mathbf{r},\omega)\hat{\mathbf{f}}^\dagger(\mathbf{r}',\omega') = [\hat{\mathbf{f}}(\mathbf{r},\omega),\hat{\mathbf{f}}^\dagger(\mathbf{r}',\omega')] + \hat{\mathbf{f}}^\dagger(\mathbf{r}',\omega')\hat{\mathbf{f}}(\mathbf{r},\omega)$. Taking the expectation value with respect to the ground state and again eliminating the second term, we get

$$\langle 0|\mathcal{S}\left[\Delta\hat{\mathbf{P}}_\mathrm{N}(\mathbf{r},\omega)\,\Delta\hat{\mathbf{P}}^\dagger_\mathrm{N}(\mathbf{r}',\omega')\right]|0\rangle = \frac{\hbar\epsilon_0}{2\pi}\sqrt{\epsilon_I(\mathbf{r}',\omega')\epsilon_I(\mathbf{r},\omega)}\;\left[\hat{\mathbf{f}}(\mathbf{r},\omega),\hat{\mathbf{f}}^\dagger(\mathbf{r}',\omega')\right].$$

Inserting the commutation relation of $\hat{\mathbf{f}}(\mathbf{r},\omega)$ and using $\epsilon = 1 + \chi$, gives Eq. (3.29).

[2] This identity perhaps seems weird since for systems with no loss ($\epsilon_I \to 0$), the imaginary Green's function on the right-hand side is still not zero even though the the left-hand side seems to vanish. The proof for this identity is given in Ref. [46], but a simpler proof for the 1D case is in Ref. [78], and more clearly solves the dilemma. The identity in 1D is $\frac{\omega^2}{c^2}\int_{-\infty}^{\infty}\mathrm{d}y\epsilon_I(y,\omega)G(x,y,\omega)G^*(x',y,\omega) = -\mathrm{Im}G(x,x',\omega)$. This identity, as well as the 3D version, is derived by an integration by parts and assumption that $\lim_{x\to\infty}G(x,y)\to 0$, which is only true when the system has a small ϵ_I. For the 1D case in homogeneous space, $G(x,y) = e^{ik|x-x'|}/(2ik)$, and then the identity for $x = x'$ is $\frac{\omega^2}{c^2}\epsilon_I(\omega)\int_{-\infty}^{\infty}\mathrm{d}y|G(x,y,\omega)|^2 = \frac{\omega^2}{c^2}\epsilon_I(\omega)\int_{-\infty}^{\infty}\mathrm{d}y\left|e^{ik|x-y|}/2k\right|^2 = \frac{\omega^2}{c^2}\epsilon_I(\omega)\int_{-\infty}^{\infty}\mathrm{d}ye^{-n_I\omega/cy^2}/4|k|^2 = \frac{\omega^2}{c^2}\epsilon_I(\omega)\sqrt{\frac{\pi}{n_I\omega/c}} = \frac{1}{2k} = -\mathrm{Im}G(x,x,\omega)$.

One more interesting result that comes out of this formalism is that fluctuations of the electric field in vacuum is related to the imaginary Green's function by

$$\langle 0|\Delta\mathbf{E}(\mathbf{r},\omega)\,\Delta\mathbf{E}^{\dagger}(\mathbf{r}',\omega')|0\rangle = \frac{\hbar}{2\pi}\mu_0\omega^2 \mathrm{Im}\,\mathbf{G}(\mathbf{r},\mathbf{r}',\omega)\delta(\omega-\omega'), \tag{3.34}$$

which is obtained by substituting Eq. (3.30) and again using the identity in Eq. (3.33). These vacuum fluctuations are related to the Casimir-Polder forces [46, 80–82].

Comparison to the eigenmode formalism

Some efforts have been made to quantize the field in the presence of real and frequency independent dielectric constants, most prominently by Glauber and Lewenstein [67], where they constructed a conservative Hamiltonian and extended the free-space scheme. While this can be a good approximation for a specific bandwidth of frequencies with low loss in the dielectric, this formulation necessarily violates causality due to the absence of loss.

It also relies on an eigenmode expansion of the electric field. The Green's function can be expanded in terms of eigenmodes (see Eq. (2.55)). We can show that the two formalisms are equivalent in the limit of real and frequency independent dielectrics. Substituting the expansion of the Green's function into the electric field operator gives

$$\hat{\mathbf{E}}(\mathbf{r},t) = \mathrm{i}\int_0^\infty \mathrm{d}\omega\sqrt{\frac{\hbar}{\pi\epsilon_0}\frac{\omega^2}{c^2}}\int \mathrm{d}^3\mathbf{r}'\sqrt{\epsilon_I(\mathbf{r}',\omega)}\,\overbrace{\left[\frac{c^2}{\omega^2}\sum_k \omega_k^2\frac{\mathbf{u}_k^*(\mathbf{r})\otimes\mathbf{u}_k(\mathbf{r}')}{\omega_k^2-\omega^2}\right]}^{\mathbf{G}(\mathbf{r},\mathbf{r}',\omega)}\cdot\hat{\mathbf{f}}(\mathbf{r}',\omega) \tag{3.35}$$

$$= \mathrm{i}\sqrt{\frac{\hbar}{\pi\epsilon_0}}\sum_k \mathbf{u}_k^*(\mathbf{r})\hat{a}_k(t) \tag{3.36}$$

where we have defined the bosonic operator

$$\hat{a}_k = \int_0^\infty \mathrm{d}\omega\frac{\omega_k^2}{\omega_k^2-\omega^2}\int \mathrm{d}^3\mathbf{r}'\sqrt{\epsilon_I(\mathbf{r}',\omega)}\,\mathbf{u}_k(\mathbf{r}')\cdot\hat{\mathbf{f}}(\mathbf{r}',\omega). \tag{3.37}$$

Assuming a uniform ϵ_I that goes to zero, and using the orthogonality of $\mathbf{u}_k(\mathbf{r})$ gives the expected commutation relations $[\hat{a}_k, \hat{a}_{k'}^{\dagger}] = \delta_{kk'}$.

3.4 Atom-light interactions with Green's functions

Since its introduction, the Green's function quantization formalism has been used to study the spontaneous emission of a single atom [69, 83–87] and the interaction of two atoms [19, 88–90]. Here we review the theoretical techniques used.

Due to the highly non-linear energy nature of the atoms, we will treat the atoms as a two-level system, with a ground state $|g\rangle$ and excited state $|e\rangle$ that are separated by an energy $\hbar\omega_A$. The Hamiltonian for the atom is

$$\hat{H}_A = \hbar\omega_A \frac{1}{2}\Big(|e\rangle\langle e| - |g\rangle\langle g|\Big) = \frac{\hbar\omega_A}{2}\hat{\sigma}^{\mathrm{z}}. \tag{3.38}$$

The Hamiltonian for the interaction between a single atom and the electromagnetic field is given by [46, 69, 88]

$$\hat{H}_{AF} = -\hat{\mathbf{E}}(\mathbf{r}, t) \cdot \hat{\boldsymbol{d}}(t). \tag{3.39}$$

The dipole operator of the atom $\hat{\boldsymbol{d}} = e\hat{\mathbf{r}}$ can be projected onto the two states as

$$\hat{\boldsymbol{d}}(t) = \Big(|g\rangle\langle g| + |e\rangle\langle e|\Big)\,\hat{\boldsymbol{d}}(t)\,\Big(|g\rangle\langle g| + |e\rangle\langle e|\Big) = \mathbf{d}\,\hat{\sigma}(t) + \mathbf{d}^*\,\hat{\sigma}^\dagger(t), \tag{3.40}$$

where the dipole matrix elements are $\mathbf{d} = \langle g|\hat{\boldsymbol{d}}|e\rangle$ and $\mathbf{d}^* = \langle e|\hat{\boldsymbol{d}}|g\rangle$, and the Pauli spin operators are the annihilation operator $\sigma = |g\rangle\langle e|$ and creation operator $\sigma^\dagger = |e\rangle\langle g|$. The matrix elements $\langle g|\hat{\boldsymbol{d}}|g\rangle$ and $\langle e|\hat{\boldsymbol{d}}|e\rangle$ are zero due to the odd parity of the dipole operator.

Using the Green's function quantization formalism, the total Hamiltonian $\hat{H} = \hat{H}_F + \hat{H}_A + \hat{H}_{AF}$ for N identical atoms is

$$\hat{H} = \int \mathrm{d}^3\mathbf{r} \int_0^\infty \mathrm{d}\omega\ \hbar\omega\,\hat{\mathbf{f}}^\dagger(\mathbf{r},\omega)\,\hat{\mathbf{f}}(\mathbf{r},\omega) + \sum_{j=1}^{N} \frac{\hbar\omega_A}{2}\hat{\sigma}_j^{\mathrm{z}} - \sum_{j=1}^{N} \hat{\mathbf{E}}(\mathbf{r}_j, t)\cdot\Big(\mathbf{d}_j\,\hat{\sigma}_j + \mathbf{d}_j^*\,\hat{\sigma}_j^\dagger\Big). \tag{3.41}$$

The time derivative of the operators is determined by the Heisenberg equation of motion,

$$\dot{\hat{O}}(t) = \frac{1}{\mathrm{i}\hbar}[\hat{O}(t), \hat{H}]. \tag{3.42}$$

Using $\hat{\sigma}^{\mathrm{z}} = 2\hat{\sigma}^\dagger\hat{\sigma} - 1$ and the commutation relations for the Pauli spin operators,

$$[\hat{\sigma}^\dagger, \sigma] = \hat{\sigma}^{\mathrm{z}}, \qquad [\hat{\sigma}^{\mathrm{z}}, \hat{\sigma}] = -2\hat{\sigma}, \qquad [\hat{\sigma}^{\mathrm{z}}, \hat{\sigma}^\dagger] = 2\hat{\sigma}^\dagger, \tag{3.43}$$

the time derivatives of the atomic operators $\hat{\sigma}_j$ and $\hat{\sigma}_j^z$ are

$$\dot{\hat{\sigma}}_j = -\mathrm{i}\omega_A \hat{\sigma} + \frac{\mathrm{i}}{\hbar}\, \hat{\sigma}_j^z\, \hat{\mathbf{E}}(\mathbf{r}_j, t) \cdot \mathbf{d}_j \tag{3.44}$$

$$\dot{\hat{\sigma}}_j^z = \frac{2\mathrm{i}}{\hbar}\, \hat{\sigma}^\dagger\, \hat{\mathbf{E}}(\mathbf{r}_j, t) \cdot \mathbf{d}_j \,+\, \text{h.c.} \tag{3.45}$$

Next we solve for the time derivative of the field operators. To help in the derivation, we expand the atom-field Hamiltonian in terms of the bosononic operators, which gives

$$H_{\mathrm{AF}} = -\mathrm{i} \sum_{j=1}^{N} \int_0^\infty \mathrm{d}\omega \sqrt{\frac{\hbar}{\pi\epsilon_0}\frac{\omega^2}{c^2}} \int \mathrm{d}^3\mathbf{r}'\, \sqrt{\epsilon_I(\mathbf{r}', \omega)}\, \hat{\boldsymbol{d}}_j(t) \cdot \big[\mathbf{G}(\mathbf{r}_j, \mathbf{r}', \omega) \cdot \hat{\mathbf{f}}(\mathbf{r}', \omega) \\ - \mathbf{G}^*(\mathbf{r}_j, \mathbf{r}', \omega) \cdot \hat{\mathbf{f}}^\dagger(\mathbf{r}', \omega)\big]\,. \tag{3.46}$$

Using the commutation relations for $\hat{\mathbf{f}}$ and $\hat{\mathbf{f}}^\dagger$, the Heisenberg equation for $\hat{\mathbf{f}}$ simplifies to

$$\dot{\hat{\mathbf{f}}}(\mathbf{r}, \omega, t) = -\mathrm{i}\omega \hat{\mathbf{f}}(\mathbf{r}, \omega, t) + \sum_{j=1}^{N} \sqrt{\frac{1}{\pi\epsilon_0\hbar}\frac{\omega^2}{c^2}} \sqrt{\epsilon_I(\mathbf{r}, \omega)}\, \hat{\boldsymbol{d}}_j(t) \cdot \mathbf{G}^*(\mathbf{r}, \mathbf{r}_j, \omega). \tag{3.47}$$

The time derivative of the electric field operator $\hat{\mathbf{E}}(\mathbf{r}, \omega, t)$ is obtained by multiplying this equation by $\mathrm{i}\mu_0\omega^2\sqrt{\frac{\hbar\epsilon_0}{\pi}}\sqrt{\epsilon_I(\mathbf{r}, \omega)}\mathbf{G}(\mathbf{r}', \mathbf{r}, \omega)$, integrating over all $\mathbf{r}$-space, and then using the Green's function identity in Eq. (3.33). The result is

$$\dot{\hat{\mathbf{E}}}(\mathbf{r}, \omega, t) = \mathrm{i}\omega \hat{\mathbf{E}}(\mathbf{r}, \omega, t) + \sum_{j=1}^{N} \mathrm{i}\frac{\mu_0\omega^2}{\pi} \mathrm{Im}\mathbf{G}(\mathbf{r}, \mathbf{r}_j, \omega) \cdot \hat{\boldsymbol{d}}_j(t). \tag{3.48}$$

Note that the total electric field $\mathbf{E}(\mathbf{r}, t) = \int_0^\infty \mathrm{d}\omega\, \mathbf{E}(\mathbf{r}, \omega)$ is given by integrating this equation over frequency space.

The equations in Eq. (3.48), (3.44), and (3.45) form a set of coupled nonlinear equations. The strategy that we will use to solve these equations is to eliminate the electric field by solving for it and substituting into the time derivatives of the atomic operators. In Sec. 3.4, we will do this procedure in the frequency domain in the low saturation limit and show that the classical results from Chapter 2 are recovered. In Sec. 3.5, we use the Markov approximation to simplify the electric field operator, and then solve for a master equation for the atoms.

The low saturation limit

In the low saturation limit, the atoms are well approximated by classical dipole oscillators. In Chapter 2, we derived a system of equations for radiatively coupled dipoles. The frequency shifts and decay rates were expressed in terms of the real and imaginary parts of the Green's function. In this section, we show these results are recovered from the quantum formalism. In the low saturation limit, the atom is mostly in the ground state and we can take $\hat{\sigma}^{\mathrm{z}} \to -1$. Then the equation for the dipole operator is linear:

$$\dot{\hat{\sigma}}_j = -\mathrm{i}\omega_A \hat{\sigma} + \frac{\mathrm{i}}{\hbar}\, \hat{\mathbf{E}}(\mathbf{r}_j, t) \cdot \mathbf{d}_j. \tag{3.49}$$

This equation is also applicable to the single excitation subspace. Just as we did in the classical case, we transform to the Fourier domain. Here we use the Laplace transformation [60, 63, 86], and define the variables $\int_0^\infty \mathrm{d}t e^{\mathrm{i}\omega t} O(t) = O(\omega)$. Using $\int_0^\infty \mathrm{d}t e^{\mathrm{i}\omega t} \dot{O}(t) = -\mathrm{i}\omega O(\omega) - O(t\!=\!0)$, the Laplace transform of Eq. (3.44) is

$$\mathrm{i}(\omega - \omega_A)\hat{\sigma}(\omega) = -\hat{\sigma}(t\!=\!0) - \mathrm{i}\frac{1}{\hbar}\mathbf{d}_j \cdot \hat{\mathbf{E}}(\mathbf{r}_j, \omega). \tag{3.50}$$

We assume the atoms is initially in the ground state and ignore $\hat{\sigma}(t = 0)$.

The Laplace transformation for the electric field is more involved and is given in the following section. The final result is the quantum analog of Dyson's equation from Eq. (2.13),

$$\hat{\mathbf{E}}(\mathbf{r}, \omega) = \mathbf{E}_{\mathrm{free}}(\mathbf{r}, \omega) - \sum_{j=1}^{N} \mu_0 \omega^2\, \mathbf{G}(\mathbf{r}, \mathbf{r}_j, \omega) \left(\mathbf{d}_j\, \hat{\sigma}_j(\omega) + \mathbf{d}_j^*\, \hat{\sigma}_j^\dagger(\omega) \right). \tag{3.51}$$

The free-field is the solution without the atoms, and the Green's function propagates the field generated by the atoms. Substituting this expression into the atomic operators gives the system of equations

$$\Delta_A\, \hat{\sigma}_i(\omega) + \sum_{j=1}^{N} \left(J_{ij} + \frac{\mathrm{i}}{2}\Gamma_{ij} \right)\, \hat{\sigma}_j(\omega) = \frac{1}{\hbar}\mathbf{d}_i \cdot \hat{\mathbf{E}}_{\mathrm{free}}(\mathbf{r}_i, \omega), \tag{3.52}$$

where we have defined the decay rates Γ_{ij} and frequency shifts J_{ij} by

$$J_{ij} = \frac{\mu_0 \omega^2}{\hbar}\, \mathrm{Re}[\mathbf{d}_i^*\, \mathbf{G}(\mathbf{r}_i, \mathbf{r}_j, \omega)\mathbf{d}_j] \tag{3.53}$$

$$\Gamma_{ij} = \frac{2\mu_0 \omega^2}{\hbar}\, \mathrm{Im}[\mathbf{d}_i^*\, \mathbf{G}(\mathbf{r}_i, \mathbf{r}_j, \omega)\mathbf{d}_j]. \tag{3.54}$$

For a single atom, the equation is

$$\left(\Delta_A + J + \frac{\mathrm{i}}{2}\Gamma\right)\hat{\sigma}(\omega) = \frac{1}{\hbar}\mathbf{d}\cdot\hat{\mathbf{E}}_{\mathrm{free}}(\mathbf{r}_i,\omega). \tag{3.55}$$

There is one problem with this equation, and that is also related to the divergence of the real part of self-GF in free-space. This would seem to give divergent frequency shifts. We also saw this problem in the classical case, where it stems from the assumption of an infinitesimally small dipole. In the quantum formalism, this problem is overcome by performing the full relativistic field theory calculation. A common trick to overcome this is to replace the real part of the self-Green's function with the scattered Green's function, and to assume that the actual Lamb-shift is already in the definition of the resonance frequency.

Derivation of the Laplace transform of the electric field operator

The proof of Eq. (3.51) is given here. The Laplace transform of Eq. (3.48) is

$$\hat{\mathbf{E}}(\mathbf{r},\omega,\omega') = \mathrm{i}\frac{\hat{\mathbf{E}}(\mathbf{r},\omega,t=0)}{\omega-\omega'} - \sum_{j=1}^{N}\frac{\mu_0\omega^2}{\pi}\frac{\mathrm{Im}\mathbf{G}(\mathbf{r},\mathbf{r}_j,\omega)}{\omega-\omega'}\left(\mathbf{d}_j\,\hat{\sigma}_j(\omega') + \mathbf{d}_j^*\,\hat{\sigma}_j^\dagger(\omega')\right).$$

The total electric field e $\mathbf{E}(\mathbf{r},\omega') = \int_0^\infty \mathrm{d}\omega\,\mathbf{E}(\mathbf{r},\omega,\omega')$ is

$$\hat{\mathbf{E}}(\mathbf{r},\omega') = \mathbf{E}_{\mathrm{free}}(\mathbf{r},\omega') - \sum_{j=1}^{N}\left(\int_0^\infty \mathrm{d}\omega\,\frac{\mu_0\omega^2}{\pi}\frac{\mathrm{Im}\mathbf{G}(\mathbf{r},\mathbf{r}_j,\omega)}{\omega-\omega'}\right)\cdot\left(\mathbf{d}\hat{\sigma}_j(\omega') + \mathbf{d}^*\hat{\sigma}_j^\dagger(\omega')\right).$$

Since the Green's function is analytic in the upper portion of the complex plane, we can use the identity

$$\lim_{y\to 0^+}\int_a^b \mathrm{d}x\,\frac{f(x)}{x+\mathrm{i}y} = -\mathrm{i}\pi\int_a^b \mathrm{d}x\,f(x)\delta(x) + \mathcal{P}\int_a^b \mathrm{d}x\,\frac{f(x)}{x}$$

to expand the integral in the parentheses into

$$\int_0^\infty \mathrm{d}\omega\,\frac{\mu_0\omega^2}{\pi}\frac{\mathrm{Im}\mathbf{G}(\mathbf{r},\mathbf{r}_j,\omega)}{\omega-\omega'} = \mu_0\omega^2\mathrm{Im}\mathbf{G}(\mathbf{r},\mathbf{r}_j,\omega) + \mathcal{P}\int_0^\infty \mathrm{d}\omega\,\frac{\mu_0\omega^2}{\pi}\frac{\mathrm{Im}\mathbf{G}(\mathbf{r},\mathbf{r}_j,\omega)}{\omega-\omega'}.$$

The Kramers-Kronig relations convert the second term in the parentheses to the real part of the Green's function, and combing the real and imaginary parts together gives the final expression (the primes in ω' are omitted)

$$\hat{\mathbf{E}}(\mathbf{r},\omega) = \hat{\mathbf{E}}_{\mathrm{free}}(\mathbf{r},\omega) - \sum_{j=1}^{N}\mu_0\omega^2\mathbf{G}(\mathbf{r},\mathbf{r}_j,\omega)\left(\mathbf{d}_j\,\hat{\sigma}_j(\omega) + \mathbf{d}_j^*\,\hat{\sigma}_j^\dagger(\omega)\right).$$

3.5 The Markov approximation

In order to simplify the system of equations for the field and atomic operators, we will eliminate the field by integrating it and substituting the solution into the atomic operators. Integrating the electric field from Eq. (3.48) gives[3]

$$\hat{\mathbf{E}}(\mathbf{r},\omega,t) = \hat{\mathbf{E}}_{\text{free}}(\mathbf{r},\omega,t) + \sum_{j=1}^{N} \mathrm{i}\frac{\mu_0\omega^2}{\pi}\,\mathrm{Im}\mathbf{G}(\mathbf{r},\mathbf{r}_j,\omega)\cdot\int_0^t \mathrm{d}t' e^{-\mathrm{i}\omega(t-t')}\hat{\boldsymbol{d}}_j(t'). \tag{3.56}$$

The free field $\hat{\mathbf{E}}_{\text{free}}(\mathbf{r},\omega,t) = \mathbf{E}(\mathbf{r},\omega,0)e^{-\mathrm{i}\omega t}$ is the free evolution of the electric field operator for the case of no interaction.

Next we substitute this expression into the field operator $\hat{\mathbf{E}}^+(\mathbf{r},t) = \int_0^\infty \mathrm{d}\omega\hat{\mathbf{E}}^+(\mathbf{r},\omega)$ to get

$$\hat{\mathbf{E}}^+(\mathbf{r},t) = \hat{\mathbf{E}}^+_{\text{free}}(\mathbf{r},t) + \mathrm{i}\sum_{j=1}^{N}\int_0^\infty \mathrm{d}\omega\,\frac{\mu_0\omega^2}{\pi}\,\mathrm{Im}\mathbf{G}(\mathbf{r},\mathbf{r}_j,\omega)\int_0^t \mathrm{d}t' e^{-\mathrm{i}\omega(t-t')}\hat{\boldsymbol{d}}_j(t'). \tag{3.57}$$

The substitution of this expression into Eq. (3.44) and Eq. (3.45) yields a system of integro-differential equations for the atomic variables. Up to this point, no assumptions or approximations have been made besides the initial Hamiltonian.

We will now make assumptions about the time scales of the field system relative to the atomic system in order to get rid of the two integrals in Eq. (3.57) and simplify the integro-differential equations into Langevin-type differential equations.

First, we take the fast time dependence out of the atomic operators by defining the slowly varying atomic operators $\hat{\tilde{\sigma}}_j(t) = \hat{\sigma}_j(t)e^{\mathrm{i}\omega_A t}$. The dipole operator is given by

$$\hat{\boldsymbol{d}}_j(t) = \mathbf{d}_j\hat{\tilde{\sigma}}_j(t)e^{-\mathrm{i}\omega_A t} + \mathbf{d}_j^*\hat{\tilde{\sigma}}_j^\dagger(t)e^{\mathrm{i}\omega_A t}. \tag{3.58}$$

---

[3] Formally, we do this by defining a slowly varying variable by $\hat{\mathbf{E}}(\mathbf{r},\omega) = e^{-\mathrm{i}\omega t}\hat{\tilde{\mathbf{E}}}(\mathbf{r},\omega)$. Substituting this into Eq. (3.48) gives

$$\dot{\hat{\tilde{\mathbf{E}}}}(\mathbf{r},w) = e^{\mathrm{i}\omega t}\sum_{j=1}^{N}\mathrm{i}\frac{\mu_0\omega^2}{\pi}\mathrm{Im}\mathbf{G}(\mathbf{r},\mathbf{r}_j,\omega)\cdot\hat{\boldsymbol{d}}_j(t'),$$

which upon integrating gives

$$\tilde{\mathbf{E}}(\mathbf{r},\omega,t) = \tilde{\mathbf{E}}(\mathbf{r},\omega,0) + \sum_{j=1}^{N}\mathrm{i}\frac{\mu_0\omega^2}{\pi}\mathrm{Im}\mathbf{G}(\mathbf{r},\mathbf{r}_j,\omega)\cdot\int_0^t \mathrm{d}t' e^{\mathrm{i}\omega(t'-t)}\hat{\boldsymbol{d}}_j(t').$$

We multiply both sides by $e^{-\mathrm{i}\omega t}$ and convert back to the normal variable to get the final expression. Note that we have defined the free field as $\hat{\mathbf{E}}_{\text{free}} = \hat{\mathbf{E}}(\mathbf{r},\omega,0)e^{-\mathrm{i}\omega t}$, which is the behavior of the field without interaction.

If the system is driven by an external coherent source with frequency ω_L, as we will assume in section 3.5, it is more appropriate to use the frequency of the laser here, $\hat{\tilde{\sigma}}_j(t) = \hat{\sigma}_j(t)e^{\mathrm{i}\omega_L t}$. For now we will assume that the initial electric field is in the ground state, so that the free field $\hat{\mathbf{E}}_{\text{free}}$ represents a Langvein noise force.

Inserting the dipole operator in Eq. (3.58) into the field gives[4]

$$\begin{aligned}\hat{\mathbf{E}}^{+}(\mathbf{r},t) = \hat{\mathbf{E}}^{+}_{\text{free}}(\mathbf{r},t) + \mathrm{i}\sum_{j=1}^{N}\int_0^\infty \mathrm{d}\omega\,\frac{\mu_0\omega^2}{\pi}\,\mathrm{Im}\mathbf{G}(\mathbf{r},\mathbf{r}_j,\omega)e^{-\mathrm{i}\omega_A t}\\ \cdot\int_0^t \mathrm{d}t'\left[\mathbf{d}_j\hat{\tilde{\sigma}}_j(t')e^{-\mathrm{i}(\omega-\omega_A)(t'-t)} + \mathbf{d}_j^{*}\hat{\tilde{\sigma}}_j^{\dagger}(t')e^{\mathrm{i}(\omega+\omega_A)(t'-t)}\right]\end{aligned}\quad. \tag{3.59}$$

Next we make the Markov approximation by assuming that after we perform the frequency integral, the time integral only contributes over a small correlation time interval τ_c [91]. The correlation time interval τ_c is determined by the bandwidth of $\mathrm{Im}\mathbf{G}(\mathbf{r},\mathbf{r}_j,\omega)$, with a broad spectrum (e.g. in a waveguide or bad cavity) producing a short time interval τ_c, and a narrow spectrum (e.g. in a good cavity) producing a long time interval τ_c. If the time scale of the atomic operator is much longer than τ_c, then we can make the approximation $\sigma(t') \approx \sigma(t)$ and take it out of the time integral. Another interpretation of this approximation is that we are assuming that the field system has no memory of the atomic system. We also assume $t \gg \tau_c$ and take the lower time integration limit to $-\infty$. The electric field operator is then

$$\begin{aligned}\hat{\mathbf{E}}^{+}(\mathbf{r},t) = \hat{\mathbf{E}}^{+}_{\text{free}}(\mathbf{r},t) + \mathrm{i}\sum_{j=1}^{N}\int_0^\infty \mathrm{d}\omega\,\frac{\mu_0\omega^2}{\pi}\,\mathrm{Im}\mathbf{G}(\mathbf{r},\mathbf{r}_j,\omega)e^{-\mathrm{i}\omega_A t}\\ \cdot\left[\mathbf{d}_j\hat{\tilde{\sigma}}_j(t)\int_{-\infty}^{t}\mathrm{d}t' e^{-\mathrm{i}(\omega-\omega_A)(t'-t)} + \mathbf{d}_j^{*}\hat{\tilde{\sigma}}_j^{\dagger}(t)\int_{-\infty}^{t}\mathrm{d}t' e^{\mathrm{i}(\omega+\omega_A)(t'-t)}\right].\end{aligned} \tag{3.60}$$

The expression in the time integral can be written in terms of a delta function and principal value part,

$$\int_{-\infty}^{t} e^{-\mathrm{i}(\omega-\omega_A)(t'-t)} = \zeta(\omega-\omega_A) = \pi\delta(\omega-\omega_A) + \mathrm{i}\mathcal{P}\left(\frac{1}{\omega-\omega_A}\right). \tag{3.61}$$

---

[4] Sometimes these integrals are solved by first performing the frequency integration. The frequency part of the integral is $\int_0^\infty \mathrm{d}\omega\,\frac{\mu_0\omega^2}{\pi}\mathrm{Im}\mathbf{G}(\mathbf{r},\mathbf{r}_j,\omega)e^{-\mathrm{i}\omega(t-t')}$. For specific systems where the Green's function is known, then we perform this integral. But for arbitrary systems, we have to perform the time integral first.

Converting the slowly varying atomic operators back into normal operator gives

$$\begin{aligned}\hat{\mathbf{E}}^{+}(\mathbf{r},t) &= \hat{\mathbf{E}}^{+}_{\text{free}}(\mathbf{r},t)\\ &+ \mathrm{i}\sum_{j=1}^{N}\int_0^\infty \mathrm{d}\omega\,\frac{\mu_0\omega^2}{\pi}\,\mathrm{Im}\mathbf{G}(\mathbf{r},\mathbf{r}_j,\omega)\cdot\left[\mathbf{d}_j\hat{\sigma}_j(t)\zeta(\omega-\omega_A)+\mathbf{d}_j^*\hat{\sigma}_j^\dagger(t)e^{2\mathrm{i}\omega_A t}\zeta(\omega+\omega_A)\right].\end{aligned} \tag{3.62}$$

The delta function in $\zeta(\omega+\omega_A)$ is not in the integral interval, and the remaining principal value integral is related to Casimir forces [81] and is typically small when far enough away from the dielectric [35].

$$\begin{aligned}\hat{\mathbf{E}}^{+}(\mathbf{r},t) &= \hat{\mathbf{E}}^{+}_{\text{free}}(\mathbf{r},t)\\ &= \sum_{j=1}^{N}\hat{\sigma}_j(t)\left[\mathrm{i}\mu_0\omega_A^2\,\mathrm{Im}\mathbf{G}(\mathbf{r},\mathbf{r}_j,\omega_A)\cdot\mathbf{d}_j+\frac{\mu_0}{\pi}\mathcal{P}\int_0^\infty \mathrm{d}\omega\frac{\omega^2\mathrm{Im}\mathbf{G}(\mathbf{r},\mathbf{r}_j,\omega)\cdot\mathbf{d}_j}{\omega-\omega_A}\right],\end{aligned} \tag{3.63}$$

where the principal value simplifies using the Kramers-Kronig relation to[5]

$$\mathcal{P}\int_0^\infty \mathrm{d}\omega\frac{\omega^2\,\mathrm{Im}\mathbf{G}(\mathbf{r},\mathbf{r}_j,\omega)}{\omega-\omega_A} = \pi\omega_A^2\,\mathrm{Re}\mathbf{G}(\mathbf{r},\mathbf{r}_j,\omega_A)+\int_0^\infty \mathrm{d}\kappa\kappa^2\mathrm{Re}\mathbf{G}(\mathbf{r},\mathbf{r}_j,\mathrm{i}\kappa)\frac{\omega_A}{\kappa^2+\omega_A^2} \tag{3.64}$$

. The last term is negligible for atom separation distances on the scale of the wavelength or larger, and will be ignored [76]. The imaginary and real parts of the Green's function combine together into the total Green's function, and the final expression for the electric field operator in the Markov approximation is

$$\boxed{\hat{\mathbf{E}}^{+}(\mathbf{r},t) = \hat{\mathbf{E}}^{+}_{\text{free}}(\mathbf{r},t)+\mu_0\omega_A^2\sum_{j=1}^{N}\mathbf{G}(\mathbf{r},\mathbf{r}_j,\omega_A)\cdot\mathbf{d}_j\,\hat{\sigma}_j(t).} \tag{3.65}$$

This equation is reminiscent of Dyson's equation for the electric field emitted from a dipole, but it is in the time domain. The meaning of the Markov approximation is made more clear by comparing this to the result in Fourier domain in

---

[5] Due to causality, $\mathbf{G}(\mathbf{r},\mathbf{r}',\omega)$ is analytic in the upper half complex plane (no poles), and the Kramers-Kronig relations are

$$\mathrm{Re}\mathbf{G}(\mathbf{r},\mathbf{r}',\omega_A) = \frac{1}{\pi}\mathcal{P}\int_{-\infty}^\infty \mathrm{d}\omega\frac{\mathrm{Im}\mathbf{G}(\mathbf{r},\mathbf{r}',\omega)}{\omega-\omega_A} = \frac{2}{\pi}\mathcal{P}\int_0^\infty \mathrm{d}\omega\frac{\omega\,\mathrm{Im}\mathbf{G}(\mathbf{r},\mathbf{r}',\omega)}{\omega^2-\omega_A^2},$$

where the second part uses the symmetry $\mathbf{G}^*(\mathbf{r},\mathbf{r}',\omega)=\mathbf{G}(\mathbf{r},\mathbf{r}',-\omega^*)$. The expression in Eq. (3.64) has an extra ω factor in the numerator, and ref. [76] derives the correction term, which is the second part of Eq. (3.64).

Eq. (3.51), where neither the Markov approximation or rotating wave approximation was required. Taking the inverse Laplace transform of Eq. (3.51) gives the non-approximate solution in the time domain

$$\hat{\mathbf{E}}(\mathbf{r},t) = \hat{\mathbf{E}}_{\text{free}}(\mathbf{r},t) - \sum_{j=1}^{N} \mu_0 \omega^2 \int_0^t \mathrm{d}\tau \mathbf{G}(\mathbf{r},\mathbf{r}_j,t-\tau)\left(\mathbf{d}\hat{\sigma}_j(\tau) + \mathbf{d}^*\hat{\sigma}_j^\dagger(\tau)\right). \quad (3.66)$$

To get to the Markov approximation, we are assuming $\mathbf{G}(\mathbf{r},\mathbf{r}',t-\tau) \approx \mathbf{G}(\mathbf{r},\mathbf{r}',\omega_A)\delta(t-\tau)$. In fact, I think this might be a more satisfying derivation of the Markov approximation for the electric field than the one given above.

The atomic system in the Markov approximation

When the Markov approximation for the electric field in Eq. (3.65) is inserted into the Heisenberg equation for the atomic operators in Eq. (3.44) and (3.45), the result is

$$\dot{\hat{\sigma}}_k = \mathrm{i}\omega_A \hat{\sigma}_k - \mathrm{i}\hat{\sigma}_k^{\mathrm{z}} \sum_{j=1}^{N} \hat{\sigma}_j \frac{\mu_0\omega^2}{\hbar} \mathbf{d}_k^* \mathbf{G}(\mathbf{r}_k,\mathbf{r}_j,\omega_A)\mathbf{d}_j - \mathrm{i}\hat{\Omega}_k \hat{\sigma}_k^{\mathrm{z}} \quad (3.67)$$

$$\dot{\hat{\sigma}}_k^{\mathrm{z}} = 2\mathrm{i}\frac{\mu_0\omega^2}{\hbar} \sum_j \left[\mathbf{d}_k^* \mathbf{G}(\mathbf{r}_k,\mathbf{r}_j,\omega_A)\mathbf{d}_j\, \hat{\sigma}_k^\dagger \hat{\sigma}_j - \text{h.c.}\right] + 2\mathrm{i}(\hat{\Omega}_k \hat{\sigma}_k^\dagger - \text{h.c.}). \quad (3.68)$$

The electric free-field operator $\hat{\Omega}_k$ is

$$\hat{\Omega}_k = \mathbf{d}_k \cdot \hat{\mathbf{E}}^+_{\text{free}}(\mathbf{r}_k,\omega)/\hbar. \quad (3.69)$$

Remember that in performing the Markov approximation, we assume that the dipole operator evolves with $e^{\mathrm{i}\omega_A t}$, which requires that the free-field is either close to resonance or in the group state. We treat the driven case in Sec. 3.5, and for now assume the initial electric field is in the ground state, in which case $\hat{\Omega}_k$ can be interpreted as a Langevin noise term.

The electric field operator in Eq. (3.67) and (3.68) has been eliminated. In the low saturation limit where we can take $\hat{\sigma}^{\mathrm{z}} \approx -1$, the first equation is reminiscent of the classical system of equations for radiatively coupled dipoles in Eq. (2.40). Just as we did for the classical case, we define the complex coupling rate

$$g_{ij} = J_{ij} + \frac{\mathrm{i}}{2}\Gamma_{ij} = \frac{\mu_0\omega_A^2}{\hbar}\mathbf{d}_i^* \mathbf{G}(\mathbf{r}_i,\mathbf{r}_j,\omega_A)\mathbf{d}_j \quad (3.70)$$

and the spin-exchange rates and dissipation rates

$$\Gamma_{ij} = \frac{2\mu_0\omega_A^2}{\hbar}\,\mathrm{Im}[\mathbf{d}_i^*\, \mathbf{G}(\mathbf{r}_i,\mathbf{r}_j,\omega_A)\mathbf{d}_j] \quad (3.71)$$

$$J_{ij} = \frac{\mu_0\omega_A^2}{\hbar}\,\mathrm{Re}[\mathbf{d}_i^*\, \mathbf{G}(\mathbf{r}_i,\mathbf{r}_j,\omega_A)\mathbf{d}_j]. \quad (3.72)$$

Then the equation for $\hat{\sigma}_k$ in the low saturation limit is

$$\dot{\hat{\sigma}}_k = \mathrm{i}(\omega_A + J_{kk})\hat{\sigma}_k - \frac{1}{2}\Gamma_{kk}\hat{\sigma}_k + \mathrm{i}\sum_{j\neq k}\hat{\sigma}_j\left(J_{kj} + \frac{\mathrm{i}}{2}\Gamma_{kj}\right) + \mathrm{i}\hat{\Omega}_k. \tag{3.73}$$

For a single atom, J_{kk} is the frequency shift, Γ_{kk} is the decay rate. The two atom rates J_{kj} and Γ_{kj} are the interactions between the atoms.

The system of equations can be solved beyond the low saturation using the quantum regression theorem [16, 20, 49].

The atomic system master equation

In the density matrix formalism, the state of the system is represented by the density matrix $\hat{\rho}(t)$, where now the time dependence is on the state rather than the operators. In this section we will use the Markov approximation for the electric field to derive a master equation for the density matrix of the atomic subspace of the system [69, 88, 92]. The final result can also be derived by tracing out the field components in a Born-Markov approximation [89, 93–96]. The master equation will show the close analogy between atoms interacting along a waveguide and spin-spin physics in condensed matter systems.

The derivation has a lot of algebra, but there are no additional assumptions made beyond what was made in the Markov approximation for the electric field. The first step is to calculate the Heisenberg equation for an arbitrary atomic operator $\hat{O}$ using the Hamiltonian from Eq. (3.41),

$$\dot{\hat{O}}(t) = \mathrm{i}\sum_{j=1}^{N}\frac{\omega_A}{2}[\hat{O},\hat{\sigma}_j^z] - \frac{1}{\mathrm{i}\hbar}\sum_{j=1}^{N}\left(\hat{\mathbf{E}}^+(\mathbf{r}_j,t)\cdot[\hat{O},\hat{\boldsymbol{d}}_j(t)] + [\hat{O},\hat{\boldsymbol{d}}_j(t)]\cdot\hat{\mathbf{E}}^-(\mathbf{r}_j,t)\right). \tag{3.74}$$

In this expression, we have substituted $\hat{\mathbf{E}}(\mathbf{r},t) = \hat{\mathbf{E}}^+(\mathbf{r},t) + \hat{\mathbf{E}}^-(\mathbf{r},t)$, and for convenience have adapted normal ordering so that $\hat{\mathbf{E}}^-(\mathbf{r},t)$ operators on the right, and $\hat{\mathbf{E}}^+(\mathbf{r},t)$ on the left. Next we substitute $\hat{\boldsymbol{d}}_j(t) = \mathbf{d}\hat{\sigma}_j(t) + \mathbf{d}^*\hat{\sigma}_j^\dagger(t)$ and the Markov approximation for the electric field in Eq. (3.65). We make the rotating wave approximation by omitting the terms $\hat{\sigma}_j\hat{\sigma}_k$ and $\hat{\sigma}_j^\dagger\hat{\sigma}_k^\dagger$ since they oscillate at $2\omega_A$ (this can more be seen more clear if we convert to the slowly varying variables).

The next step is to convert from the Heisenberg picture to the Schrodinger picture. In the density matrix formalism, the expectation value of an operator $\hat{O}(t)$ for a system represented by a density matrix $\hat{\rho}$ is given by $\langle\hat{O}\rangle = \mathrm{Tr}[\hat{\rho}O]$. We multiply both sides on the left by the density matrix $\hat{\rho}(0)$, take the trace, and then use the cyclic property of the trace to transfer the time dependence from the operator to the density matrix, for example the left side becomes $\langle \dot{\hat{O}} \rangle = \mathrm{Tr}[\hat{\rho}(0)\hat{O}(t)] = \mathrm{Tr}[\hat{\rho}(0)(U(t)\hat{O}(0)U^{\dagger}(t))] = \mathrm{Tr}[(U^{\dagger}(t)\hat{\rho}(0)U(t))\hat{O}(0)] = \mathrm{Tr}[\hat{\rho}(t)\hat{O}(0)]$. We are effectively converting from the Heisenberg picture, where the operators have the time dependence, to the Schrodinger picture, where the states have the time dependence.

The final step is to use the cyclic property of the trace to rearrange each term so that the operator $O(0)$ (which no longer is time dependent) is on the right. The final equation has the form

$$\mathrm{Tr}[\dot{\hat{\rho}}(t)\hat{O}(0)] = \mathrm{Tr}[\cdots \hat{O}(0)], \tag{3.75}$$

where the dots represent the expression which we can identify as the master equation for the atomic systems. We write separate the master equation into the conservative and dissipative parts as

$$\dot{\hat{\rho}} = \frac{\mathrm{i}}{\hbar}[H_0, \hat{\rho}] + \mathcal{L}[\hat{\rho}], \tag{3.76}$$

where the conservative Hamiltonian is given by

$$H_0 = \sum_{j=1}^{N} \frac{\hbar\omega_A}{2}\hat{\sigma}_j^z + \sum_{j,k=1}^{N} J_{jk}\hat{\sigma}_j^{\dagger}\sigma_k \tag{3.77}$$

and the dissipative Lindblad is given by

$$\mathcal{L}[\hat{\rho}] = -\frac{1}{2}\sum_{j,k=1}^{N} \Gamma_{jk}\left(\hat{\sigma}_j^{\dagger}\hat{\sigma}_k\hat{\rho} - 2\hat{\sigma}_k\hat{\rho}\hat{\sigma}_j^{\dagger} + \hat{\rho}\hat{\sigma}_j^{\dagger}\hat{\sigma}_k\right). \tag{3.78}$$

Note that since we assume that the initial electric field is in the ground state, when we take the expectation, the free electric terms $\hat{\Omega}$ vanish. This master equation is a familiar one in spin-spin physics, with the frequency-shift rates J_{jk} representing the hoping of the excitations between sites.

This type of master equation can be diagonalized to find the excited states of the system [74, 94]. For a two atom system, the eigenstates are shown in Fig. 3.1 [19, 88–90]. The first excitation manifold has a symmetric $|eg\rangle + |ge\rangle$ state and an anti-symmetric $|eg\rangle - |ge\rangle$ state. Similar to the dipole eigenmodes of the classical case of two interacting dipoles, one has a superradiant decay $\Gamma' + \Gamma_{11} + \Gamma_{12}$ and the other has a subradiant decay $\Gamma' + \Gamma_{11} - \Gamma_{12}$. The two states are separated by a frequency $2J_{12}$.

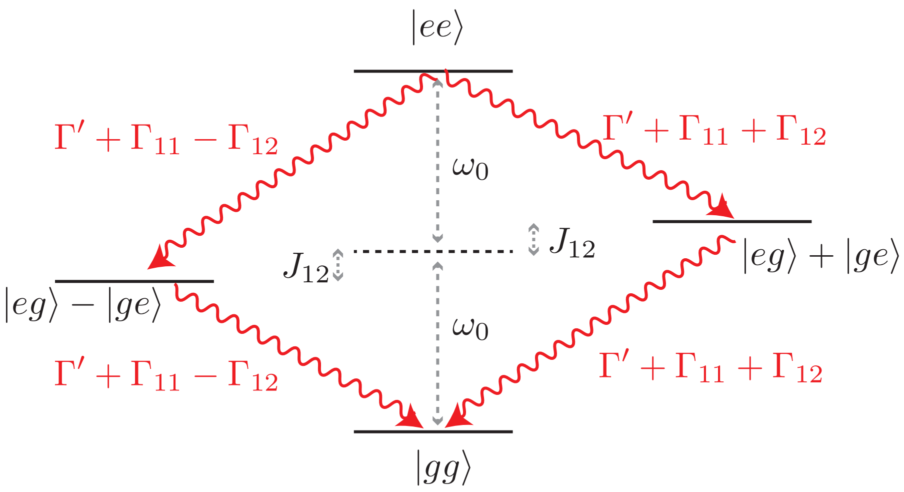

Figure 3.1: Level structure for two radiatively coupled atoms. The bright mode has supperradiant decay, white the dark mode has a subradiant decay.

A Driven System

In the derivation of the electric field in the Markov approximation, we assumed that the fast time dependence of the atomic dipole operators oscillate with the atomic resonance frequency ω_A. We now consider a system that is driven by a coherent laser source at frequency ω_L. Previously, we assumed that the initial electric field was in the ground state, so that the total electric field $\hat{\mathbf{E}}(\mathbf{r}, \omega)$ contained the vacuum fluctuations and the field emitted by the atoms. Now we write the total electric field as

$$\hat{\mathbf{E}}_{\text{tot}}(\mathbf{r}, t) = \hat{\mathbf{E}}(\mathbf{r}, t) + \mathbf{E}_{\text{laser}}(\mathbf{r})\, e^{\mathrm{i}\omega_L t}, \tag{3.79}$$

where $\mathbf{E}(\mathbf{r}, t)$ is the same as before, but now there is a classical drive field at the frequency of the laser ω_L with spatial profile $\mathbf{E}_{\text{laser}}(\mathbf{r})$. This expression can formally be obtained by assuming that the initial is in a coherent state, and then performing a transformation with the displacement operator to convert the field to the ground state and the electric field operator to Eq. (3.79).

Substituting this expression into the total Hamiltonian of Eq. (3.41) produces a drive term

$$H_{\text{drive}} = -\sum_{j=1}^{N} \hbar \left(\Omega_j e^{\mathrm{i}\omega_L t}\, \hat{\sigma}_j + \Omega_j^* e^{-\mathrm{i}\omega_L t} \hat{\sigma}_j^\dagger \right), \tag{3.80}$$

where the drive coefficient Ω_k is

$$\Omega_k = \mathbf{d}_k \cdot \mathbf{E}^+_{\text{laser}}(\mathbf{r}_k)/\hbar. \tag{3.81}$$

To get rid of the time dependence of the drive term, we can rotate to frame of the laser. In the Heisenberg picture, we define the transformed variables $\hat{\hat{O}} = \hat{U}^\dagger\hat{O}\hat{U}$, where $\hat{U} = e^{\mathrm{i}\hat{H}_u t/\hbar}$ is a unitary transformation. (Note that this is the same procedure as performed when converting to the slowly varying variables.) The Hamiltonian for the transformed variable is given by[6]

$$\hat{H}' = \hat{U}^\dagger\hat{H}\hat{U} - \hat{H}_u. \tag{3.82}$$

We use $H_u = \hbar\omega_L\left(\int \mathrm{d}^3\mathbf{r}\int \mathrm{d}\omega\, \hat{\mathbf{f}}^\dagger\hat{\mathbf{f}} + \sum_{j=1}^N \hat{\sigma}_j^\dagger\hat{\sigma}_j\right)$, which then gives the transformed Hamiltonian (ignoring the primes)

$$\begin{aligned}\hat{H} = &\int \mathrm{d}^3\mathbf{r}\int_0^\infty \mathrm{d}\omega\ \hbar(\omega-\omega_\mathrm{L})\,\hat{\mathbf{f}}^\dagger(\mathbf{r},\omega)\,\hat{\mathbf{f}}(\mathbf{r},\omega) + \sum_{j=1}^N \frac{\hbar\Delta_A}{2}\hat{\sigma}_j^\mathrm{z} \\ &- \sum_{j=1}^N \hat{\mathbf{E}}(\mathbf{r}_j,t)\cdot\left(\mathbf{d}\,\hat{\sigma}_j + \mathbf{d}^*\,\hat{\sigma}_j^\dagger\right) - \sum_{j=1}^N \hbar\left(\Omega_j\,\hat{\sigma}_j + \Omega_j^*\hat{\sigma}_j^\dagger\right).\end{aligned} \tag{3.83}$$

The detuning $\Delta_A = \omega_L - \omega_A$ is between the laser and the atomic resonance frequency.

In the frame of the laser, the Heisenberg equations for the atomic operators are

$$\dot{\hat{\sigma}}_k = \mathrm{i}\Delta_A\hat{\sigma}_k - \mathrm{i}\hat{\sigma}_k^\mathrm{z}\sum_{j=1}^N \hat{\sigma}_j\frac{\mu_0\omega^2}{\hbar}\mathbf{d}_k^*\mathbf{G}(\mathbf{r}_k,\mathbf{r}_j,\omega_L)\mathbf{d}_j - \mathrm{i}\Omega_k\hat{\sigma}_k^\mathrm{z} \tag{3.84}$$

$$\dot{\hat{\sigma}}_k^\mathrm{z} = 2\mathrm{i}\frac{\mu_0\omega^2}{\hbar}\sum_j\left[\mathbf{d}_k^*\mathbf{G}(\mathbf{r}_k,\mathbf{r}_j,\omega_L)\mathbf{d}_j\,\hat{\sigma}_k^\dagger\hat{\sigma}_j - \mathrm{h.c.}\right] + 2\mathrm{i}(\Omega_k\hat{\sigma}_k^\dagger - \mathrm{h.c.}), \tag{3.85}$$

and the master equation is again $\dot{\hat{\rho}} = \frac{\mathrm{i}}{\hbar}[H_0,\hat{\rho}] + \mathcal{L}[\hat{\rho}]$, where the conservative part is

$$H_0 = \sum_{j=1}^N \frac{\hbar\Delta_A}{2}\hat{\sigma}_j^\mathrm{z} + \sum_{j,k=1}^N J_{jk}\hat{\sigma}_j^\dagger\sigma_k \tag{3.86}$$

and the dissipative Lindblad is

$$\mathcal{L}[\hat{\rho}] = -\frac{1}{2}\sum_{j,k=1}^N \Gamma_{jk}\left(\hat{\sigma}_j^\dagger\hat{\sigma}_k\hat{\rho} - 2\hat{\sigma}_k\hat{\rho}\hat{\sigma}_j^\dagger + \hat{\rho}\hat{\sigma}_j^\dagger\hat{\sigma}_k\right), \tag{3.87}$$

---

[6] The proof in the Heisenberg picture is as follows. The Heisenberg equation for the normal variables is $\dot{\hat{O}} = \frac{1}{\mathrm{i}\hbar}[\hat{O},\hat{H}] + \delta\hat{O}/\delta t$. We assume the operator $\hat{O}$ has no explicit time dependence and ignore the last term. The derivative of the transformed operator is $\dot{\hat{\hat{O}}} = \frac{\mathrm{d}}{\mathrm{d}t}[\hat{U}^\dagger\hat{O}\hat{U}] = \dot{\hat{U}}^\dagger\hat{O}\hat{U} + \hat{U}^\dagger\hat{O}\dot{\hat{U}} + \hat{U}^\dagger\dot{\hat{O}}\hat{U}$. Substituting the original Heisenberg equation for the third term, and using $\dot{\hat{U}} = \mathrm{i}\hat{H}_u/\hbar = \hat{U}$ for the first two terms, we get $\dot{\hat{\hat{O}}} = \frac{1}{\mathrm{i}\hbar}[\hat{\hat{O}},\hat{U}^\dagger\hat{H}\hat{U} - \hat{H}_u]$, and we can identify $\hat{U}^\dagger\hat{H}\hat{U} - \hat{H}_u$ as the Hamiltonian for the transformed operator.

where now the atomic frequency ω_A in the spin-exchange rates and dissipation rates is replaced with the laser frequency,

$$\Gamma_{ij} = \frac{2\mu_0\omega_A^2}{\hbar}\,\mathrm{Im}[\mathbf{d}_i^*\,\mathbf{G}(\mathbf{r}_i, \mathbf{r}_j, \omega_L)\mathbf{d}_j] \tag{3.88}$$

$$J_{ij} = \frac{\mu_0\omega_A^2}{\hbar}\,\mathrm{Re}[\mathbf{d}_i^*\,\mathbf{G}(\mathbf{r}_i, \mathbf{r}_j, \omega_L)\mathbf{d}_j]. \tag{3.89}$$

3.6 Including angular momentum

The above formalism is for a two-level system. We have been often approximating the atom as only two-levels which are coupled by linearly polarized light. The correct description of the atom must include the all the hyperfine and Zeeman levels of the atom. While currently in our experiment, we have been assuming that the atom is in a incoherent mixture of all the Zeeman sublevels, future experiments will need to optically pump to a single m_f level in order to observe coherent dynamics. The extension of the above formalism is presented in Appendix A.

Chapter 4

ATOMS COUPLED TO A QUASI-1D NANOSTRUCTURE

Many efforts have been made in the past few decades to couple quantum emitters with the electromagnetic fields of a variety of quasi-1D nanostructured reservoirs, ranging from high-quality optical [1–5, 97] and microwave [7, 8] cavities to dielectric [9–15], metallic [16–19], and superconducting [20, 21] waveguides. The photonic crystal waveguides have more recently been proposed as a strong candidates to study long- and tunable-range coherent interactions between quantum emitters [38–41]. Due to the different character of the guided modes at various frequencies within the band structure of the photonic crystal, the interaction of the quantum emitters with the nanostructure can be remarkably distinct. Far away from the bandgap, where light propagates, the guided modes resemble those of a conventional waveguide. Close to the bandgap, but still in the propagating region, the fields of a finite length PCW are similar to those of a quasi-1D cavity, whereas inside the bandgap the fields become evanescent, decaying exponentially.

All of these regimes have been recently explored in the lab, where atoms [32, 36, 37] and quantum dots [28, 98, 99] have been interfaced with photonic crystal waveguides. Most of these experiments have been performed in conditions where the resonance frequency of the emitter lies outside the bandgap. However, very recently, the first experiments of atoms [42] and superconducting qubits [100] interacting with evanescent modes in the bandgap of photonic crystal waveguides have been reported.

Within this context, it has become a necessity to understand the rich spectral signatures of atom-like emitters interacting through the guided modes of quasi one-dimensional nanophotonic structures within a unified framework that extends beyond those of cavity [101] or waveguide QED [102]. In this work, we employ a formalism based on the classical electromagnetic Green's function [46, 78, 82, 88, 89] described in Chapter 3 to characterize the response of atoms that interact by emitting and absorbing photons through the guided mode of the nanostructure. Since the fields in the vicinity of the structure might have complex spatial and polarization patterns, the full Green's function is only known analytically for a handful of systems (such as planar multilayer stacks [103], infinite nanofibers [50, 104], and a few more [82]) and beyond that one has to resort to numerical solvers of Maxwell's equations.

However, in quasi-1D nanostructures, one can isolate the most relevant guided mode and build a simple prescription for the 1D Green's function that accounts for the behavior of this mode, greatly simplifying the problem.

In this chapter, we apply the Green's function formalism from Chapter 3 to a collection of atoms in different quasi one-dimensional dielectric environments, and analyze the atomic transmission and reflection spectra in terms of the eigenvalues of the matrix consisting of the Green's functions between every pair of atoms. We show that, in the linear (low-saturation) regime, asymmetry in the transmission spectra and frequency shifts are signatures of coherent atom-light interactions, whereas symmetric lineshapes reveal dissipation. In Sec. 4.4 and 4.5, we show how the generalized model reproduces the expected results for cavities and waveguides upon simply introducing their respective Green's functions. For example, the cavity model shows Rabi-splitting in the strong coupling limit. And the waveguide model converges to the optical depth model in the low coupling limit. Finally, in Sec. 4.6, we explore the expected spectral features near the band-edge of a photonic crystal waveguide, where we eventually hope to study many-body systems with a tunanble-range interactions.

4.1 The low-saturation atomic system

In Sec. 3.4, we derived an expression for the electric field operator and a low-saturation system of equations for the atomic dipole moments. These expressions were in terms of the free-field (the field not coming from the atoms) and the full EM Green's function. We use these two expressions, but make one change of convention. As discussed in Chapter 2, the Green's function can be decomposed into a part coming from the guided modes and a part coming from the non-guided (i.e. free-space) modes:

$$\mathbf{G}(\mathbf{r}_i, \mathbf{r}_j, \omega) = \mathbf{G}_{\mathrm{wg}}(\mathbf{r}_i, \mathbf{r}_j, \omega) + \mathbf{G}'(\mathbf{r}_i, \mathbf{r}_j, \omega). \tag{4.1}$$

Here the first term corresponds to the guided modes that propagate along the structure, and the second term accounts for all other modes (e.g. emission into free-space). For many systems, $\mathbf{G}'(\mathbf{r}_i, \mathbf{r}_j, \omega)$ is similar to the free-space Green's function from Sec. 2.2, and therefore has a fast spatial decay. This is because the quasi-1D dielectric structure does not strongly alter the free-space modes. When the atoms are spaced by more than a wavelength, we can approximate

$$\mathbf{G}'(\mathbf{r}_i, \mathbf{r}_j, \omega) \approx \mathbf{G}'(\mathbf{r}_i, \mathbf{r}_i, \omega)\delta_{ij}, \tag{4.2}$$

or equivalently $\Gamma_{ij} = \Gamma_{ij}^{\mathrm{wg}} + \Gamma'_{ii}\delta_{ij}$ and $J_{ij} = J_{ij}^{\mathrm{wg}} + J'_{ii}\delta_{ij}$, where δ_{ij} is the Kronecker delta. We assume that J' is identical for every atom and incorporate it into the definition of ω_A. That is the case for example if all the atoms are at the same position relative to the dielectric structure (see Ref. [105] for more detail).

In the Fourier domain, the electric field operator is still (see Eq. (3.51))

$$\hat{\mathbf{E}}^{+}(\mathbf{r},\omega) = \hat{\mathbf{E}}^{+}_{\mathrm{free}}(\mathbf{r},\omega) - \sum_{j=1}^{N} \mu_0\omega^2 \mathbf{G}(\mathbf{r},\mathbf{r}_j,\omega)\,\mathbf{d}_j\,\hat{\sigma}_j(\omega). \tag{4.3}$$

The first term is the free-field from some input source, and the second term is the emitted field from each of the N atoms. It is important to remember that this expression was derived without using the Markov approximation, and the results that follow in this chapter are equally valid in the non-Markovian limit, e.g. in strong-coupling limit of CQED. As long as $\mathbf{r} \neq \mathbf{r}_j$, we can replace the total Green's function with the waveguide Green's function $\mathbf{G}_{\mathrm{wg}}$.

In the low saturation regime the atoms are represented by a linear system of equations (see Eq. 3.52),

$$\left(\Delta_A + \frac{\mathrm{i}}{2}\Gamma'\right)\hat{\sigma}_i(\omega) + \sum_{j=1}^{N} g_{ij}\;\hat{\sigma}_j(\omega) = \frac{1}{\hbar}\mathbf{d}_i \cdot \hat{\mathbf{E}}^{+}_{\mathrm{free}}(\mathbf{r}_i,\omega). \tag{4.4}$$

Here, the detuning from the atomic resonance frequency is $\Delta_A = (\omega - \omega_A)$, and the complex waveguide coupling rates are

$$g_{ij} = J_{ij} + \frac{\mathrm{i}}{2}\Gamma_{ij} = \frac{\mu_0\omega^2}{\hbar}\,\mathbf{d}_i^{*}\,\mathbf{G}_{\mathrm{wg}}(\mathbf{r}_i,\mathbf{r}_j,\omega)\mathbf{d}_j, \tag{4.5}$$

where the real and imaginary parts are the decay rates Γ_{ij} and frequency shifts J_{ij} given by

$$J_{ij} = \frac{\mu_0\omega^2}{\hbar}\,\mathrm{Re}[\mathbf{d}_i^{*}\,\mathbf{G}_{\mathrm{wg}}(\mathbf{r}_i,\mathbf{r}_j,\omega)\mathbf{d}_j] \tag{4.6}$$

$$\Gamma_{ij} = \frac{2\mu_0\omega^2}{\hbar}\,\mathrm{Im}[\mathbf{d}_i^{*}\,\mathbf{G}_{\mathrm{wg}}(\mathbf{r}_i,\mathbf{r}_j,\omega)\mathbf{d}_j]. \tag{4.7}$$

Note that we have omitted the waveguide superscripts on J and Γ, which will be the convention from now on. The decay rate Γ' in Eq. (4.4) represents the non-collective decay of the atoms due to non-guided modes.

The linear systems of equations in Eq. (4.4) can be solved by inverting the left side. The solution for the atomic operators $\hat{\sigma}_j$ can then be substituted into the electric field operator in Eq. (4.3) to obtain the solution for the field at any position. But before proceeding, we simplify the notation of the system of equations and electric field operator. First, we express the free field $\mathbf{E}^{+}_{\text{free}}(\mathbf{r}_k, \omega)$ as if it is being emitted by some classical dipole $\mathbf{d}_{\text{in}}$ at a position $\mathbf{r}_{\text{in}}\sigma_{\text{in}}$ which is far outside the system,

$$\hat{\mathbf{E}}^{+}_{\text{free}}(\mathbf{r}, \omega) = \mu_0\omega^2\mathbf{G}(\mathbf{r}, \mathbf{r}_{\text{in}}, \omega)\mathbf{d}_{\text{in}}\sigma_{\text{in}}. \tag{4.8}$$

For example, plane-wave illumination can be achieved by having the dipole very far away in free-space. Or an incoming guided mode field can be achieved by having the dipole far away and coupled to the guided mode (since the free-space component is shorter range and all we are left with is the guided component). The atomic system of equations in Eq. (4.4) is then (using $g_{k,\text{in}} = \frac{\mu_0\omega^2}{\hbar}\mathbf{d}_k\mathbf{G}(\mathbf{r}_k, \mathbf{r}_{\text{in}})\mathbf{d}_{\text{in}}$)

$$(\Delta_A + \mathrm{i}\Gamma'/2)\,\sigma_k + \sum_{j=1}^{N} g_{kj}\,\sigma_j = -g_{k,\text{in}}\,\sigma_{\text{in}}, \tag{4.9}$$

and the electric field operator in Eq. (4.3) is

$$\hat{\mathbf{E}}^{+}(\mathbf{r}, \omega) = \mu_0\omega^2\left[\mathbf{G}(\mathbf{r}, \mathbf{r}_{\text{in}}, \omega)\mathbf{d}_{\text{in}}\sigma_{\text{in}} - \sum_{j=1}^{N}\mathbf{G}(\mathbf{r}, \mathbf{r}_j, \omega)\mathbf{d}_j\hat{\sigma}_j(\omega)\right]. \tag{4.10}$$

The second change of notation is to express the electric field operator in a scalar form. We can accomplish this by multiplying the both sides of Eq. (4.10) by an arbitrary dipole vector $\mathbf{d}^{*}_{\text{out}}$. We can interpret this as if we are using a negligible dipole $\mathbf{d}_{\text{out}}$ at position $\mathbf{r}_{\text{out}}$ in order to to measure the electric field. The vector can be removed at the end of a calculation, but including it lets the output electric field be conveniently expressed in terms of the complex coupling rates g_{ij} as

$$g_{\text{out,in}}\,\sigma_{\text{in}} + \sum_{j=1}^{N} g_{\text{out},j}\,\sigma_j = \frac{1}{\hbar}\mathbf{d}^{*}_{\text{out}}\cdot\mathbf{E}^{+}(\mathbf{r}_{\text{out}}, \omega). \tag{4.11}$$

Or written in matrix form and defining the vector of atomic operators $\boldsymbol{\sigma} = (\hat{\sigma}_1, \cdots, \hat{\sigma}_N)$, Eq. (4.9) and (4.10) can be expressed as

$$\left[(\Delta_A + \mathrm{i}\Gamma'/2)\mathbf{1} + \mathfrak{g}\right]\cdot\boldsymbol{\sigma} = -\mathbf{g}_{\text{in}}\,\sigma_{\text{in}} \tag{4.12}$$

$$g_{\text{out,in}}\,\sigma_{\text{in}} + \mathbf{g}_{\text{out}}\cdot\boldsymbol{\sigma} = \frac{1}{\hbar}\mathbf{d}^{*}_{\text{out}}\cdot\mathbf{E}^{+}(\mathbf{r}_{\text{out}}, \omega), \tag{4.13}$$

where the matrix $(\mathfrak{g})_{jk} = g_{jk}$ contains the propagators between the atoms, the vector $\mathbf{g}_{\text{in}} = (g_{1,\text{in}}, \cdots, g_{N,\text{in}})$ contains the propagators between the source and the atoms, and the vector $\mathbf{g}_{\text{out}} = (g_{\text{out},1}, \cdots, g_{\text{out},N})$ contains the propagators from the atoms to the output.

The solution for the atomic operator for a given input field is found by inverting Eq. (4.12) ,

$$\boldsymbol{\sigma} = -\left(\frac{1}{(\Delta_A + i\Gamma'/2)\mathbf{1} + \mathfrak{g}}\right) \cdot \mathbf{g}_{\text{in}}\sigma_{\text{in}}. \tag{4.14}$$

For a system with a single atom and a drive with amplitude proportional to $g_{1,\text{in}}$, the atom's dipole operator is

$$\sigma_1 = -\frac{g_{1,\text{in}}}{\Delta_A + J_{11} + \frac{i}{2}(\Gamma' + \Gamma_{11})}. \tag{4.15}$$

The resonance frequency is shifted by J_{11} and the total decay rate is $\Gamma_{\text{tot}} = \Gamma' + \Gamma_{11}$. When multiple atoms interact with each other, $\mathfrak{g}$ is not diagonal, and the atoms instead behave collectively. We can no longer talk about the decay rate or frequency shift of a single atom. However, we will show that we can instead use the frequency shifts and decay rates for the collective atomic modes which are uncoupled from each other. Due to the reciprocity identity from Eq. (2.15) $[\mathbf{G}^T(\mathbf{r}, \mathbf{r}', \omega) = \mathbf{G}(\mathbf{r}', \mathbf{r}, \omega)]$, the the matrix $\mathfrak{g}$ is symmetric ($\mathfrak{g}^T = \mathfrak{g}$) when the dipole matrix elements are real.[1]It is interesting to note that because of the dissipation, the matrix $\mathfrak{g}$ is not Hermitian and the eigenvectors are not orthogonal in the more traditional sense which uses the conjugate transpose. Instead, as shown in Appendix C, complex symmetric matrices have eigenvectors defined by the eigenvalue equation

$$\mathfrak{g}\,\mathbf{v}_\xi = \lambda_\xi \mathbf{v}_\xi \tag{4.17}$$

that satisfy the orthogonality and completeness relation

$$\mathbf{v}_\xi^T \cdot \mathbf{v}_{\xi'} = \delta_{\xi\xi'} \quad \text{and} \quad \sum_{\xi=1}^{N} \mathbf{v}_\xi \otimes \mathbf{v}_\xi^T = \mathbf{1}. \tag{4.18}$$

Here T is the transpose, rather than the more customary conjugate transpose for Hermitian or normal matrices. The matrix in Eq. (4.14) shares the same eigenvectors

---

[1] The orthogonality and completeness relation of the eigenmodes rely on $(\mathfrak{g})_{ij} = \frac{\mu_0\omega^2}{\hbar}\mathbf{d}_i^*\mathbf{G}(\mathbf{r}_i, \mathbf{r}_j, \omega)\mathbf{d}_j$ being a complex symmetric matrix, $\mathfrak{g}^T = \mathfrak{g}$. Taking the transpose of $\mathfrak{g}$ and using the reciprocity identity for the Green's function, $\mathbf{G}^T(\mathbf{r}_i, \mathbf{r}_j, \omega) = \mathbf{G}(\mathbf{r}_j, \mathbf{r}_i, \omega)$, gives

$$(\mathfrak{g}^{\mathrm{T}})_{ij} = \frac{\mu_0\omega^2}{\hbar}\mathbf{d}_i\mathbf{G}(\mathbf{r}_i, \mathbf{r}_j, \omega)\mathbf{d}_j^*. \tag{4.16}$$

Comparing this to $(\mathfrak{g})_{ij}$, we see that the only difference is that the complex conjugate is on the second dipole moment. The matrix is symmetric ($\mathfrak{g} = \mathfrak{g}^T$) when 1) all the dipole moments are real 2) the Green's function is linearly polarized.

as $\mathfrak{g}$, since the other term in the denominator is diagonal. Inserting the completeness relation into the right side of Eq. (4.14), using the eigenvalue equation gives an expansion of the dipole operator in terms of the N collective modes,

$$\boldsymbol{\sigma} = -\left(\frac{1}{\Delta_A + \mathrm{i}\Gamma'/2 + \mathfrak{g}}\right) \cdot \left(\sum_{\xi=1}^{N} \mathbf{v}_\xi \otimes \mathbf{v}_\xi^T\right) \mathbf{g}_{\mathrm{in}} \sigma_{\mathrm{in}} \tag{4.19}$$

$$= -\sum_{\xi=1}^{N} \frac{\mathbf{v}_\xi \cdot \mathbf{g}_{\mathrm{in}} \sigma_{\mathrm{in}}}{\Delta_A + \mathrm{i}\Gamma'/2 + \lambda_\xi} \mathbf{v}_\xi . \tag{4.20}$$

Defining the real and imaginary parts of the eigenvalue as $\lambda_\xi = J_\xi + \mathrm{i}\Gamma_\xi/2$ as the frequency shift and decay rate for the collective mode ξ, where the Greek letter signifies a collective mode rather than a single atom, the final expression for expansion is

$$\boldsymbol{\sigma} = -\sum_{\xi=1}^{N} \frac{\mathbf{v}_\xi \cdot \mathbf{g}_{\mathrm{in}} \sigma_{\mathrm{in}}}{\Delta_A + J_\xi + \mathrm{i}(\Gamma' + \Gamma_\xi)/2} \mathbf{v}_\xi . \tag{4.21}$$

The elements of eigenvector $\mathbf{v}_\xi$ give the relative amplitude and phase for the atoms in the collective mode. As a result of the interactions, the collective mode is shifted by J_ξ, and the total decay rate is either inhibited or enhanced to $\Gamma_{\mathrm{tot}} = \Gamma' + \Gamma_\xi$. Finally, the coupling between the input field and a particular collective mode is given by the scalar product $\mathbf{v}_\xi \cdot \mathbf{g}_{\mathrm{in}} \sigma_{\mathrm{in}}$.

4.2 Output field

In the previous section, we derived the solution for the atomic dipole operators in the low saturation limit. Substituting this solution from Eq. (4.14) into the expression for the output electric field operator in Eq. (4.13) results in

$$\sigma_{\mathrm{in}} \left[g_{\mathrm{out,in}} - \mathbf{g}_{\mathrm{out}} \cdot \left(\frac{1}{(\Delta_A + \mathrm{i}\Gamma'/2)\mathbf{1} + \mathfrak{g}} \right) \cdot \mathbf{g}_{\mathrm{in}} \right] = \frac{1}{\hbar} \mathbf{d}_{\mathrm{out}} \cdot \mathbf{E}^{+}(\mathbf{r}_{\mathrm{out}}, \omega). \tag{4.22}$$

Notice that in the limit of no atoms ($\mathbf{d}_k \to 0$), the second terms in the brackets vanishes, which leaves $\sigma_{\mathrm{in}}\, g_{\mathrm{out,in}} = \sigma_{\mathrm{in}} \frac{\mu_0 \omega^2}{\hbar} \mathbf{d}^*_{\mathrm{out}} \mathbf{G}(\mathbf{r}_{\mathrm{out}}, \mathbf{r}_{\mathrm{in}}, \omega) \mathbf{d}_{\mathrm{in}} = \frac{1}{\hbar} \mathbf{d}^*_{\mathrm{out}} \cdot \mathbf{E}^{+}_{N=0}(\mathbf{r}_{\mathrm{out}}, \omega)$. Removing $\hbar$ and the arbitrary vector $\mathbf{d}_{\mathrm{out}}$ from both sides gives $\mu_0 \omega^2\, \mathbf{G}(\mathbf{r}_{\mathrm{out}}, \mathbf{r}_{\mathrm{in}}, \omega) \mathbf{d}_{\mathrm{in}} \sigma_{\mathrm{in}} = \mathbf{E}^{+}_{N=0}(\mathbf{r}_{\mathrm{out}}, \omega)$, which is the expected result for the transmitted field through the system with no atoms ($N = 0$). The scattering from the atoms is captured in the second term in the brackets.

The ratio of the transmitted field with atoms to the transmitted field without atoms is given by

$$\frac{t_N(\Delta_A)}{t_0(\Delta_A)} = \frac{\mathbf{d}^*_{\mathrm{out}} \cdot \mathbf{E}^{+}(\mathbf{r}_{\mathrm{out}}, \omega)}{\mathbf{d}^*_{\mathrm{out}} \cdot \mathbf{E}^{+}_{N=0}(\mathbf{r}_{\mathrm{out}}, \omega)}, \tag{4.23}$$

which upon substitution of Eq. (4.22) gives

$$\frac{t_N(\Delta_A)}{t_0(\Delta_A)} = 1 - \frac{1}{g_{\text{out,in}}}\mathbf{g}_{\text{out}} \cdot \left(\frac{1}{(\Delta_A + \text{i}\Gamma'/2)\mathbf{1} + \mathfrak{g}}\right) \cdot \mathbf{g}_{\text{in}}. \tag{4.24}$$

The vector $\mathbf{g}_{\text{in}}$ propagates the input field to the atoms, while the vector $\mathbf{g}_{\text{out}}$ propagates the field to the output. The matrix sandwiched between the vectors is the response of the atoms and the propagation of the field between the atoms. The normalized transmission for a single atom $N = 1$ simplifies to

$$\frac{t_{N=1}(\Delta_A)}{t_0(\Delta_A)} = 1 - \frac{1}{g_{\text{out,in}}}\left(\frac{g_{\text{out},1}\; g_{1,\text{in}}}{\Delta_A + \text{i}\Gamma'/2 + g_{11}}\right). \tag{4.25}$$

The normalized transmission can also be expressed in terms of the collective modes of the atoms. Inserting the completeness relation into both sides of the matrix in Eq. (4.24) gives

$$\begin{aligned}\frac{t(\Delta_A)}{t_0(\Delta_A)} &= 1 - \frac{1}{g_{\text{out,in}}}\sum_{\xi,\xi'=1}^{N} \mathbf{g}_{\text{out}} \cdot (\mathbf{v}_\xi \otimes \mathbf{v}_\xi^T) \cdot \left(\frac{1}{(\Delta_A + \text{i}\Gamma'/2)\mathbf{1} + \mathfrak{g}}\right) \cdot (\mathbf{v}_{\xi'} \otimes \mathbf{v}_{\xi'}^T) \cdot \mathbf{g}_{\text{in}} \\ &= 1 - \frac{1}{g_{\text{out,in}}}\sum_{\xi=1}^{N} \frac{(\mathbf{v}_\xi \cdot \mathbf{g}_{\text{out}})(\mathbf{v}_\xi \cdot \mathbf{g}_{\text{in}})}{\Delta_A + J_\xi + \text{i}(\Gamma' + \Gamma_\xi)/2},\end{aligned} \tag{4.26}$$

where in the last line we used the eigenvalue equation with $\lambda_\xi = J_\xi + \text{i}\Gamma_\xi/2$, and the orthogonality of the eigenvectors. Since the collective modes are uncoupled from each other, the transmission spectrum can be written as a sum of N independent parts, each one similar to the single atom spectra.

We can also derive a similar expression for the reflected field. In contrast to a transmitted signal, the total electric field for a reflected signal has both the incoming wave as well as the reflected field. We define the reflected signal as

$$\mathbf{d}^* \cdot \mathbf{E}(x_{\text{in}}, \omega) = [1 + r_N(\Delta_A)]\, \mathbf{d}^* \cdot \mathbf{E}_{\text{free}}(\mathbf{r}_{\text{in}}, \omega). \tag{4.27}$$

Following a similar procedure as for the transmitted case, we derive

$$r_N(\Delta_A) = r_0(\Delta_A) - \frac{1}{g_{\text{out,in}}}\mathbf{g}_{\text{in}} \cdot \left(\frac{1}{(\Delta_A + \Gamma'/2)\mathbf{1} + \mathfrak{g}}\right) \cdot \mathbf{g}_{\text{in}}. \tag{4.28}$$

4.3 Transmission through a quasi-1D waveguide

For many applications in atomic physics, atoms are coupled to quasi-1D systems, where the light is confined to propagate in a single axis. Often, quasi-1D modes can be well approximated by a 1D wave equation with an effective dielectric constant $\left[\frac{\mathrm{d}^2}{\mathrm{d}x^2} + \epsilon_{\text{eff}}(x)\frac{\omega^2}{c^2}\right] E(x,\omega) = 0$, for which the Green's function is also well approximated by a 1D Green's function $G^{1\text{D}}(x, x', \omega)$ defined by the wave equation (see Appendix D for details)

$$\left[\frac{\mathrm{d}^2}{\mathrm{d}x^2} + \epsilon_{\text{eff}}(x)\frac{\omega^2}{c^2}\right] G^{1\text{D}}(x, x', \omega) = -\delta(x - x'). \tag{4.29}$$

In this section, we show that the transmission spectrum for atoms coupled to a system whose Green's function is well approximated by a 1D Green's function only depends on the eigenvalues of the Green's function matrix $\mathfrak{g}$ and the decay rate Γ'. Amazingly, the transmission spectrum is independent of the input and output vectors $\mathbf{g}_{\text{in}}$ and $\mathbf{g}_{\text{out}}$ seen in Eq. (4.24). This equation is a generalization of the optical bistability equation for cavities and the optical depth model for waveguides to arbitrary quasi-1D systems.

The derivation for multiple atoms is quite technical, so first we look at the derivation for the single atom case. From Eq. (4.25), the normalized transmission for a single atom is

$$\frac{t_{N=1}(\omega)}{t_0(\omega)} = 1 - \frac{g_{\text{out},1}\ g_{1,\text{in}}}{g_{\text{out,in}}}\left(\frac{1}{\Delta_A + \mathrm{i}\Gamma'/2 + g_{11}}\right). \tag{4.30}$$

We assume that the Green's function is well approximated by an effective 1D Green's function, and assume that the polarization of the field is the same as the dipoles. We can then write the complex coupling rate as

$$g_{ij} = \frac{\mu_0\omega^2}{\hbar}\mathbf{d}^*\mathbf{G}(\mathbf{r}_i, \mathbf{r}_j, \omega)\mathbf{d} \approx \frac{\mu_0\omega^2}{\hbar}|\mathbf{d}|^2\frac{G^{1\text{D}}(x_i, x_j, \omega)}{A_{\text{eff}}}, \tag{4.31}$$

where the effective mode area $1/A_{\text{eff}}$ includes both the mode area and group velocity, as discussed in Sec. 2.5. The front coefficient in Eq. (4.30) is then given by

$$\frac{g_{\text{out},1}\ g_{1,\text{in}}}{g_{\text{out,in}}} = \frac{\mu_0\omega^2|\mathbf{d}|^2}{\hbar A_{\text{eff}}}\left(\frac{G^{1\text{D}}(x_{\text{out}}, x_j)G^{1\text{D}}(x_k, x_{\text{in}})}{G^{1\text{D}}(x_{\text{out}}, x_{\text{in}})}\right). \tag{4.32}$$

An identity for 1D Green's function, which will be proven in the multiple atom derivation, is $G^{1\text{D}}(x_{\text{out}}, x_1)G^{1\text{D}}(x_1, x_{\text{in}}) = G^{1\text{D}}(x_{\text{out}}, x_{\text{in}})G^{1\text{D}}(x_1, x_1)$ for $x_{\text{out}} > x_1 > x_{\text{in}}$. Using this identity, the coefficient simplifies to

$$\frac{g_{\text{out},1}\ g_{1,\text{in}}}{g_{\text{out,in}}} = g_{11} \tag{4.33}$$

and the transmission spectrum is

$$\frac{t_{N=1}(\omega)}{t_0(\omega)} = 1 - \left(\frac{g_{11}}{\Delta_A + \mathrm{i}\Gamma'/2 + g_{11}}\right) = \frac{\Delta_A + \mathrm{i}\Gamma'/2}{\Delta_A + \mathrm{i}\Gamma'/2 + g_{11}}. \tag{4.34}$$

Remarkably, the normalized low saturation transmission spectrum for a quasi-1D system with one atom only depends on the self-Green's function at the position of the atom. Two completely different systems will have the same normalized transmission as long as g_{11} and Γ' are the same. For a single atom, there is a clear mapping between the spectrum lineshape and the local 1D Green's function. Examples of the single atom spectra are shown in Fig. 4.1. Figure 4.1(a) shows spectra for a dissipative interaction ($J = 0$) and increasing ratios of Γ/Γ'. For a nanostructure with a purely imaginary self-Green's function (such as a waveguide or a cavity on resonance), the spectrum is Lorentzian, and centered around the atomic frequency. Defining the total decay rate $\Gamma_{\text{tot}} = \Gamma' + \Gamma$, the transmission can be written in a form that shows the linewidth and depth of the symmetric resonance,

$$\left.\frac{T_{N=1}(\Delta_A)}{T_0(\Delta_A)}\right|_{J=0} = 1 - \overbrace{\left(1 - \frac{\Gamma'^2}{\Gamma_{\text{tot}}^2}\right)}^{\text{peak depth}} \overbrace{\left(\frac{1}{1 + \Delta_A^2/\Gamma_{\text{tot}}^2}\right)}^{\text{peak width}}. \tag{4.35}$$

As shown in the Fig. 4.1(c), the linewidth is given by the total decay rate $\Gamma_{\text{tot}} = \Gamma + \Gamma'$, and the on-resonant transmission is $T(0)/T_0(0) = \left(\frac{\Gamma'}{\Gamma_{\text{tot}}}\right)^2$.

Figure 4.1(b) shows single atom spectra for the purely dispersive self-interaction ($\Gamma = 0$) for increasing ratios of J/Γ'. If the real part of the Green's function is finite, for example in an off-resonant cavity or the bandgap of a PCW, the spectrum is shifted and asymmetric. For $J/\Gamma' \ll 1$, the lineshape is an asymmetric Gaussian. But for larger ratios, a resonance appears at frequency J from the center, as shown in Fig. 4.1(d). The height of the peak increases rapidly with $\left(\frac{J}{\Gamma'/2}\right)^2$.

The multiple atom result, which is derived in the Sec. 4.9 , is

$$\frac{t(\omega)}{t_0(\omega)} = \prod_{\xi=1}^{N} \left(\frac{\Delta_A + \mathrm{i}\Gamma'/2}{\Delta_A + \mathrm{i}\Gamma'/2 + \lambda_\xi}\right), \tag{4.36}$$

where the λ_ξ's are the eigenvalues of the matrix $\mathfrak{g}$. For the multiple atom case, the transmission spectra is a direct probe of the frequency shifts and decay rates of the collective modes. This expression extends the models for cavities and waveguides to arbitrary 1D systems. To get to this result, we have only assumed the low saturation limit and that Green's function is well approximated by a 1D Green's function. We did not use the Markov approximation, and so this result is valid in the non-Markovian limit, where the linewidth of the Green's function is narrower than the atomic linewidth. This result is also valid for systems with loss, since the 1D Green's function is well-defined for lossy systems, in contrast to the eigenmode formalism.

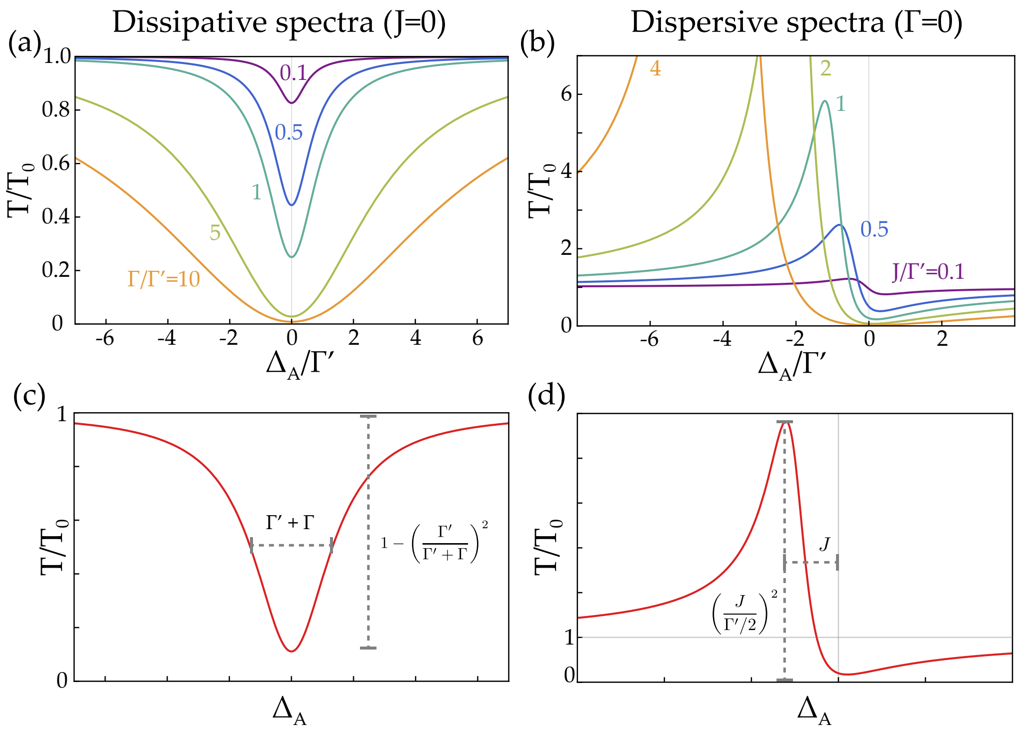

Figure 4.1: (a) Single atom transmission spectra for $J = 0$ and $\Gamma/\Gamma' = (0.1, 0.5, 1, 5, 10)$. (b) Single atom transmission spectra for $\Gamma = 0$ and $J/\Gamma' = (0.1, 0.5, 1, 2, 4)$. (c) Generic curve with the approximations for the height and width for a $J = 0$ lineshape. (d) Generic curve with the frequency shift and peak height for a $\Gamma = 0$ lineshape.

4.4 Atoms in a cavity

As a first example of atoms coupled to a quasi-1D system, we look at a cavity. For a good cavity, the interactions can be approximated as coming from a single optical mode with linewidth κ_c which is resonant with the cavity. This approximation is used in the Jaynes-Cumming (JC) formalism, which is obtained from the Green's function formalism by substituting the approximation cavity Green's function (see

---

[1] The transmittance $T = |t|^2$ can be recast into a Fano-like lineshape [106] as

$$T/T_0 = \frac{(q+\chi)^2}{1+\chi^2} + \left(\frac{\Gamma'}{\Gamma' + \Gamma_{1D}}\right)^2 \frac{1}{1+\chi^2},$$

where $\chi = 2(\Delta_A + J_{1D})/(\Gamma_{1D} + \Gamma')$ and $q = -2J_{1D}/(\Gamma_{1D} + \Gamma')$ is the so-called asymmetry parameter. For $\Gamma' \ll \Gamma_{1D}$, the second term is negligible and T/T_0 is a pure Fano resonance, with $q = -\mathrm{Re}[G_{1D}(\mathbf{r}_j, \mathbf{r}_j, \omega)]/\mathrm{Im}[G_{1D}(\mathbf{r}_j, \mathbf{r}_j, \omega)]$. Fano resonances arise whenever there is interference between two different transport channels. For instance, in a cavity far from resonance, there is interference arising from all the possible optical paths that contribute to the transmission signal due to reflections at the mirrors, whereas in an unstructured waveguide there is no such interference and thus the lineshape is Lorentzian.

Eq. (2.5)),

$$\mathbf{G}(\mathbf{r},\mathbf{r}',\omega) = \frac{c^2}{2\omega_0 V}\frac{1}{\Delta - \mathrm{i}\kappa_c/2}\mathbf{f}(\mathbf{r})\otimes\mathbf{f}^*(\mathbf{r}'), \tag{4.37}$$

where V is the mode volume and $\mathbf{f}(\mathbf{r})$ the unitless mode function which is often well approximated by $|\mathbf{f}(\mathbf{r})| \approx \cos(kx)$.

In 1D, we can obtain the exact Green's function for a cavity consisting of two mirrors with reflection R separated by a distance L. In Appendix D, we derive a simple procedure, which we call the "Wronkian method", for deriving the 1D Green's function for arbitrary systems. The full solution is given in Appendix D, but a good approximation is

$$\operatorname{Im} G^{1\mathrm{D}}(x,x',\omega) = \frac{1}{2k_c}\left(\frac{1+\sqrt{R}}{1-\sqrt{R}}\right)\left[\frac{1}{1+\mathcal{F}\sin^2(k_cL)}\right]\cos(k_cx)\cos(k_cx') \tag{4.38}$$

$$\operatorname{Re} G^{1\mathrm{D}}(x,x',\omega) = \frac{1}{k_c}\frac{\sqrt{R}}{\left(1-\sqrt{R}\right)^2}\left[\frac{\sin(k_cL)}{1+\mathcal{F}\sin^2(k_cL)}\right]\cos(k_cx)\cos(k_cx'), \tag{4.39}$$

where R is the reflection coefficient for each mirror, $k_c = n_c\omega/c$ is the intra-cavity wave-vector, L is the cavity length, and the "coefficient of Finesse" $\mathcal{F}$ — which is closely related to the Finesse [107] — is given by

$$\mathcal{F} = \frac{4R}{(1-R)^2}. \tag{4.40}$$

To derive these expressions, we have assumed $\cos(k_cL) \approx 1$ and $R \gtrsim 0.5$, but we note that they are exact for the self-Green's function $G(x,x,\omega)$ at the cavity anti-node, which is the maximum value in the cavity and will be an important quantity later. While the single-mode approximation Green's function breaks down in the very bad cavity limit, these expressions recover the uniform waveguide Green's function for $R \longrightarrow 0$, i.e. $\mathrm{Im}G = \frac{\mathrm{i}}{2kA}$ and $\mathrm{Re}G = 0$.

In the good cavity limit ($1 - R \ll 1$), we recover the approximate Green's function expression from Eq. (4.37) by replacing the reflection coefficient with the cavity linewidth. The full-width half-maximum ($T = 1/2$) linewidth in angular frequency units is

$$\kappa_c = \frac{2c}{Ln_g}\arcsin\left(\frac{1-R}{2\sqrt{R}}\right) \approx \frac{c}{Ln_g}(1-R). \tag{4.41}$$

where $n_g = c/v_g$, and $v_g = \frac{\mathrm{d}\omega}{\mathrm{d}k}$. Assuming close to resonance, we take $k_cL = m\pi + n\Delta_cL/c$ and asuume that $n\Delta_cL/c \ll 1$. Here $\Delta_c = \omega - \omega_c$ is the cavity

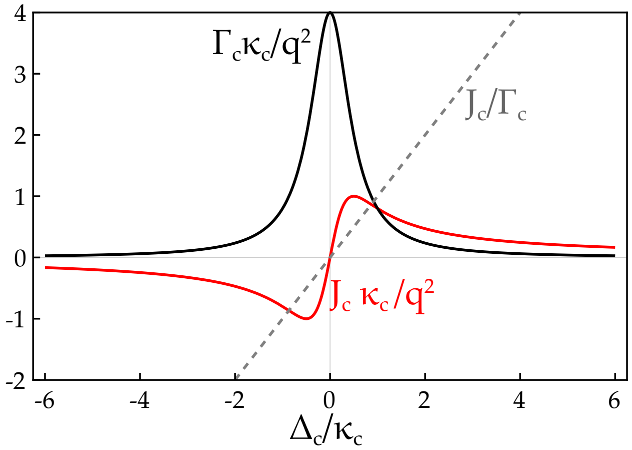

Figure 4.2: The coherent J_c and dissipative Γ_c coupling rates for a cavity. They have been normalized by κ_c/q^2 to make them unitless.

detuning. The Green's function is then

$$G^{1\mathrm{D}}(x_i, x_j, \omega) \simeq -\left(\frac{c^2}{\omega L}\right)\frac{1}{\Delta_c + \mathrm{i}\kappa_c/2}\cos(k_c x_i)\cos(k_c x_j). \tag{4.42}$$

The complex coupling rates are then given by $g_{ij} = \frac{\mu_0\omega^2}{\hbar}|\mathbf{d}|^2\frac{1}{A}G^{1\mathrm{D}}(x_i, x_j, \omega)$, where A is the effective mode area. This simplifies to

$$g_{ij} = \frac{q_i q_j}{\Delta_c + \mathrm{i}\kappa_c/2}, \quad \text{where} \quad q_i = \sqrt{\frac{|\mathbf{d}|^2\omega}{\epsilon_0\hbar L A}}\cos(k_c x) \tag{4.43}$$

is the vacuum Rabi frequency from the JC model. The atoms' spin-exchange and decay rates are plotted in Fig. 4.2 versus cavity detuning, and are given by

$$J_{\mathrm{c}}^{ij} = -q_i q_j\frac{\Delta_{\mathrm{c}}}{(\Delta_{\mathrm{c}}^2 + \kappa_{\mathrm{c}}^2/4)} \equiv J_{\mathrm{c}}\cos(k_{\mathrm{c}}x_i)\cos(k_{\mathrm{c}}x_j), \tag{4.44a}$$

$$\Gamma_{\mathrm{c}}^{ij} = q_i q_j\frac{\kappa_c}{(\Delta_{\mathrm{c}}^2 + \kappa_{\mathrm{c}}^2/4)} \equiv \Gamma_{\mathrm{c}}\cos(k_{\mathrm{c}}x_i)\cos(k_{\mathrm{c}}x_j). \tag{4.44b}$$

The ratio of the coherent to dissipative rates is $J_c^{ii}/\Gamma_c^{ii} = \Delta_c/\kappa_c$, and is the dashed line in Fig. 4.2.[2]A general feature of the coherent rate is its maximum is approximately 25% of the dissipative rate maximum, and it is shifted by one linewidth κ_c.

Since the atoms are approximately only interacting with a single optical mode, there is a decreased dimensionality in the problem as compared for example to the continuum of modes in a uniform waveguide. In fact, we will now show that only a single "bright" collective mode of the atoms is coupled to the cavity. In the low

---

[2] Using the more accurate 1D expression from Eq. (4.38), $J_c^{ii}/\Gamma_c^{ii} = \sqrt{\mathcal{F}}\sin(k_c L)$

saturation regime, the spectral features behave the same as a single "super atom" with an enhanced coupling.

We use the mathematical property that for any vector $\mathbf{a}$, the rank 1 matrix $\mathbf{a} \otimes \mathbf{a}^T$ has only nonzero eigenvalue $\lambda_B = \mathbf{a} \cdot \mathbf{a}$ with a corresponding eigenvector $\mathbf{a}$. The remainder of the $N-1$ eigenvalues are zero. The matrix $(\mathfrak{g})_{ij} \propto q_i q_j$ from Eq. (4.43) can be written as the product of two vectors. Therefore, the matrix $\mathfrak{g}$ has one eigenstate describing a superposition of atomic coherences that couples to the cavity (a "bright mode"), with eigenvalue $\lambda_{\text{B}} = \sum_{i=1}^{N} g^{ii} = (J_{\text{1D}} + \text{i}\Gamma_{\text{1D}}/2) \sum_{i=1}^{N} \cos^2(k_{\text{c}} x_i)$. The amplitude and phase of the atoms in the collective excitation are given by the eigenvector $\hat{\sigma}_i \propto \cos(k_{\text{c}} x_i)$. The matrix $\mathfrak{g}$ has also $N-1$ decoupled ("dark") modes of eigenvalue 0. Because these dark modes have a zero decay rate into the cavity mode, it is also impossible to excite them employing the cavity field. The optical response is thus entirely controlled by the bright mode, and the transmission is simply

$$t(\Delta_{\text{A}})/t_0(\Delta_{\text{A}}) = \frac{\Delta_{\text{A}} + \text{i}\Gamma'/2}{(\Delta_{\text{A}} + \sum_{i=1}^{N} J_{\text{1D}}^{ii}) + \text{i}(\Gamma' + \sum_{i=1}^{N} \Gamma_{\text{1D}}^{ii})/2}. \tag{4.45}$$

Remarkably, this expression is valid no matter the separation between the atoms or whether they form an ordered or disordered chain. The transmission spectrum corresponds to that of a ‘super-atom’, where the decay rates and the frequency shifts are enhanced (N-fold if all the diagonal components of $\mathfrak{g}$ are equal) compared to those of a single atom.

This result replicates the well-known expressions for conventional cavity QED. Substituting $\lambda_B = -\frac{\sum_{i=1}^{N} q_i^2}{\Delta_c + \text{i}\kappa_c/2}$ into Eq. (4.45), the transmission for a cavity is

$$\frac{t_N(\omega)}{t_0(\omega)} = \frac{\Delta_A + \text{i}\Gamma'/2}{\Delta_A + \text{i}\Gamma'/2 + \lambda_B} = \frac{(\Delta_c + \text{i}\kappa_c/2)(\Delta_A + \text{i}\Gamma'/2)}{(\Delta_c + \text{i}\kappa_c/2)(\Delta_A + \text{i}\Gamma'/2) - \sum_{i=1}^{N} q_i^2}. \tag{4.46}$$

The transmission of a cavity with no loss is given by (see appendix D)

$$t_0(\omega) = \frac{1-R}{1 - e^{2\text{i}kL} R} \approx \frac{\text{i}\kappa_c/2}{\Delta_c + \text{i}\kappa_c/2}, \tag{4.47}$$

where for the second expression we have made the approximation $R \approx 1$ and $\delta k L \ll 1$. The un-normalized transmission is then

$$t_N(\omega) = \frac{(\text{i}\kappa_c/2)(\Delta_A + \text{i}\Gamma'/2)}{(\Delta_c + \text{i}\kappa_c/2)(\Delta_A + \text{i}\Gamma'/2) - \sum_{i=1}^{N} q_i^2}. \tag{4.48}$$

When all the atoms are positioned at the anti-nodes of the standing wave so that they all have identical vacuum Rabi frequency q, then we can take $\sum_{i=1}^{N} q_i^2 = N^2 q^2$.

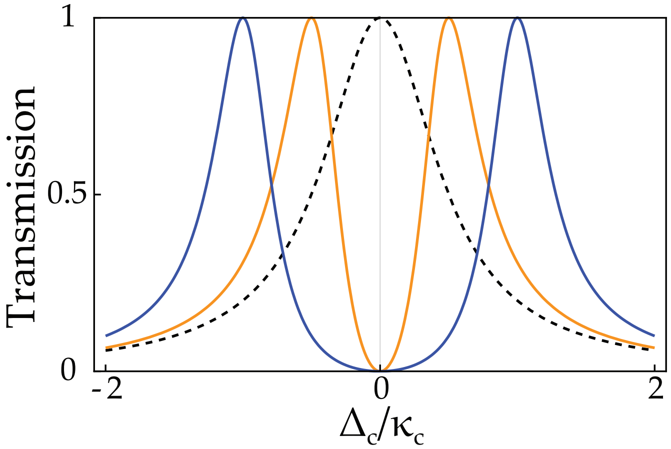

Figure 4.3: Cavity Rabi splitting. For these plots, we have taken $\Gamma' = 0$ and $Nq/\kappa = (0, 0.5, 1)$. The dashed line is the raw cavity transmission.

Figure 4.3 shows the cavity spectra for various values of qN. The dashed line is the cavity transmission with no atoms, and the orange and blue show the Rabi splitting.

4.5 Waveguides

Another paradigm that has been investigated frequently is that of "waveguide QED" [102]. The simple model of such a system consists of a single guided mode with translational invariance, and where the dispersion relation is well-approximated as linear around the atomic resonance frequency. In a 1D translationally invariant system, a source simply emits a plane wave whose phase at the detection point is proportional to the distance of separation. Therefore, the elements of the Green's function matrix $\mathfrak{g}$ depend on the distance between the atoms, and read

$$g_{ij} = \mathrm{i}\frac{\Gamma_{\mathrm{1D}}}{2} e^{\mathrm{i}k_p|x_i - x_j|}. \tag{4.49}$$

Remarkably, the self Green's function in a waveguide is purely imaginary. The coherent interactions between atom i and atom j are dictated by the Hamiltonian, and are proportional to $\mathrm{Re}\{g_{ij}\} = -(\Gamma_{\mathrm{1D}}/2)\sin k_{\mathrm{p}}|x_i - x_j|$, whereas the dissipation is given by the Lindblad operator, which is proportional to $\mathrm{Im}\{g_{ij}\} = (\Gamma_{\mathrm{1D}}/2)\cos k_{\mathrm{p}}(x_i - x_j)$ [19, 108]. It is thus clear that by carefully tuning the distance between the emitters,

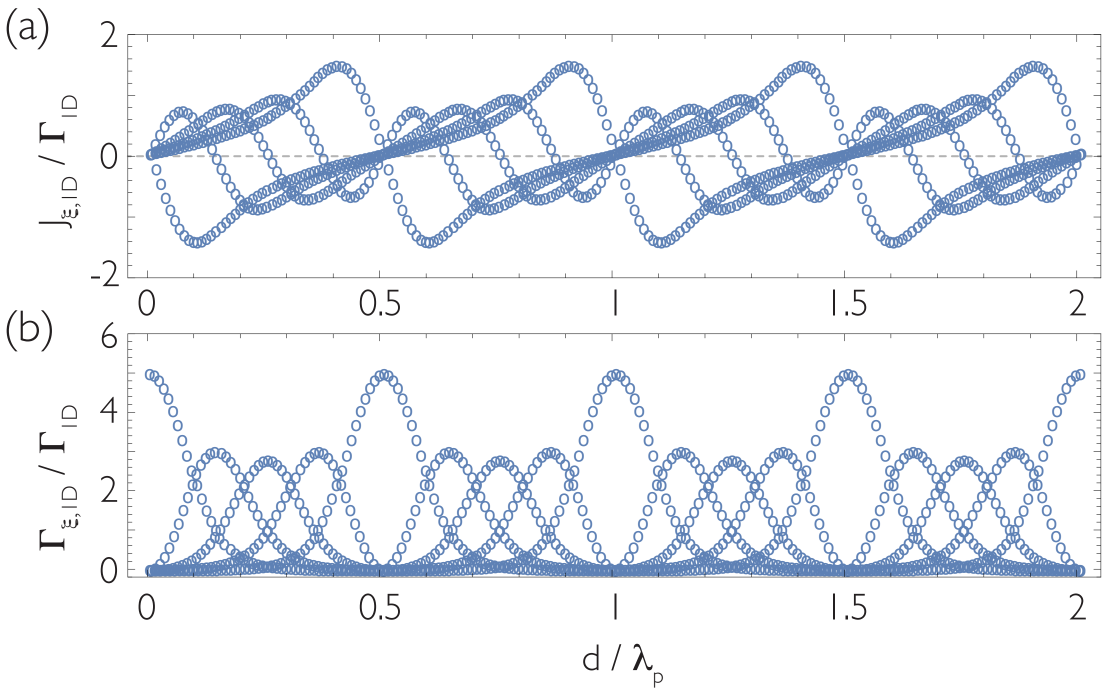

Figure 4.4: (a) Frequency shifts and (b) decay rates of the collective modes of a regular chain of 5 atoms with uniform spacing placed along a waveguide normalized to the single-atom decay rate into the guided mode Γ_{1D}, as a function of the distance d between the atoms in units of the probe wavelength. Figure adapted from [44].

one can engineer fully dissipative interactions. If the atoms form a regular chain and are spaced by a distance d such that $k_p d = n\pi$, where n is an integer number, the matrix $\mathfrak{g}$ has only one non-zero eigenvalue $\lambda_{\mathrm{B}} = \mathrm{i}N\Gamma_{1\mathrm{D}}/2$ associated with the bright atomic mode. This situation is analogous to the case of atoms interacting in an on-resonance cavity. Therefore, there will not be any collective frequency shift, and the lineshape will be a Lorentzian of width $\Gamma_{\mathrm{B}} + \Gamma'$. For n even, the phases of the dipole moments of the atoms are all identical, whereas for odd n the dipole moments of adjacent atoms are π out of phase.

For a regular chain with lattice constant different from $k_{\mathrm{p}}d = n\pi$, or for atoms placed randomly along the waveguide, the coefficients of matrix $\mathfrak{g}$ have both a real and imaginary part, and, to the best of our knowledge, there is no analytic expression for the eigenvalues of $\mathfrak{g}$. Figure 4.4 shows the frequency shifts and decay rates of the collective modes of a $N = 5$ atom chain as a function of the separation between the atoms. For separations where $k_{\mathrm{p}}d = n\pi$, the real part of the Green's function is zero and the imaginary part of all modes but one goes to zero, whereas for other spacings one generically gets a zoo of coherent and dissipative

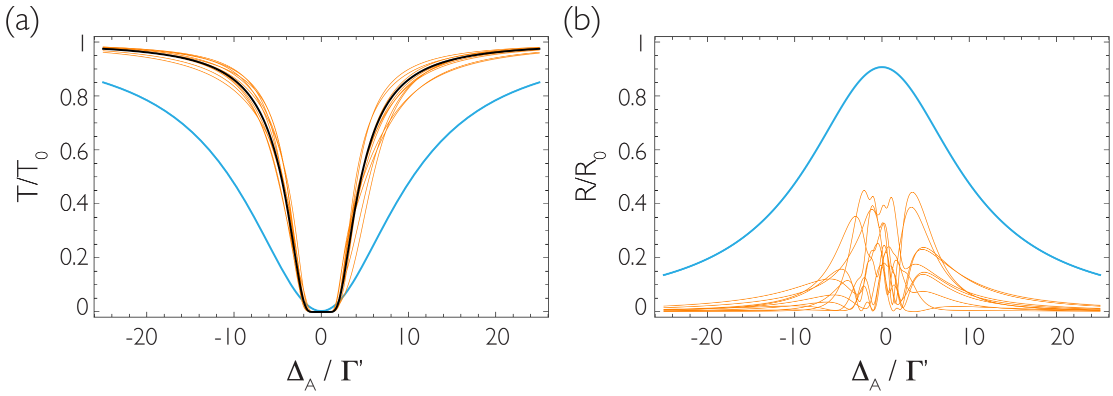

Figure 4.5: (a) Normalized transmission spectra for 20 atoms interacting through the guided modes of an unstructured waveguide. The blue line represents a regular separation between the atoms of $d = \lambda_{\rm p}/2$. The orange curves show 10 different spectra obtained by randomly placing the atoms along the nanostructure. The black curve represents the "non-interacting" case of Eq. (4.50). (b) Normalized reflection spectra for the same situations as in (a). We have chosen $\Gamma_{\rm 1D} = \Gamma'$. Figure adapted from [44].

couplings of comparable strength. This occurs because the real and imaginary parts of g_{ij} are generically of similar magnitude. Figure 4.5 shows the transmission and reflection spectra for $N = 20$ atoms separated by $k_{\rm p}d = \pi$ (blue curve), and for several random realizations where each atomic position is chosen randomly from a distribution $k_{\rm p}x_i \in [0, 2\pi]$ (orange curves). The black line represents the non-interacting case, which is obtained by setting the non-diagonal terms of $\mathfrak{g}$ to zero, yielding a transmission spectrum

$$t(\Delta_{\rm A})/t_0(\Delta_{\rm A}) = \left(\frac{\Delta_{\rm A} + {\rm i}\Gamma'/2}{\Delta_{\rm A} + {\rm i}(\Gamma' + \Gamma_{\rm 1D})/2}\right)^N, \tag{4.50}$$

where the transmission coefficient is a product of the transmission coefficient of each single atom, and the frequency shifts and decay rates are not collective quantities but, instead, single-atom parameters.

Figure **??**(a) also shows that, for random filling, although the atoms interact with each other ($\mathfrak{g}_{ij\neq i} \neq 0$), the transmission spectra follow closely that of a non-interacting system, for which all the off-diagonal elements are zero ($\mathfrak{g}_{ij\neq i} = 0$), and the eigenvalues of matrix $\mathfrak{g}$ are proportional to the self Green's functions $[\mathbf{G}(x_i, x_i)]$ at the atoms' positions. In this case, the behavior of the emitters cannot be understood in terms of the 'super-atom' picture, as the transmission spectrum of the system is significantly different from a Lorentzian. In particular, for the non-interacting scenario, one can recast Eq. (4.50) into an exponential, and the transmittance recovers the well-known form of a Beer-Lambert law, reading

$$T(\Delta_{\rm A})/T_0(\Delta_{\rm A}) = \exp\left[-N \ln \frac{\Delta_{\rm A}^2 + (\Gamma' + \Gamma_{\rm 1D})^2/4}{\Delta_{\rm A}^2 + \Gamma'^2/4}\right] \simeq \exp\left[-\frac{\rm OD}{1 + (2\Delta_{\rm A}/\Gamma')^2}\right], \tag{4.51}$$

where $\mathrm{OD} \equiv 2N\Gamma_{\rm 1D}/\Gamma'$ is the optical depth and the last equality holds for $\Gamma_{\rm 1D} \ll \Gamma'$. This is exactly the same behavior that an atomic ensemble in free space would exhibit. This occurs only for non-negligible Γ', which suppresses multiple reflections. Otherwise one would see huge fluctuations associated with Anderson localization in the spectra.

The reflectance spectrum, on the other hand, is more complex and carries more information than the transmittance, as shown in Fig. 4.5(b). In contrast to the case of the transmission coefficient, the reflection does not admit a simple formula in terms of the eigenvalues of the system. This is only possible when the Green's function is separable, namely, when the distance between the atoms is $d = n\lambda_p/2$.

4.6 Photonic crystal bandgaps

The band-gap region of a photonic crystal waveguide (PCW) is a very appealing scenario to explore coherent atom-atom interactions, as light cannot propagate, and atoms interact with each other through finite-range evanescent fields [41]. For a photonic crystal waveguide of lattice constant a the elements of matrix $\mathfrak{g}$ are well approximated by

$$g_{ij} = J_{\rm 1D} \cos(\pi x_i/a) \cos(\pi x_j/a) e^{-\kappa_x |x_i - x_j|}, \tag{4.52}$$

where the cosine terms account for the spatial profile of the Bloch modes, and κ_x^{-1} is the finite range of interaction due to the evanescent decay of the guided mode field in the bandgap, which is controlled by detuning the band-edge frequency from the atomic resonance. It should be noted that in this idealized picture, g_{ij} is purely real, indicating the absence of collective emission into the PCW. This is naturally expected, due to the absence of guided modes at the atomic frequency. In practice, residual decay might still exist to the extent that the mediating photon has a decay channel. This could be either due to the finite length of the PCW, which can cause the photon to leak out the ends and is suppressed when $\kappa_x L \gg 1$, or through scattering and absorption losses of the PCW. Given that these photonic decay processes can be made small, for conceptual simplicity here we treat the idealized case.

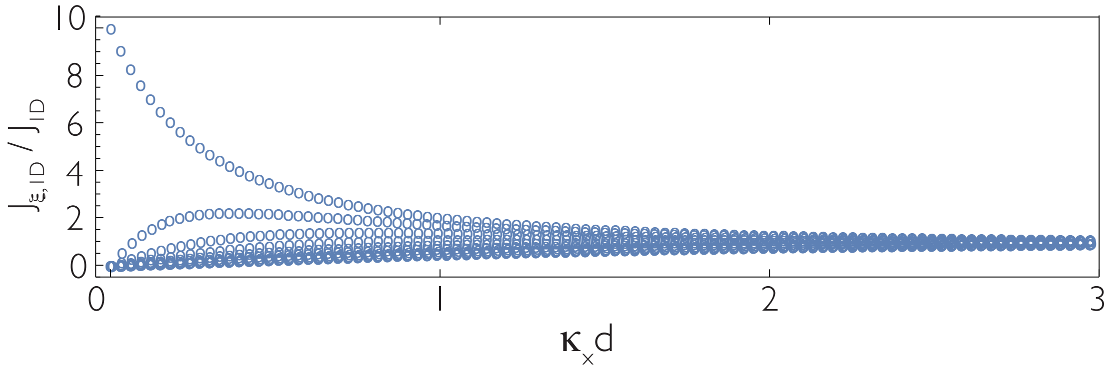

Figure 4.6: Collective frequency shifts of the modes of a regular chain of N=10 atoms in the bandgap of an infinite photonic crystal as a function of $\kappa_x d$, where κ_x^{-1} is the spatial range of the interaction and d is the distance between atoms. The atoms are placed at even anti-nodes of the Bloch modes. Figure adapted from [44].

For a chain of periodically spaced atoms placed in even antinodes of the Bloch modes, the dipole-projected Green's function matrix reads

$$\mathfrak{g} = J_{1\mathrm{D}} \begin{pmatrix} 1 & \chi & \chi^2 & \cdots & \chi^{N-1} \\ \chi & 1 & \chi & \cdots & \chi^{N-2} \\ \vdots & \vdots & \vdots & \ddots & \vdots \\ \chi^{N-1} & \chi^{N-2} & \chi^{N-3} & \cdots & 1 \end{pmatrix}, \tag{4.53}$$

where we have defined $\chi \equiv e^{-\kappa_x d}$, with d being the distance between nearest-neighbor atoms. The matrix $\mathfrak{g}$ is a real symmetric Toeplitz matrix (or bisymmetric matrix). Neglecting higher order contributions besides first-neighbor, an approximation valid for $\kappa_x d \gg 1$, $\mathfrak{g}$ becomes a tridiagonal Toeplitz matrix whose eigenvalues and eigenvectors are:

$$\lambda_\xi \equiv J_{1\mathrm{D},\xi} = 1 + 2e^{-\kappa_x d} \cos\left(\frac{\xi\pi}{N+1}\right), \tag{4.54a}$$

$$v_{\xi,j} = \sqrt{\frac{2}{N+1}} \sin\left(\frac{\xi j \pi}{N+1}\right). \tag{4.54b}$$

In this simple tight binding model, the frequency shifts of the collective atomic modes are distributed around $J_{1\mathrm{D}}$ with a frequency spread controlled by κ_x (i.e., for larger κ_x, the modes are closer in frequency). However, if the interaction length is very large compared to the distance between the atoms, the approximation of neglecting higher order neighbors falls apart, and the eigenvalues start to show a different behavior. Eventually, when the interaction length becomes infinite (or much larger than the length of the atomic cloud), there is only one bright mode, of eigenvalue $\lambda_{\mathrm{B}} = NJ_{1\mathrm{D}}$. This is analogous to the cavity case, where the interaction range is also infinite, except now the eigenvalue is purely real. This can be observed in Fig. 4.6, which shows how the collective frequency shifts coalesce towards $J_{1\mathrm{D}}$ for large $\kappa_x d$. The band-edge of a photonic crystal is thus a cross-over region in which the single bright mode approximation holds and then transitions to another regime where it breaks down, as the guided mode becomes evanescent and decays substantially within the length of the PCW. Importantly, the bandgap of a photonic crystal provides a tunable interaction range, a feature which is unique to this kind of nanostructure, and makes PCWs remarkably different reservoirs from either cavities or unstructured waveguides.

In the following section, we present some predictions for the transmission spectrum of two atoms coupled to a PCW for $\Gamma_{1\mathrm{D}}$ and $J_{1\mathrm{D}}$ values that can be achieved experimentally in the coming years. We hope that the foreseen large coherent couplings between the atoms combined with low dissipation through the guided mode help to stimulate a new generation of experiments that go beyond the current state of the art.

4.7 Experimental perspectives

In a recent experiment [42], the authors have observed signatures of collective atom-light interactions in the transmission spectra of atoms coupled to an alligator photonic crystal waveguide. They have recorded these spectra for various frequencies around the band edge of the PCW, exploring different physical regimes. Outside the bandgap, due to the finite size of the PCW, they observe the formation of a low-finesse cavity mode [as shown in Fig. 3(a) of Ref. [42], at a frequency ν_1]. At resonance with this cavity mode, the dissipative single-atom coupling to the structure is $\Gamma_{1\mathrm{D}}(\nu_1) \simeq 1.5\Gamma_0$, as obtained from steady-state transmission lineshape measurements. As before, Γ_0 is the free-space decay rate. The decay rate into leaky modes is $\Gamma'/\Gamma_0 \simeq 1.1$, estimated from finite-difference time-domain (FDTD) numerical calculations.

After tuning the spectral features of the PCW so that the resonance frequency of the atoms moves into the bandgap, they observe asymmetric lineshapes, revealing significant coherent coupling. Specifically at $\nu_{\mathrm{BG}} = 60$ GHz inside the bandgap, the spin exchange and decay rates are $J_{1\mathrm{D}}(\nu_{\mathrm{BG}})/\Gamma_0 \simeq -0.2$ and $\Gamma_{1\mathrm{D}}(\nu_{\mathrm{BG}})/\Gamma_0 \simeq 0.01$, respectively. Due to the evanescent character of the field in the bandgap, the

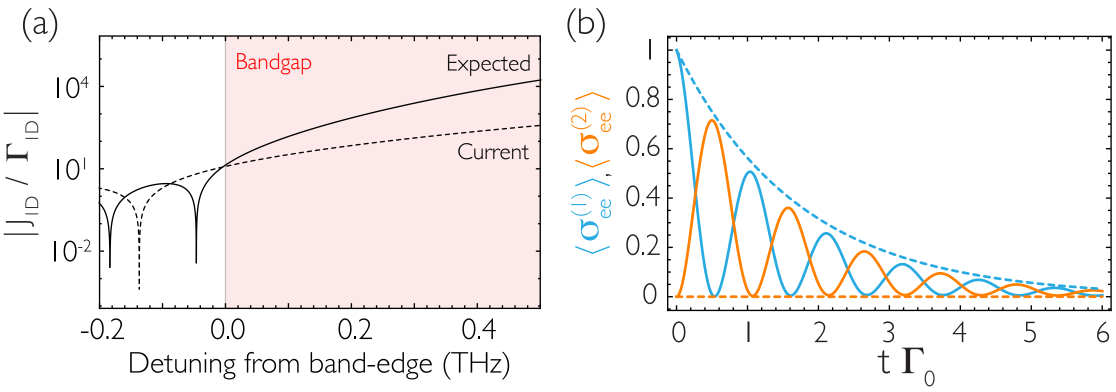

Figure 4.7: (a) Magnitude of the ratio between the coherent and dissipative couplings through the guided mode of an alligator PCW [42]. The dashed line shows the ratio as given in Fig.4 of Ref. [42], and the continuous curve represents the expected ratio that could be achieved within the next years (see text for more details). (b) Evolution of the excited state population of atom 1 (blue curve) and 2 (orange curve) after fully inverting atom 1 at the initial time. The resonance frequency of the atoms lies in the bandgap of the photonic crystal, with the atoms placed at successive even antinodes (continuous curve). The dashed line represents the non-interacting scenario, where the off-diagonal terms of $\mathfrak{g}$ are zero. The spin exchange and decay rates are chosen to be $J_{1D} = -3\Gamma_0$, $\Gamma_{1D} = 0.15\Gamma_0$, and $\Gamma' = 0.5\Gamma_0$. The lattice constant is $a = 370$ nm and the range of interaction is $\kappa_x^{-1} = 80a$. Figure adapted from [44].

interaction range is finite, and at ν_{BG} its value is $\kappa_x^{-1} \simeq 80a$, being $a = 370$ nm the lattice constant of the alligator PCW. While this experiment constitutes the first observation of more than one emitter interacting through the guided modes around the band edge of a PCW, the values of J_{1D} and Γ_{1D} are not yet good enough to observe signatures of atom-atom interactions such as time-dependent spin exchange. Nevertheless, we expect that near-term advances of the current set up will yield dramatic improvements on these rates, opening the door to exploring exciting collective atomic phenomena.

In particular, instead of using an alligator PCW, one can employ a slot photonic crystal waveguide [28, 109], i.e. a quasi-1D waveguide embedded in a 2D photonic crystal. This structure would be advantageous due to several reasons. First of all, it inhibits atomic emission into non-guided modes due to the surrounding 2D photonic bandgap that reduces the modes into which the atom can radiate. Absent inhomogeneous broadening, early simulations demonstrate that it is possible to achieve a small non-guided decay rate, i.e. $\Gamma' \simeq 0.5\Gamma_0$, while keeping the effective mode area similar to the Alligator PCW. Moreover, one can engineer flatter bands, which leads to an increase of the group index of $n_g \simeq 30$ near the band-edge (three times larger than that of the current alligator), according to FDTD simulations. Then, both J_{1D} and Γ_{1D} would experience a three-fold increase. Finally, by trapping the atoms at the center of the nanostructure, in between the two slots and not above as it is currently done, we have estimated that J_{1D} and Γ_{1D} would be five times larger. Summarizing, we project $\Gamma_{1D}(\nu_1)/\Gamma_0 \simeq 22$ at the first cavity resonance. This yields the values of $J_{1D}(\nu_{BG})/\Gamma_0 \simeq -3$ and $\Gamma_{1D}(\nu_{BG})/\Gamma_0 \simeq 0.15$ for a detuning from the band edge $\nu_{BG} = 20$ GHz, where the range of interaction is $\kappa_x^{-1} \simeq 80a$.

Figure 5.6(a) compares the ratio $|J_{1D}/\Gamma_{1D}|$ between the coherent and dissipative guided-mode rates for the current alligator PCW (dashed line) and the described slot PCW (continuous line). The improved ratio for the later structure can already be observed at frequencies just beyond the band-edge, and becomes $|J_{1D}/\Gamma_{1D}| \simeq 10^4$ at a detuning of 0.5 THz from the band-edge. An indisputable signature of collective behavior is represented in Fig. 5.6(b), which shows the evolution of the excited state populations of two atoms placed at successive even antinodes (continuous curve), after initially inverting one of them. The atoms interact through the guided modes of the already described slot PCW, and their resonance frequency lies inside the bandgap, at the frequency for which the interaction range is $\kappa_x^{-1} \simeq 80a$. The dashed lines show the expected result for non interacting atoms, where the off-diagonal terms of $\mathbb{g}$ are zero, a situation that occurs when the atoms are separated by a distance $d \gg \kappa_x^{-1}$.

To summarize, we believe that there is a bright future for experiments involving not only atoms, but also superconducting qubits interacting through the guided mode of a microwave photonic crystal. In a recent experiment, a ratio of $\Gamma_{1D}/\Gamma' = 50$ has already been achieved for transmon qubits connected to a 1D coplanar microwave transmission line [20]. Combined with the exciting recent advances in microwave photonic crystal fabrication [100], we expect a next generation of experiments where many qubits interact with each other in a mostly coherent manner.

4.8 Conclusion

We have analyzed the optical response of a chain of atoms placed along a quasi-1D nanophotonic structure in terms of the classical electromagnetic Green's function. This formalism is valid in the presence of absorptive and dispersive media.

We find that the linear response of the atoms can be understood in terms of collective atomic eigenstates of the Green's function matrix $\mathbb{g}(x_i, x_j)$ for all pairs of atoms. In particular, we have derived a closed expression for the transmission spectra that only depends on the cooperative frequency shifts and decay rates of these modes. We have shown that the transmission coefficient is a direct probe of the Green's function of the nanostructure, enabling us to determine whether the atom-light interactions are fundamentally dispersive or dissipative in character as well as to quantify the degree of cooperative interaction. We have gained insight into the interactions between atoms and quasi-1D cavities, waveguides, and photonic crystals, structures of relevance in recent experiments, as well as provided estimations of what can be observed in the near future.

The Green's function formalism provides a natural language that unifies nanophotonics and quantum optics, and our results apply not only to atoms [42], but to many other quantum emitters, such as superconducting qubits [100], NV centers [110], rare earth ions [30] and quantum dots [28], interacting with any kind of quasi-1D photonic structures or circuits.

4.9 Derivation for the multiple atom transmission spectrum

The low-saturation transmission spectrum for N atoms is

$$\frac{t(\omega)}{t_0(\omega)} = 1 - \frac{1}{g_{\text{out,in}}} \mathbf{g}_{\text{out}} \cdot \left(\frac{1}{(\Delta_A + \mathrm{i}\Gamma'/2)\mathbf{1} + \mathfrak{g}} \right) \cdot \mathbf{g}_{\text{in}}. \tag{4.55}$$

For any vectors $\mathbf{u}$ and $\mathbf{v}$ and matrix $\mathbf{A}$, the matrix determinant lemma states that

$$\frac{\det[\mathbf{A} + \mathbf{u} \otimes \mathbf{v}]}{\det[\mathbf{A}]} = 1 + \mathbf{v}^T \cdot \mathbf{A}^{-1} \cdot \mathbf{u}. \tag{4.56}$$

Defining $\mathbf{A} = -((\Delta_A + \mathrm{i}\Gamma'/2)\mathbf{1} + \mathfrak{g})$ and using the identity in Eq. (4.55) gives an alternative expression for the normalized transmission,

$$\frac{t(\omega)}{t_0(\omega)} = \frac{\det[(\Delta + \mathrm{i}\Gamma'/2)\mathbf{1} + \mathfrak{g} - \mathfrak{h}]}{\det[(\Delta + \mathrm{i}\Gamma'/2)\mathbf{1} + \mathfrak{g}]}, \tag{4.57}$$

where we have defined the matrix

$$\mathfrak{h} = \frac{1}{g_{\text{out,in}}} \mathbf{g}_{\text{in}} \otimes \mathbf{g}_{\text{out}}. \tag{4.58}$$

The matrices $\mathfrak{g}$ and $\mathfrak{h}$ are closely related to each other. In fact, we will show that for systems which are well approximated by an effective 1D wave equation, $\mathfrak{g}$ and $\mathfrak{h}$ have the same upper triangular and diagonal elements. Therefore, $\mathfrak{g} - \mathfrak{h}$ is strictly triangular (upper triangular and diagonal elements are zero) and does not contribute to the determinant in Eq. (4.57). Omitting $\mathfrak{g} - \mathfrak{h}$ leads to the final result for the low saturation quasi-1D transmission spectrum for multiple atoms:

$$\frac{t(\omega)}{t_0(\omega)} = \frac{\det[(\Delta_A + \mathrm{i}\Gamma'/2)\mathbf{1}]}{\det[(\Delta_A + \mathrm{i}\Gamma'/2)\mathbf{1} + \mathfrak{g}]} = \frac{1}{\det[1 + \frac{\mathfrak{g}}{\Delta_A + \mathrm{i}\Gamma'/2}]} = \prod_{\xi=1}^{N} \left(\frac{\Delta_A + \mathrm{i}\Gamma'/2}{\Delta_A + \mathrm{i}\Gamma'/2 + \lambda_\xi} \right). \tag{4.59}$$

Next we show that $\mathfrak{g} - \mathfrak{h}$ is strictly triangular for approximately 1D systems. Just as we did for the single atom case, we assume that the Green's function is well-approximated by a 1D Green's function of an effective 1D system, and therefore the complex rate g_{ij} can be written as

$$g_{ij} = \frac{\mu_0 \omega^2 |\mathbf{d}|^2}{\hbar A_{\text{eff}}} G^{1\text{D}}(x_i, x_j, \omega). \tag{4.60}$$

An element of the matrix $\mathfrak{h}$ is then given by

$$\mathfrak{h}_{ij} = \frac{\mu_0 \omega^2 |\mathbf{d}|^2}{\hbar A_{\text{eff}}} \overbrace{\left(\frac{G^{1\text{D}}(x_{\text{out}}, x_i) G^{1\text{D}}(x_j, x_{\text{in}})}{G^{1\text{D}}(x_{\text{out}}, x_{\text{in}})} \right)}^{\equiv H^{1\text{D}}(x_i, x_j)}. \tag{4.61}$$

We can now use unique properties of the 1D Green's function to simplify this expression. As shown in Appendix D, the solution of the 1D Green's function can be expressed in terms of the solutions $\phi_{L/R}(x)$ for a wave coming into the system from the left/right,

$$G^{1\text{D}}(x_i, x_j) = -\frac{\Theta(x_j - x_i)\phi_L(x_j)\phi_R(x_i) + \Theta(x_i - x_j)\phi_R(x_j)\phi_L(x_i)}{W}. \tag{4.62}$$

Here $\Theta(x - x')$ is the Heaviside funciton. The Wronskian given by $W = \phi_R(x)\frac{\mathrm{d}\phi_L(x)}{\mathrm{d}x} - \frac{\mathrm{d}\phi_R(x)}{\mathrm{d}x}\phi_L(x)$ and can be evaluated for any value of x since it is a constant.

We will assume that the position x_{in} is to the left of the system, and that x_{out} is to the right of the system, so that $x_{\text{out}} > x_j > x_{\text{in}}$. Then the input propagator is $G^{1\text{D}}(x_j, x_{\text{in}}) = -\phi_R(x_{\text{in}})\phi_L(x_j)/W$, the output propagator is $G^{1\text{D}}(x_{\text{out}}, x_j) = -\phi_R(x_j)\phi_L(x_{\text{out}})/W$, and the propagator through the system without atoms is $G^{1\text{D}}(x_{\text{out}}, x_{\text{in}}) = -\phi_L(x_{\text{out}})\phi_R(x_{\text{in}})/W$. Substituting these expressions for the 1D Green's function into $H^{1\text{D}}(x_i, x_j)$ results in

$$\begin{aligned} H^{1\text{D}}(x_i, x_j) = \frac{G^{1\text{D}}(x_{\text{out}}, x_i)\, G^{1\text{D}}(x_j, x_{\text{in}})}{G^{1\text{D}}(x_{\text{out}}, x_{\text{in}})} &= -\frac{1}{W} \frac{\phi_R(x_i)\phi_L(x_{\text{out}}) \times \phi_R(x_{\text{in}})\phi_L(x_j)}{\phi_L(x_{\text{out}})\phi_R(x_{\text{in}})} \\ &= -\frac{\phi_L(x_i)\phi_R(x_j)}{W}. \end{aligned} \tag{4.63}$$

Upon comparing $H^{1\mathrm{D}}(x_i, x_j)$ and $G^{1\mathrm{D}}(x_i, x_j)$ from Eq. (4.62), we see that they are the same when $x_i \geq x_j$. It then follows that $\mathfrak{g} - \mathfrak{h}$ is strictly triangular.

C h a p t e r 5

ATOMS TRAPPED ALONG AN ALLIGATOR PHOTONIC CRYSTAL WAVEGUIDE

Recent years have witnessed a spark of interest in combining atoms and other quantum emitters with photonic nanostructures [28]. Many efforts have focused on enhancing emission into preferred electromagnetic modes relative to vacuum emission, thereby establishing efficient quantum matter-light interfaces and enabling diverse protocols in quantum information processing [111]. Photonic structures developed for this purpose include high-quality cavities [1–4, 97], dielectric fibers [9–13], metallic waveguides [16–18], and superconducting circuits [20, 21, 112]. Photonic crystal waveguides (PCWs) are of particular interest since the periodicity of the dielectric structure drastically modifies the field propagation, yielding a set of Bloch bands for the guided modes [33]. For example, recent experiments have demonstrated superradiant atomic emission due to a reduction in group velocity for an atomic frequency near a band edge of a PCW [37].

A quite different paradigm for atom-light interactions in photonic crystals was proposed in Refs. [38–40, 113], but has yet to be experimentally explored. In particular, when an atomic transition frequency is situated within a bandgap of a PCW, an atom can no longer emit propagating waves into guided modes (GMs) of the structure. However, an evanescent wave surrounding the atoms can still form, resulting in the formation of atom-photon bound states [114, 115]. This phenomenon has attracted new interest recently as a means to realize dispersive interactions between atoms without dissipative decay into GMs. The spatial range of atom-atom interactions is tunable for 1D and 2D PCWs and set by the size of the photonic component of the bound state [41, 116]. Many-body physics with large spin exchange energies and low dissipation can thereby be realized, in a generalization of cavity QED arrays [117, 118]. Fueled by such perspectives, there have been recent experimental observations with atoms [32, 36, 37] and quantum dots [98, 99] interacting through the GMs of photonic crystal waveguides, albeit in frequency regions outside the bandgap, where GMs are propagating fields.

In this chapter, we report the first observation of collective dispersive shifts of the atomic resonance around the band edge of a photonic crystal. Thermal tuning

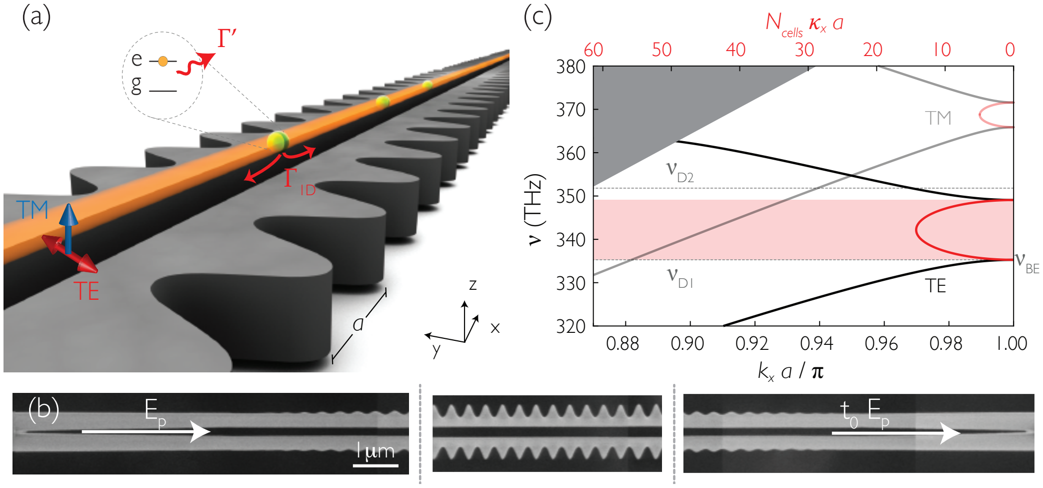

Figure 5.1: Description of the alligator photonic crystal waveguide (PCW). **(a)** Atoms are trapped above the PCW in an optical dipole trap formed by the reflection of a near normal-incidence external beam [37]. The orange cylinder represents the confinement of the atoms, which is $\Delta x_{\rm A} \simeq \pm 6\ \mu$m along the axis of the device, and $\Delta y_{\rm A} \simeq \Delta z_{\rm A} \simeq \pm 30$ nm in the transverse directions (see Chap. 6). The three green spheres represent trapped atoms that interact radiatively via the fundamental TE guided mode, polarized mainly along y. The decay rate for a single atom into the PCW is $\Gamma_{\rm 1D}$ (red arrows), and the decay rate into all other modes is Γ' (wavy red). **(b)** SEM images of portions of the tapering and PCW sections. The suspended silicon nitride device (grey) consists of 150 cells and 30 tapering cells on each side. The lattice constant is $a = 370$ nm and thickness is 185 nm. **(c)** Calculated band structure of the fundamental TE (solid) and TM (translucent) modes using an eigenmode solver [34] and the measured SEM dimensions, which are modified within their uncertainty to match the measured bands. The black curves represent the Bloch wave-vector k_x (lower axis). The red curves show the attenuation coefficient κ_x of the field for frequencies in the bandgap (upper axis), and are calculated by means of an analytical model (see Chap. 6). The dotted lines mark the frequencies of the Cs D_1 ($\nu_{\rm D1} = 335.1$ THz) and D_2 ($\nu_{\rm D2} = 351.7$ THz) transitions. The dielectric band edge is indicated as $\nu_{\rm BE}$. The pink (gray) shaded area represents the TE bandgap (the light cone). Figure adapted from [42].

allows us to control the offset of the band edge frequency (ν_{BE}) of the PCW relative to frequency ν_{D1} of the D_1 line of cesium. In both the dispersive domain (i.e., ν_{D1} outside the bandgap with electric field $E(x) \propto e^{\pm i k_x x}$) and reactive regime (i.e., ν_{D1} inside the bandgap with $E(x) \propto e^{-\kappa_x |x|}$), we record transmission spectra for atoms trapped along the PCW, as illustrated in Fig. 5.1(a).

To connect the features of the measured transmission spectra to underlying atom-atom radiative interactions, we have developed a formalism based on the electromagnetic Green's function [44]. The model allows us to infer the peak single-atom frequency shift of the atomic resonance $J_{\mathrm{1D}}(\Delta_{\mathrm{BE}})$ and guided mode decay rate $\Gamma_{\mathrm{1D}}(\Delta_{\mathrm{BE}})$ as functions of detuning $\Delta_{\mathrm{BE}} = \nu_{\mathrm{D1}} - \nu_{\mathrm{BE}}$ between the atomic ν_{D1} and band edge ν_{BE} frequencies. From the observation of superradiant emission outside the bandgap, we infer the average number of trapped atoms to be $\bar{N} = 3.0 \pm 0.5$, as described in Ref. [37] and the supporting material (see Chap. 6). For frequencies inside the bandgap ($\Delta_{\mathrm{BE}} = 50$ GHz) the ratio of dissipative to coherent rates is $\mathcal{R} = \Gamma_{\mathrm{1D}}/J_{\mathrm{1D}} = 0.05 \pm 0.17$, due to the exponential localization of the atomic radiation in the bandgap. For comparison, the prediction for our system from cavity quantum electrodynamics (CQED) models alone is $\mathcal{R}_{\mathrm{CQED}} = 0.30 \pm 0.04$. Besides yielding a more favorable ratio between coherent and dissipative guided mode rates, PCWs offer significant advantages when compared to conventional cavities as platforms for atom-light interfaces. First, the range of interaction in a PCW is tunable, ranging from effectively infinite to nearest neighbor, in contrast to the fixed infinite range of a cavity. Second, due to the multimode nature of PCWs, one can employ different guided modes as different interaction channels to which the atoms simultaneously couple.

5.1 Alligator Photonic Crystal Waveguide

Figure 5.1(a) provides an overview of our experiment with atoms trapped near and strongly interacting with the TE-like mode of an alligator PCW. The suspended silicon nitride structure consists of $N_{\mathrm{cells}} = 150$ nominally identical unit cells of lattice constant $a = 370$ nm, and is terminated by 30 tapering cells on each side, as shown in the SEM images in Fig. 5.1(b). The tapers mode-match the fields of the PCW to the fields of uncorrugated nanobeams for efficient input and output coupling. Design, fabrication, and characterization details are described in Refs. [32, 36, 37]. Figure 5.1(c) shows the nominal cell dispersion relations for the TE (polarized mainly along y) and TM-like modes (polarized mainly along z). After release of the SiN structure from the Si substrate, a low power CF4 etch is used to align the

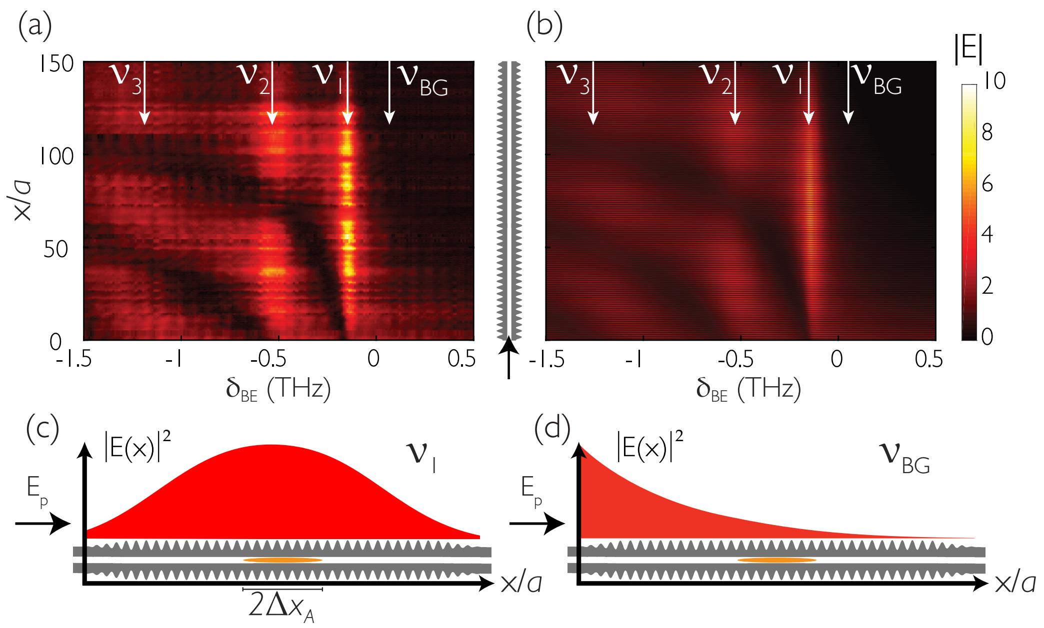

Figure 5.2: Characterization of the alligator PCW. **(a)** Measured and **(b)** calculated electric field magnitude along the PCW, as functions of position x along the PCW and probe detuning $\delta_{\mathrm{BE}} = \nu_{\mathrm{p}} - \nu_{\mathrm{BE}}$ relative to ν_{BE} for the dielectric band edge. **(c,d)** Guided mode intensity $|E(x)|^2$ along PCW at two different frequencies: (c) ν_1 for the first cavity resonance showing a resonant 'super mode' and (d) ν_{BG} inside the bandgap displaying exponential decay ($N_{\mathrm{cells}}\kappa_x a = 2.0$ at ν_{BG}). For clarity, the number of cells of the nominal and tapering sections is decreased by a factor of 5, and the Bloch periodicity ($a = 370$ nm), while present, is not shown in the intensity. The orange ovals represent the confinement of the atoms in the optical trap above the PCW, which is $\Delta x_{\mathrm{A}} \simeq \pm 6$ μm along the x-axis of the device and $\Delta y_{\mathrm{A}} \simeq \pm 30$ nm, with a PCW gap width of 220 nm. Figure adapted from [42].

lower/'dielectric' TE band edge (ν_{BE}) to the Cs D_1 transition (ν_{D1}). The TM mode has band edges far detuned from the both the Cs D_1 and D_2 lines. In our experiment, the TE mode is used to probe the atoms, while the TM mode with approximately linear dispersion serves to calibrate the density and trap properties.

In order to better understand atomic interactions with the PCW, it is helpful to visualize the spatial profile of the fields generated absent atoms, when light is input from one end. Figure 5.2(a) shows the measured intensity along the length of the PCW as a function of probe detuning $\delta_{\mathrm{BE}} = \nu_{\mathrm{p}} - \nu_{\mathrm{BE}}$ around the band edge, where ν_{p} is the probe frequency. The intensity was measured by imaging weak scatterers along the length of the alligator PCW that, after calibration, serve as local probes of the intensity (see Chap. 6). Figure 5.2(b) shows the corresponding finite-difference time-domain (FDTD) simulated intensity [54]. In both images, resonances appear at

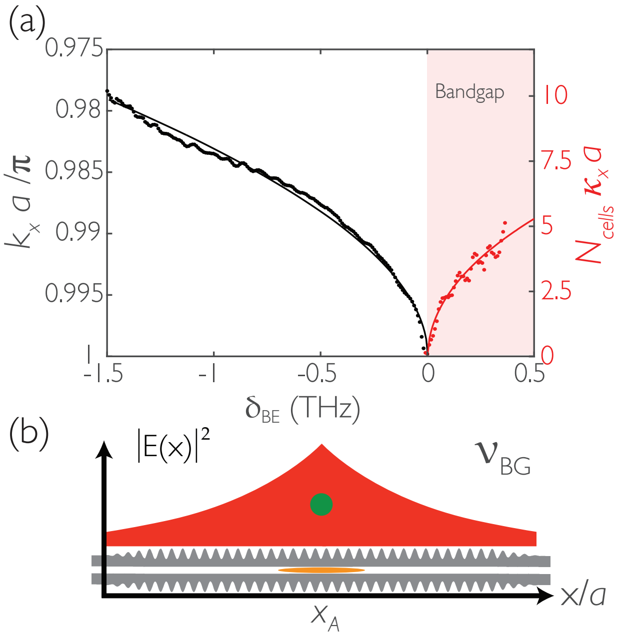

Figure 5.3: **(a)** Dispersion relation for the projected wave vector k_x and attenuation constant κ_x versus probe detuning δ_{BE} deduced for the PCW obtained by fitting the data in Fig. 5.2(a) to a model of the device (see Chap. 6). The shaded pink area represents frequencies inside the bandgap. **(b)** Plot of the exponentially localized emission $e^{-2\kappa_x|x-x_{\mathrm{A}}|}$ from an atom (green sphere) at position x_{A} with transition frequency $\nu_{\mathrm{D1}} = \nu_{\mathrm{BG}}$ inside the bandgap. Figure adapted from [42].

$\nu_{\mathrm{p}} = \nu_{1,2,3}$ due to the weak cavity formed by the reflections of the tapers. The spatial modulation of the intensity at the resonances due to the cavity effect is approximated by $|E(x)|^2 \approx \cos^2(\delta k_x\, x)$, where $\delta k_x = \pi/a - k_x$ is the effective wave-vector near the band edge. The n'th resonance at frequency ν_n is such that $\delta k_x = n\pi/L$, where L is the effective length of the PCW (including field penetration into the tapers). Fig. 5.2(c) shows a plot of $|E(x)|^2$ for a probe input at frequency $\nu_{\mathrm{p}} = \nu_1$ at the first resonance. Inside the bandgap ($\Delta_{\mathrm{BE}} > 0$) the field is evanescent, and $\delta k_x = i\kappa_x$. Fig. 5.2(d) plots $|E(x)|^2$ for probe frequency $\nu_{\mathrm{p}} = \nu_{\mathrm{BG}}$ inside the bandgap, and shows the exponential decay of the intensity. Using a model for the field in a finite photonic crystal (see Chap. 6), we fit the measured intensity for each frequency in Fig. 5.2(a) and Fig. 5.2(b) and extract δk_x and κ_x, thereby obtaining the dispersion relations shown in Fig. 5.3(a). Importantly, we determine the band edge frequency for the actual device to be $\nu_{\mathrm{BE}} - \nu_1 = 133 \pm 9$ GHz relative to the readily measured first resonance at ν_1, which is in good agreement with the FDTD simulated result of 135 GHz.

Both ν_1, ν_{BG} are relevant to our measurements of transmission spectra with trapped atoms. The presence of a 'cavity' mode at ν_1 implies that the emission of an atom with transition frequency $\nu_{\mathrm{D1}} = \nu_1$ will generate a field inside the PCW with a similar spatial profile to that of the cavity mode, as shown in Fig. 5.2(c). By contrast, atomic emission in the regime with $\nu_{\mathrm{D1}} = \nu_{\mathrm{BG}}$ within the bandgap will excite an exponentially localized mode centered around x_{A}, as illustrated in Fig. 5.3(b).

5.2 Experiment

Cs atoms are trapped above the surface of the alligator PCW, as shown in Fig. 5.1(a), using a similar experimental setup to that reported in Ref. [37]. As described in more detail in the previous reference, the decay rate into the guided mode Γ_{1D} is exponentially sensitive to the trap position above the surface of the alligator PCW. Our calculations and measurements of Γ_{1D} agree with COMSOL simulations [34] of the trap position, and thus we are able to determine that the Cs atoms are trapped 125 ± 15 nm above the surface of the alligator PCW. Atoms are cooled and trapped in a MOT around the PCW, and then loaded into a dipole trap formed by the reflection from the device of a frequency red-detuned side illumination (SI) beam. The SI beam has a waist of 50 μm, and the polarization is aligned along the x axis for maximum reflection from the PCW. We measure a $1/e$ trap life time of ~ 30 ms, and we estimate an atom temperature of ~ 30 μK from time-of-flight measurements. From the trap simulations (for details see supporting materials (see Chap. 6)), we infer that the atoms are confined to a region 125 nm above the surface with dimensions $\Delta x_{\mathrm{A}} \simeq \pm 6$ μm, $\Delta y_{\mathrm{A}} \simeq \Delta z_{\mathrm{A}} \simeq \pm 30$ nm. The simulations predict that more energetic atoms escape the trap and collide into the structure, since the weakest direction of the trap is along the diagonals of the y-z plane due to Casimir-Polder forces.

In order to estimate the average number of trapped atoms, we measure the superradiant atomic decay rate when the atom frequency ν_{D1} is tuned to the first resonance ν_1 of the PCW (Fig. 5.2(c)) [37]. Due to the strong dissipative interactions between the atoms and with $J_{\mathrm{1D}} \approx 0$, the collective decay rate is enhanced as compared to the single atom decay rate, and we infer an average atom number of $\bar{N} = 3.0 \pm 0.5$ (see Chap. 6). In the low density limit $\bar{N} \ll 1$, the measured decay rate corresponds to that of a single atom. We then measure a guided mode decay rate $\Gamma_{\mathrm{1D}} = (1.5 \pm 0.2)\,\Gamma_0$, which is in good agreement with the FDTD simulations at the calculated trap location (see Chap. 6).

After the atoms are loaded into the trap, we send a weak 5 ms probe beam E_{p}

with frequency ν_{p} in either the TE or TM guided mode through the PCW and record the transmitted intensity $|t(\nu_{\text{p}})E_{\text{p}}(\nu_{\text{p}})|^2$. The probe beam scans near the Cs $6S_{1/2},\ F = 3 \rightarrow 6P_{1/2},\ F' = 4$ transition. Each experimental cycle runs at a fixed detuning $\Delta_{\text{A}} = \nu_{\text{p}} - \nu_{\text{D1}}$ relative to the free-space atomic transition frequency ν_{D1}. We observe little change of signal during the 5 ms probing time, suggesting that the atom number is approximately constant over this interval. The band edge of the PCW is tuned thermally by shining an external laser onto a corner of the chip, where its light is absorbed by the silicon substrate. Therefore, the Cs D_1 line can be aligned to be either outside or inside the bandgap with an uncertainty $\delta\nu \simeq 5$ GHz. The transmission for each data point is normalized by the transmission with no atoms ($|t_0 E_{\text{p}}|^2$), resulting in a measurement of $T/T_0 \equiv |t/t_0|^2$. The logarithm of the measured and simulated transmission spectrum with no atoms $T_0 = |t_0(\nu_{\text{p}})|^2$ is shown in Fig. 5.4(a).

Examples of transmission spectra with atoms are shown in Figs. 5.4(b-d). Note that the spectra are shifted 12.5 MHz due to both the AC Stark shift of the dipole trap and the modified Lamb shift induced by the non-guided modes of the PCW. Notably, the transmission spectra at the first 'cavity' resonance ν_1 exhibit a characteristic Lorentzian 'dip', and they become more and more asymmetric as the frequency moves into the bandgap.

5.3 Transmission model

We have developed a model to extract quantitative values for collective decay rates and frequency shifts from these atomic transmission spectra [44]. While the formalism of waveguide [119] and cavity QED [70] is well suited for describing atoms coupled to uniform waveguides and cavities, it is not general enough to capture the rich physics of atomic interactions in the vicinity of a PCW. Instead, we describe our system by employing a spin model in terms of the classical electromagnetic Green's function, in which the atoms (or 'pseudo-spins' σ for ground and excited state) interact via the emission and re-absorption of guided photons [82, 88, 89].

The electromagnetic Green's function $\mathbf{G}(\mathbf{r}, \mathbf{r}_i, \omega)$ is related to the electric field $\mathbf{E}(\mathbf{r}, \omega)$ emitted by a dipole $\mathbf{p}_i$ oscillating at frequency ω at position $\mathbf{r}_i$ by $\mathbf{E}(\mathbf{r}, \omega) = \mu_0\omega^2\mathbf{G}(\mathbf{r}, \mathbf{r}_i, \omega) \cdot \mathbf{p}_i$ [45, 82]. The dipole moment operator for atom i is decomposed into $\hat{\mathbf{p}}_i = \mathbf{d}_i\hat{\sigma}^i + \mathbf{d}_i^*\hat{\sigma}^i$, where $\mathbf{d}_i$ is the dipole matrix element, and where $\hat{\sigma}^i = |g\rangle\langle e|$ is the atomic coherence operator between the ground and excited states. The spin model describes a system of N atoms coupled to and driven by a guided mode of the PCW. In the low saturation and steady-state regime, expectation values for the atomic coherences ($\sigma^i = \langle \hat{\sigma}^i \rangle$) are described by a linear system of equations [44]

$$\left(\tilde{\Delta}_{\mathrm{A}} + \mathrm{i}\frac{\Gamma'}{2}\right)\hat{\sigma}^i + \sum_{j=1}^{N} g_{ij}\,\hat{\sigma}^j = -\Omega_i, \tag{5.1}$$

where $\tilde{\Delta}_{\mathrm{A}} = 2\pi\Delta_{\mathrm{A}} = 2\pi(\nu_{\mathrm{p}} - \nu_{\mathrm{D1}})$ is the detuning between the probe and the atomic angular frequencies, Ω_i is the classical drive (Rabi frequency) for the i'th

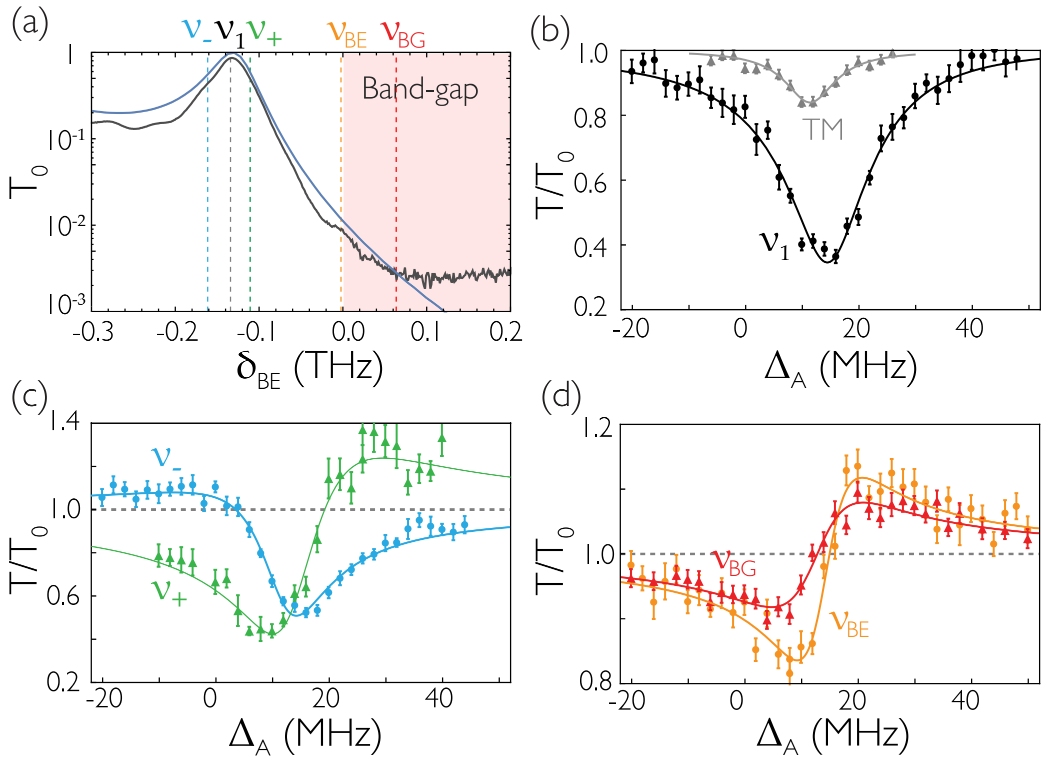

Figure 5.4: Transmission spectra of the PCW without (a) and with trapped atoms (b-d). **(a)** Measured (black) and FDTD simulated (blue) transmission spectra of the PCW without atoms as a function of the probe detuning from the band edge frequency, $\delta_{\mathrm{BE}} = \nu_{\mathrm{p}} - \nu_{\mathrm{BE}}$. There is a minimum extinction of 25 dB for the transmitted signal due to fabrication imperfections. **(b-d)** Transmission spectrum for $\bar{N} = 3.0 \pm 0.5$ trapped atoms versus probe detuning $\Delta_{\mathrm{A}} = \nu_{\mathrm{p}} - \nu_{\mathrm{D1}}$, at several frequencies around the band edge. The solid lines are fits using the transmission model in (5.4), averaged over atom positions and different atom numbers. In **(b)**, the Cs D_1 line is aligned to the first 'cavity' resonance ν_1, resulting in symmetric spectra for both the TE (black) and TM (gray) modes. The TE spectra in **(c)** are for frequencies $\nu_{-/+}$ on the two sides of the ν_1 resonance. The TE spectra in **(d)** are taken at the band edge (ν_{BE}, circles) and 60 GHz (ν_{BG}, triangles) into the bandgap. The asymmetry of the line-shapes in (c) and (d) implies a large ratio of coherent to dissipative interactions. Figure adapted from [42].

atom due to the guided mode input field, and $g_{ij} = J^{ij}_{1\mathrm{D}} + \mathrm{i}\Gamma^{ij}_{1\mathrm{D}}/2$ where $J^{ij}_{1\mathrm{D}} = \mu_0\omega_{\mathrm{p}}^2/\hbar\,\mathbf{d}_i^* \cdot \mathrm{Re}\,\mathbf{G}(\mathbf{r}_i, \mathbf{r}_j, \omega_{\mathrm{p}}) \cdot \mathbf{d}_j$, and $\Gamma^{ij}_{1\mathrm{D}} = 2\mu_0\,\omega_{\mathrm{p}}^2/\hbar\,\mathbf{d}_i^* \cdot \mathrm{Im}\,\mathbf{G}(\mathbf{r}_i, \mathbf{r}_j, \omega_{\mathrm{p}}) \cdot \mathbf{d}_j$. Each atom can also decay into non-guided modes, including free-space, with a decay rate Γ'. The appearance of the real and imaginary parts of the Green's function in the coherent and dissipative terms has the classical analogue that the in-phase and out-of-phase components of a field with respect to an oscillating dipole store time-averaged energy and perform time-averaged work, respectively. Since the first term in (6.7) is diagonal, the atomic coherences can be understood in terms of the eigenvalues $\{\lambda_\xi\}$ for $\xi = \{1, \cdots, N\}$ and eigenfunctions of the matrix $\mathfrak{g}$, whose elements are g_{ij}. The real and imaginary parts of $\{\lambda_\xi\}$ correspond to frequency shifts and guided mode decay rates, respectively, of the collective atomic mode ξ.

The transmission spectrum can be expressed in terms of the eigenvalues of $\mathfrak{g}$ as [44],

$$\frac{t(\tilde{\Delta}_A, N)}{t_0(\tilde{\Delta}_A)} = \prod_{\xi=1}^{N} \left(\frac{\tilde{\Delta}_A + \mathrm{i}\Gamma'/2}{\tilde{\Delta}_A + \mathrm{i}\Gamma'/2 + \lambda_\xi} \right), \tag{5.2}$$

where $t_0(\tilde{\Delta}_A)$ is the transmission without atoms. In the case of a single atom, the only eigenvalue is proportional to the self-Green's function, $\lambda_\xi = g_{ii}$, which implies that the transmission spectrum is a direct measurement of the self-Green's function at the atom's position. For non-interacting atoms, the off-diagonal elements of $\mathfrak{g}$ are zero, and thus the eigenvalues are single-atom quantities, $\lambda_\xi = g_{ii}$ as there is no cooperative response.

In contrast, for interacting atoms, the off-diagonal elements are non-negligible, and there is a cooperative response. In particular, for the atomic frequency inside the bandgap of a photonic crystal, the elements g_{ij} are well approximated by [41]

$$g_{ij} = (J_{\,1\mathrm{D}} + \mathrm{i}\Gamma_{\,1\mathrm{D}}/2)\cos(\pi x_i/a)\cos(\pi x_j/a)e^{-\kappa_x|x_i - x_j|}, \tag{5.3}$$

where the cosine factors arise from the Bloch mode and the decay length κ_x^{-1} is due to the exponential decay of the field and results in a finite range of interaction. For an infinite photonic crystal, $\Gamma_{\,1\mathrm{D}} = 0$, since the light is localized and there is no dissipation through the guided mode. But for a finite PCW of length L, the guided mode dissipation $\Gamma_{\,1\mathrm{D}} \sim e^{-\kappa_x L}$ is finite due to leakage of the mode out of the edges of the structure.

In the limit where the interaction range $1/\kappa_x$ is much larger than the separation $\delta x_{ij} = |x_i - x_j|$ of the atoms, $\kappa_x\,\delta x_{ij} \lesssim \kappa_x\,\Delta x_{\,\mathrm{A}} \ll 1$, the guided mode input field couples predominantly to a single collective "bright" mode of the system with eigenvalue $\lambda_B = \sum_{i=1}^N g_{ii} = \sum_{i=1}^N (J_{\text{1D}}^{ii} + \mathrm{i}\,\Gamma_{\text{1D}}^{ii}/2)$. Formally, when $\kappa_x = 0$, the matrix $\mathfrak{g}$ is separable [$g_{ij} = u_i u_j$ with $u_i \propto \cos(\pi x_i/a)$] and therefore only has one non-zero eigenvalue. In this single bright mode approximation, the transmission spectrum is given by

$$\frac{t(\tilde{\Delta}_{\text{A}}, N)}{t_0(\tilde{\Delta}_{\text{A}})} = \frac{\tilde{\Delta}_{\text{A}} + \mathrm{i}\Gamma'/2}{\left(\tilde{\Delta}_{\text{A}} + \sum_{i=1}^N J_{\text{1D}}^{ii}\right) + \mathrm{i}\left(\Gamma' + \sum_{i=1}^N \Gamma_{\text{1D}}^{ii}\right)/2}. \tag{5.4}$$

We have confirmed numerically that this single 'bright mode' picture is valid within the limits of our uncertainties for the range of frequencies of the measured spectra in Fig. 5.4 In particular, at the largest detuning into the bandgap $\Delta_{\text{BE}} = 60$ GHz, we have $\kappa_x \Delta x_{\text{A}} \simeq 0.2$. However, for atomic frequencies further away from the band edge, this approximation eventually breaks down (e.g., at the bandgap center, $\kappa_x \Delta x_{\text{A}} \simeq 1.5$).

The single bright mode approximation is also valid in conventional cavity QED. The Green's function matrix is then given by $g_{ij} = (J_{\text{1D}} + \mathrm{i}\Gamma_{\text{1D}}/2)\ \cos(k_{\text{c}} x_i)\cos(k_{\text{c}} x_j)$, where k_{c} is the wave-vector of the standing-wave cavity. In this case, $J_{\text{1D}} \propto \Delta_c/(1 + \Delta_c^2/\gamma_c^2)$ and $\Gamma_{\text{1D}} \propto \gamma_c/(1 + \Delta_c^2/\gamma_c^2)$, where Δ_{c} is the detuning from the cavity resonance and γ_c is the cavity linewidth. Importantly, the ratio between the imaginary dissipative coupling rate to the real coherent coupling rate falls off with inverse detuning, $R_{\text{CQED}} = \Gamma_{\text{1D}}/J_{\text{1D}} = \gamma_c/\Delta_c$ for large Δ_c, whereas in a PCW bandgap, the fall off is exponential with detuning from the band edge.

5.4 Analysis of measured spectra

Equation (5.4) provides a direct mapping between the observed transmission spectra of Figs. 5.4(b-d) and the electromagnetic Green's function of the PCW. In particular, the line shape is Lorentzian for purely dissipative dynamics ($J_{\text{1D}}^{ii} = 0$). This is precisely what occurs at the frequency of the first cavity mode ν_1, as shown by Fig. 5.4(b). When the GM band edge frequency is moved towards the atomic resonance ν_{D1}, the dispersive interactions are switched on, and the transmission line shape becomes asymmetric, displaying a Fano-like resonance [106], as can be observed in Figs. 5.4(c,d). The appearance of an asymmetry in the atomic spectra directly reveals a significant coherent coupling rate J_{1D}, which is evident for frequencies that lie in the bandgap region.

For all relevant frequencies, the spectra for the TM guided mode are approximately symmetric, as $J_{\text{1D}}^{\text{TM}}, \Gamma_{\text{1D}}^{\text{TM}} \ll \Gamma'$ for this GM polarization. An example of a TM spectrum is shown in the gray curve of Fig. 5.4(b). Since the TM bandgap is so far detuned, the TM spectra are insensitive to Δ_{BE} and serve as a calibration signal. Using a waveguide transmission model, we fit the TM transmission spectra and extract a TM guided mode decay rate of $\Gamma_{\mathrm{1D}}^{\mathrm{TM}} = (0.045 \pm .01)\,\Gamma_0$. This rate is ~ 30 times smaller than the TE guided mode decay rate Γ_{1D} at the first resonance ν_1. The ratio $\Gamma_{\mathrm{1D}}^{\mathrm{TE}}/\Gamma_{\mathrm{1D}}^{\mathrm{TM}} \approx 30$ is explained well by the expected slow-light and cavity enhancement of the PCW described in Ref. [37] and supporting material (see Chap. 6). From the TM fits, we also measure $\Gamma' = 2\pi \times 9.1$ MHz, which, due to inhomogeneous broadening, is larger than value $\Gamma' = 2\pi \times 5.0$ MHz from FDTD numerical calculations (see Chap. 6). While tuning the band edge to move the atomic frequency ν_{D1} into in the bandgap, TM spectra are measured in order to confirm *in situ* that the average atom number is approximately constant over the course of the measurements of TE spectra.

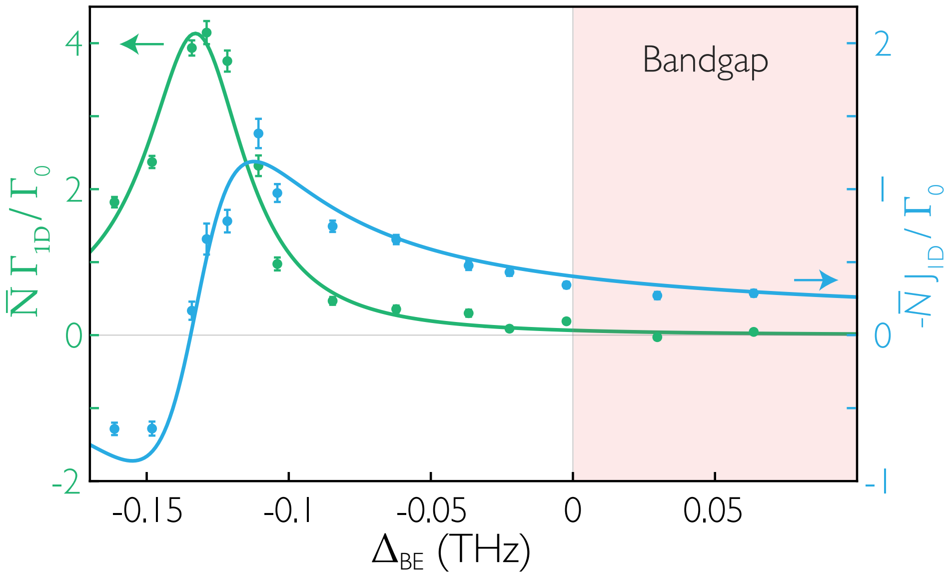

Figure 5.5: **(a)** Peak dissipative interaction rate $\bar{N}\Gamma_{\mathrm{1D}}$ (green) and coherent rate $\bar{N}J_{\mathrm{1D}}$ (blue) around the band edge. With $\bar{N}$ determined from independent decay rate measurements, the values for Γ_{1D}, J_{1D} are found from fits of the transmission model in Eq. (4) to the measured atomic spectra and are normalized by the free-space decay rate $\Gamma_0 = 2\pi \times 4.56$ MHz for the Cs D_1 line. The lines are the predictions from a numerical model based on 1D transfer matrices . Figure adapted from [42].

To obtain quantitative values for the collective frequency shifts and decay rates by fitting the TE atomic spectra to the spin model, we must account for the fluctuations in atom number and position along the x-axis. As depicted in Fig. 5.1(a) and Fig. 5.2(c), trapped atoms are aproximately free to move along the axis of the device (see Chap. 6). Their coupling rates are thus modulated by the fast oscillation of

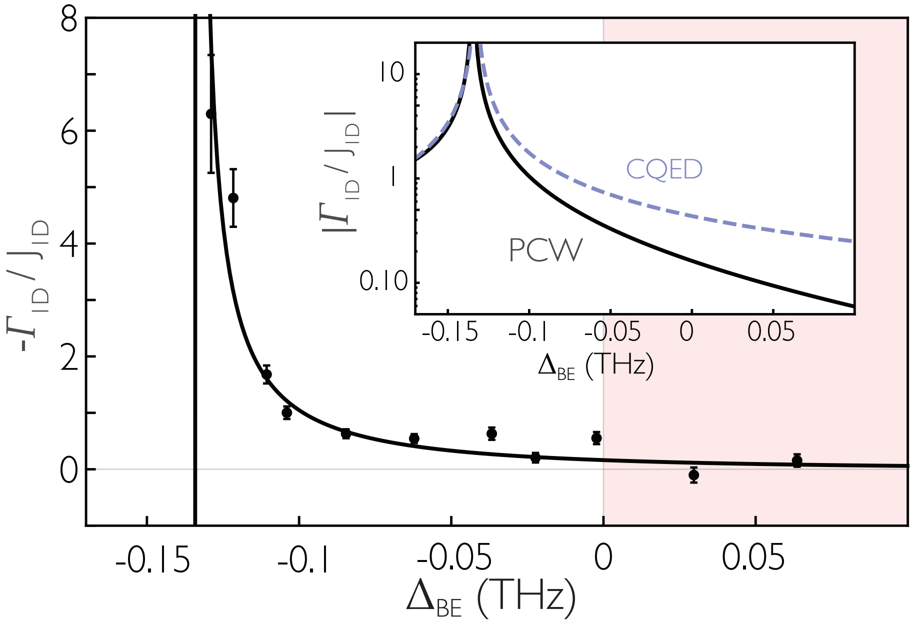

Figure 5.6: **(b)** The measured and calculated ratios $\mathcal{R} = \Gamma_{1D}/J_{1D}$. The average of the two points in the bandgap gives that the ratio of the dissipative to coherent coupling rate is $\mathcal{R} = 0.05 \pm 0.17$. The inset is a comparison of $\mathcal{R}$ for the PCW calculation (solid) and CQED model (dashed). From the measured linewidth of the first cavity resonance, $\gamma_c = 60 \pm 8$ GHz, CQED predicts that $\mathcal{R}_{CQED} = \gamma_c/\Delta_c$, where $\Delta_c = (\nu_p - \nu_1)$. Note that $-J_{1D}$ is plotted in the figure to more readily compare Γ_{1D} and J_{1D} as the band edge is approached. Figure adapted from [42].

the Bloch function, which near the band edge is approximately given by (6.11), $\Gamma_{1D}^{ii}(x_i) = \Gamma_{1D}\cos^2(x_i\pi/a)$ and $J_{1D}^{ii}(x_i) = J_{1D}\cos^2(x_i\pi/a)$. Here Γ_{1D} and J_{1D} are the peak values. Further, although we know the average atom number $\bar{N} = 3 \pm 0.5$ atoms from independent decay-rate measurements (see Chap. 6), the atom number for each experiment follows an unknown distribution. To model the experimental transmission spectra such as in Fig. 5.4, we average the expression in (5.4) over the atom positions $\{x_i\}$ along the Bloch function and assume a Poisson distribution $P_{\bar{N}}(N)$ for the atom number N. We extract peak values Γ_{1D} and J_{1D}, and plot the resulting cooperative rates $\bar{N}\Gamma_{1D}$ and $\bar{N}J_{1D}$ in Fig. 5.5. In particular, at the first resonance ν_1, the fitted single atom guided-mode decay rate is $\Gamma_{1D} = (1.4 \pm 0.2)\,\Gamma_0$, which is in good agreement with the decay time measurements, $\Gamma_{1D} = (1.5 \pm 0.2)\,\Gamma_0$ (see Chap. 6). More generally, we find good agreement between our measurements and our model for the transmission, as shown in Fig. 5.4.

The ratio $\mathcal{R} = \Gamma_{1D}/J_{1D}$ is shown in Fig. 5.6. Because of the evanescent nature of the field in the bandgap, $\mathcal{R}$ decays exponentially with increasing detuning into the bandgap, $\mathcal{R} \sim e^{-\kappa_x L}$, where $\kappa_x \propto \sqrt{\Delta_{\mathrm{BE}}}$ [41]. As displayed in the inset, the ratio between the frequency shift and the GM decay rate diminishes much faster than would be the case in traditional settings such as CQED, for which $\mathcal{R}_{\mathrm{CQED}} = \gamma_{\mathrm{c}}/\Delta_{\mathrm{c}}$, where γ_{c} is the cavity linewidth and Δ_{c} is the detuning from the cavity resonance. Indeed, by performing an average of the last two measured frequencies in the bandgap, we obtain $\mathcal{R} = 0.05 \pm 0.17$, whereas $\mathcal{R}_{\mathrm{CQED}} = 0.30 \pm 0.04$, where we have taken the cavity linewidth to be a value consistent with the linewidth of the first cavity mode of the PCW ($\gamma_{\mathrm{c}} = 60 \pm 8$ GHz). We can then infer that the ratio of dispersive to dissipative rates for guided mode atom-atom interactions (i.e., $1/\mathcal{R}$) is significantly larger than is the case in conventional optical physics (e.g., CQED).

Beyond the detailed modeling involving (5.4) averaged over fluctuations in atom number and position, we also fit the spectra with a generic transmission model with no averaging, as shown in Chap. 6. We find that the effective values for the guided mode decay rate and frequency shift are related to $\bar{N}\Gamma_{\mathrm{1D}}$ and $\bar{N}J_{\mathrm{1D}}$ in Fig. 5.5 by a simple scale factor related to the averaging of the Bloch function $\cos^2(\pi x/a)$.

Despite favorable scaling between the collective frequency shifts and the guided mode decay rates, there is still one obstacle to overcome towards purely dispersive atomic interactions, namely atomic emission into non-guided modes (characterized by Γ'). For the current PCW structure, the FDTD simulated value of this decay rate is $\Gamma' \simeq 1.1\,\Gamma_0$ [37] for the relevant frequencies of our experiment. Fortunately, it has been shown that suitable engineering of a wide variety of nanophotonic structures can lead to significant reductions in Γ'/Γ_0 [35]. For example, Ref. [28] reviews possibilities to achieve $\Gamma' \simeq 0.1\Gamma_0$.

5.5 Concluding remarks and outlook

In conclusion, we report the first observation of cooperative atom interactions in the bandgap of a photonic crystal waveguide. By tuning the band edge frequency of the photonic crystal waveguide, we are able to modify the interactions between the atoms that are trapped close to the device, reducing the dissipative relative to coherent coupling for frequencies inside the bandgap of the PCW. Equipped with a theoretical model based on the electromagnetic Green's function of the alligator photonic crystal waveguide, we infer quantitative values for the collective frequency shifts and decay rates experienced by the atoms. Moreover, we infer a suppression of the dissipative interactions with respect to the coherent ones several times larger than is customarily obtained in AMO physics. This measurement provides the first stepping stone towards the realization of quantum many body physics in bandgap systems.

Moreover, near-term extensions of our experiment open the door to exploring new physical scenarios by employing atoms coupled to PCWs. By trapping the atoms at the center of the device with guided modes [35], we expect a 6-fold increase to both coupling strengths J_{1D} and Γ_{1D} relative to Γ'. Moreover, by probing the atoms with the Cs D_2 line tuned to the upper band edge, where the intensity at the position of the atoms is larger, we expect a further improvement by a factor of two. Combining these two effects, we expect a significant enhancement of interactions via guided modes as compared to conventional free space interactions, namely $J_{\text{1D}}, \Gamma_{\text{1D}} > 10 \times \Gamma'$. This could enable investigations of new paradigms for atom-photon interactions, such as the recently proposed multi-photon dressed states [114, 115].

Chapter 6

DETAILS OF THE EXPERIMENT

In our results in Chapter 5, we measure collective frequency shifts and decay rates for atoms trapped near a photonic crystal waveguide (PCW). In our previous work in Ref. [37], we trapped multiple atoms in an optical dipole-force trap above the PCW. We operated with the atomic frequency outside the bandgap in a regime with large decay rate $\Gamma_{\rm 1D}$ and small coherent coupling rate $J_{\rm 1D}$. By varying the density and observing the superradiant decay of the atoms $\Gamma_{\rm tot}^{(\bar{N})} = \Gamma_{\rm SR}(\bar{N}) + \Gamma_{\rm 1D} + \Gamma'$, we inferred the single-atom guided-mode decay rate $\Gamma_{\rm 1D}$ and the average number of atoms $\bar{N}$. Importantly, this measured single-atom decay rate $\Gamma_{\rm 1D}$ agreed well with the finite-difference time-domain (FDTD) simulations at the calculated trap location. This good agreement is in part due to the nanometer-scale accuracy in which the alligator PCWs are fabricated, which is required for both the band-edge alignment and the device quality.

For Chapter 5, the band-edge of the PCW is tuned around the resonance frequency of the atoms, and we observe the dominance of the guided-mode coherent coupling rates $J_{\rm 1D}$ over the dissipative coupling rates $\Gamma_{\rm 1D}$, which is associated with atomic radiative processes for operation within the bandgap. To extract quantitative values for these parameters from our measurements of transmission spectra for atoms trapped along a PCW, we have developed theoretical techniques based upon Green's functions for the PCW, which are new to atomic physics. As in Ref. [37], the average number of atoms $\bar{N}$ is measured by way of transient decay. Our principal finding relates to the turning-off of the guided-mode decay rate $\Gamma_{\rm 1D}$, which in the bandgap is predicted to be exponentially suppressed, while nonetheless, retaining appreciable coherent processes described by $J_{\rm 1D}$.

For the spectra in Chapter 5, the transmission through the device decreases exponentially in the bandgap, and more time is required to measure the transmission spectra as compared to our work in Ref. [37]. Unfortunately, cesium slowly coats the PCW during the measurement, both degrading the device quality and shifting the band-edge out of the thermal tuning range. As a result, each device only has a limited lifetime for making transmission measurements. For our current experiment, we first repeated superradiance measurements outside the bandgap at the first resonance ν_1 of the PCW in order to determine the average number of atoms $\bar{N}$ and the single-atom guided-mode decay rate Γ_{1D}, and to show that the atoms behave as a collective emitter. Then, with an average number of $\bar{N} \simeq 3$, we measured transmission spectra as the atomic frequency is shifted into the bandgap. We simultaneously measured the TM spectra to verify that the atom number is constant over the course of the measurements of the TE spectra.

6.1 Alligator photonic crystal waveguide design and fabrication

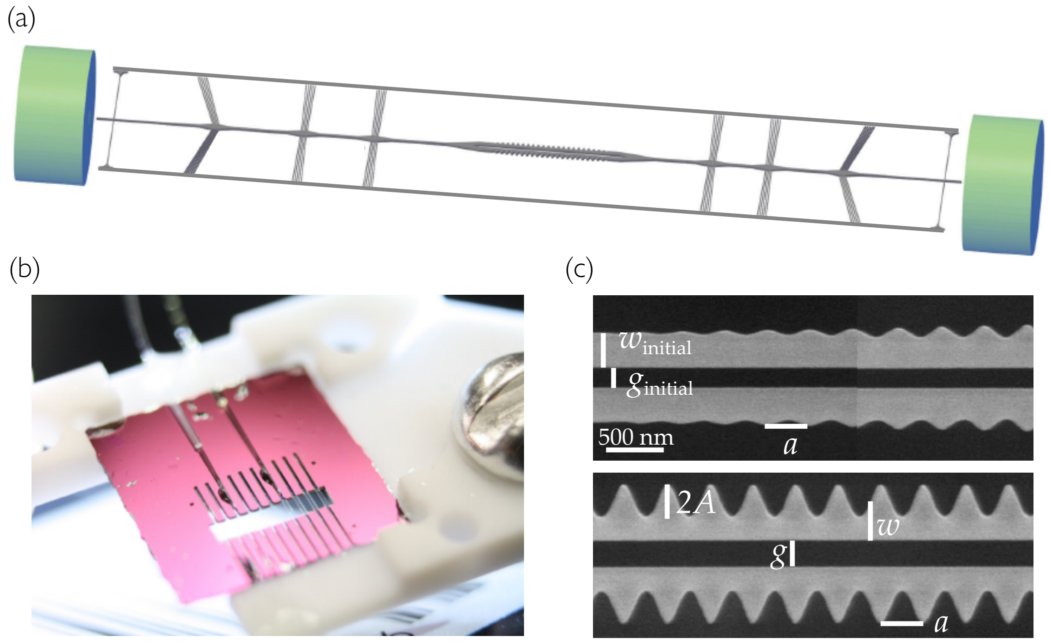

Figure 6.1: Alligator photonic crystal waveguide (PCW) chip and device overview, taken from Ref. [36]. **(a)** Schematic of the entire device. The alligator photonic crystal waveguide (PCW) is at the center. Optical fibers (green) on both ends couple light into and out of the waveguide. The waveguide is surrounded by supporting and cooling structures. **(b)** Image of a 10 × 10 mm PCW chip, taken from Ref. [36]. Multiple waveguides stretch across the window of the chip, with the PCWs at the center of the window. The window provides optical access for trapping and cooling atoms around the device. **(c)** Overview of device variables. The lattice constant for the entire device is $a = 370$ nm. The device dimensions are measured with an SEM and are calibrated to the lattice constant. The device dimensions are $w = 310 \pm 10$ nm, $2A = 262 \pm 10$ nm, $g = 220 \pm 10$ nm, $w_{\text{initial}} = 268 \pm 15$ nm, $g_{\text{initial}} = 165 \pm 10$ nm. The thickness of the silicon nitride is 185 ± 5 nm. The index of refraction for Si_3N_4 is $n = 2.0$ around our frequencies of interest. Figure adapted from [42].

The schematic of the device is shown in Fig. 6.1(a). Light is coupled into and out of the device by mode-matching the output of an optical fiber to that of a terminated rectangular-shaped waveguide on both sides of the device [36]. The fibers are glued permanently in etched v-grooves at optimized coupling positions. The design and fabrication of the alligator photonic crystal waveguide (PCW) are detailed in Ref. [36]. The PCW is fabricated on a 200 μm silicon (Si) chip coated with a 200 nm thick silicon nitride (SiN) film. The SiN device is suspended across a 2-mm-wide window after the silicon substrate beneath it is removed, as shown in the image of Fig. 6.1(b). The window allows optical access for the trapping and cooling of atoms around the device.

The dielectric TE mode band edge (ν_{BE}) is aligned to within 200 GHz of the Cs D1 line ($\nu_{\mathrm{D1}} = 335.12$ THz) via a low-power inductively-coupled reactive-ion CF_4 etch. The directional etch thins the SiN layer at a rate of 3 nm/min until a transmission measurement confirms alignment of the band edge. The final geometric dimensions of the device used in Chapter 5 are given in Fig. 6.1(c).

For the experiment, the chip is placed at the center of a ultra-high vacuum chamber, and the optical fibers exit through Teflon fiber feed-throughs. We measure the transmission through a device using a super luminescent diode (SLD) as the source and an optical spectrum analyzer (OSA) as the detector. The measured transmission and reflection spectra are shown in Fig. 6.2(a). The transmission spectra near the lower (dielectric) and upper (air) band edge are compared to an FDTD simulation in Fig. 6.2(b-c).

6.2 Alligator dispersion relation from scattering images

Here, we describe the analysis performed for the PCW dispersion relations in Fig. 6.2(e) of the manuscript. We send a single-frequency laser beam through the device and image the scattered light with a microscope. We integrate the image over the width of the PCW to produce a single plot of intensity versus position. Then we scan the laser frequency around the lower band edge to produce a 2D plot of scattered intensity as a function of position x along the device and frequency ν of the input light.

The weak scattered light comes from small fabrication imperfections or intrinsic material defects and serves as a probe of the local intensity. Since each scatterer emits light at a different rate, we have to normalize the scattered light by a reference intensity spectrum in which the intensity of the device is known. For this reference spectrum, we average over the intensities for frequencies far from the band edge, where the PCW behaves like a waveguide, and where the local intensity in the

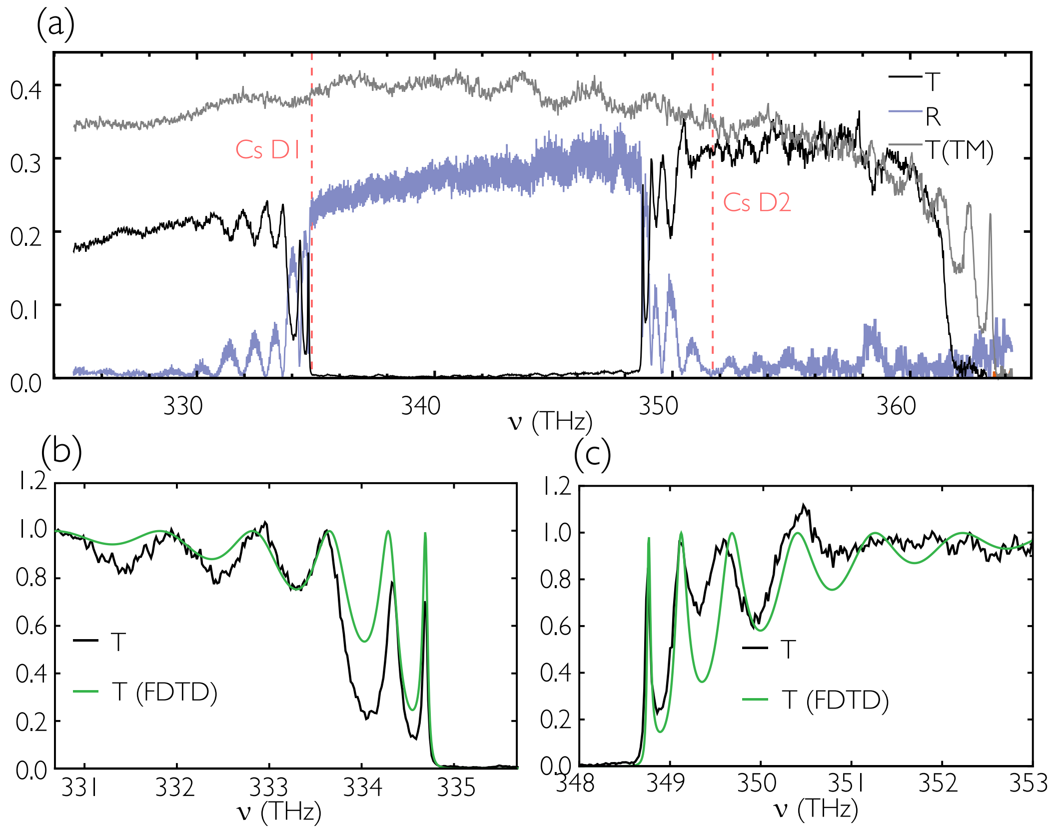

Figure 6.2: Measured and simulated transmission and reflection spectra. **(a)** Transmission (black) and reflection (blue) spectra through the entire chip for the TE mode (polarization in the plane of the device). The red dashed lines are the Cs D_1 (335.1 THz) and D_2 (351.7 THz) lines. The TE transmission efficiency through the entire device near the dielectric band edge is $\sim 23\%$, indicating that the single pass efficiency from the fiber to device is approximately 49%. Most of the loss is due to the waveguide-to-fiber coupling section. The gray line is the TM transmission (polarization perpendicular to the plane of the device). Note that the lower band edge of the TM mode is visible at around 365 THz, but is far detuned from both Cs $D_{1,2}$ transitions. **(b-c)** TE transmission data is normalized and compared to a finite-difference time-domain (FDTD) simulation [54]. The simulation uses the measured device parameters in Fig. 6.1, but adjusted within the uncertainty of the measurements so that the position of the first resonances match those in the measured spectra. Figure adapted from [42].

device is approximately constant. The normalized data is shown in Fig. 6.3, and a zoomed-in version is in Fig. 5.2(a) of the manuscript.

In the FDTD simulation described above, we calculate the intensity along the center of the device for frequencies around the band edge. Taking the maximum intensity in each unit cell and normalizing by the intensity in the waveguide regime, we

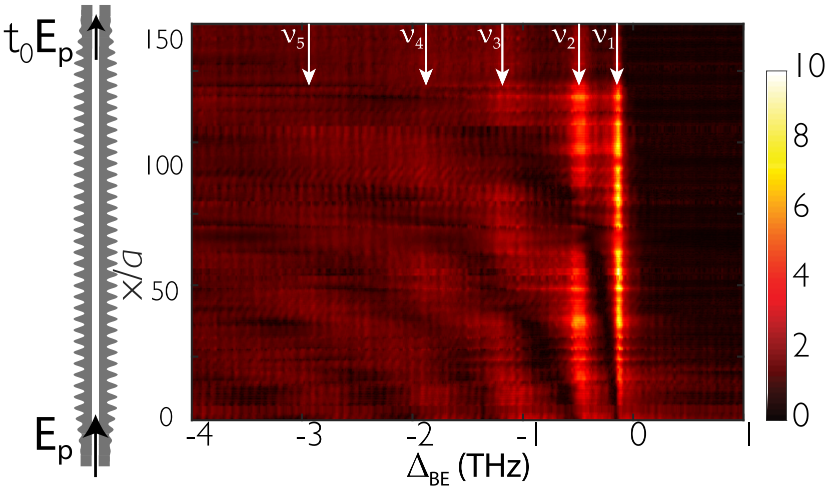

Figure 6.3: Normalized magnitude of the scattered electric field of the PCW for frequencies $\Delta_{\mathrm{BE}} = \nu_p - \nu_{\mathrm{BE}}$ around the band edge. The schematic on the left shows the PCW with the number of unit cells reduced by 5. Figure adapted from [42].

produce Fig. 5.2(b) in the Chapter 5.

Next, we fit the intensity spectrum at a given frequency to a model in order to extract the wave-vector for that frequency. Near the band edge, the field in an infinite PCW is well approximated by $E(x) \propto \cos(x\pi/a)e^{\mathrm{i}\delta k_x x}$, where $\delta k_x = \pi/a - k_x$ in the propagating band ($\Delta_{\mathrm{BE}} < 0$) and $\delta k_x = \mathrm{i}\kappa_x$ inside the bandgap ($\Delta_{\mathrm{BE}} > 0$) The edges of a finite photonic crystal reflect with R_t due to a large group index mismatch between the waveguide section and the photonic crystal waveguide. The resonances of the weak cavity result in the cavity-like intensity profiles seen at frequencies $\nu_{1,2,3,4,5}$ in Fig. 6.3. The intensity at a point x along a finite photonic crystal of length L is well approximated by a model based on the intensity in a cavity with two mirrors of reflectivity R_{t}

$$|E(x)|^2 = I_1\,|e^{\mathrm{i}\delta k_x x} - R_{\mathrm{t}}e^{2\mathrm{i}\delta k_x L}e^{-\mathrm{i}\delta k_x x}|^2, \tag{6.1}$$

where I_1 is related to the overall intensity. This expression ignores the fast oscillations of the Bloch function, which go as $\cos^2(x\pi/a)$. Note that in the bandgap (when $\kappa_x L \gg 1$), the intensity model reduces to an exponential decay: $|E(x)|^2 \approx I_1\, e^{-2\kappa_x x}$. Interestingly, at the band edge ($\delta k_x \longrightarrow 0$, $R_t \longrightarrow 1$), the intensity displays a quadratic dependence on the position, $|E(x)|^2 \propto (L - x)^2$.

For each frequency, we fit the intensity along the nominal cells with (6.1) and extract δk_x. This procedure allows us to map out the dispersion relation $\delta k_x(\Delta_{\mathrm{BE}})$, which we show in Fig. 5.3(e) for the measured and simulated data. From the simulated fits, we find that the effective length of the cavity is 162 cells, which is slightly longer than the 150 nominal cells. This is expected since the cavity field can leak into the tapering sections. We use this length for the fits of the measured data. Examples of the measured and simulated intensity are shown in Fig. 6.4. The fluctuation of the intensity, even after the normalization, is most likely due to the spatial profile of Bloch mode. The normalization trace is taken by averaging data for excitation frequencies further away from the band-edge where the Bloch mode contrast is reduced, whereas the data closer to the band-edge has a large Bloch mode fringe visibility. However, the fluctuations do not affect the statistical fits at the level of accuracy required for the dispersion relation in our current work.

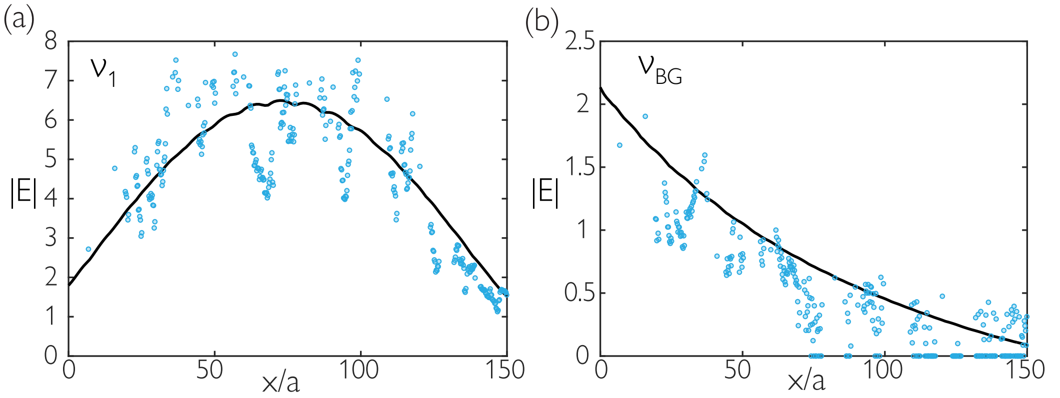

Figure 6.4: The electric field magnitude in the PCW at the first resonance ν_1 **(a)**, and in the bandgap $\nu_{\mathrm{BG}} = \nu_{\mathrm{BE}} + 60$ GHz **(b)**. The points show measured data, and the black lines are from an FDTD simulation. The electric field magnitude $|E|$ is normalized by the electric field magnitude far from the band edge; thus, these plots gives the enhancement of $|E|$ over the waveguide regime. Figure adapted from [42].

The frequency for which $\delta k_x = 0$ is defined as the band edge frequency ν_{BE}. To extract this frequency and the curvature of the dispersion relation near the band edge, we fit the measured and simulated dispersion relations with a dispersion model [37],

$$\delta k_x(\nu) = \frac{2\pi}{a}\sqrt{\frac{(\nu_{\mathrm{BE2}} - \nu)(\nu_{\mathrm{BE}} - \nu)}{4\zeta^2 - (\nu_{\mathrm{BE2}} - \nu_{\mathrm{BE}})^2}}, \tag{6.2}$$

where ν_{BE} (ν_{BE2}) is the lower (upper) band edge frequency, and ζ is a frequency related to the curvature of the band near the band edge. From the measured data fits, the distance between the first resonance and band edge is $\nu_{\mathrm{BE}} - \nu_1 = 133 \pm 9$ GHz and $\zeta = 227 \pm 3$ THz. The simulated data give $\nu_{\mathrm{BE}} - \nu_1 = 135.0$ GHz and the curvature parameter is $\zeta = 226.0$ THz. These values are in good agreement with the dispersion relation from the eigenmode simulation of the infinite PCW in Fig. 1(c) of the Chapter 5, which gives $\zeta = 229.1$ THz.

6.3 Side-illumination trap

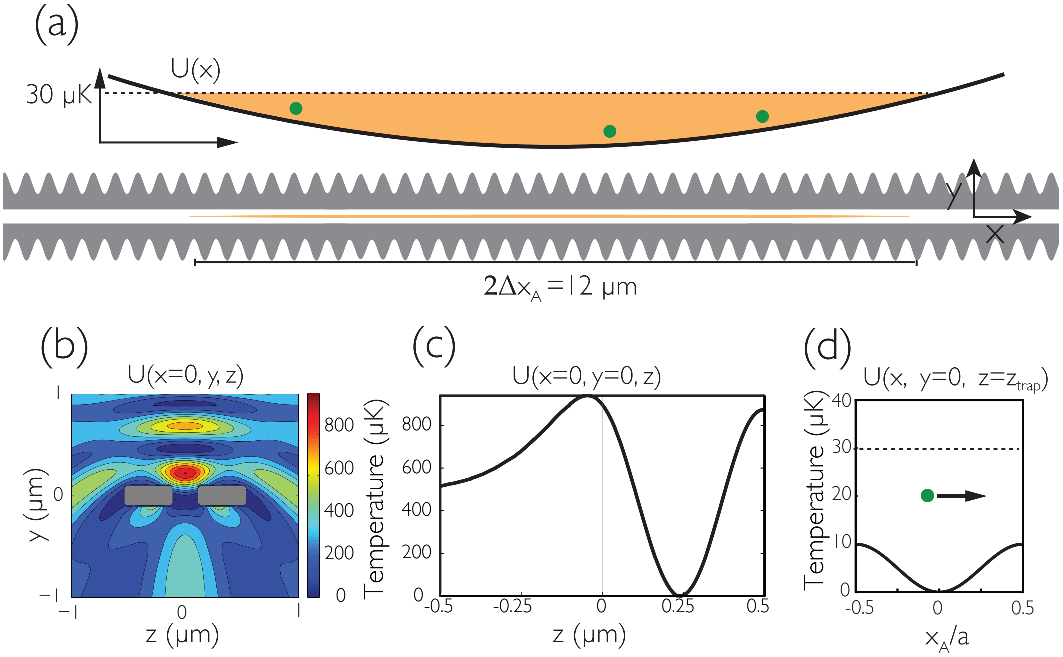

Figure 6.5: **(a)** Schematic of the atoms in the side-illumination (SI) trap. Given the estimated atom temperature of 30 μK, we infer that the atoms are confined to a length of $2\Delta x_A = 12$ μm along the x-axis. **(b,c,d)** FORT potentials for the SI trap simulation (b) in the y-z plane [37], (c) along the z-axis, and (d) along the x-axis. Figure adapted from [42].

In Fig. 6.5(a), we show a schematic of the side-illumination (SI) trap. The side-illumination beam is nearly perpendicular to the axis of the device, has a 50 μm diameter, and has a polarization aligned to the axis of the device. The orange areas represent the approximate localization of the atoms along x, y. By time-of-flight measurements of atoms in the dipole traps, we estimate an atomic 'temperature' of approximately 30 μK. From the beam waist and atom temperature, we can infer that the atoms are localized to $2\Delta x_A = 12$ μm along the x-axis.

Simulations of the FORT potential for the SI trap are shown in Fig. 6.5(b-d). The simulations are performed for the infinite structure with COMSOL. The trap depth is calibrated with the 12.5 MHz AC Stark shift measured from the atomic spectra. Figure 6.5(b) shows the trap potential in the y-z plane. Atoms that are significantly hotter than $\sim$ 100 μK are expected to crash into the device along the diagonal directions due to Casimir-Polder forces. Figure 6.5(c) shows the trapping potential along the z-axis. Atoms are trapped at $z = 240$ nm. Figure 6.5(d) shows the trap along the x-axis. Due to the photonic crystal, the trap modulates by $\sim$ 10 μK along the x-axis, but this is significantly smaller than the estimated trap temperature.

In addition to the results in Fig. 6.5, we have also carried out numerical modeling of the optical trap using Lumerical simulations [54] of the actual finite length PCW and tapers shown in Fig. 6.1. We have as well included Casimir-Polder potentials as in Ref. [35]. More details of the trap are discussed in Ref. [37].

6.4 Transmission model and atomic spectra fits

Here we give a more detailed description of the transmission model in the Chapter 5, which follows the derivation given in Ref. [44]. A system of N atoms coupled to a radiation field can be described using formalism based on the classical Green's function [82, 88]. In the Markovian limit, the field can be eliminated to obtain a master equation that describes the interactions between the atoms, $\dot{\hat{\rho}}_{\mathrm{A}} = -\frac{i}{\hbar}[H, \hat{\rho}_{\mathrm{A}}] + \mathcal{L}[\hat{\rho}_{\mathrm{A}}]$. Here the Hamiltonian H gives the coherent evolution of the system,

$$H = -\hbar \sum_{j=1}^{N} \tilde{\Delta}_{\mathrm{A}} \hat{\sigma}_j^z - \hbar \sum_{j,i=1}^{N} J_{\mathrm{1D}}^{ji} \hat{\sigma}_j^\dagger \hat{\sigma}_i - \hbar \sum_{j=1}^{N} \left(\Omega_j \hat{\sigma}_j^\dagger + \Omega_j^* \hat{\sigma}^j \right), \tag{6.3}$$

and the Lindblad operator $\mathcal{L}[\hat{\rho}_{\mathrm{A}}]$ gives the dissipation of the system,

$$\begin{aligned} \mathcal{L}[\rho_{\mathrm{A}}] = \sum_{j,i=1}^{N} & \frac{\Gamma' \delta_{ji} + \Gamma_{\mathrm{1D}}^{ji}}{2} \\ & \times \left(2\hat{\sigma}_j \hat{\rho}_{\mathrm{A}} \hat{\sigma}_i^\dagger - \hat{\sigma}_j^\dagger \hat{\sigma}_i \hat{\rho}_{\mathrm{A}} - \hat{\rho}_{\mathrm{A}} \hat{\sigma}_j^\dagger \hat{\sigma}_i \right). \end{aligned} \tag{6.4}$$

The Hamiltonian and Lindblad are expressed in terms of the atomic coherence operator $\hat{\sigma}^j = |g\rangle\langle e|$ between the ground and excited states of atom j. The Hamiltonian contains terms for the free-atom evolution, the coherent atom-atom interactions, and the classical drive, respectively. $\tilde{\Delta}_{\mathrm{A}} = 2\pi\Delta_{\mathrm{A}} = 2\pi(\nu_{\mathrm{p}} - \nu_{\mathrm{D1}})$ is the detuning between the probe and the atomic angular frequencies. Ω_j is the Rabi frequency for atom j due to the guided-mode field. The atom-atom spin-exchange rate J_{1D}^{ji} is expressed in terms of the real part of the guided mode Green's function as

$$J_{\mathrm{1D}}^{ji} = (\mu_0 \omega_{\mathrm{p}}^2/\hbar)\, \mathbf{d}_j^* \cdot \mathrm{Re}\, \mathbf{G}(\mathbf{r}_j, \mathbf{r}_i, \omega_{\mathrm{p}}) \cdot \mathbf{d}_i, \tag{6.5}$$

where $\omega_{\mathrm{p}} = 2\pi\nu_{\mathrm{p}}$ and $\mathbf{d}_j$ is the dipole matrix element of atom j. The Lindblad term is responsible for the dissipative interactions in the system, which include atomic decay into non-guided (Γ') and guided ($\Gamma_{\mathrm{1D}}^{ji}$) modes. The decay rate into the guided mode is written in terms of the imaginary part of the Green's function as

$$\Gamma_{\mathrm{1D}}^{ji} = 2(\mu_0 \omega_{\mathrm{p}}^2/\hbar)\, \mathbf{d}_j^* \cdot \mathrm{Im}\, \mathbf{G}(\mathbf{r}_j, \mathbf{r}_i, \omega_{\mathrm{p}}) \cdot \mathbf{d}_i. \tag{6.6}$$

For low atomic density along the PCW, the non-guided emission rate Γ' is not cooperative, and is described here as a single-atom effect, with δ_{ji} as the Kronecker delta.

In the low saturation regime, the Heisenberg equations for the expectation value of the atomic coherences ($\langle\hat{\sigma}_{eg}\rangle = \sigma_{eg}$) can be solved for with the master equation leading to

$$\dot{\sigma}^j = \mathrm{i}\left(\tilde{\Delta}_{\mathrm{A}} + \mathrm{i}\frac{\Gamma'}{2}\right)\hat{\sigma}_j + \mathrm{i}\,\Omega_j + \mathrm{i}\sum_{i=1}^{N} g_{ji}\,\hat{\sigma}_i, \tag{6.7}$$

where the complex coupling rate is

$$g_{ij} = J_{\mathrm{1D}}^{ij} + \mathrm{i}\Gamma_{\mathrm{1D}}^{ij}/2 = (\mu_0\omega_{\mathrm{p}}^2/\hbar)\,\mathbf{d}_i^* \cdot \mathbf{G}(\mathbf{r}_i, \mathbf{r}_j, \omega_{\mathrm{p}}) \cdot \mathbf{d}_j, \tag{6.8}$$

which is the Green's function between atoms i and j projected onto the respective dipole matrix elements. In the steady-state solution, the time derivative is set to zero and result is the linear system of equations for the atomic coherences given in Chapter 5.

The electric field in the system can be expressed in terms of the input probe field $\mathbf{E}^+(\mathbf{r}, \omega_p)$ and solutions for the atomic coherences [44],

$$\mathbf{E}^+(\mathbf{r}, \omega_{\mathrm{p}}) = \mathbf{E}_{\mathrm{p}}^+(\mathbf{r}, \omega_{\mathrm{p}}) + \mu_0\omega_{\mathrm{p}}^2 \sum_j \mathbf{G}(\mathbf{r}, \mathbf{r}_j, \omega_{\mathrm{p}}) \cdot \mathbf{d}_j \sigma^j. \tag{6.9}$$

An expression for the transmission through a quasi-1D structure can be derived by solving the steady state system of equations in (6.7) for the atomic coherences σ^j and substituting them into (6.9). The expression can then be simplified in the case where the dipole moments are real, in which case $\mathfrak{g}$ is a complex symmetric matrix with eigenvectors and eigenvalues $\mathfrak{g}\,\mathbf{u}_\xi = \lambda_\xi\,\mathbf{u}_\xi$, and when the Green's function is well represented by a 1D Green's function. The final result is [44],

$$\frac{t(\tilde{\Delta}_A, N)}{t_0(\tilde{\Delta}_A)} = \prod_{\xi=1}^{N}\left(\frac{\tilde{\Delta}_A + \mathrm{i}\Gamma'/2}{\tilde{\Delta}_A + \mathrm{i}\Gamma'/2 + \lambda_\xi}\right), \tag{6.10}$$

where $t_0(\tilde{\Delta}_A)$ is the transmission without atoms.

In the bandgap, the matrix $\mathfrak{g}$ of elements g_{ij} is well approximated by

$$g_{ij} = (J_{\mathrm{1D}} + \mathrm{i}\Gamma_{\mathrm{1D}}/2)\cos(\pi x_i/a)\cos(\pi x_j/a)e^{-\kappa_x|x_i - x_j|}. \tag{6.11}$$

As discussed in Chapter 5, when the interaction range $1/\kappa_x$ is much larger than the separation distance ($\kappa_x|x_i - x_j| \ll 1$), there is only a single atomic 'bright mode', for which the frequency shift and guided-mode decay rate are given by $\sum_{i=1}^{N} J^{ii}_{1\mathrm{D}}$ and $\sum_{i=1}^{N} \Gamma^{ii}_{1\mathrm{D}}$. The transmission spectra for N atoms in the 'single-bright-mode' approximation is given by

$$T(\Delta_{\mathrm{A}}, N) = T_0(\Delta_{\mathrm{A}}) \left| \frac{\tilde{\Delta}_{\mathrm{A}} + \mathrm{i}\Gamma'/2}{\tilde{\Delta}_{\mathrm{A}} + \mathrm{i}\Gamma'/2 + \sum_i (J^{ii}_{1\mathrm{D}} + \mathrm{i}\Gamma^{ii}_{1\mathrm{D}}/2)} \right|^2, \tag{6.12}$$

where $\tilde{\Delta}_{\mathrm{A}} = 2\pi\Delta_{\mathrm{A}} = 2\pi(\nu_p - \nu_{D1})$ is the detuning between the pump and the atomic frequency, and $T_0(\Delta_{\mathrm{A}})$ is the device transmission when no atoms are present.

Explicitly accounting for the atoms' positions by substituting (6.11) into (6.12), the transmission is given by

$$\begin{aligned} &T(\Delta_{\mathrm{A}}, N; x_1, ..., x_N)/T_0(\Delta_{\mathrm{A}}) = \\ &\left| \frac{\Delta'_{\mathrm{A}} + \mathrm{i}\Gamma'/2}{\Delta'_{\mathrm{A}} + \mathrm{i}\Gamma'/2 + \sum_{j=1}^{N} (J_{1\mathrm{D}} + \mathrm{i}\Gamma_{1\mathrm{D}}/2)\cos^2(x_j\pi/a)} \right|^2 . \end{aligned} \tag{6.13}$$

We have defined $\Delta'_{\mathrm{A}} \equiv \tilde{\Delta}_{\mathrm{A}} + \Delta_0$ in order to account for the AC-Stark shift Δ_0 of the atoms due to the dipole trap.

In order to accurately model the experimental conditions, we average the transmission model over atom positions and atom number. During a single measurement, the atoms are free to move along the length of the device over the range $2\Delta x_A$ as in Fig. 6.5(a), evenly sampling the Bloch function. We let $\langle T(\Delta_{\mathrm{A}}, N; x_1, ..., x_N)\rangle_x$ be an average over all positions, i.e.,

$$\begin{aligned} &\langle T(\Delta_{\mathrm{A}}, N; x_1, ..., x_N)\rangle_x = T_0(\Delta_{\mathrm{A}}) \\ &\times \int_0^a \mathrm{d}x_1 ... \mathrm{d}x_N \left| \frac{\Delta'_{\mathrm{A}} + \mathrm{i}\Gamma'/2}{\Delta'_{\mathrm{A}} + \mathrm{i}\Gamma'/2 + \sum_{j=1}^{N} (J_{1\mathrm{D}} + \mathrm{i}\Gamma_{1\mathrm{D}}/2)\cos^2(x_j\pi/a)} \right|^2 . \end{aligned} \tag{6.14}$$

We repeat the measurement multiple times for each frequency Δ_{A}. Each experiment can have a different number of atoms, and so we average the transmission expression over a Poisson distribution $P_{\bar{N}}(N)$, which is a function of the average atom number $\bar{N}$. The transmission model averaged over both atom positions and atom numbers is given by

$$\begin{aligned} &\langle T(\Delta_{\mathrm{A}}, N; x_1, ..., x_N)\rangle_{x,N} = \\ &T_0(\Delta_{\mathrm{A}}) \sum_N P_{\bar{N}}(N)\ \langle T(\Delta_{\mathrm{A}}, N; x_1, ..., x_N)\rangle_x . \end{aligned} \tag{6.15}$$

This is the final form of the transmission model that we use to fit the atomic spectra.

Assuming $\bar{N} = 3.0$, which is obtained from the atom decay rate measurement, we fit the TE atomic spectra with (6.15) and extract Γ_{1D}, J_{1D}, Γ', and Δ_0 for each frequency. We show the values of Γ_{1D} and J_{1D} in Fig. 5.5 of Chapter 5. We show the AC Stark shift and non-guided decay rate in Fig. 6.6.

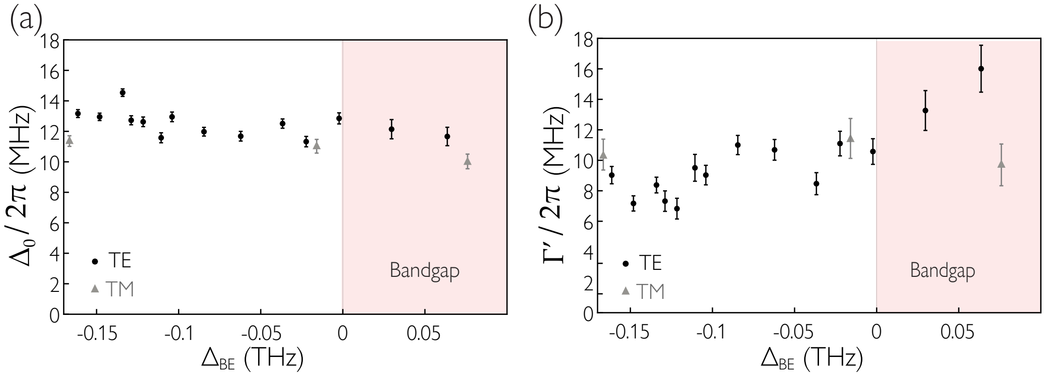

Figure 6.6: Fitted values from averaged transmission model for TE (black, circles) and TM (gray, triangles) spectra. **(a)** Fitted AC Stark shift Δ_0. **(b)** Fitted Γ'. Figure adapted from [42].

The average of the non-guided decay rate Γ' for the TE data outside the bandgap is $\Gamma' = 2\pi \times 9.1$ MHz. This is significantly larger than the expected value from the FDTD simulation, $\Gamma' = 2\pi \times 5.0$ MHz. This additional inhomogeneous broadening could be due to finite temperature of the trapped atoms, vector shifts from circular light in the SI beam, atom density dependent collisional broadening, stray magnetic fields, and electric fields from charges in the dielectric. We estimate the contributions individually, and find that they likely do not explain the extraneous broadening. We note that the estimate of 'temperature' of trapped atoms could be improved in the future, and it may help shed light on our excess broadening.

Interestingly, the fitted Γ' increases in the bandgap, and is as high as $\Gamma' = 2\pi \times 16$ MHz for the last measured point. One possible explanation is that this is due to the break-down of the single bright mode approximation, as coupling to multiple collective atomic modes should result in a broadened linewidth. Another possibility is since there is a large extinction of the TE mode in the bandgap, there might be some mixing between the TE and TM modes.

We also measure transmission spectra for the TM mode, whose band edges are far-detuned from the Cs transitions. The transmission in this waveguide regime is described by an optical density model

$$T/T_0 = \exp\left[\frac{-\mathrm{OD}}{1+\left(\frac{2\Delta'_\mathrm{A}}{\Gamma^{\mathrm{TM}}_{\mathrm{1D}}+\Gamma'}\right)^2}\right], \tag{6.16}$$

where the resonant optical density is given by $\mathrm{OD} = 2\bar{N}\Gamma^{\mathrm{TM}}_{\mathrm{1D}}/\tilde{\Gamma}'$. We fit the TM spectra with this model and extract Γ', Δ_0, and $\Gamma^{\mathrm{TM}}_{\mathrm{1D}}$ (assuming $\bar{N} = 3$). The values of Γ' and Δ_0 are shown with the TE data in Fig. 6.6. The averaged $\Gamma^{\mathrm{TM}}_{\mathrm{1D}}$ value is $0.044\,\Gamma_0$, which is ~ 30 times smaller than Γ_{1D} for the TE mode at the first resonance ν_1, and clearly demonstrates the enhanced interaction due to the PCW.

6.5 Simple transmission model

In Chapter 5, we fit atomic transmission spectra with the averaged transmission model from (6.15) in order to extract the peak guided-mode decay rate Γ_{1D} and frequency shift J_{1D}. In this section, we fit the spectra with a transmission model which involves no averaging, and we extract an effective decay rate $\Gamma^{\mathrm{eff}}_{\mathrm{1D}}$ and frequency shift $J^{\mathrm{eff}}_{\mathrm{1D}}$, which will be smaller than the corresponding peak values due to the averaging of the $\cos^2(\pi x/a)$ Bloch function as the atoms move along the x-axis of the trap. In the “single-bright-mode" approximation discussed in Chapter 5, the transmission for a single collective mode with total decay rate A and frequency shift B is given by

$$\frac{T(\Delta_\mathrm{A})}{T_0(\Delta_\mathrm{A})} = \left|\frac{\Delta'_\mathrm{A} + \mathrm{i}\Gamma'/2}{\Delta'_\mathrm{A} + B + \mathrm{i}(\Gamma' + A)/2}\right|^2. \tag{6.17}$$

Here, the detuning Δ'_A includes the AC stark shift $\Delta'_A = \Delta_A + \Delta_0$. Since the average number of atoms $\bar{N} \approx 3$ is measured independently in a decay rate measurement, the collective rates A and B are related to the effective rates by $A = \bar{N}\Gamma^{\mathrm{eff}}_{\mathrm{1D}}$ and $B = \bar{N}J^{\mathrm{eff}}_{\mathrm{1D}}$. Examples of the fitted spectra for atoms outside and inside the band-gap are shown in Fig. 6.7. The translucent lines are the expected signals for an average atom number of $\bar{N} = 1$ and $\bar{N} = 9$.

The fitted values of A and B are plotted for each detuning from the band-edge Δ_{BE} in Fig. 6.8(a). The results are qualitatively similar to the corresponding plot in Fig. 5.5 in the manuscript, except the effective rates $A = \bar{N}\Gamma^{\mathrm{eff}}_{\mathrm{1D}}$ and $B = \bar{N}\Gamma^{\mathrm{eff}}_{\mathrm{1D}}$ are scaled down by $\eta = 0.42$ due to the modulation of the Bloch function $\cos^2(\pi x/a)$. The solid line in Fig. 6.8(a) is the same theoretical curve as in Fig 4(a) except scaled by $\eta = 0.42$.

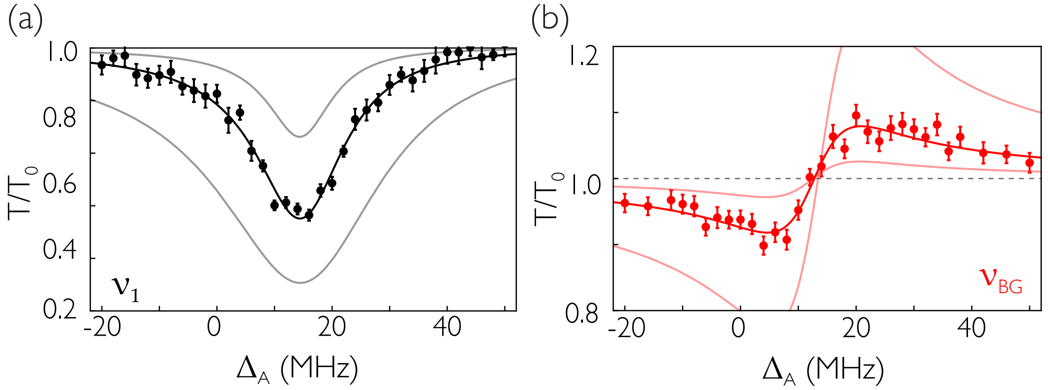

Figure 6.7: Fits of transmission spectra with model of (6.17) for when the atomic resonance frequency is aligned to the first resonance **(a)** and in the bandgap **(b)**. From the decay rate measurement, the average number of atoms is $\bar{N} \approx 3$, and the translucent curves give the expected spectra for $\bar{N} = 1$ and $\bar{N} = 9$ atoms. Figure adapted from [42].

The ratio of $A/B = \Gamma_{1D}^{\text{eff}}/J_{1D}^{\text{eff}}$ is plotted in Fig. 6.8(b). Since the scale factors η cancel, the result is in good agreement with the corresponding plot of $\mathcal{R} = \Gamma_{1D}/J_{1D}$ in Fig. 5.6 of Chapter 5. The black theory curve is the same as in the manuscript. Whereas the peak decay rate and frequency shift is sensitive to the specific model, the ratio of dissipative to coherent coupling is mostly model insensitive.

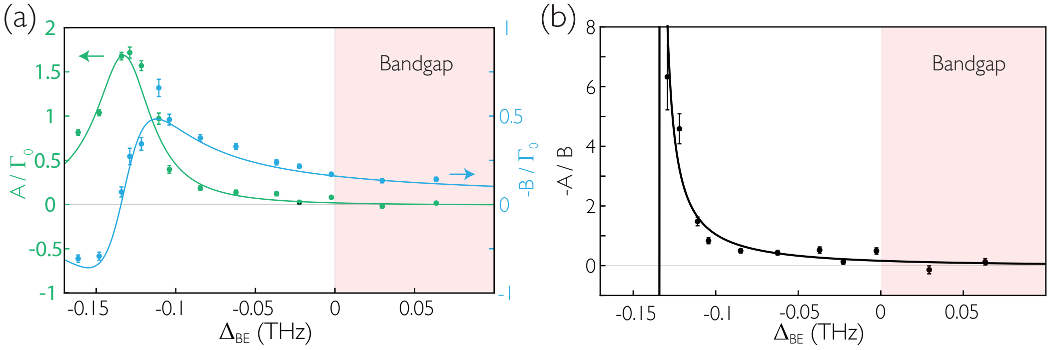

Figure 6.8: **(a)** Fitted values for the effective collective decay rates A and frequency shifts B for various detunings from the band-edge Δ_{BE}. The solid lines are the expected result for the peak values, except scaled down by $\eta = 0.42$. **(b)** Ratio $A/B = \Gamma_{1D}^{\text{eff}}/J_{1D}^{\text{eff}}$, along with the theoretical prediction for the peak ratio Γ_{1D}/J_{1D} from Fig. 5.6 of Chapter 5. Figure adapted from [42].

6.6 Atom decay measurement

We exploit the superradiance of atoms trapped near the alligator PCW to determine the mean atom number $\bar{N}$ and the peak atom decay rate Γ_{1D} (at ν_1) into the guided-modes.

As established in Ref. [37], the total exponential decay rates of the atoms is $\bar{\Gamma}_{\mathrm{tot}}(\bar{N}) = \bar{\Gamma}_{\mathrm{SR}}(\bar{N}) + \bar{\Gamma}^{(1)}_{\mathrm{tot}}$, where $\bar{\Gamma}_{\mathrm{SR}}$ is the $\bar{N}$-dependent superradiance decay rate, and $\bar{\Gamma}^{(1)}_{\mathrm{tot}}$ is the observed single-atom decay rate. We note that when $\bar{N} \ll 1$, $\bar{\Gamma}_{\mathrm{tot}} \sim \bar{\Gamma}^{(1)}_{\mathrm{tot}} = \bar{\Gamma}_{\mathrm{1D}} + \Gamma'$, since only the single-atom decay rate into GM $\bar{\Gamma}_{\mathrm{1D}}$ and into environment Γ' remain. Γ' is numerically calculated to be $2\pi \times 5.0$ MHz for cesium D_1 line at the trapping site near the PCW [37].

We excite the atoms with a weak resonant light pulse through the guided-mode, while the first resonance ν_1 near the band edge is aligned with cesium D_1 line. Pulse properties are as in Ref. [37]. The subsequent fluorescence decay rates $\bar{\Gamma}_{\mathrm{tot}}$ are determined through exponential fits. By varying the trap holding time t_{m} after loading, the mean atom numbers for the decay measurements are varied. The decay rates are empirically fitted in an exponential form as a function of holding time t_{m} [37]: $\bar{\Gamma}_{\mathrm{tot}}(t_{\mathrm{m}}) = \bar{\Gamma}_{\mathrm{SR}} e^{-t_{\mathrm{m}}/\tau_{\mathrm{SR}}} + \bar{\Gamma}^{(1)}_{\mathrm{tot}}$, as shown in Fig. 6.9. From the fitted asymptotic-value of the decay rates, we deduce that the apparent single-atom decay rate is $\bar{\Gamma}_{\mathrm{1D}} = (1.12 \pm 0.14)\Gamma'$.

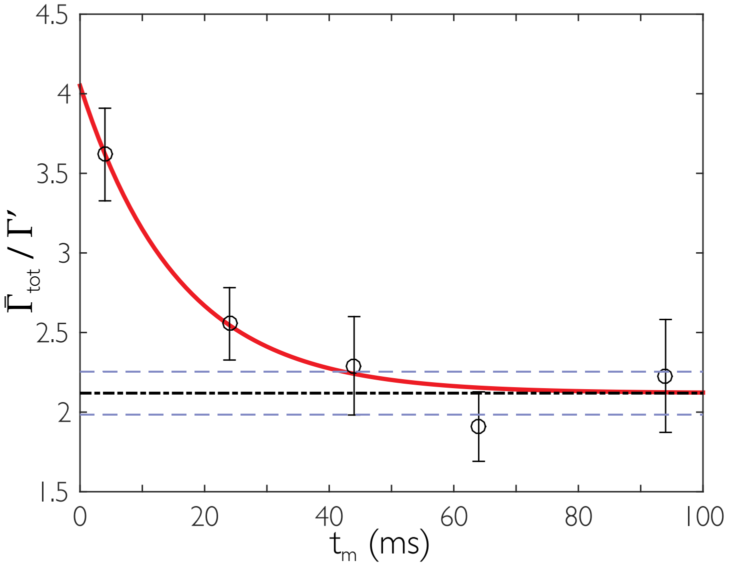

Figure 6.9: Total decay rates as a function of holding time t_{m}. The red solid curve is the empirical fit and the dash-dot line represents the fitted asymptotic total decay rate at very long times. The blue dashed lines specify fitted error boundaries. The fit yields $\tau_{\mathrm{SR}} = 16$ ms, $\bar{\Gamma}_{\mathrm{SR}} = 1.5\Gamma'$ and the asymptote $\bar{\Gamma}^{(1)}_{\mathrm{tot}}/\Gamma' = 2.12 \pm 0.14$. Figure adapted from [42].

Because the atoms are randomly distributed along x direction in the trap, the observed decay curves are results after spatial averaging the coupling rates $\Gamma_{\mathrm{1D}}(x)$.

Assuming an uniform distribution of N atoms around the center of the PCW, a more detailed model specifies the form of fluorescence intensity decay as [37]:

$$\begin{aligned}\mathcal{I}_N(t) = \gamma^2 e^{-(N\gamma+\Gamma')t} \cdot I_0\left(\gamma t\right)^{N-2} \cdot \Bigg[\frac{N(N+1)}{4} I_0\left(\gamma t\right)^2 \\ -\left(\frac{N}{4\gamma t}+\frac{N^2}{2}\right) I_0\left(\gamma t\right) I_1\left(\gamma t\right) + \frac{N(N-1)}{4} I_1\left(\gamma t\right)^2\Bigg],\end{aligned} \tag{6.18}$$

where $\gamma = \Gamma_{\mathrm{1D}}/2$, and I_k is the modified Bessel function. Numerically simulating the decay of single atoms in the trap by using $\mathcal{I}_1(t)$, we compare between the exponentially fitted value $\bar{\Gamma}_{\mathrm{1D}}$ and the value of Γ_{1D} used for $\mathcal{I}_1(t)$, which yields a ratio of $\bar{\Gamma}_{\mathrm{1D}}/\Gamma_{\mathrm{1D}} = 0.81$. This is consistent with the ratio of 0.8 ± 0.3 from measurement at long hold time $t_{\mathrm{m}} = 94$ ms, when single-atom decay predominates (shown as the asymptote in Fig. 6.9). Based on the values of $\bar{\Gamma}_{\mathrm{1D}}$ deduced above, we conclude that $\Gamma_{\mathrm{1D}} = (1.4 \pm 0.2)\Gamma'$.

At early holding times, the atom number N noticeably fluctuates around some mean values $\bar{N} \gtrsim 1$. To capture this $\bar{N}$-dependent variation, we fit the decay curves by averaging $\mathcal{I}_N(t)$ with weight function of Poisson distribution probability $P_{\bar{N}}(N)$ [37]. The fitting parameter here is $\bar{N}$, while we fix the value of Γ_{1D} in Eq. 6.18. The fit is consistent with $\bar{N} = 3.0 \pm 0.5$ at $t_{\mathrm{m}} = 4$ ms when we carry out the transmission spectra measurement. Based on the trap life time $\tau = 30$ ms, we further deduce that $\bar{N} \sim 0.1$ at $t_{\mathrm{m}} = 94$ ms .

The linear $\bar{N}$-dependence of superradiance is given by $\bar{\Gamma}_{\mathrm{SR}} = \eta \cdot \bar{N} \cdot \Gamma_{\mathrm{1D}}$, where $\eta = 0.36 \pm 0.06$ is some linear coefficient whose value is consistent with that reported in Ref. [37].

BIBLIOGRAPHY

[1] J. Vučković, and Y. Yamamoto, “Photonic crystal microcavities for cavity quantum electrodynamics with a single quantum dot”, Applied Physics Letters **82**, 2374–2376 (2003) `10.1063/1.1567824`.

[2] T. Yoshie, A. Scherer, J. Hendrickson, G. Khitrova, H. M. Gibbs, G. Rupper, C. Ell, O. B. Shchekin, and D. G. Deppe, “Vacuum Rabi splitting with a single quantum dot in a photonic crystal nanocavity”, Nature **432**, 9–12 (2004) `10.1038/nature02969.1.`, `http://www.ncbi.nlm.nih.gov/pubmed/15538363`.

[3] T. Aoki, B. Dayan, E. Wilcut, W. P. Bowen, A. S. Parkins, T. J. Kippenberg, K. J. Vahala, and H. J. Kimble, “Observation of Strong Coupling between One Atom and a Monolithic Microresonator”, Nature **1**, 1–6 (2006) `10.1038/nature05147`, `http://arxiv.org/abs/quant-ph/0606033%20http://www.ncbi.nlm.nih.gov/pubmed/17035998`.

[4] K. J. Hennessy, A. Badolato, M. Winger, D. Gerace, M. Atature, S. Gulde, S. Falt, E. L. Hu, and A. Imamoglu, “Quantum nature of a strongly coupled single quantum dot-cavity system.”, Nature **445**, 896–9 (2007) `10.1038/nature05586`, `http://www.ncbi.nlm.nih.gov/pubmed/17259971`.

[5] D. Hunger, T. Steinmetz, Y. Colombe, C. Deutsch, T. W. Hänsch, and J. Reichel, “A fiber Fabry-Perot cavity with high finesse”, New Journal of Physics **12** (2010).

[6] J. D. Thompson, T. G. Tiecke, N. P. de Leon, J. Feist, a. V. Akimov, M. Gullans, A. S. Zibrov, V. Vuletic, and M. D. Lukin, “Coupling a single trapped atom to a nanoscale optical cavity.”, Science (New York, N.Y.) **340**, 1202–5 (2013) `10.1126/science.1237125`, `http://www.ncbi.nlm.nih.gov/pubmed/23618764`.

[7] H. Paik, D. I. Schuster, L. S. Bishop, G. Kirchmair, G. Catelani, A. P. Sears, B. R. Johnson, M. J. Reagor, L. Frunzio, L. I. Glazman, S. M. Girvin, M. H. Devoret, and R. J. Schoelkopf, “Observation of high coherence in Josephson junction qubits measured in a three-dimensional circuit QED architecture”, Physical Review Letters **107**, 1–5 (2011) `10.1103/PhysRevLett.107.240501`.

[8] C. Rigetti, J. M. Gambetta, S. Poletto, B. L. T. Plourde, J. M. Chow, A. D. Córcoles, J. A. Smolin, S. T. Merkel, J. R. Rozen, G. A. Keefe, M. B. Rothwell, M. B. Ketchen, and M. Steffen, “Superconducting qubit in a waveguide cavity with a coherence time approaching 0.1 ms”, Physical Review B - Condensed Matter and Materials Physics **86**, 1–5 (2012) `10.1103/PhysRevB.86.100506`.

[9] M. Bajcsy, S. Hofferberth, V. Balic, T. Peyronel, M. Hafezi, A. S. Zibrov, V. Vuletic, and M. D. Lukin, “Efficient All-Optical Switching Using Slow Light within a Hollow Fiber”, Physical Review Letters **102**, 1–4 (2009) `10.1103/`

`PhysRevLett.102.203902`, `http://link.aps.org/doi/10.1103/PhysRevLett.102.203902`.

[10] V. I. Balykin, K. Hakuta, F. Le Kien, J. Q. Liang, and M. Morinaga, "Atom trapping and guiding with a subwavelength-diameter optical fiber", Physical Review A **70**, 2–5 (2004) `10.1103/PhysRevA.70.011401`, `http://link.aps.org/doi/10.1103/PhysRevA.70.011401`.

[11] P. Londero, V. Venkataraman, A. R. Bhagwat, A. D. Slepkov, and A. L. Gaeta, "Ultralow-power four-wave mixing with RB in a hollow-core photonic band-gap fiber", Physical Review Letters **103**, 1–4 (2009) `10.1103/PhysRevLett.103.043602`.

[12] E. Vetsch, D. H. Reitze, G. Sagué, R. Schmidt, S. T. Dawkins, and A. Rauschenbeutel, "Optical Interface Created by Laser-Cooled Atoms Trapped in the Evanescent Field Surrounding an Optical Nanofiber", Physical Review Letters **104**, 1–4 (2010) `10.1103/PhysRevLett.104.203603`, `http://link.aps.org/doi/10.1103/PhysRevLett.104.203603`.

[13] A. Goban, K. S. Choi, D. J. Alton, D. Ding, C. Lacroûte, M. Pototschnig, T. Thiele, N. P. Stern, and H. J. Kimble, "Demonstration of a state-insensitive, compensated nanofiber trap", Physical Review Letters **109**, 7 (2012) `10.1103/PhysRevLett.109.033603`, `http://arxiv.org/abs/1203.5108`.

[14] H. L. Sørensen, J. B. Béguin, K. W. Kluge, I. Iakoupov, A. S. Sørensen, J. H. Müller, E. S. Polzik, and J. Appel, "Coherent Backscattering of Light off One-Dimensional Atomic Strings", Physical Review Letters **117**, 1–10 (2016) `10.1103/PhysRevLett.117.133604`, `http://arxiv.org/abs/1601.04869`.

[15] N. V. Corzo, B. Gouraud, A. Chandra, A. Goban, A. S. Sheremet, D. V. Kupriyanov, and J. Laurat, "Large Bragg Reflection from One-Dimensional Chains of Trapped Atoms Near a Nanoscale Waveguide", Physical Review Letters **117**, 1–8 (2016) `10.1103/PhysRevLett.117.133603`, `http://arxiv.org/abs/1604.03129`.

[16] D. E. Chang, A. S. Sørensen, E. A. Demler, and M. D. Lukin, "A single-photon transistor using nano-scale surface plasmons", Nature Physics **3**, 807–812 (2007) `10.1038/nphys708`, `http://arxiv.org/abs/0706.4335%0Ahttp://dx.doi.org/10.1038/nphys708`.

[17] a. V. Akimov, A. Mukherjee, C. L. Yu, D. E. Chang, A. S. Zibrov, P. R. Hemmer, H. Park, and M. D. Lukin, "Generation of single optical plasmons in metallic nanowires coupled to quantum dots.", Nature **450**, 402–6 (2007) `10.1038/nature06230`, `http://www.ncbi.nlm.nih.gov/pubmed/18004381`.

[18] A. Huck, S. Kumar, A. Shakoor, and U. L. Andersen, "Controlled coupling of a single nitrogen-vacancy center to a silver nanowire", Physical Review Letters **106**, 2–5 (2011) `10.1103/PhysRevLett.106.096801`.

[19] A. Gonzalez-Tudela, D. Martin-Cano, E. Moreno, L. Martin-Moreno, C. Tejedor, and F. J. Garcia-Vidal, “Entanglement of two qubits mediated by one-dimensional plasmonic waveguides”, Physical Review Letters **106**, 4 (2011) `10.1103/PhysRevLett.106.020501`, `http://arxiv.org/abs/1010.5048`.

[20] A. F. van Loo, A. Fedorov, K. Lalumiere, B. C. Sanders, A. Blais, and A. Wallraff, “Photon-Mediated Interactions Between Distant Artificial Atoms”, Science **342**, 1494–1496 (2013) `10.1126/science.1244324`, `http://www.sciencemag.org/content/342/6165/1494.abstract%20http://www.sciencemag.org/cgi/doi/10.1126/science.1244324`.

[21] M. H. Devoret, and R. J. Schoelkopf, “Superconducting circuits for quantum information: an outlook.”, Science **339**, 1169–74 (2013) `10.1126/science.1231930`, `http://www.ncbi.nlm.nih.gov/pubmed/23471399`.

[22] H. J. Kimble, “Strong Interactions of Single Atoms and Photons in Cavity QED”, Physica Scripta **T76**, 127 (1998) `10.1238/Physica.Topical.076a00127`, `http://www.physica.org/xml/article.asp?article=t076a00127.xml`.

[23] S. Haroche, and J.-M. Raimond, *Exploring the quantum: atoms, cavities, and photons* (Oxford university press, 2006).

[24] R. Miller, T. E. Northup, K. M. Birnbaum, A. Boca, A. D. Boozer, and H. J. Kimble, “Trapped atoms in cavity QED: coupling quantized light and matter”, Journal of Physics B: Atomic, Molecular and Optical Physics **38**, S551–S565 (2005) `10.1088/0953-4075/38/9/007`, `http://stacks.iop.org/0953-4075/38/i=9/a=007?key=crossref.67783944d3e5fda8caa9be236bf33e35`.

[25] J. Volz, M. Scheucher, C. Junge, and A. Rauschenbeutel, “Nonlinear π phase shift for single fibre-guided photons interacting with a single resonator-enhanced atom”, Nature Photonics **8**, 965–970 (2014) `10.1038/nphoton.2014.253`, `http://www.nature.com/doifinder/10.1038/nphoton.2014.253`.

[26] K. P. Nayak, P. N. Melentiev, M. Morinaga, F. L. Kien, V. I. Balykin, and K. Hakuta, “Optical nanofiber as an efficient tool for manipulating and probing atomic Fluorescence.”, Optics express **15**, 5431–5438 (2007) `10.1364/OE.15.005431`.

[27] F. Le Kien, V. I. Balykin, and K. Hakuta, “Scattering of an evanescent light field by a single cesium atom near a nanofiber”, Physical Review A - Atomic, Molecular, and Optical Physics **73**, 1–11 (2006) `10.1103/PhysRevA.73.013819`.

[28] P. Lodahl, S. Mahmoodian, and S. Stobbe, “Interfacing single photons and single quantum dots with photonic nanostructures”, Review of Modern Physics **87** (2013), `http://arxiv.org/abs/1312.1079`.

[29] T. Schröder, S. Mouradian, J. Zheng, M. E. Trusheim, M. Walsh, E. H. Chen, L. Li, I. Bayn, and D. Englund, “Review Article: Quantum Nanophotonics in Diamond”, Journal of Optics B **33**, 1–23 (2016) `10.1364/JOSAB.33.000B65`, `http://arxiv.org/abs/1603.05339`.

[30] T. Zhong, J. M. Kindem, E. Miyazono, and A. Faraon, “Nanophotonic coherent light-matter interfaces based on rare-earth-doped crystals.”, Nature communications **6**, 8206 (2015) `10.1038/ncomms9206`, `http://www.nature.com/ncomms/2015/150914/ncomms9206/full/ncomms9206.html`.

[31] J. D. Thompson, T. G. Tiecke, A. S. Zibrov, V. Vuletic, and M. D. Lukin, “Coherence and Raman sideband cooling of a single atom in an optical tweezer”, Physical Review Letters **110**, 1–5 (2013) `10.1103/PhysRevLett.110.133001`, `http://arxiv.org/abs/1209.3028`.

[32] A. Goban, C.-L. Hung, Y. Yu, J. D. Hood, J. A. Muniz, J. H. Lee, M. J. Martin, A. C. McClung, K. S. Choi, D. E. Chang, O. Painter, and H. J. Kimble, “Atom-light interactions in photonic crystals”, Nature communications **5**, 3808 (2014) `10.1038/ncomms4808`, `https://www.nature.com/articles/ncomms4808`,

[33] J. D. Joannopoulos, S. Johnson, J. N. Winn, and R. D. Meade, *Photonic crystals: molding the flow of light* (Time, 2008).

[34] COMSOL, *COMSOL Multiphysics*.

[35] C. L. Hung, S. M. Meenehan, D. E. Chang, O. Painter, and H. J. Kimble, “Trapped atoms in one-dimensional photonic crystals”, New Journal of Physics **15**, 7 (2013) `10.1088/1367-2630/15/8/083026`, `http://arxiv.org/abs/1301.5252`.

[36] S. P. Yu, J. D. Hood, J. A. Muniz, M. J. Martin, R. Norte, C. L. Hung, S. M. Meenehan, J. D. Cohen, O. Painter, and H. J. Kimble, “Nanowire photonic crystal waveguides for single-atom trapping and strong light-matter interactions”, Applied Physics Letters **104** (2014) `10.1063/1.4868975`, `http://aip.scitation.org/doi/abs/10.1063/1.4868975`,

[37] A. Goban, C.-L. Hung, J. D. Hood, Y. Yu, J. A. Muniz, O. Painter, and H. J. Kimble, “Superradiance for Atoms Trapped along a Photonic Crystal Waveguide”, Physical Review Letters **115**, 063601 (2015) `10.1103/PhysRevLett.115.063601`, `http://link.aps.org/doi/10.1103/PhysRevLett.115.063601`,

[38] S. John, “Strong localization of photons in certain disordered dielectric superlattices”, Physical Review Letters **58**, 2486–2489 (1987) `10.1103/PhysRevLett.58.2486`.

[39] S. John, and J. Wang, “Quantum electrodynamics near a photonic band gap: Photon bound states and dressed atoms”, Physical review letters **64**, 2418–2421 (1990), `http://prl.aps.org/abstract/PRL/v64/i20/p2418_1`.

[40] G. Kurizki, “Two-atom resonant radiative coupling in photonic band structures”, Physical Review A **42**, 2915–2924 (1990) `10.1103/PhysRevA.42.2915`, `http://scholar.google.com/scholar?hl=en&btnG=Search&q=intitle:No+Title#0%20http://journals.aps.org/pra/abstract/10.1103/PhysRevA.42.2915`.

[41] J. S. Douglas, H. Habibian, C.-L. Hung, A. V. Gorshkov, H. J. Kimble, and D. E. Chang, "Quantum many-body models with cold atoms coupled to photonic crystals", Nature Photonics **9**, 326–331 (2015) `10.1038/nphoton.2015.57`, `http://dx.doi.org/10.1038/nphoton.2015.57`.

[42] J. D. Hood, A. Goban, A. Asenjo-Garcia, M. Lu, Y. Yu, D. E. Chang, and H. J. Kimble, "Atom-atom interactions around the band edge of a photonic crystal waveguide", Proceedings of the National Academy of Sciences **113**, 10507–10512 (2016) `10.1073/pnas.1603788113`, `http://www.pnas.org/content/113/38/10507.full.pdf`,

[43] M. T. Manzoni, L. Mathey, and D. E. Chang, "Designing exotic many-body states of atomic spin and motion in photonic crystals", Nature Publishing Group **8**, 1–9 (2016) `10.1038/ncomms14696`, `http://arxiv.org/abs/1606.05582`.

[44] A. Asenjo-Garcia, J. D. Hood, D. E. Chang, and H. J. Kimble, "Atom-light interactions in quasi-one-dimensional nanostructures: A Green's-function perspective", Physical Review A - Atomic, Molecular, and Optical Physics **95**, 1–16 (2017) `10.1103/PhysRevA.95.033818`, `https://journals.aps.org/pra/abstract/10.1103/PhysRevA.95.033818`,

[45] L. Novotny, and B. Hecht, *Principle of Nano-optics*, Vol. 1 (Cambridge university press, 2012), `10.1017/CBO9781107415324.004`.

[46] S. Y. Buhmann, *Dispersion forces I: Macroscopic quantum electrodynamics and ground-state Casimir, Casimir–Polder and van der Waals Forces*, Vol. 247 (Springer, 2013), `10.1007/978-3-642-32484-0`, `http://link.springer.com/10.1007/978-3-642-32484-0`.

[47] E. M. Purcell, "Spontaneous Emission Probabilities at Radio Frquencies", Physical Review **69**, 674–674 (1946) `10.1103/PhysRev.69.674.2`, `http://prola.aps.org/abstract/PR/v69/i11-12/p674_2%5Cnhttp://link.aps.org/doi/10.1103/PhysRev.69.674.2`.

[48] M. O. Scully, and M. S. Zubairy, *Quantum Optics* (Cambridge university press, 1997).

[49] D. A. Steck, *Quantum and Atom Optics*, revision 0 (http://steck.us/teaching, 2007).

[50] V. V. Klimov, and M. Ducloy, "Spontaneous emission rate of an excited atom placed near a nanofiber", Physical Review A **69**, 19 (2004) `10.1016/S0030-4018(02)01802-3`, `http://link.aps.org/doi/10.1103/PhysRevA.69.013812`.

[51] F. Le Kien, S. Gupta, K. P. Nayak, and K. Hakuta, "Nanofiber-mediated radiative transfer between two distant atoms", Physical Review A **72**, 063815 (2005) `10.1103/PhysRevA.72.063815`, `http://link.aps.org/doi/10.1103/PhysRevA.72.063815`.

[52] C.-T. Tai, *Dyadic Green's Functions In Electromagnetic Theory* (International Textbook Company, 1971).

[53] C. G. Poulton, C. Koos, M. Fujii, A. Pfrang, T. Schimmel, J. Leuthold, and W. Freude, "Radiation modes and roughness loss in high index-contrast waveguides", IEEE Journal of Quantum Electronics **12**, 1306–1320 (2006) `10.1109/JSTQE.2006.881648`, `http://ieeexplore.ieee.org/xpls/abs_all.jsp?arnumber=4032688`.

[54] *Lumerical Solutions, Inc.*

[55] Ardavan F Oskooi, D. Roundy, M. Ibanescu, P. Bermelc, J. D. Joannopoulos, and Steven G. Johnson, *MEEP*, `http://math.mit.edu/~stevenj/papers/OskooiRo10.pdf`.

[56] S. G. Johnson, and J. D. Joannopoulos, *MIT Photonic Bandgap (MPB).*

[57] K. Sakoda, and K. Ohtaka, "Optical response of three-dimensional photonic lattices: Solutions of inhomogeneous Maxwell's equations and their applications", Physical Review B **54**, 5732–5741 (1996) `10.1103/PhysRevB.54.5732`, `http://link.aps.org/doi/10.1103/PhysRevB.54.5732`.

[58] K. Sakoda, *Optical Properties of Photonic Crystals* (Springer Science & Business Media, 2005), `10.1007/b138376`.

[59] N. W. Ashcroft, and N. D. Mermin, *Solid State Physics* (1976).

[60] M. Wubs, L. G. Suttorp, and A. Lagendijk, "Multiple-scattering approach to interatomic interactions and superradiance in inhomogeneous dielectrics", Physical Review A **70**, 1–17 (2004) `10.1103/PhysRevA.70.053823`.

[61] P. Yao, V. Manga Rao, and S. Hughes, "On-chip single photon sources using planar photonic crystals and single quantum dots", Laser & Photonics Reviews **4**, 499–516 (2009) `10.1002/lpor.200810081`, `http://doi.wiley.com/10.1002/lpor.200810081`.

[62] M. Patterson, "Classical and Quantum Optical Properties of Slow Light Photonic Crystal Waveguides", PhD thesis (Queen's University, 2009).

[63] C. P. V. Vlack, "Dyadic Green Functions and Their Applications", PhD thesis (Queen's University, Kingston, 2012).

[64] G. Barton, *Elements of Green's Functions and Propagation* (Clarendon Press, 1989).

[65] X. Qi, B. Q. Baragiola, P. S. Jessen, and I. Deutsch, "Dispersive response of atoms trapped near the surface of an optical nanofiber with applications to quantum nondemolition measurement and spin squeezing", Physical Review A **93**, 1–17 (2016) `10.1103/PhysRevA.93.023817`.

[66] Claude Cohen-Tannoudji, J. Dupont-Roc, and G. Grynberg, *Atom-Photon Interactions* (Wiley, 1992), pp. 1–660, `10.1002/9783527617197`, `papers2://publication/uuid/794705AA-C281-47AF-9096-8CEF65BE1820`.

[67] R. Glauber, and M. Lewenstein, "Quantum optics of dielectric media", Physical Review A **43** (1991), `http://pra.aps.org/abstract/PRA/v43/i1/p467_1`.

[68] B. Huttner, and S. M. Barnett, "Quantization of the electromagnetic field in dielectrics", Physical Review A **46** (1992), `http://pra.aps.org/abstract/PRA/v46/i7/p4306_1`.

[69] L. Knöll, S. Scheel, and D.-G. Welsch, "QED in dispersing and absorbing media", Coherence and Statistics of Photons and Atoms, 60 (2000), `http://arxiv.org/abs/quant-ph/0006121`.

[70] C. Gardiner, and M. Collett, "Input and output in damped quantum systems: Quantum stochastic differential equations and the master equation", Physical Review A **31**, 3761–3774 (1985), `http://pra.aps.org/abstract/PRA/v31/i6/p3761_1`.

[71] P. Domokos, P. Horak, and H. Ritsch, "Quantum description of light-pulse scattering on a single atom in waveguides", Physical Review A **65**, 033832 (2002) `10.1103/PhysRevA.65.033832`, `https://link.aps.org/doi/10.1103/PhysRevA.65.033832`.

[72] D. E. Chang, a. S. Sorensen, E. A. Demler, and M. D. Lukin, "Single-photon transistor using nanoscale plasmons - Supplemental information", 2–5 (2007).

[73] S. Fan, Ş. E. Kocabaş, and J.-T. Shen, "Input-output formalism for few-photon transport in one-dimensional nanophotonic waveguides coupled to a qubit", Physical Review A **82**, 063821 (2010) `10.1103/PhysRevA.82.063821`, `http://link.aps.org/doi/10.1103/PhysRevA.82.063821`.

[74] K. Lalumière, B. C. Sanders, A. F. van Loo, A. Fedorov, A. Wallraff, and A. Blais, "Input-output theory for waveguide QED with an ensemble of inhomogeneous atoms", Physical Review A **88**, 043806 (2013) `10.1103/PhysRevA.88.043806`, `http://link.aps.org/doi/10.1103/PhysRevA.88.043806`.

[75] J. D. Jackson, *Electrodynamics* (Wiley-VCH Verlag GmbH & Co. KGaA, 1975), `10.1038/2241334a0`.

[76] D. Dzsotjan, J. Kästel, and M. Fleischhauer, "Dipole-dipole shift of quantum emitters coupled to surface plasmons of a nanowire", Physical Review B **84**, 1–6 (2011) `10.1103/PhysRevB.84.075419`.

[77] H. Callen, and T. Welton, "Irreversibility and Generalized Noise", Physical Review **83** (1951), `http://lptms.u-psud.fr/membres/trizac/Ens/M2MQPL/CallenWelton.pdf`.

[78] T. Gruner, and D.-G. Welsch, "Green-function approach to the radiation-field quantization for homogeneous and inhomogeneous Kramers-Kronig dielectrics", Physical Review A **53**, 1818–1829 (1996) `10.1103/PhysRevA.53.1818`.

[79] H. T. Dung, L. Knöll, D.-G. Welsch, L. Knoell, L. Knoll, and D.-G. Welsch, "Three-dimensional quantization of the electromagnetic field in dispersive and absorbing inhomogeneous dielectrics", Physical Review A **57** (1997) `10.1103/PhysRevA.57.3931`, `http://arxiv.org/abs/quant-ph/9711039%20http://pra.aps.org/abstract/PRA/v57/i5/p3931_1`.

[80] S. Y. Buhmann, L. Knöll, D.-G. Welsch, and H. T. Dung, "Casimir-Polder forces: A nonperturbative approach", Physical Review A **052117**, 1–23 (2004) `10.1103/PhysRevA.70.052117`, `http://pra.aps.org/abstract/PRA/v70/i5/e052117`.

[81] D. E. Chang, K. Sinha, J. M. Taylor, and H. J. Kimble, "Trapping atoms using nanoscale quantum vacuum forces", Nature communications, 13 (2013) `10.1038/ncomms5343`, `http://arxiv.org/abs/1310.5970`.

[82] S. Y. Buhmann, and D.-G. Welsch, "Dispersion Forces in Macroscopic quantum electrodynamics", (2007).

[83] S. Scheel, L. Knoll, and D.-G. Welsch, "Spontaneous decay of an excited atom in an absorbing dielectric", Technical Digest. CLEO/Pacific Rim '99. Pacific Rim Conference on Lasers and Electro-Optics (Cat. No.99TH8464) **1**, 4094–4104 (1999) `10.1109/CLEOPR.1999.811620`.

[84] H. T. Dung, L. Knöll, and D. G. Welsch, "Spontaneous decay in the presence of dispersing and absorbing bodies: General theory and application to a spherical cavity", Physical Review A - Atomic, Molecular, and Optical Physics **62**, 053804–053801 (2000) `10.1103/PhysRevA.62.053804`.

[85] H. T. Dung, S. Y. Buhmann, L. Knöll, D.-G. Welsch, S. Scheel, and J. Kästel, "Electromagnetic-field quantization and spontaneous decay in left-handed media", Physical Review A **68**, 043816 (2003) `10.1103/PhysRevA.68.043816`, `http://link.aps.org/doi/10.1103/PhysRevA.68.043816`.

[86] P. Yao, C. Van Vlack, A. Reza, M. Patterson, M. M. Dignam, and S. Hughes, "Ultrahigh Purcell factors and Lamb shifts in slow-light metamaterial waveguides", Physical Review B **80**, 1–11 (2009) `10.1103/PhysRevB.80.195106`.

[87] T. Hümmer, F. J. García-Vidal, L. Martín-Moreno, and D. Zueco, "Weak and strong coupling regimes in plasmonic QED", Physical Review B - Condensed Matter and Materials Physics **87**, 1–18 (2013) `10.1103/PhysRevB.87.115419`, `http://arxiv.org/abs/1209.1724`.

[88] H. T. Dung, L. Knöll, and D.-G. Welsch, "Resonant dipole-dipole interaction in the presence of dispersing and absorbing surroundings", Phys Rev A **66**, 063810 (2002) `10.1103/PhysRevA.66.063810`.

[89] D. Dzsotjan, a. S. Sorensen, and M. Fleischhauer, "Quantum emitters coupled to surface plasmons of a nanowire: A Green's function approach", Physical Review B **82**, 075427 (2010) `10.1103/PhysRevB.82.075427`, `http://link.aps.org/doi/10.1103/PhysRevB.82.075427`.

[90] D. Martín-Cano, A. Gonzalez-Tudela, L. Martín-Moreno, F. J. García-Vidal, C. Tejedor, and E. Moreno, "Dissipation-driven generation of two-qubit entanglement mediated by plasmonic waveguides", Physical Review B **84**, 1–12 (2011) `10.1103/PhysRevB.84.235306`.

[91] A. Gonzalez-Tudela, F. J. Rodríguez, L. Quiroga, and C. Tejedor, "Dissipative dynamics of a solid-state qubit coupled to surface plasmons: From non-Markov to Markov regimes", Physical Review B **82**, 115334 (2010) `10.1103/PhysRevB.82.115334`.

[92] D. Martín-Cano, "Plasmonic Waveguides: Classical Applications and Quantum Phenomena", PhD thesis (Universidad Autonoma de Madrid, 2013).

[93] J. Kästel, and M. Fleischhauer, "Suppression of spontaneous emission and superradiance over macroscopic distances in media with negative refraction", Physical Review A **71**, 1–4 (2005) `10.1103/PhysRevA.71.011804`.

[94] D. Dzsotjan, and M. Fleischhauer, "Interaction of Atoms with Frequency-Chirped Pulses and Surface Plasmons", Thesis (2011).

[95] R. C. Ge, and S. Hughes, "Quantum dynamics of two quantum dots coupled through localized plasmons: An intuitive and accurate quantum optics approach using quasinormal modes", Physical Review B - Condensed Matter and Materials Physics **92** (2015) `10.1103/PhysRevB.92.205420`.

[96] A. Asenjo-Garcia, "Spin-spin Interactions within the Green's function formalism", Internal Notes (2015).

[97] J. D. Thompson, T. G. Tiecke, N. P. de Leon, J. Feist, a. V. Akimov, M. Gullans, A. S. Zibrov, V. Vuletic, and M. D. Lukin, "Coupling a single trapped atom to a nanoscale optical cavity.", Science (New York, N.Y.) **340**, 1202–5 (2013) `10.1126/science.1237125`, `http://www.ncbi.nlm.nih.gov/pubmed/23618764`.

[98] T. Lund-Hansen, S. Stobbe, B. Julsgaard, H. Thyrrestrup, T. Sünner, M. Kamp, A. Forchel, and P. Lodahl, "Experimental realization of highly efficient broadband coupling of single quantum dots to a photonic crystal waveguide", Physical Review Letters **101**, 1–4 (2008) `10.1103/PhysRevLett.101.113903`.

[99] A. B. Young, A. C. T. Thijssen, D. M. Beggs, P. Androvitsaneas, L. Kuipers, J. G. Rarity, S. Hughes, and R. Oulton, "Polarization Engineering in Photonic Crystal Waveguides for Spin-Photon Entanglers", Physical Review Letters **115**, 1–5 (2015) `10.1103/PhysRevLett.115.153901`.

[100] Y. Liu, and A. A. Houck, "Quantum electrodynamics near a photonic band-gap", Nature Physics **13**, 48–52 (2017) `10.1038/nphys3834`, `http://arxiv.org/abs/1603.02998%0Ahttp://dx.doi.org/10.1038/nphys3834`.

[101] P. Meystre, and M. Sargent, *Elements of Quantum Optics* (Springer-Verlag, Berlin, 2007).

[102] J.-T. Shen, and S. Fan, “Coherent single photon transport in one-dimensional waveguide coupledwith superconducting quantum bits”, Physical Review Letters **95**, 213001 (2005) `10.1109/CLEO.2006.4628866`.

[103] M. Tomaš, “Green function for multilayers: Light scattering in planar cavities”, Physical Review A **51** (1995), `http://pra.aps.org/abstract/PRA/v51/i3/p2545_1`.

[104] F. Le Kien, S. Dutta Gupta, V. I. Balykin, and K. Hakuta, “Spontaneous emission of a cesium atom near a nanofiber: Efficient coupling of light to guided modes”, Physical Review A **72**, 1–7 (2005) `10.1103/PhysRevA.72.032509`, `http://link.aps.org/doi/10.1103/PhysRevA.72.032509`.

[105] A. Asenjo-Garcia, M. Moreno-Cardoner, A. Albrecht, H. J. Kimble, and D. E. Chang, “Exponential improvement in photon storage fidelities using subradiance and "selective radiance" in atomic arrays”, arXiv **1703.03382**, 1–35 (2017), `http://arxiv.org/abs/1703.03382`.

[106] U. Fano, “Effects of configuration interaction on intensities and phase shifts”, Physical Review **124**, 1866–1878 (1961) `10.1103/PhysRev.124.1866`.

[107] E. Hecht, *Optics* (Addison Wesley, 1998).

[108] D. E. Chang, L. Jiang, A. V. Gorshkov, and H. J. Kimble, “Cavity QED with atomic mirrors”, 20 (2012), `http://arxiv.org/abs/1201.0643`.

[109] T. K. Paraso, M. Kalaee, L. Zang, H. Pfeifer, F. Marquardt, and O. Painter, “Position-squared coupling in a tunable photonic crystal optomechanical cavity”, Physical Review X **5**, 1–12 (2015) `10.1103/PhysRevX.5.041024`.

[110] I. Aharonovich, A. D. Greentree, and S. Prawer, “Diamond photonics”, Nature Photonics **5**, 397–405 (2011) `10.1038/nphoton.2011.54`, `http://dx.doi.org/10.1038/nphoton.2011.54`.

[111] H. J. Kimble, “The quantum internet.”, Nature **453**, 1023–30 (2008) `10.1038/nature07127`, `http://www.ncbi.nlm.nih.gov/pubmed/18563153`.

[112] A. Wallraff, D. Schuster, A. Blais, L. Frunzio, R. Huang, J. Majer, S. Kumar, S. Girvin, and R. Schoelkopf, “Strong coupling of a single photon to a superconducting qubit using circuit quantum electrodynamics”, Nature **431**, 162–167 (2004) `10.1038/nature02831.1.`, `http://links.isiglobalnet2.com/gateway/Gateway.cgi?GWVersion=2&SrcAuth=mekentosj&SrcApp=Papers&DestLinkType=FullRecord&DestApp=WOS&KeyUT=000223746000038`.

[113] E. Yablonovitch, “Inhibited spontaneous emission in solid-state physics and electronics”, Physical review letters **58**, 2059–2062 (1987), `http://link.aps.org/doi/10.1103/PhysRevLett.58.2059`.

[114] T. Shi, Y.-H. Wu, A. Gonzalez-Tudela, and J. I. Cirac, “Bound States in Boson Impurity Models”, Physical Review X **6**, 021027 (2016) `10.1103/PhysRevX.6.021027`, `http://link.aps.org/doi/10.1103/PhysRevX.6.021027`.

[115] G. Calajó, F. Ciccarello, D. E. Chang, and P. Rabl, "Atom-field dressed states in slow-light waveguide QED", Physical Review A **93**, 1–16 (2016) `10.1103/PhysRevA.93.033833`.

[116] A. Gonzalez-Tudela, V. Paulisch, D. E. Chang, H. J. Kimble, and J. I. Cirac, "Deterministic generation of arbitrary photonic states assisted by dissipation.", **1**, 1–15 (2015).

[117] M. J. Hartmann, F. G. S. L. Brandão, and M. B. Plenio, "Strongly interacting polaritons in coupled arrays of cavities", Nature Physics **2**, 849–855 (2006) `10.1038/nphys462`, `http://www.nature.com/doifinder/10.1038/nphys462`.

[118] A. D. Greentree, C. Tahan, J. H. Cole, and L. C. L. Hollenberg, "Quantum phase transitions of light", Nature Physics **2**, 856–861 (2006) `10.1038/nphys466`, `http://www.nature.com/doifinder/10.1038/nphys466`.

[119] J. Shen, and S. Fan, "Coherent photon transport from spontaneous emission in one-dimensional waveguides", Optics letters **30**, 2001–2003 (2005), `http://www.opticsinfobase.org/abstract.cfm?&id=84782`.

[120] F. L. Kien, and A. Rauschenbeutel, "Propagation of nanofiber-guided light through an array of atoms", Physical Review A **90**, 063816–1 (2014) `10.1103/PhysRevA.90.063816`.

[121] F. Le Kien, P. Schneeweiss, and A. Rauschenbeutel, "Dynamical polarizability of atoms in arbitrary light fields: general theory and application to cesium", The European Physical Journal D **67**, 92 (2013) `10.1140/epjd/e2013-30729-x`, `http://link.springer.com/10.1140/epjd/e2013-30729-x`.

[122] A. R. Edmonds, *Angular momentum in quantum mechanics* (Princeton University Press, 1996).

[123] D. Varshalovich, Aleksandrovich, A. Moskalev, and V. Khersonskii, *Quantum theory of angular momentum* (World Scientific, 1988).

[124] K. Beloy, "Theory of the ac Stark Effect on the Atomic Hyperfine Structure and Applications to Microwave Atomic Clocks", PhD thesis (University of Nevada, Reno, 2009).

[125] P. Rosenbusch, S. Ghezali, V. Dzuba, V. Flambaum, K. Beloy, and A. Derevianko, "ac Stark shift of the Cs microwave atomic clock transitions", Physical Review A **79**, 013404 (2009) `10.1103/PhysRevA.79.013404`, `http://link.aps.org/doi/10.1103/PhysRevA.79.013404`.

[126] G. B. Arfken, H. J. Weber, and F. E. Harris, *Mathematical methods for physicists: a comprehensive guide* (Academic press, 2011).

Appendix A

GREEN'S FUNCTION FORMALISM WITH ANGULAR MOMENTUM

Next we extend the quantum formalism for atoms in Chapter 3 beyond two levels systems. For Alkali atoms such as cesium, we will include the hyperfine and Zeeman levels into the formalism. While Cs atoms coupled to a waveguide has been treated in Ref. [120], I have not seen any reference that expands the Green's function formalism of Chapter 3 to include the hyperfine and Zeeman levels. A brief review of angular momentum theory is given in Appendix B.

A.1 Master equation with hyperfine levels

First we consider just one hyperfine level for the ground state F_g and one for the excited state F_e. In the next section, I will expand this to the case of arbitrary levels. The dipole operator $\hat{\mathbf{d}}$ in Eq. 3.40 is expanded into the basis of two-levels of the atom. Now the basis is expanded to include multiple Zeeman sublevels. The unity projection operator for the i'th atom is given by

$$\mathbf{I} = \sum_{m_g} |iF_g m_g\rangle\langle iF_g m_g| + \sum_{m_e} |iF_e m_e\rangle\langle iF_e m_e|. \tag{A.1}$$

Multiplying the dipole operator $\hat{\mathbf{d}}_i$ on both sides with the unity operator gives

$$\hat{\mathbf{d}}_i = \sum_{m_g m_e} \langle iF_g m_g|\hat{\mathbf{d}}|iF_e m_e\rangle \hat{\sigma}_{im_g m_e} + \text{h.c.}, \tag{A.2}$$

where the atomic lowering operator from a particular excited state to a particular ground state is

$$\hat{\sigma}_{im_g m_e} = |iF_g m_g\rangle\langle iF_e m_e|. \tag{A.3}$$

Next I express the dipole operator $\hat{\mathbf{d}}$ in Eq. (A.2) in terms of the spherical vector basis,

$$\hat{\mathbf{d}} = \sum_q \hat{d}_q \mathbf{e}_q^*. \tag{A.4}$$

The spherical basis vectors are $\hat{\mathbf{e}}_q$ given by

$$\hat{\mathbf{e}}_{\pm 1} = \mp\frac{1}{\sqrt{2}}(\hat{\mathbf{x}} \pm \mathrm{i}\hat{\mathbf{y}}), \qquad \hat{\mathbf{e}}_0 = \hat{\mathbf{z}}. \tag{A.5}$$

and the normalization of these unit vectors is $\hat{\mathbf{e}}_q \cdot \hat{\mathbf{e}}^*_q = \delta_{qq'}$.

Next I use the Wigner-Eckert theorem from Eq. (B.18) to simplify the resulting expression in terms of the reduced matrix element. The dipole operator simplifies to

$$\hat{\mathbf{d}}_i = \sum_q \hat{d}_{i,q}\mathbf{e}^*_q \quad \text{where} \quad \hat{d}_{i,q} = \frac{\langle iF_g||\hat{\mathbf{d}}||iF_e\rangle}{\sqrt{2F_e+1}}\left(\hat{\Sigma}_{i,q} + (-1)^q\hat{\Sigma}^\dagger_{i,-q}\right), \tag{A.6}$$

where the combined raising and lower operators $\hat{\Sigma}_{i,q}$ are expressed in terms of the two-level raising and lowering operators and the oscillators strengths:

$$\hat{\Sigma}_{i,q} = \sum_{m_g m_e} f_{q\,F_g m_g F_e m_e}\;\hat{\sigma}_{i m_g m_e}. \tag{A.7}$$

The oscillator strengths $f_{q\,F_g m_g F_e m_e}$ are given by

$$f_{qF_g m_g F_e m_e} = (-1)^{F_g - m_g}\sqrt{2F_e+1}\begin{pmatrix} F_g & 1 & F_e \\ -m_g & q & m_e \end{pmatrix}. \tag{A.8}$$

The oscillator strengths have the property that the sum of the square of the oscillator strength of all ground states m_g and polarizations q is unity (which can be shown using the orthogonality of the 3-J symbols),

$$\sum_{q\,m_g}(f_{q\,F_g m_g F_e m_e})^2 = 1. \tag{A.9}$$

Now we can substitute the dipole operator of Eq. (A.6) into the Hamiltonian from Eq. (3.41) in Chapter 3 and proceed with the derivations. For example, the resulting master equation is given by:

$$\begin{aligned}\dot{\hat{\rho}} = -\mathrm{i}[H_A, \rho] + \mathrm{i}\sum_{ijqq'} J_{ijqq'}[\Sigma^\dagger_{iq}\Sigma_{jq'}, \hat{\rho}] - \frac{1}{2}\sum_{ijqq'}\Gamma_{ijqq'}\left(\Sigma^\dagger_{iq}\Sigma_{jq'}\hat{\rho} - 2\Sigma_{jq'}\hat{\rho}\Sigma^\dagger_{iq} + \hat{\rho}\Sigma^\dagger_{iq}\Sigma_{jq'}\right) \\ +\mathrm{i}\sum_{iq}[\hbar\Omega_{iq}\Sigma^\dagger_{iq} + \text{h.c.}, \hat{\rho}].\end{aligned} \tag{A.10}$$

The second and third terms are the spin-exchange and dissipation. The the new dissipation and coupling parameters are given by

$$J_{ijqq'} = \frac{\tilde{\omega}^2}{\hbar\epsilon_0 c^2}\frac{|\langle iF_g||\hat{\mathbf{d}}||iF_e\rangle|^2}{2F_e+1}\;\mathbf{e}_q\cdot\mathrm{Re}[\mathbf{G}(\mathbf{r}_i, \mathbf{r}_j, \tilde{\omega})]\cdot\mathbf{e}^*_{q'} \tag{A.11}$$

$$\Gamma_{ijqq'} = \frac{2\tilde{\omega}^2}{\hbar\epsilon_0 c^2}\frac{|\langle iF_g||\hat{\mathbf{d}}||iF_e\rangle|^2}{2F_e+1}\;\mathbf{e}_q\cdot\mathrm{Im}[\mathbf{G}(\mathbf{r}_i, \mathbf{r}_j, \tilde{\omega})]\cdot\mathbf{e}^*_{q'} \tag{A.12}$$

The drive term is expressed in terms of the electric field in the spherical basis $E_q(\mathbf{r}, t) = \mathbf{E}(\mathbf{r}, t) \cdot \hat{\mathbf{e}}_q^*$:

$$\Omega_{iq} = \frac{1}{\hbar} \frac{|\langle iF_g || \hat{\mathbf{d}} || iF_e \rangle|}{\sqrt{2F_e + 1}} E_q(\mathbf{r}, \mathbf{t}) \tag{A.13}$$

Including multiple hyperfine levels in each ground and excited state

The previous case treated a single hyperfine level for the ground state and single hyperfine level for the excited state. Now we allow multiple hyperfine levels for both the ground state and excited state. We use the the Wigner-Eckert identity from Eq. (B.23),

$$\begin{aligned}\langle \gamma J_g I F_g || T^{(k)} || \gamma J_e I F_e \rangle = (-1)^{J_g+I+F_e+k} &\sqrt{(2F_g + 1)(2F_e + 1)} \\ &\begin{Bmatrix} F_g & k & F_e \\ J_e & I & J_g \end{Bmatrix} \langle \gamma J_g || T^{(k)} || \gamma J_e \rangle,\end{aligned} \tag{A.14}$$

to express the dipole operator as

$$\hat{\mathbf{d}}_i = \sum_q \hat{d}_{i,q} \mathbf{e}_q^* \quad \text{where} \quad \hat{d}_{i,q} = \frac{\langle iJ_g || \hat{\mathbf{d}} || iJ_e \rangle}{\sqrt{2J_e + 1}} \left(\hat{\Sigma}_{i,q} + (-1)^q \hat{\Sigma}_{i,-q}^\dagger \right) \tag{A.15}$$

where

$$\hat{\Sigma}_{i,q} = \sum_{F_g m_g F_e m_e} f^{\mathrm{HF}}_{qF_g m_g F_e m_e} \, \hat{\sigma}_{iF_g m_g F_e m_e} \tag{A.16}$$

and the new hyperfine oscillator strengths are expressed in terms of the previous oscillator strengths from Eq. A.8,

$$f^{\mathrm{HF}}_{qF_g m_g F_e m_e} = (-1)^{J_g+I+F_e+1} \sqrt{(2F_g + 1)(2J_e + 1)} \begin{Bmatrix} F_g & 1 & F_e \\ J_e & I & J_g \end{Bmatrix} f_{qF_g m_g F_e m_e}. \tag{A.17}$$

The hyperfine oscillator strengths have the property that the sum the square over all ground states and polarizations is unity (which can be shown using Eq (A.9) and the orthogonality of the 6-J symbols):

$$\sum_{q\, F_g\, m_g} (f^{\mathrm{HF}}_{qF_g m_g F_e m_e})^2 = 1. \tag{A.18}$$

The parameters $J_{ijqq'}$, $\Gamma_{ijqq'}$, and Ω_{iq} are the same as before except with F_g and F_e replaced with J_g and J_e respectively.

From La Kien's paper [121], the reduced matrix elements for the Cs D1 and D2 line are given by

$$|\langle 6P_{1/2} || \mathbf{d} || 6S_{1/2} \rangle| = 4.489 \, ea_0 \tag{A.19}$$

$$|\langle 6P_{3/2} || \mathbf{d} || 6S_{1/2} \rangle| = 6.324 \, ea_0 \tag{A.20}$$

Appendix B

ANGULAR MOMENTUM REVIEW

This is to serve as a brief review of spherical tensor operators. Steck's "Quantum and Atom Optics" notes are great for an introduction, but there are many small errors and the convention for the reduced matrix element is different than the one used by many groups. The textbooks "Angular Momentum in Quantum Mechanics" by A.R. Edmunds [122], and "Quantum Theory of Angular Momentum" by D.A. Varshakovich [123] are the main references I have used. Other great references include Kyle Beloy's thesis [124] and Ref. [125]. The formalism worked out here is used in the next appendix to derive the master equation for multiple atoms coupled to an arbitrary waveguide.

B.1 Cartesian Tensor Operators

The definition of a Cartesian vector operator is an operator that rotates as

$$\sum_{\mathrm{j}} R_{\mathrm{ij}} V_{\mathrm{j}} = V'_{\mathrm{i}}. \tag{B.1}$$

Similarly, a Cartesian tensor operator is defined as

$$\sum_{\mathrm{ij}\cdots} R_{\mathrm{kj}} R_{\mathrm{li}} \cdots T_{\mathrm{ji}\cdots} = T'_{\mathrm{ij}\cdots}. \tag{B.2}$$

The scalar Cartesian product between tensors $T_{\mathrm{uv}\cdots}$ and $S_{\mathrm{uv}\cdots}$ is defined as

$$\mathbf{T}\cdot\mathbf{S} = \sum_{\mathrm{uv}\cdots} T_{\mathrm{uv}\cdots} S_{\mathrm{uv}\cdots}$$

An irreducible tensor implies that under a rotation, the elements transform into themselves. Any 2x2 cartesian tensor T_{uv} can be decomposed into a scalar $T^{(0)}$ (rank 0) related to the trace, a vector $\mathbf{T}^{(1)}$ (rank 1) related to the anti-symmetry of the tensor, and a symmetric traceless matrix $\mathbf{T}^{(2)}$ (rank 2). This is shown here:

$$T_{\mathrm{uv}} = -\frac{1}{\sqrt{3}} T^{(0)} \delta_{\mathrm{uv}} - \frac{\mathrm{i}}{\sqrt{2}} \epsilon_{\mathrm{uvw}} T^{(1)}_{\mathrm{w}} + T^{(2)}_{\mathrm{uv}}, \tag{B.3}$$

where

$$\begin{aligned}\mathbf{T}^{(0)} &= -\frac{1}{\sqrt{3}}\mathrm{Tr}[T] \\ \mathbf{T}^{(1)} &= \frac{\mathrm{i}}{\sqrt{2}}\epsilon_{\mathrm{uvw}}T_{\mathrm{vw}} \\ \mathbf{T}^{(2)} &= \frac{1}{2}(T_{\mathrm{uv}}+T_{\mathrm{vu}}) - \frac{1}{3}\mathrm{Tr}[T]\delta_{\mathrm{uv}}.\end{aligned} \tag{B.4}$$

Note that each term here has an arbitrary normalization, since the normalization can be compensated by changing Eq. (B.3). We choose the normalization so that the Cartesian scalar product between two tensors T_{uv} and S_{uv} is given by

$$\mathbf{T}\cdot\mathbf{S} = \sum_{\mathrm{uv}} T_{\mathrm{uv}}S_{\mathrm{uv}} = \sum_{k}(-1)^k\mathbf{T}^{(k)}\cdot\mathbf{S}^{(k)}$$

This convention is chosen so that it will later be easier to convert between Cartesian and Spherical tensors.

B.2 Spherical Tensor Operators

The spherical tensor operator of rank k is defined as an operator that rotates like a rank k spherical harmonic:

$$U(R)T_q^{(k)}U(R)^{-1} = \sum_{q'} T_{q'}^{(k)}\mathcal{D}_{q'q}^{(k)}(R), \tag{B.5}$$

where $\mathcal{D}_{q'q}^{(k)}(R)$ is the Wigner D-matrix elements defined by $\mathcal{D}_{q'q}^{(k)}(R) = \langle kq'|U(R)|kq\rangle$. $U(R)$ is the unitary rotation operator. The tensor operator has elements $|q| \leq k$.

One useful relation is that the complex conjugate of a spherical operator component is just

$$(T_q^{(k)})^* = (-1)^q T_{-q}^{(k)}. \tag{B.6}$$

Given two spherical tensors $A^{(k_1)}$ and $B^{(k_2)}$, we can construct a new spherical tensor $C_q^{(k)}$ by the spherical tensor product relation

$$C_q^{(k)} = \sum_{q_1q_2}\langle kq|k_1q_1k_2q_2\rangle\ A_{q_1}^{(k_1)}B_{q_2}^{(k_2)} \equiv \{A^{(k_1)}\otimes B^{(k_2)}\}_q^{(k)}. \tag{B.7}$$

One can prove that $C_q^{(k)}$ is a tensor operator by showing that it rotates as a spherical tensor operator. The brackets in the final expression is a convenient way to express the spherical tensor product.

A quantity that is convenient to define is the spherical scalar product between two rank k tensors:

$$A^{(k)} \cdot B^{(k)} \equiv \sum_q (-1)^q A_q^{(k)} B_{-q}^{(k)} = \sqrt{2k+1}\{A^{(k)} \otimes B^{(k)}\}^{(0)}. \tag{B.8}$$

Later, we will find that this relation is related to the Cartesian scalar product.

The rank 1 spherical harmonics Y_l^m are given by $Y_1^0 = \sqrt{\frac{3}{4\pi}}\frac{z}{r}$ and $Y_1^{\pm 1} = \mp\sqrt{\frac{3}{4\pi}}\frac{x \pm \mathrm{i}y}{\sqrt{2}r}$. Since the rank 1 spherical tensor rotates the same, we can relate the rank 1 spherical tensor $A^{(1)}$ to the Cartesian vector $\mathbf{A} = A_\mathrm{x}\hat{\mathbf{x}} + A_\mathrm{y}\hat{\mathbf{y}} + A_\mathrm{z}\hat{\mathbf{z}}$ by

$$\begin{aligned} A_{\pm 1}^{(1)} &= \mp\frac{1}{\sqrt{2}}(A_\mathrm{x} \pm iA_\mathrm{y}) \\ A_0^{(0)} &= A_\mathrm{z}. \end{aligned} \tag{B.9}$$

Note that the normalization is different than for the spherical harmonic. It is chosen here so that the spherical scalar product from Eq. (B.8) matches the Cartesian scalar product

$$\mathbf{A} \cdot \mathbf{B} = \sum_\mathrm{u} A_\mathrm{u} B_\mathrm{u} = \sum_q (-1)^q A_q B_{-q}. \tag{B.10}$$

I use the convention that roman subscripts are Cartesian tensors and italicized are spherical tensors. With this normalization, the scalar product for two vectors gives the same answer as if we first converted them both to rank 1 spherical tensors, and then took the spherical scalar product.

We can also define spherical unit vectors

$$\begin{aligned} \hat{\mathbf{e}}_{\pm 1} &= \mp\frac{1}{\sqrt{2}}(\hat{\mathbf{x}} \pm i\hat{\mathbf{y}}), \\ \hat{\mathbf{e}}_0 &= \hat{\mathbf{z}}. \end{aligned} \tag{B.11}$$

For some vector $\mathbf{A}$, the component in the $\hat{\mathbf{e}}_q$ direction is given by

$$\mathbf{A} \cdot \hat{\mathbf{e}}_q = \sum_q (-1)^q A_q \, \hat{\mathbf{e}}_{-q} = (-1)^q A_{-q}.$$

Therefore, the vector $\mathbf{A}$ can expressed in terms of the spherical unit vectors as

$$\mathbf{A} = \sum_q (-1)^q A_q \, \hat{\mathbf{e}}_{-q} = \sum_q A_q \, \hat{\mathbf{e}}_q^*. \tag{B.12}$$

Now we repeat the same procedure that we did for rank 1 tensors for rank 2 tensors. A rank 2 symmetric traceless tensor $T^{(2)}_{\mathrm{uv}}$ has 5 DOF (degrees of freedom) and is irreducible. Remember that roman subscripts are reserved for Cartesian tensors, and italicized subscripts are for spherical tensors. The rank 2 spherical tensor is also irreducible and has the same DOF. The spherical tensor can be expressed in terms of the rank 2 Cartesian matrix elements by

$$\begin{aligned} T^{(2)}_0 &= \sqrt{\frac{3}{2}} T_{\mathrm{zz}} \\ T^{(2)}_{\pm 1} &= \mp (T_{\mathrm{xz}} \pm i T_{\mathrm{yz}}) \\ T^{(2)}_{\pm 2} &= \frac{1}{2}(T_{\mathrm{xx}} - T_{\mathrm{yy}} \pm i2T_{\mathrm{xy}}). \end{aligned} \tag{B.13}$$

This relation can be derived by forming the rank 2 spherical product of two spherical vectors, and then expressing the spherical vectors in terms of the cartesian vectors using Eq. (B.12). Note that there is again a single arbitrary normalization factor here. Just as we did for the rank 1 case, we define the normalization term so that if we convert two rank 2 Cartesian tensors B_{uv} and A_{uv} into rank 2 spherical tensors $A^{(2)}_q$ and $B^{(2)}_q$, the spherical scalar product of the two spherical tensors gives the same as as the Cartesian scalar product of the Cartesian tensors:

$$\sum_{\mathrm{uv}} A_{\mathrm{uv}} B_{\mathrm{uv}} = \sum_q (-1)^q A^{(2)}_q B^{(2)}_{-q} \equiv \mathbf{A} \cdot \mathbf{B}. \tag{B.14}$$

For the more general case of two 2x2 Cartesian tensors A_{uv} and B_{uv}, each Cartesian tensor can be decomposed into a rank 2, 1, and 0 Cartesian tensor using Eq. (B.4). The Cartesian scalar product is given by $\mathbf{A} \cdot \mathbf{B} = \sum_{\mathrm{uv}} A_{\mathrm{uv}} B_{\mathrm{uv}}$. But because of our normalization conventions, this is the same as taking the spherical scalar product of the spherical tensors and adding them as

$$\mathbf{A} \cdot \mathbf{B} = \sum_{\mathrm{uv}} A_{\mathrm{uv}} B_{\mathrm{uv}} = \sum_k (-1)^k A^{(k)} \cdot B^{(k)} = \sum_{kq} (-1)^{k+q} A^{(k)}_q \cdot B^{(k)}_{-q}.$$

For an example, we consider the 2x2 cartesian matrix

$$G = \begin{pmatrix} G_{\mathrm{xx}} & G_{\mathrm{xy}} & G_{\mathrm{xz}} \\ G_{\mathrm{yx}} & G_{\mathrm{yy}} & G_{\mathrm{yz}} \\ G_{\mathrm{zx}} & G_{\mathrm{zy}} & G_{\mathrm{zz}} \end{pmatrix}. \tag{B.15}$$

This can be for example the Green's function matrix. This matrix can be decomposed into irreducible Cartesian tensors $G^{(0)}$, $G^{(1)}_{\mathrm{u}}$, and $G^{(2)}_{\mathrm{uv}}$ using Eq. (B.4). Then each of these can be converted into their corresponding spherical tensors $G_q^{(k)}$. For convenience, I give the spherical tensor elements $G_q^{(k)}$ in terms of the cartesian matrix elements G_{uv}:

$$\begin{aligned}
G^{(0)} &= -\frac{1}{\sqrt{3}}\mathrm{Tr}[G] \qquad (B.16)\\
G_{\pm1}^{(1)} &= \frac{1}{2}\left[G_{\mathrm{zx}} - G_{\mathrm{xz}} \pm i(G_{\mathrm{zy}} - G_{\mathrm{yz}})\right]\\
G_0^{(1)} &= \frac{i}{\sqrt{2}}\left[G_{\mathrm{xy}} - G_{\mathrm{yx}}\right]\\
G_{\pm2}^{(2)} &= \frac{1}{2}\left[G_{\mathrm{xx}} - G_{\mathrm{yy}} \pm i(G_{\mathrm{xy}} + G_{\mathrm{yx}})\right]\\
G_{\pm1}^{(2)} &= \mp\frac{1}{2}\left[G_{\mathrm{xz}} + G_{\mathrm{zx}} \pm i(G_{\mathrm{yz}} + G_{\mathrm{zy}})\right]\\
G_0^{(2)} &= \frac{1}{\sqrt{6}}\left[3G_{\mathrm{zz}} - \mathrm{Tr}[G]\right].
\end{aligned}$$

These equations will be used for the decay rate equations to decompose the Green's function tensor into its spherical tensors.

B.3 Reduced Matrix Element Identities

The Wigner-Eckert theorem is

$$\begin{aligned}
\langle\gamma' j' m'|T_q^{(k)}|\gamma j m\rangle &= \frac{(-1)^{2k}}{\sqrt{2j'+1}}\langle j'm'|jm\,kq\rangle\langle\gamma' j'||T^{(k)}||\gamma j\rangle \qquad (B.17)\\
&= (-1)^{j'-m'}\begin{pmatrix} j' & k & j \\ -m' & q & m \end{pmatrix}\langle\gamma' j'||T^{(k)}||nj\rangle. \qquad (B.18)
\end{aligned}$$

I follow the convention in Varshakovich, Edmunds, and Beloy by adding the $\sqrt{2j'+1}$. Note that Steck does not include this term. The convenience of our convention is that the complex conjugate takes a simple form:

$$\langle\gamma j||T^{(k)}||\gamma' j'\rangle = (-1)^{(j'-j)}\langle\gamma' j'||T^{(k)}||\gamma j\rangle^*. \qquad (B.19)$$

The three-J symbol is related to the Clebsch-Gordon coefficient is

$$\frac{\langle j'm'|jmkq\rangle}{\sqrt{2j'+1}} = (-1)^{j'-m'}\begin{pmatrix} j' & k & j \\ -m' & q & m \end{pmatrix}. \qquad (B.20)$$

The convenience of the three-J symbols is that the symmetries takes a simple form. The three-J symbols are invariant under an even permutation of the columns. An odd permutation of the columns gives a phase factor $(-1)^{j_1+j_2+j_3}$. Changing the sign of all the m quantum numbers gives the same factor:

$$\begin{pmatrix} j_1 & j_2 & j_3 \\ m_1 & m_2 & m_3 \end{pmatrix} = (-1)^{j_1+j_2+j_3} \begin{pmatrix} j_1 & j_2 & j_3 \\ -m_1 & -m_2 & -m_3 \end{pmatrix}. \tag{B.21}$$

The orthogonality condition is

$$(2j+1) \sum_{m_1 m_2} \begin{pmatrix} j_1 & j_2 & j \\ m_1 & m_2 & m \end{pmatrix} \begin{pmatrix} j_1 & j_2 & j' \\ m_1 & m_2 & m' \end{pmatrix} = \delta_{jj'}\delta_{mm'}. \tag{B.22}$$

There are several useful identities for simplifying the reduced matrix element. If we have a reduced matrix element $\langle \gamma j_1' j_2' j' || P^{(k)} || \gamma j_1 j_2 j \rangle$, where $\mathbf{J} = \mathbf{J}_1 + \mathbf{J}_2$, and a tensor operator $P^{(k)}$ only operates in $\mathbf{J}_1$ space, then we can simplify it to

$$\begin{aligned} \langle \gamma j_1' j_2' j' || P^{(k)} || \gamma j_1 j_2 j \rangle = {} & (-1)^{j_1'+j_2+j+k} \sqrt{(2j'+1)(2j+1)} \\ & \begin{Bmatrix} j' & k & j \\ j_1 & j_2 & j_1' \end{Bmatrix} \langle \gamma j_1' || P^{(k)} || \gamma j_1 \rangle. \end{aligned} \tag{B.23}$$

The term in the brackets is the 6-j symbol. It is left invariant by any permutation of the columns, and against interchange of the upper and lower arguments in each of any two columns.

Another useful identity is for simplifying the reduced matrix element for a spherical tensor product:

$$\begin{aligned} \langle \gamma' j' || \{P^{(k_1)} \otimes Q^{(k_2)}\}^{(k)} || \gamma j \rangle = {} & \sqrt{2k+1} \sum_{j''} (-1)^{j'+j+k} \begin{Bmatrix} j' & k & j \\ k_2 & j'' & k_1 \end{Bmatrix} \\ & \times \sum_{\gamma''} \langle \gamma' j' || P^{(k_1)} || \gamma'' j'' \rangle \langle \gamma'' j'' || Q^{(k_2)} || \gamma j \rangle. \end{aligned} \tag{B.24}$$

Appendix C

COMPLEX SYMMETRIC MATRICES

C.1 Diagonalization formalism for complex symmetric matrices

Here we derive the orthogonality and completeness relation for the eigenvectors of a complex symmetric matrix. The eigenvectors and eigenvalues of a matrix $\mathbf{A}$ are defined by the the eigenvalue

$$\mathbf{A}\,\mathbf{u}_i = a_i\,\mathbf{u}_i. \tag{C.1}$$

If $\mathbf{A}$ is Hermitian ($\mathbf{A}^\dagger = \mathbf{A}$), or more generally if normal $[\mathbf{A}, \mathbf{A}^\dagger] = 0$, then the eigenvectors have the orthogonality condition $\mathbf{u}_i^\dagger \cdot \mathbf{u}_j = \delta_{ij}$ and completeness relation $\sum_i \mathbf{u}_i \otimes \mathbf{u}_i^\dagger = \mathbf{1}$. However, the matrix $\mathfrak{g}$ of the Green's function between the atoms is complex and symmetric (see Chapter 4). It is only Hermitian if there is no dissipative terms, in which case $\mathfrak{g}$ is real. In this section, we derive the orthogonality relation for the eigenvectors of a complex symmetric matrix.

First we review the general diagonalization formalism. Any invertible matrix $\mathbf{A}$ has a set of right eigenvectors

$$\mathbf{A}\,\mathbf{u}_i = a_i\,\mathbf{u}_i \tag{C.2}$$

which can be written as

$$\mathbf{AR} = \mathbf{R\Lambda}, \quad \text{where} \quad \mathbf{\Lambda} = a_i\delta_{ij} \tag{C.3}$$

Here $\mathbf{R}$ contains the eigenvectors in the columns (there is an arbitrary normalization for each eigenvector),

$$\mathbf{R}_{ij} = (\mathbf{u}_j)_i \tag{C.4}$$

We can rearrange Eq (C.3) to get

$$\mathbf{R}^{-1}\mathbf{AR} = \mathbf{\Lambda} \tag{C.5}$$

So we see that performing a similarity transformation with $\mathbf{R}$ converts $\mathbf{A}$ into a diagonal matrix consisting of the the eigenvalues.

Similarly, the matrix $\mathbf{A}$ also has a set of left eigenvectors which has the same eigenvalues as the right eigenvalues,

$$\mathbf{v}_i{}^{\mathrm{T}}\mathbf{A} = \mathbf{u}_i{}^{\mathrm{T}}a_i, \quad \text{or} \quad \mathbf{A}^{\mathrm{T}}\mathbf{v}_i = a_i\mathbf{v}_i \tag{C.6}$$

where the second equation is the transpose of the first and shows that the left eigenvectors are the same as the right eigenvectors of the matrix $\mathbf{A}^{\mathrm{T}}$. We can write the eigenvector equation using **L**, which contains the left eigenvectors in its rows,

$$\mathbf{LA} = \mathbf{\Lambda L}, \quad \text{where} \quad \mathbf{L}_{ij} = (\mathbf{v}_i)_j \tag{C.7}$$

The matrix **L** also diagonalizes **A**,

$$\mathbf{LAL}^{-1} = \mathbf{\Lambda} \tag{C.8}$$

Multiplying **L** and **R** together, we get

$$(\mathbf{LR})_{ik} = \sum_j \mathbf{\Lambda}_{ij} \mathbf{R}_{jk} = \sum_j (\mathbf{v}_i)_j (\mathbf{u}_k)_j = \mathbf{v}_i \cdot \mathbf{u}_k \tag{C.9}$$

Multiplying Eq (C.7) by **R** on the right, and Eq (C.3) on the left with **L**, and then setting the two equal, we get

$$[\mathbf{LR}, \mathbf{\Lambda}] = 0 \tag{C.10}$$

which requires that **LR** is diagonal, or that

$$\mathbf{v}_i \cdot \mathbf{u}_k = 0 \quad \text{for} \quad i \neq k \tag{C.11}$$

All the above formalism is true for any invertible matrix **A**. Now I consider the special case where **A** is a complex symmetric matrix, $\mathbf{A} = \mathbf{A}^{\mathrm{T}}$. From the second part of Eq (C.6), we see that $\mathbf{u}_i$ and $\mathbf{v}_i$ are the same set of vectors. However it is important to remember that every eigenvectors has an arbitrary normalization. I fix the normalization in the following way. First I assume $\mathbf{v}_i = \mathbf{u}_i$. Then it follows that

$$\mathbf{L} = \mathbf{R}^{\mathrm{T}} \tag{C.12}$$

Then I normalize $\mathbf{u}_i$ so that $\mathbf{u}_i^{\mathrm{T}} \cdot \mathbf{u} = 1$, so then we get $\mathbf{LR} = 1$ (see Eq (C.9)), or

$$\mathbf{L} = \mathbf{R}^{-1} \tag{C.13}$$

and combining the last two equations

$$\mathbf{R}^{T} = \mathbf{R}^{-1} \tag{C.14}$$

So in summary, we have shown that a complex symmetric matrix $\mathbf{A} = \mathbf{A}^{\mathrm{T}}$ has the same left and right eigenvectors, that **A** is diagonalized by **R** where $\mathbf{R}^{-1} = \mathbf{R}^{\mathrm{T}}$, that **R** contains the eigenvectors $\mathbf{u}_i$ in its columns, and that the eigenvectors obey

$$\mathbf{u}_i \cdot \mathbf{u}_j = \delta_{ij} \tag{C.15}$$

C.2 Circulant Matrices

An $N \times N$ circulant matrix $\mathbf{A}$ has the form

$$\mathbf{A} = \begin{pmatrix} c_0 & c_{N-1} & \dots & c_2 & c_1 \\ c_1 & c_0 & c_{N-1} & & c_2 \\ \dots & & & & \end{pmatrix}$$

The eigenmodes of an $N \times N$ circulant matrix are

$$\mathbf{u}_j = \frac{1}{\sqrt{N}} \left(1, \quad w_j, \quad w_j^2, \quad \cdots, \quad w_j^{N-1}\right) \quad \text{for} \quad j = 0, 1, \cdots, N-1, \quad \text{where} \quad w_j = e^{2\pi \mathrm{i} j/N} \tag{C.16}$$

The corresponding eigenvalues are

$$\lambda_j = c_0 + c_{N-1}\omega_j + +c_{N-2}\omega_j^2 + \ldots + c_1\omega_j^{N-1}, \quad j + 0, 1, \ldots, N-1. \tag{C.17}$$

C.3 Nearest neighbor interactions

For a chain of periodically spaced atoms placed in even antinodes of the Bloch modes, the dipole-projected Green's function matrix reads

$$\mathfrak{g} = J_{1\mathrm{D}} \begin{pmatrix} 1 & \chi & \chi^2 & \cdots & \chi^{N-1} \\ \chi & 1 & \chi & \cdots & \chi^{N-2} \\ \vdots & \vdots & \vdots & \ddots & \vdots \\ \chi^{N-1} & \chi^{N-2} & \chi^{N-3} & \cdots & 1 \end{pmatrix}, \tag{C.18}$$

where we have defined $\chi \equiv e^{-\kappa_x d}$, with d being the distance between nearest-neighbor atoms. The matrix $\mathfrak{g}$ is a real symmetric Toeplitz matrix (or bisymmetric matrix). Neglecting higher order contributions besides first-neighbor, an approximation valid for $\kappa_x d \gg 1$, $\mathfrak{g}$ becomes a tridiagonal Toeplitz matrix whose eigenvalues and eigenvectors are:

$$\lambda_\xi \equiv J_{1\mathrm{D},\xi} = 1 + 2e^{-\kappa_x d} \cos\left(\frac{\xi\pi}{N+1}\right), \tag{C.19a}$$

$$v_{\xi,j} = \sqrt{\frac{2}{N+1}} \sin\left(\frac{\xi j \pi}{N+1}\right). \tag{C.19b}$$

Appendix D

1D WAVE EQUATION AND GREEN'S FUNCTION

D.1 3D to 1D

We start with the Maxwell's three dimensional wave equation in the frequency domain (see Eq. (2.11)) :

$$\nabla \times \nabla \times \mathbf{E}(\mathbf{r}, \omega) - \frac{\omega^2}{c^2}\epsilon(\mathbf{r})\mathbf{E}(\mathbf{r}, \omega) = \frac{1}{\epsilon_0}\frac{\omega^2}{c^2}\mathbf{P}(\mathbf{r}, \omega) \tag{D.1}$$

Here the source term $\mathbf{p}(\mathbf{r}, \omega)$ is an oscillating polarization density. The three dimensional Green's Function equation is (see Eq. (2.12))

$$\nabla \times \nabla \times \mathbf{G}(\mathbf{r}, \mathbf{r}', \omega) - \frac{\omega^2}{c^2}\epsilon(\mathbf{r})\mathbf{G}(\mathbf{r}, \mathbf{r}', \omega) = \frac{\omega^2}{c^2}\delta(\mathbf{r} - \mathbf{r}')\mathbf{1} \tag{D.2}$$

Here the Green's function is normalized to have units $1/L^3$.

The Dyson equation (see Eq. (2.13)) gives the electric field response for a given oscillating polarization density:

$$\mathbf{E}(\mathbf{r}, \omega) = \mathbf{E}_0(\mathbf{r}, \omega) + \int \mathrm{d}^3\mathbf{r}'\, \mathbf{G}(\mathbf{r}, \mathbf{r}', \omega)\frac{\mathbf{P}(\mathbf{r}', \omega)}{\epsilon_0} \tag{D.3}$$

Now I will convert these equations to their 1D counterpart. I assume that the electric field and polarization density are universe in the yz plane. Then I can take $\nabla \times \nabla \times = \nabla(\nabla\ ) - \nabla^2 \rightarrow -\frac{d^2}{dx^2}$. Next I assume that all the vectors are aligned in the same direction so that I can treat them as scalars. The wave equation then becomes

$$\left[\frac{d^2}{dx^2} + \frac{\omega^2}{c^2}\epsilon(x)\right] E(x, \omega) = -\frac{1}{\epsilon_0}\frac{\omega^2}{c^2}P(x, \omega) \tag{D.4}$$

The 3D Green's function is written in terms of a point source in 3D space, but now I am interested in planar source. I can integrate over the area of the transverse plane and define $G^{1\mathrm{D}}(x, x', \omega) = \int \mathrm{d}A G(\mathbf{r}, \mathbf{r}', \omega) = A\, G(\mathbf{r}, \mathbf{r}', \omega)$, where A is the area integrated over the yz plane. This 1D Green's function has units $1/L$. Now the 1D Green's function is

$$\left[\frac{d^2}{dx^2} + \frac{\omega^2}{c^2}\epsilon(x)\right] G^{1\mathrm{D}}(x, x', \omega) = -\frac{\omega^2}{c^2}\delta(x - x') \tag{D.5}$$

Finally the Dyson equation becomes

$$\boxed{E(x,\omega) = \int \mathrm{d}x' G^{1\mathrm{D}}(x,x',\omega)\frac{P(x',\omega)}{\epsilon_0}} \tag{D.6}$$

It is important to note that $P(x',\omega)$ is still a three dimensional polarization density. But since we have assumed uniformity in the yz plane, we can view it as sheet of oscillating polarization. For an oscillating point dipole $\mathbf{p}$ at position $\mathbf{r}_0$ in three-dimensional space, we previously could write the emitted electric field as $\mathbf{E}_{\text{dipole}}(\mathbf{r},\omega) = \mathbf{G}(\mathbf{r},\mathbf{r}_0,\omega)\,\mathbf{p}/\epsilon_0$. Similarly, we can write the electric field from an oscillating sheet of dipole $P(x) = \delta(x)p\eta$, where p is an oscillating dipole, and η is dipoles density per unit area, as $E(x') = G^{1\mathrm{D}}(x,x';\omega)\,p\,\eta/\epsilon_0$.

D.2 Solution to the 1D Green's function

There are multiple ways to solve the for the 1D Green's function. We could express it as a sum of eigenmodes of a Hermetian operator, as is done for three-dimensional photonic crystal. For the Helmoltz equation, we could use complex integration. However, there are usually easier solutions in the 1D case. We could just treat the delta function as a dipole source and sum up the resulting fields everywhere, using the transfer matrices to assist. However, there is usually an even easier solution in 1D.

The Green's function can be written in terms of just the left-incoming $\phi_L(x)$ and right-incoming $\phi_R(x)$ solutions to the wave equation. $\phi_L(x)$ is the solution to the wave equation for incoming wave e^{ikx} from the left, and $\phi_R(x)$ is the solution to the wave equation for incoming wave e^{-ikx} from the right. The derivation is given in the next section. The solution is

$$G^{1\mathrm{D}}(x,x';\omega) = -\left(\frac{\omega^2}{c^2}\right)\left[\frac{\Theta(x'-x)\phi_L(x')\phi_R(x) + \Theta(x-x')\phi_R(x')\phi_L(x)}{W(x')}\right] \tag{D.7}$$

$$W(x') = \phi_R(x')\phi_L'(x') - \phi_R'(x')\phi_L(x') = 2itk \tag{D.8}$$

where the Wronskian $W(x')$ is a constant (independent of x', although it is convenient to define it at x') proportional to t, the complex the transmission through the entire system. $\Theta(x)$ is the Heaviside function. Also $k = \omega/c$.

When L is real and Hermitian (see Barton chapter 2), then the Green's function has the property

$$G^{1\mathrm{D}}(x,x') = G^{1\mathrm{D}}(x',x) \tag{D.9}$$

Using this equation, we find that the free-space Green's function is given by

$$G_{\text{free-space}}(x, x'; w) = \frac{\mathrm{i}}{2k}\, e^{\mathrm{i}k|x'-x|} \tag{D.10}$$

This result is the same as obtained by the complex integral technique (Appendix E in [64]).

One more comment is that this solution also works for lossy dielectrics, when $\epsilon(x)$ has an imaginary component. But then I don't think the previous Green's symmetry holds.

D.3 Derivation of 1D Green's function solution

We want to find a solution to the 1D Green's function of Eq. (D.5). The proof is outlined here because I think it provides an intuitive way to think about the 1D Green's function. The reader should refer to Ref. [64] or Ref. [126] for more details. We treat x' as just a constant in this equation. When $x \neq x'$, then the equation is just a 2nd order linear homogeneous ODE. We define a more general 2nd order linear homogeneous ODE as

$$-\left(\frac{d^2}{dx^2} + q(x)\frac{d}{dx} + r(x)\right)\phi(x) = L\phi(x) = 0 \tag{D.11}$$

For the 1D Green's function, $q(x) = 0$ and $r(x) = \epsilon(x)\omega^2/c^2$. The Wronskian for two solutions $\phi_1(x)$ and $\phi_2(x)$ is defined as

$$W(x) = \phi_1(x)\phi_2'(x) - \phi_1'(x)\phi_2(x) \tag{D.12}$$

If two solutions ϕ_1 and ϕ_2 are linearly dependent, then their Wronskian is equal to zero. If the solutions are linearly independent, then the Wronskian is equal to

$$W(x) = \text{const}\ \exp(-\int dx\, q(x)) \tag{D.13}$$

Therefore, if $q(x) = 0$, then the Wronskian is a constant. Using the Wronskian, it is easy to show that for the homogenous operator L, there are two and only two linearly independent solutions $\phi_1(x)$ and $\phi_2(x)$.

Next we consider Green's function

$$L\, G(x, x') = \alpha\, \delta(x - x') \tag{D.14}$$

For the 1D wave equation Green's function, $\alpha = \omega^2/c^2$. When $x \neq x'$, then $LG(x, x') = 0$ and it is homogeneous. Our strategy for the solution of the Green's function is the following. We will start with two boundary conditions (BC's), one for the left-hand side and one for the right-hand side. One example could be $\phi(x_1) = 0$ for $x_1 < x'$ and $\phi(x_2) = 0$ for $x_2 > x'$. For the wave equation, we will instead use asymptotic BC's:

$$\text{left-hand BC: } \phi(x_1) \propto e^{-\mathrm{i}kx_1} \quad \text{for} \quad x_1 \to -\infty \tag{D.15}$$

$$\text{right-hand BC: } \phi(x_2) \propto e^{+\mathrm{i}kx_2} \quad \text{for} \quad x_2 \to \infty \tag{D.16}$$

We find a solution $\phi_1(x)$ that satisfies the left-hand BC and a solution $\phi_2(x)$ that satisfies the right-hand BC. Then Green's function is then of the form

$$G(x, x') = \Theta(x' - x)\, C\, \phi_1(x) + \Theta(x - x')\, D\, \phi_2(x) \tag{D.17}$$

The constants C and D can be a function of x', because we are treating x' as a constant. Since we have two more constants, we need two more BC's. By integrating Eq. (D.14) around the delta function $\delta(x)$ once and twice, we obtain two more constraints (the jump condition and the continuity condition) for the Green's function. The final solution is given here

$$G(x, x') = -\alpha \frac{\Theta(x' - x)\phi_2(x')\phi_1(x) + \Theta(x - x')\phi_1(x')\phi_2(x)}{W(x')} \tag{D.18}$$

where $\Theta(x)$ is the Heaviside function.

Now we consider specifically for the 1D wave equation and Green's function, where

$$L = \frac{d^2}{dx^2} + \frac{\omega^2}{c^2}\epsilon(x) \quad \text{and} \quad \alpha = \frac{\omega^2}{c^2} \tag{D.19}$$

First I define two solutions. Let $\phi_L(x)$ be the solution to the wave equation for an incoming traveling wave $e^{\mathrm{i}kx}$ from the left. Let $\phi_R(x)$ be the solution to the wave equation for an incoming traveling wave $e^{-\mathrm{i}kx}$ from the right. Note that $\phi_R(x)$ satisfies the asymptotic left-hand BC of Eq. (D.15), and $\phi_L(x)$ satisfies the right-hand BC of Eq. (D.16). We can therefore use $\phi_1(x) = \phi_R(x)$ and $\phi_2(x) = \phi_L(x)$.

Since the Wronskian is a constant, we can calculate it far from the system. For example, we consider the Wronskian far to the right of our system (where the index of refraction is one). Let the total system have reflection and transmission r and t. Then the solutions far to the right of the system are $\phi_L(x) = te^{\mathrm{i}kx}$ and $\phi_R(x) = e^{-\mathrm{i}kx} + re^{\mathrm{i}kx}$. The Wronskian is then

$$W(x') = 2\mathrm{i}\, t\, k \tag{D.20}$$

Then the solution for the 1D Green's function to the wave equation is

$$G^{\mathrm{1D}}(x,x';\omega)=\left(\frac{\mathrm{i}\omega^2}{2tkc^2}\right)\left[\Theta(x'-x)\phi_L(x')\phi_R(x)+\Theta(x-x')\phi_R(x')\phi_L(x)\right] \tag{D.21}$$

where again t is complex the transmission through the entire system, and $\phi_L(x)$ is the solution for incoming wave $e^{\mathrm{i}kx}$ from the left, and $\phi_R(x)$ is the solution for incoming wave $e^{-\mathrm{i}kx}$ from the right.

D.4 1D Cavity Green's Function

The case with no mirrors is just the free-space Green's function:

$$G_{\text{free-space}}(x,x';w)=\frac{\mathrm{i}}{2k}\,e^{\mathrm{i}k|x'-x|} \tag{D.22}$$

Using the transfer matrix formalism, or just summing the series of traveling waves, we find that the fields inside a cavity centered at $x=0$ from a wave from the left ϕ_L^{cavity} and right ϕ_R^{cavity} are

$$\phi_{\mathrm{L}}^{\text{cavity}}=\frac{te^{\mathrm{i}kL}(e^{\mathrm{i}kx-\mathrm{i}kL/2}+re^{-\mathrm{i}kx+\mathrm{i}kL/2})}{1-r^2e^{2\mathrm{i}kL}}\quad\text{and}\quad\phi_{\mathrm{R}}^{\text{cavity}}=\phi_{\mathrm{L}}^{\text{cavity}}(x\to -x) \tag{D.23}$$

Note that, as always in these notes, I am using $e^{\mathrm{i}kx}$ as a left-going wave. By putting these solutions in Eq. (D.21) and simplifying, we obtain the cavity Green's function. Because the the Green's function is symmetric with respect to x and x', I only give the solution for $x'>x$. We assume that r is real and negative, and use $R=r^2$. The real and imaginary parts of the unit-less Green's function are

$$\begin{aligned}\operatorname{Im}G_{\text{cavity}}(x'>x)&=\frac{1}{2}\frac{(1-R)}{(1-R)^2+4R\sin^2[kL]}\\ &\times\Big((1+R)\cos[k(x'-x)]-2\sqrt{R}\cos[k(x+x')]\cos[kL]\Big)\end{aligned} \tag{D.24}$$

$$\begin{aligned}\operatorname{Re}G_{\text{cavity}}(x'>x)&=\frac{1}{2}\sin[k(x'-x)]-\frac{\sqrt{R}\sin[kL]}{(1-R)^2+4R\sin^2[kL]}\\ &\times\Big((1+R)\cos[k(x+x')]-2\sqrt{R}\cos[k(x'-x)]\cos[kL]\Big)\end{aligned} \tag{D.25}$$

The maximum from ImG occurs when on-resonant, where the front coefficient is $\frac{1}{2(1-R)}$. The half-maximum occurs at $\sin(kL)\approx\pm\frac{1-R}{2\sqrt{R}}$. Ignoring the first term, the maximum for ReG instead occurs at the half-maximum and the front coefficient is $\frac{1}{4(1-R)}$. So the maximum ReG is 1/2 of the maximum ImG.

We can look at a few scenarios. As a sanity check, we can check that we recover the free-space Green's function from Eq. (D.10) when $r=0$.

Self-Green's function or $\lambda/2$ spacing, $k(x' - x) = m\pi$

Note that this case includes the self-Green's function, $x = x'$. Here we can take $k(x + x') = 2kx + m\pi$. We get

$$\operatorname{Im} G_{\text{cavity}}(x' = x{+}m\lambda/2) = (-1)^m \frac{1}{2} \frac{(1-R)}{(1-R)^2 + 4R\sin^2[kL]} \Big((1+R) - 2\sqrt{R}\cos[2kx]\cos[kL] \Big) \tag{D.26}$$

$$\operatorname{Re} G_{\text{cavity}}(x' = x{+}m\lambda/2) = (-1)^m \frac{\sqrt{R}\sin[kL]}{(1-R)^2 + 4R\sin^2[kL]} \Big((1+R)\cos[2kx] - 2\sqrt{R}\cos[kL] \Big) \tag{D.27}$$

A useful identity is $\cos[a+b] + \cos[a-b] = 2\cos[a]\cos[b]$ and $\cos[a+b] - \cos[a-b] = -2\sin[a]\sin[b]$. I can use these to show how interactions are infinite range for when $R \approx 1$.